

QUANTITATIVE SPECTROSCOPY OF
STELLAR ATMOSPHERES AND CLUMPED
HOT STAR WINDS
- NEW METHODS AND FIRST RESULTS FOR
DERIVING MASS-LOSS RATES.



Jon Sundqvist

QUANTITATIVE SPECTROSCOPY OF
STELLAR ATMOSPHERES AND CLUMPED
HOT STAR WINDS
- NEW METHODS AND FIRST RESULTS FOR
DERIVING MASS-LOSS RATES.

Dissertation

an der Fakultät für Physik
der Ludwig–Maximilians–Universität (LMU) München

Ph.D. Thesis

at the faculty of Physics
of the Ludwig–Maximilians–University (LMU) Munich

submitted by

Jon Sundqvist

from Östersund, Sweden

Munich, September 29th 2010

1st Evaluator: Priv. Doz. Dr. Joachim Puls

2nd Evaluator: Prof. Dr. Andreas Burkert

Date of the oral Defense: 20th December 2010

Contents

Contents	vii
List of Figures	xiv
List of Tables	xv
Zusammenfassung	xvii
Preface	xix
1 Introduction	1
1.1 The role of mass loss from hot, massive stars in modern astrophysics	1
1.2 Stellar winds, mass loss, and evolution	2
1.3 Radiation driven winds of hot, massive stars	3
1.4 A clumped hot star wind?	3
1.4.1 Theoretical predictions of a small-scale inhomogeneous wind	4
1.4.2 Observational indications of an inhomogeneous wind	4
1.4.3 Indirect indications of an inhomogeneous wind	5
1.4.4 Some implications of modified mass-loss rates due to wind clumping	9
1.5 Spectroscopic analyses of stars using model atmospheres	11
1.5.1 Model atmospheres and spectrum synthesis	11
1.5.2 Spectral line formation and the assumption of LTE	11
Particle velocities.	12
Level population numbers and the Kirchoff-Planck relation.	13
Spectral line formation.	14
The equations of statistical equilibrium.	15
1.5.3 Comparisons of atmospheric codes - photospheric models	16
1.5.4 NLTE line formation in the infra red	18
1.5.5 Comparisons of atmospheric codes - unified models	19
2 Mass loss from OB-stars	22
2.1 Abstract	22
2.2 Introduction	22
2.3 Line-driven winds from hot stars – theoretical predictions	23
2.3.1 Scaling relations and WLR	24

2.3.2	Theoretical 1-D models	24
	Results and predictions from hydrodynamic modeling.	25
2.4	Observations vs. Theory	25
2.4.1	Central results	26
2.4.2	The bi-stability jump: predictions and observations	26
2.4.3	The FLAMES survey of massive stars	26
2.5	Weak winds	27
2.6	Wind clumping	28
2.7	Weak winds again – Br_α as a diagnostic tool	31
2.8	Addendum	31
3	Radiative transfer in stochastic media and hot star winds	
	- microclumping, vorosity, and porosity revisited	33
3.1	Transfer in stochastic media	33
3.2	Microclumping	36
3.3	Vorosity	37
3.4	Porosity	38
3.4.1	Isotropic clumps	39
3.4.2	Fragmented shells, radial streaming of photons.	40
3.4.3	Fragmented shells, including non-radial photons.	40
3.4.4	A porosity formalism for ρ^2 -diagnostics.	41
4	Mass loss from inhomogeneous hot star winds	
	I. Resonance line formation in 2D models	43
4.1	Abstract	43
4.2	Introduction	44
	Optically thin vs. optically thick clumps.	45
4.3	Wind models	45
4.3.1	Radiation-hydrodynamic wind models	45
4.3.2	Stochastic wind models	46
	A model clumped in density.	47
	A model clumped in density and velocity.	48
4.4	Radiative transfer	49
4.5	First results from 2D inhomogeneous winds	49
4.5.1	Observer’s position and opening angles	50
4.5.2	Radiation-hydrodynamic models	51
4.5.3	Stochastic models	51
	Strong lines.	51
	Intermediate lines.	53
	Weak lines.	53
4.5.4	Comparison between stochastic and radiation-hydrodynamic models	54
4.6	Parameter study	55
4.6.1	The effective escape ratio	55
4.6.2	Density parameters	56
4.6.3	Velocity parameters	58

4.7	Discussion	59
4.7.1	The shapes of the intermediate lines	59
4.7.2	The onset of clumping and the blue edge absorption dip	61
4.7.3	The velocity spans of the clumps	62
4.7.4	3D effects	64
4.7.5	Comparison to other studies	64
4.7.6	Comparison to observations	65
4.8	Summary and future work	67
4.8.1	Summary	67
4.8.2	Future work	68
4.9	The Monte-Carlo transfer code	69
4.9.1	The code	69
	Geometry.	69
	Releasing photons.	70
	Absorption.	70
	Re-emission.	71
4.9.2	Radiative transfer code tests	72
4.10	The effective escape ratio	73
5	Mass loss from inhomogeneous hot star winds	
	II. Constraints from a combined optical/UV study	75
5.1	Abstract	75
5.2	Introduction	76
5.3	Wind models and radiative transfer	77
5.3.1	Geometry	79
5.3.2	Parameters describing a structured wind	80
5.3.3	Code verifications	81
	The He II blend in H_{α}	81
5.4	Theoretical considerations of resonance and recombination line formation in clumpy winds	82
5.4.1	Analytic treatment of resonance lines in clumpy winds	82
5.4.2	Recombination lines in clumpy winds	84
	Analytic treatment of recombination lines.	86
5.5	A multi-diagnostic study of λ Cep	86
5.5.1	Clump optical depths	87
5.5.2	Constraints from inhomogeneous radiation-hydrodynamic models	87
	Comparison with the microclumping technique.	88
5.5.3	Constraints from empirical stochastic models	90
	Comparison with the microclumping technique.	92
5.6	Discussion	92
5.6.1	Are O star mass-loss rates reliable?	92
	Theoretical rates.	92
	Empirical rates.	93
5.6.2	Structure properties of the clumped wind	93
5.7	Additional considerations	94

5.7.1	Weak wind stars	94
5.7.2	Resonance line doublets	96
5.8	Summary and future work	97
5.9	Analytic treatment of line formation in clumped hot star winds	98
	Resonance lines.	98
	Recombination lines.	100
6	Mg I emission lines at 12 & 18 μm in K giants	102
6.1	Abstract	102
6.2	Introduction	103
6.3	Observations	104
6.4	Departure coefficient ratios	105
6.5	Modeling	106
6.5.1	Model atmospheres and stellar parameters	106
6.5.2	The model atom	107
	Enlargement of the model atom	107
	Collisional data	108
	Collisions with neutral hydrogen	108
	Collisional excitation from electrons	110
	l-changing collisions	110
6.6	Results	111
6.6.1	Emission lines at 12 μm	111
6.6.2	Mg I emission lines at 18 μm	114
6.7	Discussion and conclusions	116
6.7.1	The model atom extension	116
6.7.2	Effects from extra collisions	116
6.7.3	Observations of Rydberg emission lines around 12 μm	117
6.7.4	Comparison with other studies	117
7	Summary and outlook	119
7.1	Summary	119
7.2	Outlook	120
7.2.1	Quantitative spectroscopy	120
7.2.2	Theoretical wind models of hot stars	122
7.2.3	Further applications	123
A	More on the radiative transfer codes	124
A.0.4	Geometry - the Monte-Carlo resonance line code	124
	Updating the radiation coordinates.	126
	The path length l	126
	Crossing wind-slice borders in Θ	126
	Collecting escaping photons.	128
A.0.5	Geometry - the recombination line code	129
A.0.6	Geometry - the patch wind model	129
	Modifying the patch geometry.	130

A.0.7	Line opacities	131
	Resonance lines.	131
	Recombination lines - H_{α}	132
	Recombination lines - He II 4686 Å.	134
	Bibliography	135
	Acknowledgments	145
	Curriculum Vitae	147

List of Figures

1.1	Snapshot from a time-dependent, radiation-hydrodynamic wind model of λ Cep . . .	5
1.2	Observed and synthetic PV and H_α line profiles in λ Cep.	6
1.3	Ionization fractions of NV	8
1.4	Sketch of photon line scattering through an atmosphere	12
2.1	Density contours of and line profiles calculated from inhomogeneous wind models . .	30
3.1	Illustration of vorosity	38
4.1	Density contours and density and velocity structures of RH and stochastic wind models	46
4.2	Non-monotonic velocity field and corresponding parameters in a stochastic model. .	49
4.3	Synthetic line profiles calculated from 2D RH models.	50
4.4	Synthetic line profiles calculated from 2D stochastic models	52
4.5	Velocity and density structures of comparable RH and stochastic models	54
4.6	Schematics of velocity gaps between clumps and the effective escape ratio	55
4.7	Equivalent widths of the absorption parts of resonance line profiles	57
4.8	Velocity structures of a stochastic model and a corresponding strong synthetic resonance line profile	60
4.9	Resonance line profiles calculated from smooth models and stochastic ones	60
4.10	Absorption parts of resonance line profiles with varying ionization fractions	61
4.11	Velocity spans of density enhancements in a RH model	63
4.12	Observed and modeled PV line profiles for λ Cep	65
4.13	Illustration of the 2D coordinate system used in resonance line modeling	70
4.14	Comparison of resonance line profiles modeled by different techniques	72
5.1	Illustration of the wind geometry	79
5.2	ξ parameter and analytic and MC resonance absorption part line profiles	82
5.3	Theoretical H_α lines in clumpy winds	85
5.4	Radial clump optical depths for PV and H_α	87
5.5	Clumping factors, ion fractions, and departure coefficients in λ Cep	88
5.6	Observed and synthetic line profiles for λ Cep	89
5.7	Observed and synthetic line profiles for λ Cep	90
5.8	Equivalent widths for the absorption part of the NV resonance line at 1240 \AA	95
6.1	Illustration of the ‘Rydberg ladder’ for Mg I	106
6.2	Solar departure coefficients for Mg I Rydberg state energy levels with $n \geq 5$	109

6.3	Mg I 12.22 μm lines in Arcturus and Aldebaran	112
6.4	Mg I 12.22 μm lines in Pollux and the Sun	112
6.5	Observed spectra around 12.3 μm region	113
6.6	The Mg I 18.83 μm in Pollux, Arcturus, and the Sun	115
A.1	Illustration of the coordinate system used in resonance line modeling	124

List of Tables

4.1	Basic parameters defining a stochastic wind model	48
4.2	Primary stochastic wind models and parameters	51
5.1	Parameters for the time-dependent RH model of λ Cep (see text).	78
5.2	Basic structure parameters defining a stochastic wind model.	80
5.3	Structure parameters for an empirical stochastic wind model of λ Cep	86
6.1	Summary of observed magnesium emission line properties	114
6.2	Emission line properties around $12 \mu\text{m}$ in Pollux and Arcturus (not magnesium) . . .	115

Zusammenfassung

Der stellare Massenverlust (und insbesondere die entsprechende *Rate*) ist eine zentrale Größe in der Beschreibung heißer, massereicher Sterne. Er beeinflusst ihre Entwicklung und ihr finales Schicksal, und ist entscheidend für verschiedene ‘feedback’-Effekte, wie beispielsweise ionisierende Flüsse, stellare ‘yields’ und Energie- und Impulsabgabe. Gegenwärtige Untersuchungen legen es nahe, dass die derzeit verwendeten Massenverlustraten von O-Sternen aufgrund des Einflusses von Windinhomogenitäten (‘Klumpung’) reduziert werden müssen, um eine Größenordnung oder sogar mehr. Falls zutreffend, würde dies enorme Auswirkungen auf die Sternentwicklung massereicher Sterne und deren feedback implizieren, und auf die große Zahl damit verbundener astrophysikalischer Anwendungen.

Sowohl die Modellierung der Atmosphären massereicher Sterne als auch ihrer spektraler Energieverteilung unter Berücksichtigung der Windklumpung befinden sich jedoch noch in einem Anfangsstadium, und die Resultate oben genannter Untersuchungen wurden kürzlich in Frage gestellt, insbesondere im Hinblick auf die übliche Annahme, dass die Klumpen *optisch dünn* für typische Spektrallinien seien.

In vorliegender Arbeit werden neue, verbesserte Methoden für die Modellierung der Linienbildung in strukturierten Winden heißer Sterne entwickelt. Es wurde eine detaillierte Untersuchung des Einflusses *optisch dicker* Klumpung auf die Bildung von UV Resonanz- und optischen Rekombinationslinien durchgeführt, wobei diese Linien die gebräuchlichsten Massenverlustindikatoren sind. Unsere Untersuchungen zeigen, dass unter typischen Bedingungen die Klumpen *nicht* optisch dünn bzgl. obiger Prozesse sind. Würde man trotzdem – und wie derzeit ‘üblich’ – in einer Analyse der Resonanzlinien optisch dünne Klumpen annehmen, könnte man die Massenverlustraten bis zu eine Größenordnung *unterschätzen*.

Erste quantitative Ergebnisse wurden anhand einer exemplarischen *Multi-Diagnostik* Analyse des galaktischen O-Überriesen λ Cep erzielt. Synthetische Spektrallinien, die auf inhomogenen strahlungshydrodynamischen Windmodellen basieren, können die *beobachteten* Linien nicht reproduzieren. Deshalb wurden entsprechende stochastische Modelle entwickelt, mit dem Ziel, die Essenz des strukturierten Mediums empirisch zu erfassen. Mit Hilfe dieser Modelle wurden konsistente Fits der beobachteten Daten erreicht, die darauf hindeuten, dass der innere Windbereich (erheblich) stärker geklumpt ist als von der Theorie vorhergesagt, und dass der Bereich beitragender Geschwindigkeiten in den Klumpen kleiner als prognostiziert ist. Die abgeleitete Massenverlustrate für λ Cep ist ca. zweimal niedriger als von der Theorie vorhergesagt, allerdings um einen Faktor fünf höher als diejenige, die man aus der Annahme optisch dünner Klumpung ableiten würde. Unsere prototypische Analyse hat damit die derzeitig diskutierte signifikante Diskrepanz zwischen Theorie und Beobachtung gemildert, aber nicht vollständig aufgelöst.

Darüber hinaus haben wir neue analytische Methoden zur Spektralanalyse in inhomogenen Winden

entwickelt, die unabhängig von Annahmen bzgl. der optischen Dicke der Klumpen ist. Erste vielversprechende Ergebnisse wurden vorgestellt, und wir schlagen vor, die neue Methoden auf eine quantitative Multi-Wellenlängenstudie (vom Röntgen- bis zum Radiobereich) inhomogener heißer Sternwinde anzuwenden.

Ein Nebenprojekt vorliegender Arbeit ist die Untersuchung der Bildung photosphärischer Emissionslinien von (hauptsächlich) Mg I bei $12/18 \mu\text{m}$ in kühlen Sternen. Diese Linien können (u.a.) potenziell dahingehend genutzt werden, Magnetfeldstärken in der oberen Photosphäre abzuleiten, aufgrund ihrer Empfindlichkeit bzgl. der Zeeman-Aufspaltung. Bisher wurden Analysen dieser Linien jedoch nur für zwei Zwergsterne (einschliesslich der Sonne) und zwei kühle Riesen versucht, mit sehr unbefriedigenden Ergebnissen für letztere Objekte.

In dieser Arbeit präsentieren wir neuen Beobachtungen der $12/18\mu\text{m}$ Emissionslinien in K-Riesen und zeigen durch eine detaillierte non-LTE Modellierung für Magnesium, dass der Linienbildungsmechanismus der gleiche wie in der Sonne ist. Wir zeigen auf, warum frühere Versuche einer Modellierung erfolglos waren, und betonen, dass die Synthetisierung dieser Linien sehr empfindlich von den atomaren Daten abhängt. Damit zeigen sich diese Linien auch als entscheidende Konsistenzindikatoren für Modellatome, wie sie in Multi-Wellenlängenstudien von Oberflächenhäufigkeiten verwendet werden.

Preface

The bulk of this thesis consists of three so-called first-author papers, two of which already have been published in the refereed journal *Astronomy & Astrophysics* (Chapters 4 and 6), and one which recently has been submitted to the same journal (Chapter 5). These papers are kept in their original form, and may be read quite independently of each other. In addition, Chapter 3 attempts to examine a little further the main topic of this thesis, namely transfer of radiation through clumpy hot star winds. Actually, some of the results given in Chapter 3 were found *after* the connected Chapters 4 and 5 had been written (and published, for the former), but the chapter is nevertheless placed before them in the thesis, for I personally believe that after having read it one may better appreciate the basic methods used later on. Naturally, this introduces some repetition of subjects in Chapters 3-5, which might be annoying for the reader who wishes to read the thesis from ‘cover to cover’. But I hope that for most readers, this approach instead simplifies whenever they find time to peruse their copies. Chapter 2 is a recent review by Puls, Sundqvist et al. (2009) and complements Chapters 3-5 by providing further insight into the main field studied in this thesis. To this chapter is added an addendum, which updates some of the material as well as discusses it in connection to the other chapters. In the following, however, I shall start with an introduction of the basic topics covered. The introduction roughly is divided into two parts, the first dealing with *mass loss from hot, massive stars* and the second with *quantitative spectroscopy of stellar atmospheres* (but surely these topics are highly interconnected). Finally, Appendix A provides some more details on the radiative transfer codes developed in Chapters 4 and 5, and Chapter 7 summarizes our results and outlines some future work.

Chapter 1

Introduction

1.1 The role of mass loss from hot, massive stars in modern astrophysics

Massive stars are fundamental in many fields of modern astrophysics. They are crucial for Galactic evolution: In the present Universe, they dynamically and chemically shape their surroundings and the inter-stellar medium by their output of ionizing radiation, energy and momentum, and nuclear processed material. In the distant Universe, they dominate the ultra-violet (UV) light from young Galaxies. Indeed, massive stars may be regarded as ‘cosmic engines’ (Bresolin et al., 2008). Furthermore, very massive First Stars are thought to play a dominant role in the re-ionization of the Universe and in the first enrichment of metals (Bromm & Larson, 2004; Bromm et al., 2009), and rapidly rotating massive stars are believed to be the progenitors of the most energetic cosmic flash known, the (long-duration) gamma-ray burst (GRB) (Woosley, 1993). Hence, an accurate knowledge of massive stars and their evolution is pivotal for understanding the Universe as a whole.

Recently, great progress has been made in evolutionary as well as in atmospheric modeling of these objects. Nevertheless, a number of very distinct problems remains, especially concerning *dynamical* processes in the stellar interior as well as in the atmosphere (mass loss, rotation, convection, pulsation). Arguably most important in this respect is the *mass loss*. Hot, massive stars possess strong and powerful winds, which affect evolutionary time scales, chemical surface abundances, and luminosities. Indeed, changing the mass-loss rates of massive stars by only a factor of two has a dramatic effect on their overall evolution (Meynet et al., 1994), and even the nature of the supernova explosion critically depends on the precursor’s mass-loss history (Woosley et al., 2002). Reliable mass-loss rates are needed when calculating stellar yields from massive stars, and thereby mass loss is important also for the chemical evolution of galaxies (Romano et al., 2010). Furthermore, ionizing fluxes from hot, massive stars for usage in nebula codes, spectral libraries, and population synthesis are strongly influenced by mass loss. An important application for population synthesis is the modeling of rest-frame UV spectra of high-redshift, star-forming, Lyman-break galaxies, whose spectral features, e.g., provide critical information on star formation at redshifts $z \gtrsim 3$ (Leitherer et al., 2010). Finally, at yet earlier cosmic times, it is currently debated whether or not the very First Stars underwent mass loss strong enough to alter their evolution and the chemical signatures of their deaths (Ekström et al., 2008; Smith, 2008).

Clearly, if research fields such as those outlined above are to move forward with confidence, *reliable prescriptions of mass-loss rates from hot, massive stars are essential.*

1.2 Stellar winds, mass loss, and evolution

Nearly all stars lose mass through a, in principle, steady and continuous surface outflow, a *stellar wind*. The basic requirement for driving such a wind is that there in the outer layers of the star exists an outwards directed force able to overcome the inwards directed gravity, so that material may escape the star. For thorough introductions to stellar winds, see the book by Lamers & Cassinelli (1999) and the book-chapter by Owocki (2010).

Examples of stellar winds are the solar wind, which is driven by gas pressure gradients in the hot corona, and the strong, but slow, winds from red supergiants (RSGs) and asymptotic giant branch (AGB) stars, which are believed to be driven by stellar pulsations and radiation pressure on dust grains. Although these AGB and RSG stars are thought to share driving mechanisms for their winds, the two stellar stages do not share evolutionary origin. An AGB star is the final stage of a low/intermediate-mass star with zero-age main-sequence mass $M_{\text{ZAMS}} \lesssim 8M_{\odot}$ (with M_{\odot} the mass of the Sun). Here the intense AGB mass loss is able to reduce the initial stellar mass to below the Chandrasekhar limit ($M_* \lesssim 1.4M_{\odot}$), leaving behind a planetary nebula and a white dwarf remnant. RSGs, on the other hand, presumably are the evolutionary successors to hot, massive main-sequence stars in the mass range $M_{\text{ZAMS}} \approx 8 - 40M_{\odot}$. According to the standard scenario (Conti, 1976, see also Massey 2003), they are in a Helium burning phase and the end-result of a fast and nearly horizontal evolution from the blue to the red part of the Hertzsprung-Russell (HR) diagram. Some massive stars terminate their lives after this RSG stage, exploding as hydrogen rich core-collapse supernovae, whereas some evolve back to the hot part of the HR diagram (see, e.g., Levesque, 2009), either entering a new yellow/blue supergiant phase or forming hydrogen deficient so-called Wolf-Rayet (WR) stars (which also experience severe mass loss). In this last case, mass loss in the RSG stage may significantly help strip the star's initial hydrogen envelope.

Even more massive stars ($M_{\text{ZAMS}} \gtrsim 40M_{\odot}$) are believed to never leave the blue part of the HR diagram, for they evolve to the WR stage either directly (stars with $M_{\text{ZAMS}} \lesssim 85M_{\odot}$, in one version of the 'Conti-scenario, see Massey 2003) or via a *hot* Luminous Blue Variable (LBV) phase, rather than via a *cool* RSG stage. LBVs represent a short lived phase in massive star evolution in which the star undergoes significant effective temperature changes, as well as in some cases violent eruptive phases with extreme mass loss (see discussion in Puls et al., 2008b). The typical Galactic examples of LBVs are P Cygni and η Carina. Normally it is assumed that these very massive stars after the WR stage explode as hydrogen poor supernovae, but recently it has been shown that the progenitor star to the supernova 2005gl was likely in its LBV phase (Gal-Yam & Leonard, 2009), suggesting that some stars in this mass range may actually meet death already as LBVs. Clearly, our understanding of the late stages in massive star evolution is still far from complete. Nonetheless, it is commonly accepted that *after* the supernova explosions most of the massive stars leave behind them neutron star remnants or even black holes. Note also that the above stated mass ranges may perhaps only be regarded as illustrative; they certainly depend on details in the evolutionary modeling of massive stars, and may also be functions of metallicity. Indeed, mass-loss rates in all the evolved stages discussed above are very challenging to determine, and pose a major uncertainty in present-day evolution models (Woosley et al., 2002).

Another important ingredient in massive star evolution is *stellar rotation*, which can significantly alter the stars' predicted evolution tracks (e.g., Maeder & Meynet, 2000, and subsequent papers; 'evolution with mass loss and rotation'). For example, rapidly rotating massive stars may experience very efficient internal mixing and thereby undergo *chemical homogeneous evolution*, in which strong chemical

gradients never can be established (in contrast to the classic onion like structure of an evolved massive star). Under these conditions, massive helium stars with rapidly rotating cores may form, which presumably are the progenitor stars to the long-duration GRBs (e.g., Yoon et al., 2006). Moreover, *mass loss* and *rotation* are connected in at least two crucial ways: i) The *global* mass-loss rates of rapidly rotating stars may be significantly increased¹, for the centrifugal force decreases the effective gravity that whatever driving force of the wind must overcome, thus making it easier for the stellar material to escape, and ii) mass loss tends to remove angular momentum from the star, thereby decreasing its rotation rate (Langer, 1998). Although this thesis deals mostly with ‘normal’ hot, massive stars, whose mass losses are not believed to be significantly modified by rotation, we shall comment on, for example, the second point above (Sect. 1.4.4) and its effect on the potential creation of RGBs within the scenario just described, which demands that the star keeps a rapid rotation until its death.

1.3 Radiation driven winds of hot, massive stars

The winds from *hot*, massive stars are described by the radiative line-driven wind theory, where the standard model (based on the pioneering works by Lucy & Solomon, 1970; Castor et al., 1975) assumes the wind to be stationary, spherically symmetric, and homogeneous. The (major part of the) driving force within this theory comes from metal UV resonance lines, whose accumulated line force has been shown sufficient to drive the strong and fast winds of OB-stars, A-supergiants, LBVs in their quiet phase, and most probably also WR stars. The main interest in this thesis has been OB-stars, with typical mass-loss rates of $0.1 - 10.0 \times 10^{-6} M_{\odot} \text{yr}^{-1}$. These rates are 10^{7-9} times higher than the rate of the solar wind, but on the same orders of magnitudes, or actually somewhat lower than, the rates of the more evolved hot and cool stars mentioned earlier (i.e., the LBVs, WRs, RSGs, and AGB stars). Details on fundamental theoretical predictions for line-driven winds of OB stars, as well as comparisons to observations, are given in Chapter 2, where for example the wind momentum luminosity relation and the metallicity dependence of mass loss are outlined. Moreover, the so-called ‘weak wind’ problem is covered in that Chapter, whereas ‘clumping’ (the main topic of this thesis) is introduced already here, in the following sections.

1.4 A clumped hot star wind?

In general, numerous observational studies of hot star winds support the line-driven wind theory (Chapter 2). Nevertheless, the theory is probably over-simplified. Comprehensive summaries of current issues² are given in the proceedings from the workshop ‘Clumping in hot star winds’ (Hamann et al., 2008) and in the review of mass loss from hot, massive stars by Puls et al. (2008b). In particular, evidence for an inhomogeneous, time-dependent wind has accumulated over the past years and become overwhelming, from the theoretical as well as the observational side.

¹ If the star also have a luminosity close enough to the Eddington limit, which is the luminosity at which the gravity is precisely balanced by the radiative acceleration from electron scattering in a *spherically symmetric, homogeneous, and radiative* atmosphere.

² which comprise effects of, e.g., stellar rotation and magnetic fields, in addition to the ‘clumping’ and ‘weak-wind’ phenomena discussed here.

1.4.1 Theoretical predictions of a small-scale inhomogeneous wind

It was pointed out already by Lucy & Solomon (1970) that radiation line-driven winds should be intrinsically unstable. This was later confirmed first by linear stability analyses and then by direct radiation-hydrodynamic modeling of the time dependent wind (e.g., Owocki & Rybicki, 1984; Owocki et al., 1988; Feldmeier, 1995; Dessart & Owocki, 2005). The intrinsic line-driven (or line de-shadowing) instability of hot star winds emerges from velocity perturbations on small scales and gives rise to density and velocity inhomogeneities, also occurring on small spatial scales. Numerical simulations following the non-linear evolution of the line-driven flow instability reveal that the intermediate and outer wind (typically, at radii outside $1.3 R_*$, see Fig. 1.1 and Chapter 4) develop a structure consisting of strong reverse shocks separating denser and slower shells from rarefied regions with higher velocities. Most of the material is compressed into these spatially narrow and dense ‘clumps’ (or shells within a spherically symmetric configuration), which are separated by large regions of much lower densities. This characteristic structure (Fig. 1.1) is the basis to our current interpretation of *wind clumping*. However, the *time/spatial-averaged* mass loss from a theoretical inhomogeneous wind is very similar to that of a homogeneous one, even if the overall wind structure at a given point in time only weakly resembles that of a smooth wind. This is important because it suggests that the clumpy medium might not significantly affect theoretical mass-loss predictions calculated from the standard line-driven wind theory³. Instead, the main effect of the inhomogeneities (at least regarding mass loss) is thought to be on mass-loss rates derived from observations, since ‘clumping’ seriously affects the radiative transfer models that are needed to correctly interpret the spectral signatures of stellar winds.

1.4.2 Observational indications of an inhomogeneous wind

In addition to the theoretical considerations discussed above, many observational findings strongly suggest that hot star winds are structured and time dependent. Below we (very) briefly summarize two of these (see Puls et al. 2008b for a more comprehensive overview), namely *line profile variability* and *X-ray emission*.

Line profile variability in the form of narrow sub-peaks, superimposed on broader emission lines, that propagate from the line center to the line wings in time scales similar to the wind flow time, was detected in WR stars already by Moffat et al. (1988) and Robert (1994). A similar discovery was made for the O supergiant ζ Pup by Eversberg et al. (1998). More recently, Lépine & Moffat (2008) showed that these moving sub-peaks existed in a number of WR and O stars, which they suggested being strong support for that stochastic wind clumping is a universal phenomenon in the radiation driven winds of hot, massive stars.

X-ray emission from hot stars was detected already by the EINSTEIN satellite some 30 years ago (Harnden et al., 1979). Later on, the advent of the X-ray satellites XMM-NEWTON and CHANDRA provided increased sensitivity as well as made it possible to perform high-resolution spectroscopy of X-ray emission *lines*. An extensive review on X-ray emission from stars (hot as well as cool) has recently been given by Güdel & Nazé (2009), to which we refer for details. Roughly, the (soft) X-ray luminosity from hot stars scales with the bolometric luminosity as $L_x/L_{\text{bol}} \approx 10^{-7}$. The X-rays are believed to originate in clump-clump collisions in the shock-heated stellar wind (Feldmeier et al., 1997). Generally, the broad emission lines revealed by high-resolution spectra seem to support

³ but see Chapter 5, and also the outlook in Chapter 7, where we comment on that important effects from clumping on, e.g., the ionization wind balance might influence also theoretical predictions.

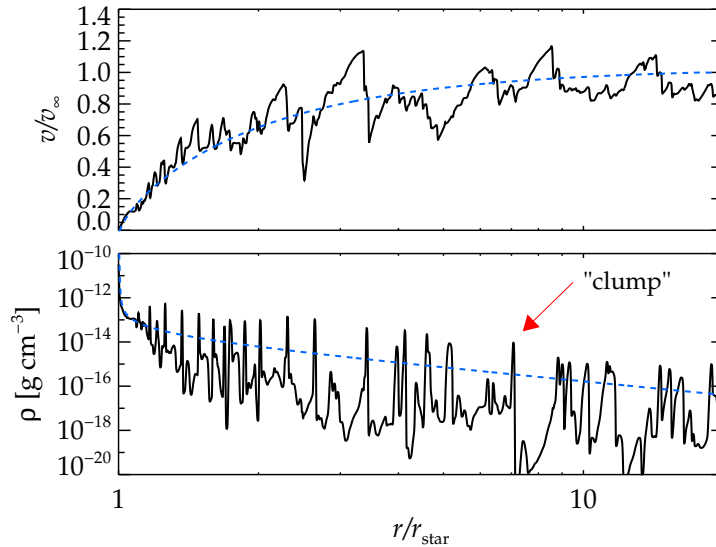


Figure 1.1: Velocity and density structures from a snapshot of a spherically symmetric, time-dependent, radiation-hydrodynamic wind model of λ Cep (Chapter 5). The characteristic structure of spatially narrow regions of very high density in these models (as indicated in the lower panel) is the basis to our current interpretation of wind clumping .

a wind origin for the X-rays, but a number of problems have been identified with the wind-shock scenario, arising from the line-driven instability, and various adjustments to this model in order to better reproduce the observations are currently being debated within the community (see Güdel & Nazé 2009 for a discussion). Regarding mass loss, the most important discovery was the one of more symmetric observed line profiles than expected. ‘Standard’ mass-loss rates predict a heavy attenuation of X-rays, caused by absorption in the ‘cool’ part of the wind. However, photons reaching the observer from the *receding* part of the stellar wind (as seen by the observer) must travel longer within the wind volume than those coming from the advancing part. Consequently photons at the red side of the line-center will be more absorbed than those on the blue side, i.e. strongly skewed profiles are predicted, in contrast with the more symmetric ones observed. This problem can be naturally solved by simply lowering the mass-loss rates, for then the attenuation of X-rays is reduced, which in turn implies more symmetric profiles, consistent with the observations. However, an alternative scenario is that the effects of *optically thick clumps* are important to consider when modeling the observations. If clumps are optically thick for X rays, a *porous* wind results, and the effective opacity may consequently be reduced (Chapter 3). Essentially, this has the same effect on the line profiles as reducing the mass-loss rates, and it remains to be settled which of the two scenarios is more liable (see the next subsection).

1.4.3 Indirect indications of an inhomogeneous wind

Much indirect evidence of wind clumping has arisen from *quantitative spectroscopy* (see Sect. 1.5 for an overview of quantitative spectroscopy of stellar atmospheres). As already mentioned, clumping has severe consequences for the interpretation of observed spectra, and especially mass-loss rates derived from the observations are affected. The main observational diagnostics of OB-star winds are

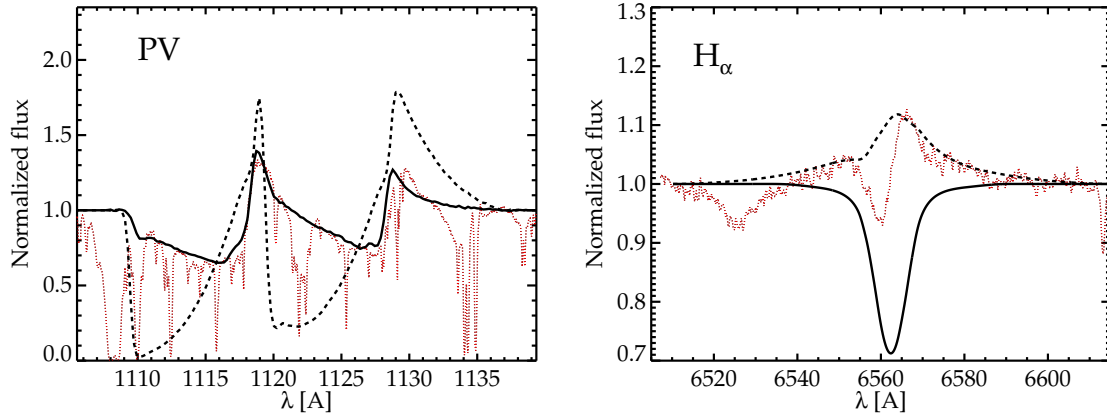


Figure 1.2: Observed (dotted lines) and synthetic (solid and dashed lines) PV and H_α line profiles in λ Cep. Observed spectra are from Fullerton et al. (2006) (PV) and Markova et al. (2005) (H_α). The synthetic line profiles of H_α were calculated with the unified, NLTE atmospheric code FASTWIND (see Sect. 1.5.3), assuming a *smooth* wind. The profiles of PV were calculated with the Monte-Carlo code developed in Chapter 4, also assuming a smooth wind and using FASTWIND ionization fractions. The dashed lines were calculated using a 20 times higher mass-loss rate than the solid lines.

UV resonance lines, H_α line emission (and other recombination lines, for example He II 4686), and infra-red (IR) and radio continuum emission. Recently, X-ray emission *lines* have also been added to the set (see the previous subsection). Obviously, independent of which diagnostic is used, the same mass-loss rate for a given star should be derived. However, as outlined below, this is presently *not* the case.

When smooth wind models are used, the mass-loss rates inferred from different diagnostics, but for the same star, can vary substantially. As an example, we in Fig. 1.2 plot observed and synthetic profiles of H_α and the phosphorus v (PV) UV resonance lines, for the prototypical Galactic O6 supergiant λ Cep. Clearly, the two mass-loss indicators may not be fitted using the same rate; the PV lines suggest a mass-loss rate approximately 20 times lower than the one required for a decent fit of the H_α emission. Moreover, Puls et al. (2006) used a third diagnostic, radio continuum emission, and derived a mass-loss rate for λ Cep that was roughly half of the H_α rate suggested from Fig. 1.2, and thereby again much higher than the one suggested by the PV lines. That is, depending on which diagnostic is used, the ‘observed’ mass-loss rate of λ Cep can vary by more than an order of magnitude! This inconsistency has been interpreted as a consequence of neglecting clumping when deriving these rates⁴. We notice also that the modeled line *shape* of the H_α core is not well matched in Fig. 1.2 (the observed absorption dip on the blue side of the line center is missing); this as well is improved when clumping is considered in the analysis (see Chapter 5).

Wind clumping has meanwhile been included in diagnostic tools by assuming statistically distributed *optically thin* clumps and a void inter-clump medium, while keeping a smooth velocity field (we shall often refer to this prescription as the ‘*microclumping*’ approach). This microclumping limit for radiative transfer is discussed in detail in Chapter 3. Below we summarize some basic *results* arising from using this methodology. The first (and main) result is that mass-loss rates derived from

⁴ Actually, the stated Puls et al. rate is an upper limit of the mass-loss rate, derived by assuming a smooth wind only in the outermost radio emitting region, whereas allowing for microclumping in the inner (H_α forming) wind regions.

smooth models and diagnostics depending on the square of the density (such as H_α and IR/radio emission) must be scaled down by the square root of the clumping factor f_{cl} (the clumping factor essentially describes the over-density of the clumps as compared to the mean density, see Chapter 3), and secondly, the wind ionization balance becomes significantly modified because of the changed recombination rates (e.g., Bouret et al. 2005). Another important effect of wind clumping, which however is due only to the shock-heated wind and *not* specifically connected to the microclumping approximation, is the X-ray emission believed to originate in clump-clump collisions in the wind (see the previous subsection), which can strongly influence the metallic ionization/excitation balance (Macfarlane et al., 1993; Pauldrach et al., 1994).

Note that, *within the microclumping model*, the UV resonance lines are not affected by the first point, because they depend only linearly on density. That is, no direct down scaling of the mass-loss rates derived from smooth models is necessary for these lines, when using the microclumping model (Chapter 3). The major advantage with the microclumping model is that it allows for a relatively simple implementation into diagnostic tools. Only one extra parameter is required, f_{cl} , and one may simply scale the opacities/emissivities in corresponding smooth models as described above (that is, opacities are unaffected in ρ -dependent processes and enhanced by a factor of f_{cl} in ρ^2 -dependent processes). Nonetheless, both the occupation numbers and the radiative transfer are affected by microclumping (see above), so some effort is still required when modifying already existing diagnostic tools to properly account for it (e.g., Schmutz, 1995).

For diagnostics of WR stars, microclumping has been accounted for since the pioneering work by Hillier (1991), and has led to a downward revision of empirical mass-loss rates from WR stars by roughly a factor of three (reviewed in Crowther, 2007). On the other hand, for O stars clumping started to attract considerable attention within the community only in the 21st century (although it had been pointed out already by Abbott et al., 1981). Using newly developed line-blanketed model atmospheres, Repolust et al. (2004) presented an optical analysis of a large Galactic O-star sample. By comparing the observationally inferred wind-momentum luminosity relation (WLR, see Chapter 2) with theoretical predictions, discrepancies were found and wind clumping, which was not included in the analysis, suggested as the origin of those. The authors argued that the derived mass-loss rates for objects with H_α in emission (primarily supergiants) were over-estimated by factors of 2...3. Such reductions would agree well with those suggested for WR stars (see above). However, subsequent analyses indicated even more drastic reductions. Perhaps most alarming in this respect, the so-called 'Pv problem', highlighted by the analysis of 40 Galactic O stars by Fullerton et al. (2006) (and illustrated here in Fig. 1.2). These authors used the UV resonance lines of Pv and derived values of the mean ionization fraction times the mass-loss rate, $\langle q \rangle \dot{M}$, that were factors of (at least) 10...100 lower than corresponding \dot{M} values derived by smooth models and H_α /radio emission. Since NLTE atmospheres that include *microclumping* predict Pv to be the dominant ionization stage, i.e. $\langle q \rangle \approx 1$, for stars of mid O type, this would imply extremely low mass-loss rates. These results are confirmed by us in Chapter 5, where we (for comparison reasons) use the microclumping approximation and from a combined UV/optical analysis derive a mass-loss rate for λ Cep that is approximately an order of magnitude lower than what is predicted by theory. In addition, in order to simultaneously fit the UV and optical diagnostics, we had to invoke extremely high clumping factors, at false with predictions from RH models of the line-driven instability. Similar results for B stars have been found by Prinja et al. (2005), where also more diagnostic UV resonance lines were considered, indicating that the problem is not isolated to Pv. It should be mentioned though, that these UV results rely heavily on the ability of present-day unified model atmospheres to predict accurate ionization fractions in the

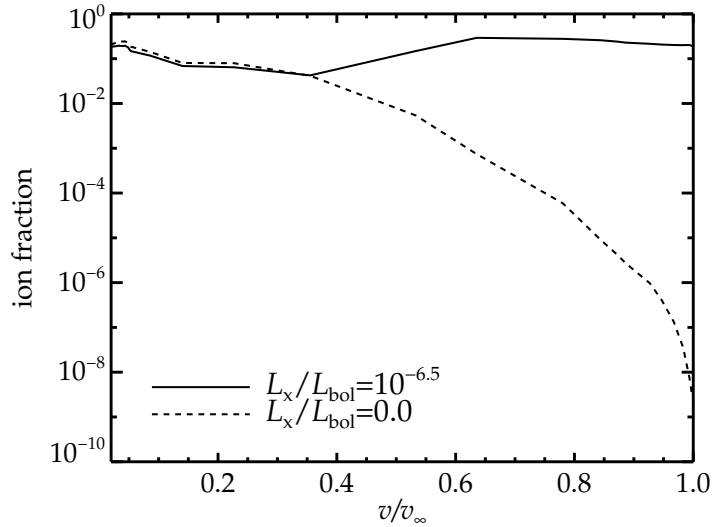


Figure 1.3: Ionization fractions of NV (four times ionized nitrogen), for two wind models of λ Cep, calculated by the unified model atmosphere code WM-Basic (not including wind clumping) (Pauldrach et al., 2001), with and without X-rays.

wind. Recently, Waldron & Cassinelli (2010) suggested that $\langle q \rangle$ for PV may be drastically reduced due to the influence from X-rays and XUV/EUV radiation. But a similar investigation by Krtićka & Kubát (2009) indicated a negligible impact, so further investigations certainly are needed regarding the influence of these hot radiation bands upon the formation of diagnostic UV lines (a first, tentative, discussion on this is given by us in Chapter 5). Here we mention only that in some cases X-rays definitely are vital to obtain reasonable ionization fractions, for example in the formation of the strong observed UV NV lines, which are modeled much too weak when not considering X-rays, as illustrated by the corresponding ionization fractions in Fig. 1.3.

Moreover, the basic result from X-ray line modeling for O stars is either that empirical mass-loss rates are lower than previously thought or that *optically thick clumping* is important for the line formation (e.g., Feldmeier et al., 2003; Oskinova et al., 2004; Owocki & Cohen, 2006). However, some inconsistencies exist in the quantitative results obtained from the X-ray line modeling performed by different groups. Oskinova et al. (2006) used Monte-Carlo simulations and showed that the X-ray lines in the O4 supergiant ζ Pup could be reproduced when using the upper limit mass-loss rate of Puls et al. (2006) (see footnote 4), *only if* optically thick clumping were properly accounted for. When these effects were neglected, much more asymmetric synthetic line profiles than indicated by the observations were obtained, and a substantial mass-loss reduction would be necessary to obtain reasonable fits. On the other hand, Cohen et al. (2010), from X-ray lines and without including effects of optically thick clumping, *derived* a mass-loss rate for ζ Pup that was only marginally ($\sim 20\%$) lower than the upper limit of Puls et al. It was argued that this mass-loss rate, much higher than those indicated by earlier X-ray analyses neglecting optically thick clumping, stemmed from a more careful consideration of the atomic opacity in the wind, which for example accounted for the presumably sub-solar abundance of the sum of the CNO elements in ζ Pup. Also, Cohen et al. found a wavelength dependence in the

observed X-ray line profile strengths, which they interpreted as an argument against optically thick clumps, for (very) optically thick clumps would result in gray opacities (Chapter 3). Note that it also previously had been argued by Owocki & Cohen (2006), that for significant effects of optically thick clumping on the line profiles to occur, unrealistically large distances between clumps had to be invoked. In contrast to this, Oskinova et al. (2006) *did* find significant effects also when invoking distances between the clumps *in accordance* with current RH simulations of the line-driven instability. In conclusion, more investigations certainly are needed to clarify the role of optically thick clumping in the formation of X-ray line profiles.

Naturally, the inconsistencies and large discrepancies among different studies outlined in this subsection drastically lowers the reliability of mass-loss rates for hot, massive stars currently in use, and an explanation is urgently needed. Indeed, the ‘hot star community’ has started to question the validity of the microclumping approximation for more diagnostics than the X-ray lines (Oskinova et al., 2007; Owocki, 2008; Massa et al., 2008); May the failure of this approximation be the chief reason for the apparent discrepancies, between different studies as well as between observations and theory?

The development of radiative transfer methods that relax the microclumping approximation and properly account for clumpy wind structures with non-monotonic velocity fields occupies the bulk of this thesis work, together with the corresponding incorporation into diagnostic tools and interpretations of observed stellar spectra (Chapters 3-5). Developing such new and improved diagnostic methods is important because, as discussed, mass-loss estimates based on smooth wind descriptions might actually be quite erroneous.

1.4.4 Some implications of modified mass-loss rates due to wind clumping

Should mass-loss rates from hot, massive stars have to be further modified due to wind clumping, it would have profound consequences for many astrophysical applications. Here we discuss a few of those, with emphasis on the effects on massive star evolution. In the standard single evolution scenario of very massive stars (Sect. 1.2), the hydrogen burning O star evolves into a LBV phase after which it enters the hydrogen deficient WR stage, where it finally meets death⁵. All these phases experience significant mass loss, however with quantitatively different rates. So when discussing mass loss in this context, we must distinguish between the various stellar stages.

WR stars are observed with significantly lower masses than O stars. That is, if O-star mass-loss rates are indeed lower than previously thought, very strong mass-loss rates would have to be invoked in the LBV phase in order to preserve the ‘standard’ evolutionary scenario. Smith & Owocki (2006) suggested that inefficient mass loss for O stars could be compensated for by *eruptive* LBV phases, in which the star sheds enormous amounts of mass in very short time scales. Indeed, it is an observational fact that such eruptive phases exist; in the 19th Century η Carina lost more than 10 solar masses during one to two decades (estimated from the surrounding Homunculus nebula, Smith et al., 2003). Another possibility is of course that WR stars are *not* the descendants of O stars; for example it has been suggested that all WR stars are part of a close binary system (Kobulnicky & Fryer, 2007), but this is strongly disfavored by the observed binary rate of WR stars in the MCs (Foellmi et al., 2003a,b), which is only $\sim 30 - 40\%$. So, let us for now assume that fierce mass loss during short outbursts of LBVs is the more liable explanation.

⁵ As discussed in Sect. 1.2, the nature of the evolved stages depends on the initial stellar mass; in the evolution models of Meynet & Maeder 2003 a star with initial mass $60 M_{\odot}$ (an early O star) evolves into the LBV and WR phases, whereas a star with initial mass $20 M_{\odot}$ (a late O star) instead evolves into the red supergiant (RSG) phase, see Leitherer (2010).

Now, the standard line-driven wind theory cannot drive a wind as the one indicated for η Carina by the Homunculus nebula, with such an extreme mass loss and quite high terminal speed (Smith & Owocki, 2006). A proposed driving mechanism for these eruptive phases is instead *continuum radiative acceleration* (from Thomson scattering) moderated by optically thick clumps in inhomogeneous atmospheres (Owocki et al., 2004). In comparison with an inhomogeneous atmosphere consisting of clumps optically thin for Thomson scattering, a clumpy but for this process optically thick atmosphere leads to a decrease in the effective opacity of the medium (in the same manner as the proposed reduction of X-ray line opacity, see Sect. 1.4.3), which in turn reduces the radiative acceleration.

The key to initializing a stellar wind under these conditions is that the reduced opacity in *optically thick layers* makes it possible there for the star to formally exceed the Eddington luminosity, without becoming gravitationally unbound. But as photons travel outward in the atmosphere, the medium becomes less opaque and at some point clumps will inevitably become optically thin. Consequently then, the opacity in these outer layers once again takes the corresponding homogeneous value (Thomson scattering depends only linearly on density, and so is unaffected by microclumping, Sect. 1.4.3). Thus, if the star's luminosity indeed exceeds the Eddington luminosity, gravity may then be overcome and a very strong stellar wind initialized. It was shown by Owocki et al. (2004) that the mass loss from such 'super-Eddington' atmospheres can be much higher than the mass loss from line-driven winds, suggesting that continuum driving is a promising mechanism for driving 'super-winds' during eruptive LBV phases. Moreover, the Thomson scattering that is the basic component of this driving force should *not* be metallicity dependent, which might open up for considerable mass loss also in the primordial Universe and perhaps even for the very First Stars (Smith & Owocki, 2006; van Marle et al., 2008), which generally are believed to suffer no significant mass loss because of their lack of driving metals (recall that the primary drivers of line-driven winds are *metal* UV resonance lines). Actually, strong mass loss has been suggested as a way to avoid that the presumably very massive First Stars undergo Pair Instability Supernova (PISN) explosions (Ekström et al., 2008), whose distinct chemical signatures never have been observed in the atmospheres of the 2nd generation low-mass, extremely metal-poor halo stars that have survived until today (but see also Karlsson et al., 2008, who argued that this absence might simply be due to selection effects in the observational surveys aimed to find these stars).

Obviously, to invoke extreme mass loss in short outbursts of LBVs as a general (rather than deviant) ingredient in the evolution of very massive stars, it must be observationally established that these eruptions actually occur regularly and are not unusual events (see discussion in Smith, 2008). Furthermore, more quantitative predictions for mass-loss rates than those given in the studies discussed above certainly are required.

Another example illustrating the importance of reliable quantitative mass-loss rates was provided by Yoon et al. (2006). They demonstrated how the presumed decreasing mass loss with decreasing metallicity created a threshold ($Z \lesssim 0.004$) above which they predicted that no long-duration GRBs should occur within the collapsar scenario (Woosley, 1993). In their calculations, the threshold came about because at higher metallicities the strong mass loss effectively removed angular momentum, which in turn made the stars spin down and thereby prevented creations of GRBs (recall that the collapsar scenario requires a fast rotating stellar core to produce a GRB, Sect. 1.2). However, it was also pointed out how their results strongly depended on the adopted mass-loss prescriptions; an increase in the predicted metallicity threshold would occur *if* the uncertain mass-loss rates of WR stars were reduced, for example due to the effects of wind clumping.

Finally, in yet another context Voss et al. (2010) performed population synthesis of massive stars in

Orion, and argued that the kinematic and radioactive properties of this region would be very hard to reproduce if the *integrated* mass loss in current stellar models were drastically reduced due to wind clumping.

1.5 Spectroscopic analyses of stars using model atmospheres

In the previous sections we have quite extensively discussed various *results* of studies aiming to obtain reliable *observed* values of, e.g., mass-loss rates of hot, massive stars. We now turn to take a closer look on (some of) the methods used to actually extract this type of information from the observations. In particular, we discuss *quantitative spectroscopy* of stellar atmospheres, which is the method that most of the aforementioned results rely on.

The standard procedure when comparing theoretical predictions with observed stellar and wind properties, such as effective temperatures, mass-loss rates, or chemical abundances, is to derive the properties by fitting calculated synthetic spectra to observed ones (=quantitative spectroscopy). Customary then is to use *model atmospheres* together with suitable spectrum synthesis codes. Thus, the validity of ‘observed’ stellar and wind properties relies heavily on the authenticity of these codes. And as we shall see, a substantial modeling effort is required for the non-trivial task of constructing reliable model atmospheres and synthetic spectra.

1.5.1 Model atmospheres and spectrum synthesis

The classical model atmosphere is computed on the assumptions of flux conservation, hydrostatic equilibrium, a one-dimensional (1D) plane-parallel stratification, and Local Thermodynamic Equilibrium (LTE) (cf. Mihalas, 1978). Also, quite often one in the computations considers only the *stellar photosphere*, which essentially is the atmospheric regions from which the (main part of the) star’s *optical* light emerges.

However, depending on the stellar type, as well as on the objective of the particular analysis, some of these standard assumptions may need to be relaxed. For example, when analyzing the extended atmospheres of giants and supergiants, the spherical extension of the star must be accounted for (by dropping the plane-parallel assumption), and for at least supergiants of types A and earlier the *stellar wind* significantly influences most of the strategic spectral lines, and should therefore be considered in the analysis (which obviously means that the hydrostatic assumption must be dropped). Moreover, the intense radiation field and the low densities in the atmospheres of early-type (hot) stars make the assumption of LTE dubious for these objects. Actually, the question whether LTE is a good approximation is a fundamental one in stellar atmosphere work; accordingly we discuss it in a little more detail.

1.5.2 Spectral line formation and the assumption of LTE

In thermodynamic equilibrium (TE), the distribution of atoms and ions over all possible micro-states is described by merely two thermodynamic state variables, say temperature and pressure, via the traditional equilibrium relations of statistical mechanics (the Saha and Boltzmann relations). Moreover, particle velocities are given by the Maxwellian distribution and the relation between thermal emission and absorption of radiation obeys Kirchhoff’s law, or in this case the Kirchhoff-Planck relation,

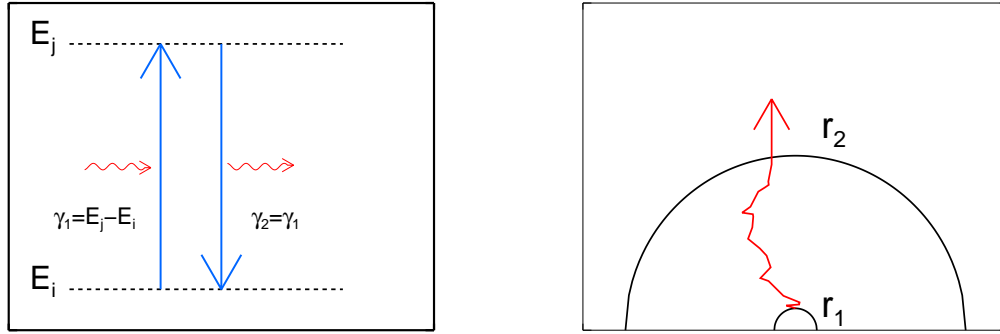


Figure 1.4: *Left*: Schematic of the line scattering process. A photon of energy γ_1 is first absorbed and then re-emitted with the same energy. *Right*: Sketch of a photon's scattering path between radii r_1 and r_2 through an atmosphere, before its escape into free space.

$$j_\nu = \chi_\nu B_\nu(T), \quad (1.1)$$

with extinction coefficient χ , emission coefficient j , and $B_\nu(T)$ the Planck function for frequency ν at temperature T . Strictly speaking, the Kirchhoff-Planck relation and the Saha-Boltzmann and Maxwellian distributions only apply under TE conditions with a (spatially) constant temperature T . Assuming LTE essentially means assuming that these relations still hold *locally* at every point in the gas, despite that temperature as well as pressure gradients may exist. To establish LTE, several requirements should be satisfied. A discussion is given below, but surely the topic is way too complex to be thoroughly covered here. For more details we refer the reader to Mihalas (1978).

Particle velocities. A Maxwellian velocity distribution is secured *if* processes that only redistribute the ‘available’ energy among particles occur more frequently than processes that actually remove, or add, energy from, or to, the particles in the thermal pool. *Elastic collisions* is the important process of the first type, i.e. these collisions are the ones that simply shuffle the particles around and lead to equilibrium. Two examples of the second type (perturbing processes that disturb the establishment of an equilibrium, here taking the example of free electrons) are i) recombinations, because when a free electron recombines this obviously hinders it from undergoing further elastic collisions, and ii) collisional excitations followed by radiative de-excitations, because then some of the electron’s kinetic energy is transferred to the radiation field (in the form of an emitted photon), which creates a local sink in the electron velocities, deviating from the Maxwellian distribution. However, Mihalas (1978) concludes that under representative stellar atmosphere conditions⁶, such as those considered in this thesis, an *enormous* number of elastic collisions occur per perturbing process, for electrons as well as for atoms and ions. Essentially this means that this aspect of the LTE assumption may safely be assumed, and that all particles are indeed ‘Maxwellian’, characterized by a *single* and unique kinetic gas temperature T . Actually, already this is a quite powerful assumption, for it means that we may

⁶ which here do not include the conditions in for example the solar corona or supernovae.

use this absolute T (usually taken to be the electron temperature) in the calculations of the level populations for *all* atoms and ions in all atomic states, as well as in the calculations of the thermal emissions (see below).

Level population numbers and the Kirchoff-Planck relation. As described, collisions determine the *velocities* within the atmosphere, and are in equilibrium. Concerning the atomic *level populations*, however, the situation is different, because here both collisions and the *radiation field* may be important in determining the distribution over the atomic states. And, in contrast to the collisions, the radiation field only takes its equilibrium value (the Planck function) in very deep atmospheric layers, because the outer layers of a stellar atmosphere are rapidly leaking photons (as we know because we can observe it) and are therefore highly anisotropic and dilute and very different from the classical ‘hohlraum’ picture of a perfect black body. In principle, when radiative processes are important, one might expect LTE to be a reasonable assumption for the level populations *if* photons are thermalized by some collisional process before they have traveled long enough that the gas has significantly changed its thermodynamic properties. In other words, for this aspect of LTE to be valid the atmosphere should not be subject to large temperature/pressure gradients over a photon’s mean free path.

Under the LTE assumption one may still calculate from the Saha-Boltzmann relations (assuming, of course, that the atmospheric temperature and pressure structures are known, as well as the chemical composition of the gas) the number density n_i of excitation state i , of all chemical species and all ionization states that are present in the atmosphere. The extinction coefficient is essentially this number density times the atomic cross-section, so if we know the latter (from for example quantum mechanical calculations or laboratory experiments), we can obtain a complete picture of extinction coefficients. Then we may use Eq. 1.1 to obtain the corresponding emission coefficients, after which the equations of radiative transfer

$$\frac{dI_\nu}{ds} = -\chi_\nu I_\nu + j_\nu \Leftrightarrow \frac{dI_\nu}{\chi_\nu ds} = -I_\nu + S_\nu \quad (1.2)$$

can be solved for the specific intensity I_ν at any given frequency ν . The second expression introduces the so-called source function, $S_\nu \equiv j_\nu/\chi_\nu$, which for this case is *equal to the Planck function* (Eq. 1.1). Naturally, the calculated radiation field (I_ν) is allowed to depart from its equilibrium value (see above). However, quite often the LTE assumption is interpreted in a less strict manner than just done, by accounting also for *scattering* terms in the total continuum extinction. A scattering process depends upon the radiation field itself, and the Planck function in Eq. 1.1 must therefore, for these processes, be replaced with the actual calculated mean intensity. That is, $j_\nu^s/\chi_\nu^s = J_\nu$, where J_ν is the mean intensity, obtained by angle averaging the specific intensity I_ν , and a superscript s has been added to the scattering terms to separate them from the thermal ones. Examples of scattering processes are Thomson (electron) scattering, which always is an important opacity contributor in the atmospheres of hot stars, and Rayleigh scattering, which can be important in the atmospheres of cool stars. A standard way of modifying the source function to account for scattering is to write the total extinction and emission coefficients as linear combinations consisting of a *true absorption* component (below denoted with superscript a) and a *scattering* component,

$$S_\nu = \frac{j_\nu^{\text{tot}}}{\chi_\nu^{\text{tot}}} = \frac{j_\nu^{\text{a}} + j_\nu^{\text{s}}}{\chi_\nu^{\text{a}} + \chi_\nu^{\text{s}}} = \epsilon_\nu B_\nu(T) + (1 - \epsilon_\nu) J_\nu, \quad (1.3)$$

where $\epsilon_\nu = \chi_\nu^{\text{a}}/\chi_\nu^{\text{tot}}$ is the fraction of true absorptions⁷. Clearly, this ‘LTE interpretation’ is less strict, because it allows for scattering components and consequently for deviations from the Kirchhoff-Planck relation. The level populations are still calculated from the Saha-Boltzmann relations though, which is why we still call it a LTE approach. Actually, we notice that this method, although very useful, may be said to be internally inconsistent; scattering can transport photons over large distances, in violation with the discussed requirements for LTE, but, nevertheless, feedback effects from the scattering terms upon the level population numbers are simply ignored. On the other hand, entirely neglecting scattering in LTE calculations is not very fruitful either, since we know that these terms are there and (sometimes) do play an important role for the resulting radiation field. This is a first indication that the LTE assumption for quantitative analyses of stellar atmospheres is somewhat ambiguous, and it also suggests that one should always strive to check the validity of LTE for a given situation with more rigorous so-called non-LTE calculations (see below and next subsection). In any case, however, a source function such as in Eq. 1.3 is, for example, implemented in the widely used LTE MARCS stellar atmosphere code designed for analyses of late-type stars (Gustafsson et al., 2008).

Spectral line formation. In LTE, the effects of scattering for *line absorption* are not considered (compare to the continuum case just discussed). Therefore, a spectral absorption line in LTE is formed only by *true* bound-bound absorptions, in which an atomic excitation always is followed by a collision that transfers the energy of the absorbed photon to the ‘thermal pool’, and *thermal* emissions, which obey Eq. 1.1. In terms of Eq. 1.3, this means that the true absorption component for frequencies at which one (or more) spectral line is present is modified according to $\chi_\nu^{\text{a}} = \chi_\nu^{\text{a,c}} + \chi_\nu^{\text{a,l}}$, with superscripts *c* and *l* denoting continuum and line, respectively. Naturally, the same modification is made for the thermal emission component.

As described in the previous paragraph, LTE generally is valid when interactions between matter and radiation are dominated by *collisions*, and therefore it normally prevails in the deep layers of stellar atmospheres, where densities are high. However, as we reach the outer and observable layers of the star, (line) photons may travel large distances before being thermalized, and thereby other processes than those just stated, perhaps other radiative such, may become important in the formation of a spectral line.

For example, an excitation from atomic level *i* to *j* may now be followed by a radiative spontaneous (or stimulated) de-excitation from level *j* to *i*, so that no energy is transferred to the thermal pool and a new photon is emitted, which essentially has the same properties as the old one (Fig. 1.4, left panel). Thus, one may regard it as if the old photon ‘survives’ its absorption. When this type of process occurs repeatedly, a single photon⁸ may carry with it information over large distances in the atmosphere (Fig. 1.4, right panel). This information now reflects the conditions in the part of the atmosphere at which the photon was originally emitted, conditions that may be quite different from those at the physical location at which the photon experiences its final interaction with the gas (a final

⁷ The inclusion of scattering is the reason why we chose to call χ the *extinction* coefficient instead of the *absorption* coefficient, which sometimes is done.

⁸ of course this is not really the *same* photon. But it simplifies to take that point of view, also for practical purposes, see the Monte-Carlo simulations in Chapter 4.

interaction which may be a collisional thermalization or an emission into free space). We call this type of process *line scattering* (in analogy with the continuum scattering introduced in the previous paragraph), and it is extensively studied in Chapters 4 & 5, for the case of resonance line formation in inhomogeneous hot star winds. Clearly, line scattering is a highly ‘non-local’ process, distinctly different from processes maintaining the LTE assumption.

Another important process is when a de-excitation occurs to another atomic level than to the one from which the first absorption came about. As an example, imagine a photon ripping an atom of its outermost electron (i.e., photoionizing it). Eventually the atom will capture another free electron and recombine. When doing so, the captured electron may connect to an atomic state with higher excitation potential than the state from which the photoionization occurred. The electron may then start to (collisionally or radiatively) de-excite toward lower states, and in every radiative step of this cascade, a new photon with a wavelength corresponding to that particular line transition will be emitted. Now, these emitted photons may have quite different wavelengths than the photon had that gave rise to the ionization. Thus, here we in the line formation have a coupling both among different *atomic states* and among different *spectral regions*. These types of cascading processes are important for, e.g., the formation of hydrogen lines in early-type stars and infra-red emission lines in late-type stars, both of which are studied in this thesis (Chapters 2, 5, & 6).

The equations of statistical equilibrium. The qualitative notions above suggest that in rather many situations one may wish to replace the LTE assumption by more general non-LTE (NLTE) calculations. Although NLTE is a general (and often quite loosely defined) term for whenever the conditions for LTE are not satisfied, in stellar atmosphere work one almost always equates NLTE with assuming *statistical equilibrium* when calculating the level population numbers (and so we shall do throughout this thesis as well).

More generally, however, we may write a conservation equation for quantities such as mass, momentum, or particles, as

$$\frac{\partial}{\partial t}(\text{density of quantity}) + \text{div}(\text{flux of quantity}) = \text{sources} - \text{sinks}. \quad (1.4)$$

The first term on the left hand side in this equation describes the time variation of the investigated quantity within a unit volume and the second one describes the transfer of this quantity across the unit volume due to macroscopic motions. The right hand side represents any ‘creations’ and/or ‘destructions’ of the quantity that may occur, per unit time. To get the customary statistical equilibrium equations from applying Eq. 1.4 to the level population of any state i , n_i , we will assume *steady state* ($\partial n_i / \partial t = 0$), and also that changes of n_i in a given unit volume due to macroscopic motions are much slower than the atomic transition time scales (i.e., we neglect the divergence term in Eq. 1.4). Both these assumptions may be regarded as safe under typical stellar atmosphere conditions⁹, due to the very brief transition timescales. We thus arrive at the equations of statistical equilibrium (SE), sometimes also called the NLTE rate equations, which are

$$0 = n_j \sum_{j \neq i} (R_{ji} + C_{ji}) - n_i \sum_{j \neq i} (R_{ij} + C_{ij}), \quad (1.5)$$

and essentially state that the processes that populate any atomic level i are exactly balanced by those that depopulate level i . C and R are the collision and radiative rates, per unit time, respectively.

⁹ here excluding, e.g., Supernova remnants.

As outlined in the previous paragraphs, radiative rates may be highly ‘non-local’ in nature, whereas the collision rates depend only on local quantities, so the rule of thumb is that more collisions tend to drive the line formation closer to the LTE case (there are, however, subtle exceptions to this rule, one of which is studied in Chapter 6). This explains why, generally, early-type stars with low densities (less collisions) and strong radiation fields (higher radiative rates) are very prone to NLTE effects.

The SE equations are solved numerically for most practical purposes. Various techniques for this have been developed over the past decades, of which the class of Accelerated Lambda Iteration (ALI) methods are the most popular ones in stellar atmosphere work nowadays. ALI methods are operator splitting methods for which one avoids a full matrix inversion of the so-called ‘ Λ -operator’, used to obtain the source function, by introducing an (cleverly chosen) *approximate* operator, which is inverted instead. ALI has been used by stellar atmosphere modelers for a few decades now (e.g., Cannon, 1973; Scharmer, 1981), but the basic mathematical method is very similar to the well-known Jacobi method for solving systems of linear equations, and is, thus, much older. For details on ALI methods, see for example Rybicki & Hummer (1991).

The main problem in solving the SE equations lies in the dependence of R upon the radiation field itself. That is, the occupation numbers depend on the radiation field, which in turn depends on the occupation numbers. Therefore these equations and the equations of radiative transfer (Eq. 1.2) must be solved *simultaneously*, in principle for all atomic species as well as for all frequencies across the spectrum. Obviously this is an immense problem; we now realize why the LTE assumption sometimes appears so attractive, for it avoids all problems arising with the aforementioned couplings by simply saying that the level populations may be calculated considering only local thermodynamic conditions. NLTE also introduces the concept of *model atoms*, because of the coupling among, in principle, all states of all atoms that are present in the atmosphere. Much work has been devoted to constructing reliable model atoms for various types of stellar atmosphere applications. It is a delicate problem, mostly because large amounts of atomic data (oscillator strengths, ionization cross-sections, collision cross-sections, etc.) are needed to compute the radiative and collision rates in Eq. 1.5, and it is seldom clear *a priori* what levels are actually important for the formation of the spectral lines of interest, i.e., what levels must be included in a given model atom. This problem will be clearly demonstrated in Chapter 6, in a NLTE analysis of infra-red Mg I lines. Moreover, the *accuracy* of the input atomic data is not always convincing. The collision cross-sections are especially problematic in this respect, because few reliable quantum mechanical calculations or laboratory experiments exist for those. Quite often one must rely on various semi-classical and/or semi-empirical recipes, which essentially only provide order of magnitude estimates, at the best (see Chapter 6).

1.5.3 Comparisons of atmospheric codes - photospheric models

From the previous subsection it should be clear that atmospheric and spectrum synthesis codes may be designed quite differently depending on what stellar domains and what applications are the main targets. Here we discuss some major codes currently in use, and their various domains of application. First, however, let us point out that not only have the standard assumptions stated in the beginning of the previous subsection started to become more and more relaxed in stellar atmosphere work, but also have the modeling techniques *within* given assumptions become ever more refined. Perhaps most important in this respect is that over the past decades it has become standard to consider line-blocking/blanketing effects from up to millions of spectral lines when computing the atmospheric structure and the emergent synthetic spectra (e.g., Gustafsson et al., 1975; Hubeny & Lanz, 1995).

Gustafsson et al. (2008) compared different LTE codes of late-type stars, and found excellent agreement between their own MARCS models and, e.g., the Kurucz models (Kurucz, 1979; Castelli & Kurucz, 2004). However, no comparisons to NLTE atmospheres were made in that study; constructions of NLTE atmospheres of late-type stars are problematic because of the wealth of atomic and molecular species that affects the radiation field. Often there is a lack of corresponding atomic and molecular data, and especially cross-sections for collisions with neutral hydrogen are very uncertain (cf. Asplund, 2005, and references therein). Nevertheless, some efforts to compute NLTE atmospheres of late-type stars have been made, in particular by the PHOENIX team (e.g., Hauschildt & Baron, 2005), but general results regarding the importance of NLTE feedback effects on the atmospheric structure are still largely missing in this domain. For example, the effects from major opacity contributors such as the negative hydrogen atom and/or iron-group elements are still open questions, and might turn out to be important. In any case, the treatment of convection is considered more problematic for late-type stars than LTE versus NLTE (at least regarding the atmospheric structure, although perhaps not for spectral line formation, see below). Pioneered by Nordlund and collaborators, much work has been devoted to construct realistic 3D, time-dependent, radiation-hydrodynamic surface convection simulations (e.g., Stein & Nordlund, 1998), and it has been shown that the temperature structures in these models, as well as the mean synthetic line profiles calculated from these models, can be significantly different from those resulting from classical 1D atmospheres (which normally treat convection by the mixing-length theory). A notable example in this context is, of course, the revision of the photospheric solar chemical abundances that emerged with the advent of line synthesis based on these models (even though these revisions also partly are due to other observational as well as modeling improvements, for example in atomic data) (see the review by Asplund et al., 2009). Another example that may be worth mentioning here is the differences between classical 1D and hydrodynamical 3D model atmospheres of low metallicity stars, which can be profound (Collet et al., 2007) and might turn out to be important for the many observational attempts to constraint surface abundance properties of the very old metal-poor stars that are used as tracers of conditions in the very early Universe.

Hotter stars¹⁰ are not believed to have these strong convective zones in their photospheres. However, recently there has been increasing interest regarding *sub*-surface convection (just below the photosphere), due primarily to an iron-peak in opacity (Iglesias et al., 1992). Cantiello et al. (2009) propose that gravity and/or acoustic waves emitted in these weak convection zones may travel through the radiative layer and induce surface fluctuations in density and velocity, with clumping at the base of the wind and ‘microturbulence’ in the photosphere (in analogy with cool stars) as consequences. Both clumping and microturbulence are indeed observed in hot stars with winds, so it is important that careful more-D hydrodynamic simulations of these layers be carried out in the future, to confirm or refute the above suggestions.

In any case, the focus for stellar atmosphere modelers in this domain has generally not been on relaxing the 1D assumption but instead on developing realistic NLTE model atmospheres (e.g., Auer & Mihalas, 1972; Hubeny & Lanz, 1995). Nieva & Przybilla (2007) compared results for dwarfs of B and late O types calculated from full NLTE model photospheres with those obtained using a so-called hybrid NLTE approach. In the hybrid approach the photospheric structure is calculated in LTE, whereas the level populations and synthetic spectra of the element(s) under consideration are

¹⁰It may be interesting (and perhaps a little amusing?) to note here that stellar atmosphere workers traditionally appear to have been divided into, sometimes quite sharp, ‘hot’ and ‘cool’ groups, whereas the natural division regarding stellar evolution appears to be ‘massive’ and ‘low-mass’ stars. May the RSGs perhaps work as a bridge bringing these various groups somewhat closer together? (See, e.g., a few contributions in Bresolin et al. 2008.)

calculated in NLTE. For late-type stars, this technique is also called the restricted NLTE problem for trace elements (since if the considered element is a major contributor to the total opacity one could not validate neglecting the impact upon the atmospheric structure), and is very often used in abundance analyses. (For some recent critique on the general applicability of this method, see Kubat 2010.) Also in this thesis is the trace elements method used (Chapter 6), to model and analyze the photospheric IR Mg I lines in the Sun as well as in K giants, using the above mentioned MARCS models together with the NLTE code MULTI (Carlsson, 1986, 1992). Accordingly, we now introduce some basic features of NLTE line formation of IR lines in general and the Mg I lines in particular. (We shall return to our discussion on different atmospheric codes shortly.)

1.5.4 NLTE line formation in the infra red

The formation of the prominent solar $12\ \mu\text{m}$ Mg I emission lines had been subject to many controversies before it was realized that the emission originated in the photosphere and simply stemmed from NLTE effects (rather than from, e.g., the temperature inversion in the chromosphere) (Chang et al., 1991; Carlsson et al., 1992). Solar emission lines from other chemical neutrals have also been identified in this spectral region (Brault & Noyes, 1983; Chang & Noyes, 1983), of which at least the Al I lines are confirmed by detailed photospheric NLTE modeling to share the Mg I formation scenario (Baumueller & Gehren, 1996). (It is however believed that all these lines are of photospheric origin and formed similarly, see Rutten & Carlsson 1994.)

The essential point why the formation of IR lines is particularly sensitive to departures from LTE lies in the behaviour of the *line* source function, $S_v^l \equiv j_v^l/\chi_v^l$, where superscript l as before denotes line. The NLTE line source function is (cf. Mihalas, 1978)

$$S_v^l = \frac{2h\nu^3}{c^2} \frac{1}{\frac{b_l}{b_u} e^{h\nu/kT} - 1}, \quad (1.6)$$

where $b_i = n_i/n_i^*$ are the NLTE *departure coefficients*, with n_i^* the LTE number density with respect to the ground level of the next ionization state (see Appendix A for a definition). l and u denote the lower and upper levels of the transition, respectively. Note that for $b_i = 1$, $S_v^l = B_v$, as it should¹¹. Now, in the limit that $\delta = h\nu/kT < 1$ (Rayleigh-Jeans limit), and writing $b_l/b_u = 1 + \beta$, we get for the ratio of the NLTE and LTE line source functions (cf. Mihalas, 1978, Sect. 12.4)

$$\frac{S_v^l}{B_v} = \frac{e^{h\nu/kT} - 1}{\frac{b_l}{b_u} e^{h\nu/kT} - 1} \approx \frac{\delta}{\frac{b_l}{b_u}(\delta + 1) - 1} \approx \frac{1}{1 + \beta/\delta}, \quad (1.7)$$

which directly shows how for a *given* departure β the NLTE effects amplify with δ^{-1} . The physical reason for this is the increasing importance of stimulated emission at longer wavelengths. Actually, S_v^l becomes *negative* when $b_u/b_l > 1 + \delta$ (see the middle expression), i.e., we then enter the *laser regime* for which light amplification instead of extinction occurs along the beam (because the total contribution from spontaneous and stimulated emissions dominate the absorption). The solar Mg I lines have $\delta \approx 0.23$ (for $T = 5000\text{ K}$) but do not ‘laser’ in this sense ($b_u/b_l < 1.23$ in line forming layers). Nevertheless, the overpopulation of the upper level as compared to the lower one is still

¹¹ Actually, the LTE line source function may be recovered also when population numbers departure from LTE, if $b_l = b_u$.

large enough to make the lines appear in *emission* rather than in absorption, which a photospheric line formed in LTE always must do. Moreover, let us point out that these IR amplifications of NLTE effects may be even more pronounced in hot stars, because of their higher temperatures (see expression for δ). We in the addendum to Chapter 2 discuss this in connection with the formation of hydrogen Br $_{\alpha}$ in O stars (which for a characteristic $T = 35\,000\text{K}$ has $\delta \approx 0.1$), and whether this increased sensitivity to the predicted departure coefficients might complicate the potential use of this line as a mass-loss indicator.

The potential use of the Mg I lines as probes of upper photospheric magnetic fields in cool stars was recognized early, and the prominent splitting of the lines seen in the active Sun has been thoroughly analyzed (e.g., Bruls et al., 1995). In general, Zeeman line splitting from an external magnetic field increases with the square of the wavelength, whereas the competing Doppler broadening only has a linear dependence. That is, the further out in the IR, the greater the sensitivity to magnetic fields. However, *stellar* applications of these emission lines have so far been limited. The Mg I lines have been observed in very few stars, due to the low stellar flux in the IR and the lack of suitable spectrometers, and modeling attempts had previously been carried out only for two dwarfs (including the Sun) (e.g., Carlsson et al., 1992; Zhao et al., 1998; Ryde et al., 2004) and two cool giants (Uitenbroek & Noyes, 1996), with very unsatisfactory results for the latter.

In Chapter 6, we present new observations of IR emission lines at 12 and 18 μm in giants of K type, for the first time identifying stellar (i.e. non-solar) Mg I emission lines at 18 μm , as well as Al I, Si I, and Ca I lines at 12 μm . We show by a detailed magnesium NLTE modeling that the same line formation mechanism as for the solar case is at work there. We also point out why previous modeling attempts have been unsuccessful. Especially, we investigate the great sensitivity on the formation of these lines to the input *atomic data* of the model atom, and thereby emphasize how the lines, in addition to magnetic field studies, may be utilized as important consistency checks for model atoms used in future *multi-wavelength* abundance studies.

1.5.5 Comparisons of atmospheric codes - unified models

We now leave our little excursion to the infra-red, and turn once more to our ongoing discussion of different atmospheric codes. In their investigation (see Sect. 1.5.3), Nieva & Przybilla (2007) found that results from the full NLTE code TLUSTY (Hubeny & Lanz, 1995) agreed well with their hybrid results using ATLAS9 (the Kurucz models) for the atmospheric structure and an updated version of DETAIL/SURFACE (Butler & Giddings, 1985) for the NLTE calculations. In general, a good agreement was also found when comparing to observations, however for the O star τ Sco the simulated cores of H $_{\alpha}$ and He II 4686 \AA were too deep, because of the neglect of the *stellar wind*. This leads us to the so-called *unified* NLTE atmospheres, which simultaneously treat the photosphere and the stellar wind. The development of these types of models was pioneered by the Munich group (e.g., Gabler et al., 1989), and has meanwhile become the standard tool when analyzing the atmospheres of hot stars with significant wind strengths. Puls (2009) suggests that unified atmospheres should be used if the mass-loss rate is higher than $\dot{M} \approx 6 \times 10^{-8} M_{\odot} \text{yr}^{-1} (R_{\star}/10R_{\odot})(v_{\infty}/1000 \text{km s}^{-1})$, which approximately corresponds to all O stars except for late dwarfs, early B stars of luminosity classes higher than II, and late B and A stars of classes higher than Ib. Note that, within this stellar domain, a simple check to see whether a unified approach is necessary is provided by the observed strength of the H $_{\alpha}$ line core, as mentioned above. But let us also point out that the unified code FASTWIND (described below) may be reliably used also for pure *photospheric* analyses of hot stars with negligi-

ble wind strengths, as recently demonstrated by Simón-Díaz (2010), who derived stellar parameters and chemical abundances for main-sequence B stars in Orion. In addition to ‘normal’ OBA-stars, the unified models may also be used to analyze WR stars, LBVs, and even Central Stars of Planetary Nebulae (CSPN) (see Pauldrach et al., 2004, for an example of the last).

Naturally, calculating realistic unified NLTE model atmospheres is a tremendous challenge. Mainly four different codes¹², all developed with specific objectives and all with different advantages and disadvantages, are presently in use; the two codes developed by the Munich hot-star group, FASTWIND (Puls et al., 2005) and WM-Basic (Pauldrach et al., 2001), and CMFGEN (Hillier & Miller, 1998) and POWR (W.-R. Hamann and collaborators, see Gräfener et al., 2002). Since both CMFGEN and POWR originally were designed for analyses of the very dense winds of WR stars, the photospheric density stratification is only approximate in these codes (assuming constant photospheric scale height). In analyses, this shortage is often circumvented by coupling CMFGEN with the plane-parallel, hydrostatic code TLUSTY. CMFGEN, POWR, and FASTWIND all use a pre-described mass-loss rate and velocity field for the wind structure, whereas in WM-Basic the model atmosphere is calculated by actually solving the (stationary) hydrodynamic equations reaching deep into the photosphere. However, WM-Basic was designed mainly for giving accurate predictions of the wind dominated (E)UV fluxes and line profiles, and the photospheric treatment in this code is therefore only approximate, making its current version ill-suited for spectral analyses in, e.g., the optical (however a code-update including a more appropriate photospheric treatment is underway). Extensive comparisons between the different codes have been carried out by our Munich group, mainly between FASTWIND, WM-Basic, and CMFGEN, with generally satisfying results.

The model atmosphere code used for the main part (with the exception of Chapter 6) of the quantitative spectroscopy performed here is FASTWIND. FASTWIND was designed for optical and IR spectroscopy of ‘normal’ OBA-stars of all luminosity classes and wind strengths. Because of the targeted wavelength ranges, no treatment of X rays has yet been included in FASTWIND (but we intend to do this shortly, see Chapter 7). A major advantage of this code is its computational speed; a typical computation time for one model is only 30 minutes, whereas a corresponding calculation takes a few hours for WM-Basic and 10-12 hours for CMFGEN. This remarkable gain in computational speed is achieved by applying appropriate physical approximations to processes where very high accuracy is not needed, in particular an efficient treatment of the metal-line background opacities has been developed (for details, see Puls et al., 2005). The parameter space to be considered within one spectroscopic analysis using FASTWIND is large. A simultaneous derivation must be carried out for effective temperature T_{eff} , gravity $\log g$, stellar radius R_* , mass-loss rate \dot{M} , terminal wind velocity v_∞ , velocity field parameter¹³ β , individual abundances (including the helium abundance Y_{He}), and the global background metallicity z . Standard procedures to derive these stellar and wind parameters from observed optical spectra are described in, e.g., Repolust et al. (2004).

As discussed in Sect. 1.4.3, *wind clumping* most probably is crucial for a correct interpretation of stellar spectra from hot, massive stars. Clumping is currently included in FASTWIND, as well as in CMFGEN and POWR, by means of the microclumping approach. No treatment of clumping is currently included in WM-Basic (but also this is work underway). In Chapters 4 and 5 we develop detailed radiative transfer techniques that relax this questionable assumption, and use them to show that deviations

¹²We thereby disregard the earlier mentioned PHOENIX code, since this is mainly used to analyze cool stars and supernovae, although a few hotter stars have been considered, e.g., the A supergiant Deneb (Aufdenberg et al., 2002).

¹³The stationary velocity structure of these winds is usually described by $v(r) \approx v_\infty(1 - R_*/r)^\beta$, as predicted by the line-driven wind theory.

from the microclumping approximation can be important for several spectral diagnostics of hot star winds. Accordingly the derived mass-loss rates are affected as well. Thus, as a consequence of these results, it has become desirable to incorporate a better description of wind clumping in the unified atmospheric codes, which indeed is a planned project within our group (see Chapter 7).

Chapter 2

Mass loss from OB-stars

This chapter is a copy of Puls, Sundqvist, Najarro, & Hanson (2009), ‘Mass loss from OB-stars’. At the end of the Chapter is added an addendum, which updates some of the material as well as discusses it in connection to the other chapters.

2.1 Abstract

We review recent developments regarding radiation driven mass loss from OB-stars. We first summarize the fundamental theoretical predictions, and then compare these to observational results (including the VLT-FLAMES survey of massive stars). Especially we focus on the mass loss-metallicity dependence and on the so-called bi-stability jump.

Subsequently we concentrate on two urgent problems, weak winds and wind clumping, that have been identified from various diagnostics and that challenge our present understanding of radiation driven winds. We discuss the problems of ‘measuring’ mass-loss rates from weak winds and the potential of the near infrared, Br-alpha line as a tool to enable a more precise quantification, and comment on physical explanations for mass-loss rates that are much lower than predicted by the standard model.

Wind clumping, conventionally interpreted as the consequence of a strong instability inherent to radiative line-driving, has severe implications for the interpretation of observational diagnostics, since derived mass-loss rates are usually overestimated when clumping is present but ignored in the analyses. Simplified techniques to account for clumping indicate overestimates by factors of 2 to 10, or even more. If actually true, these results would have a dramatic impact on the evolution of, and the feedback from, massive stars. We discuss ongoing attempts (including own work) to interpret the corresponding observations in terms of more sophisticated models. By allowing for porosity in density and velocity space, and for a non-void inter-clump medium, such models might require only moderate reductions of mass-loss rates.

2.2 Introduction

Massive stars are critical agents in galactic evolution, both in the present and in the early Universe (e.g., re-ionization and first enrichment). *Mass loss* is a key process, which modifies chemical profiles, surface abundances, and luminosities. Furthermore, *mass loss* has to be understood *quantitatively* in order to describe and predict massive star evolution in a correct way. The standard theory to describe

hot, massive star winds is based on radiative line-driving, and has been proven to work successfully in most evolutionary phases (OB-stars, A-supergiants, and LBVs in their ‘quiet’ phase). Also for the pivotal Wolf-Rayet (WR) stadium, line-driving is still the most promising acceleration mechanism (Gräfener & Hamann, 2005, 2008).

In this review, we summarize fundamental predictions of the theory, as well as corresponding observational evidence, and subsequently concentrate on two urgent problems that challenge our understanding of line-driven winds, the so-called weak-wind problem and wind clumping. We concentrate on the winds from ‘normal’ OB-stars in all evolutionary phases (for corresponding results and problems regarding WR-winds and additional material, see the contributions by Hamann and Hillier, this volume).

2.3 Line-driven winds from hot stars – theoretical predictions

To be efficient, radiative line-driving requires a large number of photons, i.e., a high luminosity L . Since $L \propto T_{\text{eff}}^4 R_*^2$, not only OB-supergiants, but also hot dwarfs and A-supergiants undergo significant mass loss via this mechanism. Typical mass-loss rates are of the order of $\dot{M} \approx 0.1 \dots 10 \times 10^{-6} M_{\odot} \text{yr}^{-1}$, with terminal velocities $v_{\infty} \approx 200 \dots 3,000 \text{ km s}^{-1}$. Another prerequisite is the presence of a multitude of spectral lines, with high interaction probabilities, close to flux maximum, implying that the strength of line-driven winds should strongly depend on metallicity.

Pioneering work on this subject were performed by Lucy & Solomon (1970) and Castor et al. (1975) (‘CAK’), where the latter still builds the theoretical foundation of our present understanding. Improvements with respect to a *quantitative* description and first applications were provided by Friend & Abbott (1986) and Pauldrach et al. (1986), whereas recent reviews on the topic have been published by Kudritzki & Puls (2000) and Puls et al. (2008b).

The principle idea of radiative line-driving relies on two processes.

1. Momentum is transferred to the wind matter via line absorption/emission processes, mostly resonance scattering, with a net change in *radial* momentum

$$\Delta P_{\text{radial}} = \frac{h}{c} (v_{\text{in}} \cos \theta_{\text{in}} - v_{\text{out}} \cos \theta_{\text{out}}) \quad (2.1)$$

where v_{in} and v_{out} are the frequencies of the absorbed and emitted photons, and θ is the angle between the photon’s direction and the radial unit vector. Thanks to the fore-aft symmetry of the emission process, on average $\langle \cos \theta_{\text{out}} \rangle = 0$, whereas $\langle \cos \theta_{\text{in}} \rangle \approx 1$, since (most) of the absorbed photons originate from the stellar surface. Thus, $\langle \Delta P_{\text{radial}} \rangle \approx h v_{\text{in}} / c$, and the total radiative acceleration exerted on a mass element Δm per time interval Δt can be derived from considering all participating lines,

$$g_{\text{rad}} = \frac{\langle \Delta P \rangle_{\text{tot}}}{\Delta t \Delta m} = \frac{\sum_{\text{all lines}} \langle \Delta P \rangle_i}{\Delta t \Delta m}. \quad (2.2)$$

2. Due to the huge number of metallic lines as compared to the few dozens from hydrogen and helium, mostly just the metal ions are *directly* accelerated. Their momentum needs to be transferred to the bulk plasma (H, He), via Coulomb collisions. The velocity drift of the metal ions with respect to H/He is compensated for by a frictional force (‘Stokes law’) as long as the ratio between drift and thermal velocity is small (e.g., (Springmann & Pauldrach, 1992; Krtićka & Kubát, 2000; Owocki &

Puls, 2002)). Otherwise (at very low wind-densities) the metallic ions might decouple from the wind, and the wind no longer becomes accelerated.

The real challenge is to evaluate Eq. 2.2. Following CAK, this is conventionally done by (i) applying the Sobolev theory (Sobolev, 1960) to approximate the line optical depths and thus the interaction probabilities, and (ii) to replace the summation by appropriate integrals over the line-strength distribution (resulting from detailed NLTE calculations), where the line-strength k is the line-opacity measured in units of the Thomson-scattering opacity. This distribution can be fairly well approximated by a power-law, $dN(k)/dk \propto N_{\text{eff}} k^{\alpha-2}$, with N_{eff} the effective (flux-weighted) number of lines and $\alpha \approx 0.6 \dots 0.7$ (e.g., (Puls et al., 2000)). Note that both quantities depend on metallicity and spectral type. As a final result, $g_{\text{rad}} \propto ((dv/dr)/\rho)^\alpha$, i.e., depends on the *spatial* velocity gradient and on the inverse of the density.

2.3.1 Scaling relations and WLR

Once the above quantities are inserted into the hydrodynamic equations (adopting stationarity), the latter can be solved (almost) analytically, returning the following scaling relations for mass-loss rate, velocity law, and terminal velocity:

$$\dot{M} \propto N_{\text{eff}}^{1/\alpha'} L^{1/\alpha'} (M(1-\Gamma))^{1-1/\alpha'}, \quad v(r) = v_\infty \left(1 - \frac{R_*}{r}\right)^\beta \quad (2.3)$$

$$v_\infty \approx 2.25 \frac{\alpha}{1-\alpha} v_{\text{esc}}, \quad v_{\text{esc}} = \left(\frac{2GM(1-\Gamma)}{R_*}\right)^{1/2}. \quad (2.4)$$

with Eddington- Γ , (photospheric) escape velocity v_{esc} , and $\alpha' = \alpha - \delta$, where $\delta \approx 0.1$ describes the run of the ionization (Abbott, 1982). The velocity-field exponent, β , is of the order of 0.8 (for O-stars) to 2 (for BA-supergiants).

Using these scaling relations, a fundamental prediction for line-driven winds becomes apparent if one calculates the so-called modified wind-momentum rate,

$$\dot{M}v_\infty(R_*/R_\odot)^{1/2} \propto N_{\text{eff}}^{1/\alpha'} L^{1/\alpha'} (M(1-\Gamma))^{3/2-1/\alpha'}, \quad (2.5)$$

and accounts for the fact that α' is of the order of 2/3. Then the wind-momentum rate becomes independent on mass and Γ , and can be expressed in terms of the *wind-momentum luminosity relation* (WLR), discovered first by Kudritzki et al. (1995),

$$\log\left(\dot{M}v_\infty(R_*/R_\odot)^{1/2}\right) \approx x \log(L/L_\odot) + D(z, \text{spectral type}) \quad (2.6)$$

with slope $x = 1/\alpha'$ and offset D , which depends on N_{eff} and thus on metallicity z and spectral type. Originally, it was proposed to exploit the WLR for measuring extragalactic distances on intermediate scales (up to the Virgo cluster), but nowadays the relation is mostly used to test the theory itself (see below).

2.3.2 Theoretical 1-D models

Though the basic scaling relations for line-driven winds are known since the key paper by CAK (and updates by (Abbott, 1982; Friend & Abbott, 1986; Pauldrach et al., 1986)), *quantitative* predictions require consistent NLTE/radiative-transfer calculations, to derive the line-force as a function of spectral

type and metallicity, as well as the inclusion of processes neglected in the original work, for example line-overlap (e.g., Friend & Castor, 1983; Puls, 1987).

The most frequently cited theoretical wind models (stationary, 1-D, homogeneous) are those from Vink et al. (2000, 2001). Based on the Monte-Carlo approach developed by Abbott & Lucy (1985), they allow multi-line effects to be considered. In these models, the mass-loss rate is derived (iterated) from *global* energy conservation, whilst the (β -) velocity field is pre-described and the NLTE rate equations are treated in a simplified way. Pauldrach (1987) and Pauldrach et al. (1994, 2001), on the other hand, obtain a consistent hydrodynamic solution by integrating the (modified) CAK equations based on a rigorous NLTE line-force using Sobolev line transfer. Moreover, Krtićka & Kubát (2000, 2001, 2004, 2009) and Krtićka (2006) solve the equation of motion by means of a NLTE, Sobolev line-force, including a more-component description of the fluid (accelerated metal ions plus H/He) that allows them to consider questions regarding drift-velocities, non-thermal heating, and ion decoupling. Also, Kudritzki (2002) (see also Kudritzki et al. (1989)) provides an analytic “cooking recipe” for mass-loss rate and terminal velocity, based on an approximate NLTE treatment, and Gräfener & Hamann (2005, 2008) obtain self-consistent solutions (applied to WR winds) by means of a NLTE line-force evaluated in the comoving frame (see Mihalas et al. 1975). Finally, Lucy (2007a,b) and Müller & Vink (2008) derive the wind-properties from a *regularity* condition at the *sonic point*, in contrast to most other solutions that invoke a *singularity* condition at the CAK-critical point of the wind.

Results and predictions from hydrodynamic modeling. Most of the various approaches yield consistent results, e.g., when comparing the “mass-loss recipe” from Vink et al. (2000) with similar investigations utilizing different codes (Kudritzki, 2002; Pauldrach et al., 2001; Krtićka & Kubát, 2004). Moreover, the WLR concept is impressively confirmed by the simulations performed by Vink et al.: The obtained modified wind-momenta follow an almost perfect power-law with respect to stellar luminosity alone, *independent of luminosity class*, and, for solar abundances, “only” two distinct relations covering the complete spectral range have been found, one for $50 \text{ kK} > T_{\text{eff}} > 27.5 \text{ kK}$ and the other for $22.5 \text{ kK} > T_{\text{eff}} > 12 \text{ kK}$, respectively. In other words, the spectral type dependence of x and D in Eq. 2.6 seems to be rather mild.

Also regarding the predicted metallicity dependence, the various results agree satisfactorily (note that the z -dependence of v_{∞} is rather weak):

$$\begin{aligned} \text{Kudritzki (2002):} \quad v_{\infty} &\propto z^{0.12}, & \text{Krtićka (2006):} \quad v_{\infty} &\propto z^{0.06}, \\ \text{Vink et al. (2001):} \quad \dot{M} &\propto z^{0.69} \text{ for O-stars,} & \dot{M} &\propto z^{0.64} \text{ for B-supergiants,} \\ \text{Krtićka (2006):} \quad \dot{M} &\propto z^{0.67} \text{ for O-stars,} \end{aligned}$$

2.4 Observations vs. Theory

In the last decade, various spectroscopic NLTE analyses of hot stars *and their winds* have been undertaken, in the Galaxy and in the Magellanic Clouds, in the UV, in the optical, and in a combination of both. For a compilation of these publications (without Galactic Center objects and objects analyzed within the FLAMES survey of massive stars, see below), see Tables 2 and 3 in Puls et al. (2008b), to be augmented by the UV-PV investigation of Galactic O-stars by Fullerton et al. (2006), the UV+optical analysis of Galactic O-dwarfs by Marcolino et al. (2009), and the optical analysis of LMC/SMC O-stars by Massey et al. (2009). Most of this work has been performed by means of 1-D, line-blanketed,

NLTE, atmosphere/spectrum-synthesis codes allowing for the presence of winds, in particular CMFGEN (Hillier & Miller 1998), WM-Basic (Pauldrach et al. 2001), and FASTWIND (Puls et al. 2005).

2.4.1 Central results

The results of these investigations can be roughly summarized as follows. (i) The mass-loss rates from SMC stars (with $z \approx 0.2 z_{\odot}$, see (Mokiem et al., 2007b) and references therein) are indeed lower than those from their Galactic counterparts. (ii) For O- and early B-stars, the theoretically predicted WLR from Vink et al. (2000) is met, except for O-supergiants with rather dense winds, in which the observed wind-momenta are higher (by factors around three) than the predictions (which might be explained by wind-clumping effects, see Sect. 2.6), and for a number of late O-dwarfs (and a few O-giants), in which the observed wind-momenta are much lower than the predictions (this is the so-called ‘weak-wind problem’, see Sect. 2.5). (iii) B-supergiants below the ‘bi-stability jump’ ($T_{\text{eff}} < 22$ kK) show lower wind-momenta than predicted, as outlined in the following.

2.4.2 The bi-stability jump: predictions and observations

A fundamental prediction by Vink et al. (2000) is the occurrence of two distinct WLRs, one for hotter objects and one for cooler objects, with the division located around 25 ± 2.5 kK. This rather abrupt change is due to the so-called bi-stability mechanism¹, which relies on the fact that the mass-loss rates of line-driven winds are, for typical chemical compositions, primarily controlled by the number and distribution of *iron*-lines, because of their dominant contribution ($\sim 50\%$) to the total line acceleration in the lower wind (Puls et al., 2000; Vink et al., 2000; Krtićka, 2006). Below roughly 25 kK, the ionization of iron is predicted to switch abruptly from Fe IV to Fe III, and since Fe III has more driving lines than Fe IV at flux maximum, the mass-loss rate must increase. Quantitatively, Vink et al. (2000) predict an increase in \dot{M} by a factor of five and a decrease of v_{∞} by a factor of two, so that, overall, B-supergiants (except for the earliest sub-types) should have higher wind-momenta than their O-star counterparts at the same luminosity.

Observations confirm the ‘velocity-part’ of this picture, at least qualitatively. For stars with $T_{\text{eff}} \geq 23$ kK, the observed ratio is $v_{\infty}/v_{\text{esc}} \approx 3$, whereas it decreases *gradually* towards cooler temperatures, reaching values of $v_{\infty}/v_{\text{esc}} \approx 1.3 \dots 1.5$ for stars with $T_{\text{eff}} \leq 18$ kK (Evans et al., 2004; Crowther et al., 2006; Markova & Puls, 2008). With respect to the predicted increase in \dot{M} , however, the situation is different. As shown by Markova & Puls (2008), the mass-loss rates of B-supergiants below the *observed* bi-stability jump ($T_{\text{eff}} < 22$ kK) actually *decrease* or at least do no change. This is a first indication that there are still problems in our understanding of line-driven winds.

2.4.3 The FLAMES survey of massive stars

Further progress has been obtained within the FLAMES survey of massive stars (P.I. S. Smartt), a project that performed high resolution multi-object spectroscopy of stars located within eight young and old clusters in the Galaxy and the Magellanic Clouds. In total, 86 O-stars and 615 B-stars were observed (for introductory papers and a brief summary, see Evans et al. 2005, 2006, 2008). The major scientific objectives of this survey were to investigate (i) the relation between stellar rotation

¹ denoted after some peculiar behaviour of theoretical models for the wind of P Cygni (Pauldrach & Puls, 1990).

and abundances (i.e., to test the present theory of rotational mixing), (ii) the role of binarity, and (iii) stellar mass-loss as a function of metallicity.

Regarding the last objective, Mokiem et al. (2006, 2007a) analyzed a total of ~ 60 O- and early B-stars in the SMC and LMC, by means of FASTWIND and using a genetic algorithm (Mokiem et al., 2005). The results were combined by Mokiem et al. (2007b) with data from previous investigations, to infer the metallicity dependence of line-driven mass-loss based on a significant sample of stars. Using mean abundances of $z = 0.5 z_{\odot}$ (LMC) and $z = 0.2 z_{\odot}$ (SMC), a metallicity dependence of $v_{\infty} \propto (z/z_{\odot})^{0.13}$, and a correction for clumping effects (see below) following Repolust et al. (2004), they derived an *empirical* relation

$$\dot{M} \propto (z/z_{\odot})^{0.72 \pm 0.15}, \quad (2.7)$$

with rather narrow confidence intervals. This result is consistent with theoretical predictions, both from line-statistics (Puls et al., 2000) and from hydrodynamic models (see above).

2.5 Weak winds

The results as summarized above imply that line-driven mass loss seems to be basically understood, though certain problems need further consideration. In particular, from early on there were indications that the (simple) theory might break down for low-density winds. E.g., Chlebowski & Garmany (1991) have derived mass-loss rates for late O-dwarfs that are factors of ten lower than expected. By means of UV-line diagnostics, Kudritzki et al. (1991) and Drew et al. (1994) have derived mass-loss rates for two BII stars that are a factor of five lower than predicted, and Puls et al. (1996) have shown that the wind-momentum rates for low-luminosity dwarfs and giants ($\log L/L_{\odot} < 5.3$) lie well below the empirical relation for “normal” O-stars.

The last investigation illuminated an immediate problem arising for low-density winds. For $\dot{M} < (5 \dots 1) \cdot 10^{-8} M_{\odot} \text{yr}^{-1}$, the conventional mass-loss indicator, H_{α} , becomes insensitive, and only upper limits for \dot{M} can be derived (for a recent illustration of this problem, see (Marcolino et al., 2009)). Instead, unsaturated UV resonance lines (C IV, Si IV, C III) might be used to obtain actual values for \dot{M} (e.g., Martins et al., 2004; Puls et al., 2008b; Marcolino et al., 2009).

By means of such UV-diagnostics, strong evidence has accumulated that a large number of late type O-dwarfs (and a few giants of intermediate spectral type) have mass-loss rates that are factors of 10 to 100 lower than corresponding rates from both predictions and extrapolations of empirical WLRs. In particular, such *weak winds* have been found in the Magellanic Clouds (O-dwarfs in NCG 346 (LMC): Bouret et al. 2003; extremely young O-dwarfs in N81 (SMC): Martins et al. 2004) and in the Milky Way (O-dwarfs and giants: Martins et al. 2005; late O-dwarfs: Marcolino et al. 2009).

Two points have to be stressed. (i) Until now, it is not clear whether *all* or only part of the late type dwarfs are affected by this problem. (ii) The derived UV mass-loss rates are not very well constrained, since they might be contaminated² from X-rays embedded in the wind (due to shocks, see next Section). The higher the X-ray emission, the weaker the lines, and the higher the *actual* mass-loss rates (see Figs. 19 and 20 in Puls et al. (2008b)). However, to “unify” the present, very low, \dot{M} -values with “normal” mass-loss rates by invoking X-rays, *unrealistically high* X-ray luminosities would be required (Marcolino et al., 2009).

² via a modified ionization equilibrium.

The weak-wind problem is a prime challenge for the radiative line-driven wind theory. Martins et al. (2004) investigated a variety of candidate processes (e.g., ionic decoupling, shadowing by photospheric lines, curvature effects of velocity fields), but none of those turned out to be strong enough to explain the very low mass-loss rates that seem to be present. At the end of this review, we will return to this problem.

2.6 Wind clumping

During the last years, overwhelming direct and indirect evidence has accumulated that one of the standard assumptions of conventional wind models, *homogeneity*, needs to be relaxed. Nowadays the winds are thought to be clumpy, consisting of *small scale* density inhomogeneities, where the wind matter is compressed into over-dense clumps, separated by an (almost) void inter-clump medium (ICM). Details on observations and theory can be found in the proceedings of a recent workshop, ‘Clumping in hot star winds’ (Hamann et al., 2008).

Theoretically, such inhomogeneities are considered related to structure formation due to the line-driven (‘de-shadowing’) instability, a strong instability inherent to radiative line-driving. Time-dependent hydrodynamic models allowing for this instability to operate have been developed by Owocki and coworkers (1-D:Owocki et al. 1988; Runacres & Owocki 2002, 2005; 2-D:Dessart & Owocki 2003, 2005) and by Feldmeier (Feldmeier, 1995; Feldmeier et al., 1997), and show that the wind, for $r \gtrsim 1.3R_*$, develops extensive structure consisting of strong *reverse* shocks separating slower, dense material from high-speed rarefied regions in between. Such structure is the most prominent and robust result from time-dependent modeling, and *the basis for our interpretation and description of wind clumping*. Within the shocks, the material is heated to a couple of million Kelvin, and subsequently cooled by X-ray emission (which has been observed by all X-ray observatories), with typical X-ray luminosities $L_X/L_{\text{bol}} \approx 10^{-7}$ (for newest results, see Sana et al. 2006).

Clumping effects. Until now, most diagnostic methods to investigate the effects of clumping use the following assumptions: The clumps are *optically thin*, the ICM is void, the velocity field remains undisturbed, and the so-called clumping factor, f_{cl} , measures the over-density inside the clumps with respect to the average density. This simple model of *micro-clumping* allows one to incorporate clumping into NLTE-codes without any major effort, namely by multiplying the average (wind-) density by f_{cl} and by multiplying all opacities/emissivities by the inverse of f_{cl} (i.e., by the volume filling factor). The most important consequence of such optically thin clumps is a reduction of any \dot{M} derived from ρ^2 -dependent diagnostics (e.g., recombination based processes such as H_α or radio-emission), assuming smooth models, by a factor of $\sqrt{f_{\text{cl}}}$. That there is a *reduction* is conceivable, since, under the assumptions made, the square of the over-density ‘wins’ against the smaller absorbing/emitting volume. Thus, a lower \dot{M} is sufficient to produce the same optical depths/emission measures as in smooth models.

Note, however, that in this scenario any \dot{M} derived from ρ -dependent diagnostics (e.g., UV-resonance lines) remains uncontaminated, since in this case the over-density cancels against the smaller absorbing/emitting volume. Finally, it should be mentioned that a clumpy medium also affects the ionization equilibrium, due to enhanced recombination (e.g., Bouret et al., 2005).

Results from NLTE-spectroscopy allowing for micro-clumped winds are as follows. (i) Typical clumping factors are $f_{\text{cl}} \approx 10 \dots 50$, and clumping starts at or close to the wind base, the latter in conflict with theoretical predictions. Derived mass-loss rates are factors of 3 to 7 lower than previ-

ously thought (Crowther et al., 2002; Hillier et al., 2003; Bouret et al., 2003, 2005). In strong winds, the inner region is more clumped than the outer one ($f_{\text{cl}}^{\text{in}} \approx 4 \dots 6 \times f_{\text{cl}}^{\text{out}}$), and the minimum reduction of smooth $\text{H}\alpha$ mass-loss rates is by factors between 2 and 3 (Puls et al., 2006).

The P v problem. From a mass-loss analysis using the FUV P v resonance line³ for a large sample of O-stars, Fullerton et al. (2006) (see also Massa et al. 2003) concluded that the resulting mass-loss rates are a factor of 10 or more lower than derived from $\text{H}\alpha$ and/or radio emission using homogeneous models, implying $f_{\text{cl}} \gtrsim 100$! Similar results have been found from unsaturated P Cygni lines from lower luminosity B-supergiants (Prinja et al., 2005).

If such large reductions in \dot{M} were true, the consequences for stellar evolution and feed-back would be enormous. Note that an ‘allowed’ reduction from evolutionary constraints is at most by a factor of 2 to 4 (Hirschi, 2008).

Porosity and vorosity. A possible resolution of this dilemma might be provided by considering the porosity (Owocki et al., 2004) of the medium, also suggested to explain the observed X-ray line emission (cf. the contributions by Oskinova et al. and Cohen et al. in Hamann et al. 2008, and particularly the discussion on X-rays). Whenever the clumps become optically thick for certain processes, as might be true for the P v-line, the geometrical distribution of the clumps becomes important (size vs. separation, shape). In this *macro-clumping* approach (see also Hamann, this volume), the effective opacity becomes reduced, i.e., the wind becomes more transparent (‘porous’), because radiation can propagate through the ‘holes’ provided by the ICM. Additionally, clumps hidden behind other clumps become ineffective because the first clump is already optically thick.

Oskinova et al. (2007) used a simple, quasi-analytic treatment of macro-clumping (still assuming a smooth velocity law) to investigate P v in parallel with $\text{H}\alpha$ from ζ Pup. Whereas macro-clumping had almost no effect on $\text{H}\alpha$, since the transition is optically thin in the clumps, P v turned out to be severely affected. Thus, only a moderate reduction of the smooth mass-loss rate (factors 2 to 3) was necessary to fit the observations, consistent with the evolutionary constraints from above.

This model has been criticized by Owocki (2008), who pointed out that not only the distribution/optical thickness of the clumps is important, but also the distribution of the velocity field, since the interaction between photons and *lines* is controlled by the Doppler-effect. Also the ‘holes’ in *velocity space*, due to the non-monotonic character of the velocity field, lead to an increased escape (thus, he called this process velocity-porosity = ‘vorosity’), whilst the different velocity gradients inside the clumps lead to an additional modification of the optical depth.

Resonance line formation with porosity and vorosity. To clarify in how far the above arguments/simulations depend on the various assumptions, and to characterize/quantify the various effects from inhomogeneous winds of *different sub-structures*, a current project in our group investigates the resonance-line formation in such winds. To this end, pseudo 2-D hydrodynamic models (based on different snapshots of corresponding 1-D models from Owocki and Feldmeier, aligned as independent slices of opening angle Θ), as well as 2-D models based on a stochastic description, have been created (Fig. 2.1, left panel). For these models then, a *detailed* Monte-Carlo line transfer (discarding the Sobolev-approximation) is performed. The right panel of Fig. 2.1 shows prototypical profiles from such simulations, based on the stochastic 2-D wind description, for an intermediate strong line that would be marginally saturated in smooth models (dashed). The grey dashed-dotted profile displays the effects of porosity alone (i.e., a smooth velocity field has been used), using a rather low clumping

³ unsaturated due to the low phosphorus abundance.

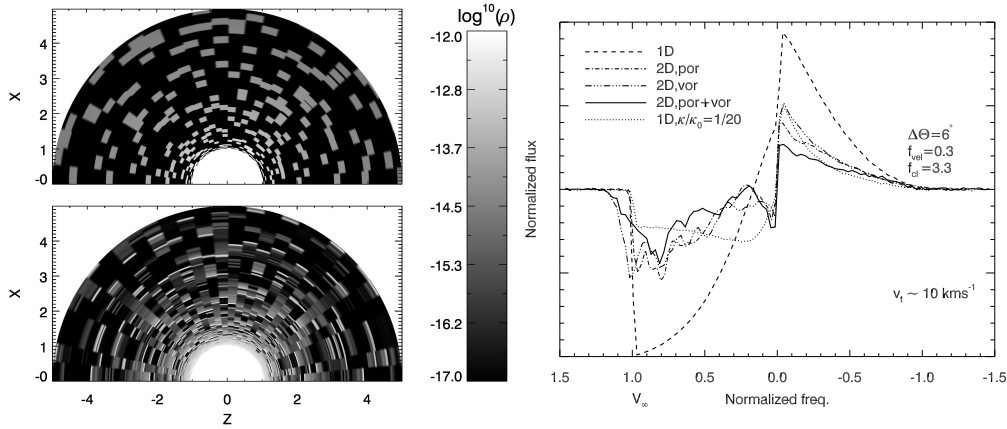


Figure 2.1: **Left:** Density contours of stochastic (upper) and pseudo 2-D hydrodynamic wind models as investigated by our group. **Right:** Line profiles for an intermediate strong line formed in inhomogeneous winds with different sub-structures. See text.

factor, $f_{\text{cl}} = 3.3$, and an average separation of clumps $\sim R_*$ in the outer wind. Already here, a strong de-saturation of the profile is visible. The grey dashed-dotted-dotted line displays the other extreme, namely vorosity alone (i.e., now the density is smooth), using a stochastic description of the velocity field, characterized by a “velocity clumping factor” (as defined in Owocki 2008, Fig. 1) $f_{\text{vel}} = 0.3$. Interestingly, the de-saturation of the profile is similar to the porosity-effect alone. The solid black line displays the combined effect from porosity and vorosity, with a further de-saturation. If compared to a line from a smooth model of similar profile strength (dotted), it turns out that the effective opacity in the structured model(s) has been reduced by a factor of 20, i.e., the actual \dot{M} would be a factor of 20 higher than derived from a smooth model. Thus, structured models invoking porosity and vorosity might indeed resolve the discordance between the results by Fullerton et al. and evolutionary constraints.

We note, however, that the profile-strength reduction presented in Fig. 2.1 corresponds to a ‘most favourable case’, using rather ideal parameters. Our investigations have shown how details on porosity, vorosity, and the ICM, all are important for the formation of the line profiles. In fact, the strengths of similar profiles calculated from our pseudo 2-D hydrodynamic models are only reduced by $\approx 10\%$, because of insufficient vorosity inherent to structures from present time-dependent modeling (see also Owocki 2008). Such a modest reduction is much lower than needed to alleviate the discrepancy discussed above. Also, as it turns out, the ICM is a crucial parameter if to de-saturate intermediate strong lines and, at the same time, allowing the formation of the observed saturated profiles. Tests have shown that, with a void ICM, the formation of saturated profiles is only possible if the average clump separation (controlling the porosity) is very small, but then the de-saturation of intermediate strong lines becomes marginal. Only by assuming an ICM with sufficient density ($\approx 0.01\rho_{\text{smooth}}$) we have been able to form saturated lines in parallel with de-saturated ones of intermediate strength. This finding is consistent with results from Zsargó et al. (2008), who pointed out that the ICM is crucial for the formation of highly ionized species such as O VI.

Further details and results from our investigations will be given in a forthcoming paper (Sundqvist et al., in prep for A&A, *added note: Chapter 4*), including a systematic investigation of different key parameters and effects. Future plans include a comparison with emission lines, and the development

of simplified approaches to incorporate porosity/vorosity effects into NLTE models.

2.7 Weak winds again – Br_α as a diagnostic tool

In the preceding paragraphs, we have argued that (i) mass-loss rates from unsaturated UV line-profiles are *much* lower than those from H_α or radio emission, and that (ii) this discordance might be mitigated by porosity/vorosity effects. Recall here that the mass-loss rates from weak winds discussed so far (Sect. 2.5) rely on the same UV-line diagnostics, and the question arises whether one encounters a similar problem, i.e., an under-estimation of the “true” mass-loss rates due to insufficient physics accounted for in the diagnostics. Thus, to clarify in how far the weak wind problem is a real one, independent diagnostics are required!

Already in 1969, Auer & Mihalas, based on their first generation of NLTE, hot-star model atmospheres, predicted that the IR Br_α -line should show significant *photospheric* core emission, due to an under-population of its lower level ($n = 4$) relative to the upper one ($n = 5$), resulting from a very efficient decay channel $4 \rightarrow 3$. Indeed, such core emission has meanwhile been observed in various weak wind candidates such as τ Sco (B0.2V), HD 36861 (O8III(f)), and HD 37468 (O9.5V) (Najarro, Hanson and Puls, in prep. for A&A). Recent simulations (Puls et al. 2008b, Figs. 21/22) actually show that such photospheric + wind emission can fit the observations quite nicely, and that the core of Br_α is a perfect tracer for the wind density also for thinner winds (as opposed to H_α). Astonishingly, the *height of the peak increases for decreasing \dot{M}* , which is related to the *onset* of the wind, i.e., the density/velocity structure in the transition zone between photosphere and wind, and not due to radiative transfer effects. The higher the wind-density, the deeper (with respect to optical depth) this onset, which subsequently suppresses the relative under-population of $n = 4$ due to efficient pumping from the hydrogen ground-state. Moreover, Br_α is only weakly affected by the presence of X-rays, and thus an ideal tool to infer very low mass-loss rates. From fits to the observations, it turns out that \dot{M} is actually very low (of the order of $10^{-10} M_\odot \text{yr}^{-1}$ for HD 37468, and even lower, if the wind-base were clumped). *Thus, weak winds seem to be a reality!*

What may then be the origin of weak winds? Krtićka & Kubát (2009) argue that weak-winded stars display enhanced X-ray emission, maybe related to extended cooling zones because of the low wind density. Already Drew et al. (1994) pointed out that strong X-ray emission can lead to a reduced line acceleration, because of a modified ionization equilibrium, and since higher ions have fewer lines. Thus, weak-winded stars might be the result of strong X-ray emission. Let us now speculate whether such strong emission might be related to magnetic fields. Note that weak winds can be strongly affected by relatively weak B -fields, of the order of 40 Gauss according to the scaling relations provided by ud-Doula & Owocki (2002), which is below the present detection threshold. In this case then, colliding loops might be generated, which in turn generate strong and hard X-ray emission in the lower wind, which finally might influence the ionization and thus radiative driving. Future simulations coupling magneto-radiation-hydrodynamic wind codes with a *self-consistent* description of the line-acceleration will tell whether this mechanism might work.

2.8 Addendum

Obviously, wind clumping is much more thoroughly covered in Chapters 1 and 3-5 than here, and these chapters adequately update some of the clumping related results discussed in this review. Below

we use this addendum to discuss the weak wind problem a little further.

It was pointed out in Sect. 2.5 that X-rays as well as *optically thick clumping* may affect the formation of diagnostic UV lines in so-called weak winded stars. Concerning the latter effect, we in Chapters 4 & 5 indeed show that one may underestimate the ‘observed’ mass-loss rates by as much as an order of magnitude if optically thick clumps are present in the wind but ignored in the analysis. Moreover, we illustrate that the clump optical depths τ_{cl} for the PV resonance lines in a model of the O6 supergiant λ Cep are $\tau_{cl} \approx 100$ (see Fig. 5.4). Since the predicted theoretical mass-loss rates for the stars analyzed by Marcolino et al. (2009) are ≈ 30 times lower than the corresponding rate of λ Cep, this may indicate that clumps could be optically thick for PV also in these stars (if the corresponding ionization fractions are similar), and thereby that the mass-loss rates inferred from PV could be underestimated. Also, in Chapter 5 we demonstrate how the formation of another resonance line doublet used as a mass-loss indicator in Marcolino et al., NV at 1240 Å, also may be strongly affected by optically thick clumping in these stars. In view of the simple estimate for PV above, this is not surprising, since the higher nitrogen abundance generally makes these lines stronger than the PV lines. Thus, these ‘weak winded’ objects should in the future be re-analyzed using sufficient descriptions of optically thick clumping and X-rays, in order to investigate to which extent the results discussed earlier might be a consequence of in-sufficient physics accounted for when modeling the diagnostic lines. Meanwhile, however, independent diagnostics are required to clarify in how far the weak wind problem is real. This was discussed in Sect. 2.7, in terms of Br_α as a good candidate for such a diagnostic.

However, let us point out here that the Br_α modeling may be problematic for other reasons than X-rays and/or optically thick clumping. Deviations from the LTE source function for given departure coefficients are greatly amplified in the IR (because of the increasing contribution from stimulated emission, see Sect. 1.5.4), which in turn means that the Br_α NLTE modeling is very sensitive to the input *atomic data* of the hydrogen model atom. Actually, although for other chemical species and in a completely different stellar domain, in this respect the Br_α situation appears somewhat similar to the one analyzed in detail in Chapter 6, namely the NLTE formation of the *photospheric* IR metallic emission lines in late-type stars. In that chapter, we show that the modeled emission lines (at 12 and 18 μm) from highly excited states of Mg I ($n = 7 \rightarrow 6$ for the 12 μm lines) are very sensitive to the input magnesium atomic data, because small changes in the departure coefficients can cause large changes in the modeled line source function, which in turn drastically affects the line core emission. Figs. 6.3 & 6.4 illustrate how the modeled Mg I emission peaks react strongly when the total collision rates are modified (in this case by the inclusion of collisions between magnesium and neutral hydrogen atoms), because the changed balance between radiative and collision rates affects the decay channels feeding the participating levels, which in turn influences the predicted departure coefficients.

Now, regarding the NLTE modeling of Br_α , there might still be problems with the input atomic data for collisions between hydrogen and free electrons, which are the collisions that must be included in appropriate hydrogen model atoms for hot stars. Repolust et al. (2005) pointed out that newly computed rates based on *ab initio* quantum mechanical calculations by Przybilla & Butler (2004) actually resulted in worse agreement between the IR and optical hydrogen lines than what was obtained when using older data. Because of this, the standard option for the hydrogen model atom in, e.g., FASTWIND actually still is an older, presumably less accurate, collision data set. Thus the modeled Br_α emission will be sensitive not only to the adopted mass-loss rate but also to the actual choice of input atomic data, which of course brings additional uncertainties to mass-loss rates derived from this line. In conclusion, a careful study of the impact from the atomic data certainly is required *before* Br_α should be routinely used as a mass-loss indicator.

Chapter 3

Radiative transfer in stochastic media and hot star winds

- microclumping, vorosity, and porosity revisited

In this chapter we shall concern ourselves with some results derived for the equation of transport in stochastic media. In particular, we show that a model derived by Levermore et al. (1986), in a quite different context than astrophysics, may be explored to understand the basic radiative transfer effects arising in clumped hot star winds; microclumping, vorosity, and porosity. These results may be of great help to better understand the specific techniques developed, elsewhere as well as in Chapters 4 and 5, to model the effects of these three phenomena. Moreover, we present a very simple extension of the porosity formalisms developed for ρ -dependent processes in hot star winds, to handle also ρ^2 -processes.

3.1 Transfer in stochastic media

For simplicity we shall consider only the very simplest case of a *purely continuum absorbing medium with a constant extinction coefficient*. We thus disregard all frequency (setting $\chi_\nu = \chi$) as well as spatial dependencies of the quantities, and furthermore neglect all emission contributions. Then the standard equation of radiative transfer (Eq. 1.2) becomes

$$\frac{dI_\nu}{ds} = -I_\nu\chi_\nu + j_\nu \rightarrow \frac{dI}{\chi ds} = \frac{dI}{d\tau} = -I, \quad (3.1)$$

with extinction coefficient (or opacity) χ and optical depth τ . The solution over some path s is the well known exponential law for attenuation of light

$$I/I_0 = e^{-\chi s} = e^{-\tau}, \quad (3.2)$$

with I_0 the incident intensity. In a stochastic medium we may obtain a similar ‘transport-like’ solution for the ensemble averaged intensity, by averaging over *all possible physical realizations*

$$\langle I \rangle / I_0 = \langle e^{-\tau} \rangle, \quad (3.3)$$

where we have assumed that the incident intensity is non-stochastic. We will for convenience absorb I_0 into the expression for the averaged intensity in the following, i.e. $\langle I \rangle / I_0 \rightarrow \langle I \rangle$.

Of course, one can hope to obtain a good estimate of $\langle I \rangle$ by considering different realizations *one by one*, after which one sums them up and average them. For that task one may, for example, use Monte-Carlo simulations (a variant of this is done in Chapter 4). However, it would (obviously) be more convenient if it were possible to obtain a deterministic ‘effective’ value for χ , i.e. a χ_{eff} that could account for the statistical nature of the problem, because then one could go back to the traditional equation of transfer (Eq. 3.1) and only solve it *once*. Similarly, if one could obtain effective values also for the source function, generalizations to more complex situations than the pure absorption case considered here could readily be done. (As we will see later, this is in principle what is attempted with the *microclumping* and *porosity* formalisms that have been developed for radiation transport in clumped hot star winds.)

Defining an effective value of χ is appropriate if each considered realization (here meaning each contribution to the optical depth) is *optically thin*, for then we may in Eq. 3.3 replace the averaging over intensities by an averaging over optical depths, i.e. $\langle e^{-\tau} \rangle \rightarrow e^{-\langle \tau \rangle}$, and obtain

$$\langle I \rangle = e^{-\langle \tau \rangle}, \quad (3.4)$$

which means just this; that if we can find an average (or effective) opacity, we can obtain the ensemble averaged intensity just by considering this quantity.

We will from now on consider a *two component stochastic medium*. Later on the components will be identified with ‘clumps’ and the ‘inter-clump medium’ in a hot star wind, but for now we designate the components i as $i = 0, 1$. Then the averaged opacity is

$$\langle \chi \rangle = p_0 \chi_0 + p_1 \chi_1, \quad (3.5)$$

with probability p_i to find the matter in component i , within the domain of s . Obviously $p_0 + p_1 = 1$. Eq. 3.4 will be valid *if* the characteristic *length scale* l_i (sometimes called the chord length) of a fluid packet in component i is small as compared to the photon mean free path (which may be written as the inverse of the absorption coefficient, χ_i^{-1} , Pomraning 1991), i.e., *if*

$$\chi_i l_i \ll 1. \quad (3.6)$$

This is called the *atomic mix* limit, for the smallest possible fluid packet is of course a single atom. It is equivalent to assuming *optically thin clumps* in a clumped hot star winds (since $\chi_i l_i = \tau_i$). In general, however, Eq. 3.6 will not be satisfied, and if we still attempt to use the atomic mix model, quite erroneous results may follow. We illustrate this with the following example, taken from Pomraning (1991).

Let fluid 0 be composed of optically thin packets ($\chi_0 l_0 \ll 1$) and fluid 1 of optically thick ones ($\chi_1 l_1 \gg 1$). Furthermore, assume that fluid 1 is very sparse ($p_1 \ll p_0$). The picture now is that of a nearly perfect vacuum with a few ‘completely black’ fluid packets in it. Radiation (or particles in Pomraning’s description, for these authors deal with particle rather than radiation transport) incident upon this mixture will have a great chance of escaping the matter without ever interacting with any of the small black packets. But the atomic mixture model will still predict the exponential attenuation for $\langle I \rangle$, and since χ_1 in principle can be made arbitrarily large, it is easy to set up a situation for which Eq. 3.4 predicts *no* transmission through the medium. Clearly, this is very wrong, and it is the essential

effect of *porosity* (an effect that currently is quite intensively discussed in the hot star wind literature, for example in this thesis) which here is missing from the atomic mix model.

Thus, in general, the ensemble averaged intensity must be obtained via Eq. 3.3 instead of Eq. 3.4. We mentioned earlier that the most straightforward approach for this probably is Monte-Carlo simulations. However, such methods are often quite costly (as the one in Chapter 4, for example) and may not always be applied to the more general problem, so it may also be worthwhile to try and find a *direct* solution to $\langle I \rangle$, with the help of a number of variables describing the structured medium, as was done above for the atomic mix model. This task turns out to be quite intricate and problematic though, even for the simplest case of pure continuum absorption. Levermore et al. (1986) demonstrate the mathematical complexity involved, when they derive an *analytic* expression for a *two component Markovian mixture*. Their derivation will not be repeated here, but a few essential points will be pointed out¹.

First, the Markovian assumption is that the future state of a system depends *only* on its present state, and *not* on its history. For example, the angle with which a resonance line photon in a hot star wind is re-emitted after absorption (Chapter 4) may be said to be a Markovian process; it depends *only* on the conditions at the point where the last absorption occurred, and *not* on previous scatterings or on how the photon actually got there (that is, not on its history). The Markovian assumption enters the Levermore et al. model in the following way: if at some spatial point r the fluid is of type 0, then the probability of finding fluid 1 at the point $r + dr$ is $P_{0,1}dr$. Now, this probability is assumed to be *independent* of how far back along the path the last transition (from medium 1 to 0) occurred, i.e. it is assumed to depend only on its present state, hence to be Markovian. Under these assumptions, one can show that the distribution of chord lengths L_0 in fluid 0 will form a classical Poisson process and be exponentially distributed according to the probability density function

$$f_0(L_0) = l_0^{-1} e^{-L_0/l_0}, \quad (3.7)$$

with the *mean* of L_0 thus being l_0 . Furthermore, for this model one can show that the mean segment length l_0 *equals* the inverse of the transition probability $P_{0,1}$, i.e. that $P_{0,1}^{-1} = l_0$. Of course, all these arguments apply also for transitions from fluid 1 to 0. These results may be used to identify the probabilities p_i to at any given point find the fluid in component i , either with

$$p_i = \frac{l_i}{l_0 + l_1}, \quad (3.8)$$

or with the *volume filling fractions*,

$$p_i = \frac{V_i}{V_0 + V_1}, \quad (3.9)$$

because according to Levermore et al. (using the results of Debye et al., 1957) the average chord lengths are given by $l_i = 4V_i/A$, with V_i the associated volume of fluid i and A the common surface area between packets of type 0 and 1.

In summary, the key point here was the identification of the inverse of the transition probability density, $P_{0,1}^{-1}$, with the mean chord length, l_0 . These results may then be used to set up a probability

¹ The Levermore et al. model has been recognized before by the hot star community, e.g. by Shaviv (2001b) and Feldmeier et al. (2008), but not discussed in detail.

density distribution $f(\tau, s)$ for the optical depth random variable (which indeed takes a very complicated expression) and a given path length s . Finally then, the authors solve for the ensemble averaged mean intensity

$$\langle I(s) \rangle = \langle e^{-\tau} \rangle = \int_0^\infty f(\tau, s) e^{-\tau} d\tau. \quad (3.10)$$

Eq. 3.10 is solved *analytically*, by Laplace transformation, with the end result

$$\langle I \rangle = \left(\frac{r_+ - \hat{\sigma}}{r_+ - r_-} \right) e^{-r_+ s} + \left(\frac{\hat{\sigma} - r_-}{r_+ - r_-} \right) e^{-r_- s}, \quad (3.11)$$

with

$$2r_\pm = \langle \chi \rangle + \hat{\sigma} \pm \sqrt{(\langle \chi \rangle - \hat{\sigma})^2 + 4\beta}, \quad (3.12)$$

$$\hat{\sigma} = p_1 \chi_0 + p_0 \chi_1 + \frac{1}{l_0} + \frac{1}{l_1}, \quad (3.13)$$

$$\beta = (\chi_0 - \chi_1)^2 p_0 p_1, \quad (3.14)$$

and the averaged opacity $\langle \chi \rangle$ defined by Eq. 3.5.

We now show that the radiative transfer formalisms developed for describing the effects of *microclumping*, *vorosity*, and *porosity*, in hot star winds may all, in principle, be understood as limiting cases of this basic equation, despite the fact that they have *not* been developed for the specific case of a Markovian mixture.

3.2 Microclumping

The microclumping, or atomic mix, model is recovered from Eq. 3.11 when $l_i \ll \chi_i^{-1}$. Then $r_+ \sim \hat{\sigma}$, so that the first term in Eq. 3.11 vanishes, and $r_- \rightarrow p_0 \chi_0 + p_1 \chi_1$. Thus

$$\langle I \rangle = e^{-\langle \chi \rangle s} = e^{-\langle \tau \rangle}. \quad (3.15)$$

Now we assume that our medium is a clumped hot star wind, in which the clumps are component *cl* and the inter-clump medium component *ic*. The volume filling fraction f_V shall be the fraction of the *dense* gas (as is customary assumed, see Chapters 4 and 5). For the averaged optical depth we then can write

$$\langle \tau \rangle = (f_V \chi_{cl} + (1 - f_V) \chi_{ic}) s. \quad (3.16)$$

First we consider processes depending *linearly* on the density, so that we may write the opacity as $\chi = \kappa \rho$, with *mass absorption coefficient* κ . The averaged density is of course

$$\langle \rho \rangle = f_V \rho_{cl} + (1 - f_V) \rho_{ic}, \quad (3.17)$$

and, thus, $\langle \tau \rangle = \langle \rho \rangle \kappa s$. Since we require $\langle \rho \rangle = \rho_{sm}$, with ρ_{sm} the density in a *smooth* wind model, we have recovered the well-known result that ‘smooth’ optical depths are preserved within the microclumping model for processes depending linearly on density.

Next we consider so-called ρ^2 -processes (see previous Chapters). Then the opacity can be written $\chi = \kappa_2 \rho^2$, where κ_2 may be regarded as a line-strength parameter defined somewhat in analogy with the mass absorption coefficient (see Appendix A for detailed opacity expressions of ρ^2 -processes for line transitions), and we obtain

$$\langle \tau \rangle = \langle \rho^2 \rangle \kappa_2 s, \quad (3.18)$$

with

$$\langle \rho^2 \rangle = f_V \rho_{cl}^2 + (1 - f_V) \rho_{ic}^2. \quad (3.19)$$

Defining the so-called *clumping factor* as

$$f_{cl} = \frac{\langle \rho^2 \rangle}{\langle \rho \rangle^2} = \frac{f_V + (1 - f_V) x_{ic}^2}{(f_V + (1 - f_V) x_{ic})^2}, \quad (3.20)$$

with

$$x_{ic} = \frac{\rho_{ic}}{\rho_{cl}}, \quad (3.21)$$

we may re-write the optical depth as

$$\langle \tau \rangle = f_{cl} \langle \rho \rangle^2 \kappa_2 s, \quad (3.22)$$

which is the equally well-known result that optical depths in processes depending on the square of the density are enhanced with a factor of f_{cl} in the microclumping model. Note that we need not to assume a void inter-clump medium for these relations to hold (which sometimes is stated). However, *only if* we let $x_{ic} \rightarrow 0$ do we get the additional relation $f_{cl} = f_V^{-1}$, essentially meaning that a description using f_{cl} , instead of f_V , is preferred within the microclumping model.

3.3 Vorosity

Owocki (2008) first pointed out that *line formation* in hot star winds with *optically thick clumps* should be controlled primarily by the velocity field. In analogy with the case of a spatially *porous* wind (next subsection), line photons may now escape through ‘holes’ in the velocity field (velocity porosity=’vorosity’). This is an effect caused by the rapid wind acceleration, which Doppler-shifts line photons and makes it possible for them to interact with the material only within very narrow spatial ranges, within the so-called *resonance zones*. The situation is sketched in Fig. 3.1.

By considering Fig. 3.1, we realize that the essence of the vorosity effect may be described by Eq. 3.11, in the limit that the chord lengths are *much larger* than the domain of integration, i.e. $l_0, l_1 \rightarrow \infty$. In this limit $r_+ \rightarrow \chi_1$ and $r_- \rightarrow \chi_0$, so that

$$\langle I \rangle = p_0 e^{-\chi_0 s} + p_1 e^{-\chi_1 s}, \quad (3.23)$$

or, for our two component wind,

$$\langle I \rangle = f_V e^{-\tau_{cl}} + (1 - f_V) e^{-\tau_{ic}}. \quad (3.24)$$

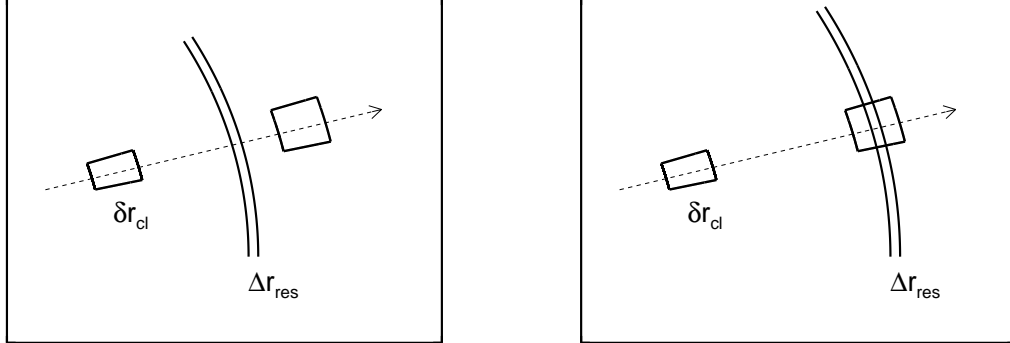


Figure 3.1: Illustration of the vorosity effect. A line photon of a given frequency can only interact with the wind material within narrow resonance zones, denoted here by Δr_{res} , and clumps are of sizes δr_{cl} . The dashed arrows are typical radial rays of radiation. The right and left plot, respectively, illustrate the typical ‘hit or miss’ situation; to the right we have a photon with a frequency that makes its resonance zone coincide with one of the clumps, and vice versa to the left.

Obviously, the continuum optical depths must here be replaced by corresponding *line* optical depths. A modified version of this equation is extensively used and discussed in Chapter 5. This modification is necessary because the basic assumption of chord lengths (=clump lengths) longer than the resonance zones simply is not valid for, primarily, the very slowly accelerating outer wind (resulting in radially extended resonance zones). Moreover, we have also modified the equation to handle non-monotonic velocity fields, by considering the *velocity* rather than the *volume* filling fractions (for a smooth velocity field and neglecting curvature terms they are equal, see Chapter 5). Note also that this equation is not mentioned in Chapter 4, simply because we had not ‘discovered’ it when that paper was published.

3.4 Porosity

Porosity effects in the context of clumped hot star winds have already been mentioned several times, for example when discussing the formation of X-ray line profiles and the proposed radiative driving of LBV ‘super-winds’ (Chapter 1), and we also commented on it in a more conceptual sense in Sect. 3.1. A ‘fully’ porous medium may be said to consist of a small number of absorbers with essentially infinite optical depth, embedded in a void background medium. Thus the relevant limit of Eq. 3.11 is $\chi_0 \rightarrow \infty, \chi_1 \rightarrow 0$ and $p_0 \ll p_1$. Then Eq. 3.11 takes the form

$$\langle I \rangle = e^{-s/l_1}. \quad (3.25)$$

Notice how this equation is *opacity independent*, depending only on the chord length l_1 . Of course this makes physical sense, because the matter properties are such that one fluid component already has reached maximum optical depth, and therefore absorbs everything that comes in its way, and the other is *assumed* to be completely transparent for all impinging radiation. Thus only *geometric* distributions and sizes matter.

The characteristic chord length of the ‘vacuum’, l_1 , can be connected to l_0 via the volume filling factor of the *dense* component,

$$f_V = \frac{l_0}{l_0 + l_1} \approx \frac{l_0}{l_1} \quad \rightarrow \quad l_1 \approx \frac{l_0}{f_V} \equiv h, \quad (3.26)$$

where the last equality defines the *porosity length* h (Owocki et al., 2004), and $l_1 = h$ here may be interpreted as the mean free path of a photon traveling through the medium.

‘Porosity formalisms’ for hot star wind applications have been developed differently than the statistical description of Levermore et al.. Formalisms have been provided by, e.g., Feldmeier et al. (2003) and Owocki et al. (2004). In the following, we use the basic arguments given by Feldmeier et al. (2003) (although the derivations differ somewhat), but the end results are equivalent also to those obtained by Owocki and collaborators. The same ‘two component’ (clumps and an inter-clump medium) stellar wind as before is assumed.

In analogy with the atomic opacity, we may write the effective opacity of a clump ensemble as

$$\chi_{\text{eff}} = n_{\text{cl}} A_{\text{cl}} (1 - e^{-\tau_{\text{cl}}}), \quad (3.27)$$

where n_{cl} and A_{cl} are the number density of clumps and the *effective* cross-section of a clump, respectively. The last term accounts for the probability $P = 1 - e^{-\tau_{\text{cl}}}$ that the photon impinging on a clump gets absorbed (compare to the result just presented, which assumed $P = 1$). We slightly reformulate Eq. 3.27 using $n_{\text{cl}} = 1/V_t$, where V_t is the total volume associated with exactly one clump,

$$\chi_{\text{eff}} = \frac{A_{\text{cl}}}{V_t} (1 - e^{-\tau_{\text{cl}}}). \quad (3.28)$$

The optical depth of a clump for *continuum opacity depending linearly on the density* is $\tau_{\text{cl}} = \kappa \rho_{\text{cl}} l_{\text{cl}}$. We shall here consider only the case of a void inter-clump medium ($x_{\text{ic}} = 0$), so the clump optical depth is (Sect. 3.2)

$$\tau_{\text{cl}} = \rho_{\text{cl}} \kappa l_{\text{cl}} = \langle \rho \rangle \kappa l_{\text{cl}} / f_V = \langle \chi \rangle (l_{\text{cl}} / f_V) = \langle \chi \rangle h, \quad (3.29)$$

where the last equality again (see above) uses the definition of the porosity length, $h \equiv l_{\text{cl}} / f_V$. Eq. 3.28 and 3.29 will below be used to consider the cases of i) isotropic clumps, ii) fragmented shells in a radial stream of photons, and iii) fragmented shells including non-radial photons.

3.4.1 Isotropic clumps

This corresponds to the case studied by Owocki et al. (2004) and Owocki & Cohen (2006). For isotropic clumps with characteristic length scales l_{cl} , we may write the volume of a clump as $V_{\text{cl}} \approx l_{\text{cl}}^3 = A_{\text{cl}} l_{\text{cl}}$, and express Eq. 3.28 as

$$\chi_{\text{eff}} = \frac{V_{\text{cl}}}{V_t l_{\text{cl}}} (1 - e^{-\tau_{\text{cl}}}) = \frac{1 - e^{-\tau_{\text{cl}}}}{h}, \quad (3.30)$$

where we have used the definition of the volume filling factor, $f_V \equiv V_{\text{cl}} / (V_{\text{cl}} + V_{\text{ic}}) = V_{\text{cl}} / V_t$. Using Eq. 3.29, we obtain the scaling of the corresponding smooth opacity

$$\chi_{\text{eff}} = \langle \chi \rangle \frac{1 - e^{-\tau_{\text{cl}}}}{\tau_{\text{cl}}}, \quad (3.31)$$

which (as it should) preserves the atomic opacity for optically thin clumps, and returns our previous result based on the Levermore et al. model (Eq. 3.25) for the case of very large clump optical depths, $\chi_{\text{eff}} = 1/h$. This *opacity independent* result is the base for the expectation of frequency independent (gray) opacities in the X-ray line formation in hot star winds, *should* the clumps be (very) optically thick for this process (Sect. 1.4.3).

We notice also that we made no explicit assumption about the geometry of the inter-clump medium when deriving this equation, i.e., we did *not* assume the distance between two clumps to be equal in all spatial directions ($V_t = l_{\text{ic}}^3$), as is sometimes done.

3.4.2 Fragmented shells, radial streaming of photons.

This and the next paragraph correspond to the Feldmeier et al. (2003) and Oskinova et al. (2004) models. The area of a given fragmented shell at radius r is $A_{\text{cl}} = \Delta\Omega r^2$, with $\Delta\Omega$ the subtended solid angle, whereas the volume associated with the distance between two shell fragments is $V_t = \Delta\Omega r^2 \Delta r$, with Δr the radial distance between two shells. Thus Eq. 3.28 becomes

$$\chi_{\text{eff}} = \frac{1 - e^{-\tau_{\text{cl}}}}{\Delta r}. \quad (3.32)$$

However, in this picture of radial photons and fragmented shells, we must have $\Delta r = \delta r / f_V = l_{\text{cl}} / f_V = h$, i.e.,

$$\chi_{\text{eff}} = \frac{1 - e^{-\tau_{\text{cl}}}}{h}, \quad (3.33)$$

which is *the same result as in the case of isotropic clumps*. Actually, this is not very surprising; since all photons hit the clumps perpendicularly, the latter are of course ‘isotropic’ in a sense.

The dependence on the lateral extensions of the clumps has vanished in Eq. 3.32. Thus one might be tempted to suggest that the same expression would apply for a clumped but *spherically symmetric* wind as well, i.e. one consisting of shells covering the complete sphere ($\Delta\Omega = 4\pi$). However, for a spherically symmetric wind we may no longer use the analogy with the atomic opacity, and thereby we cannot write χ_{eff} for the optically thick clump ensemble as $\chi_{\text{eff}} = A_{\text{cl}} V_t^{-1}$ (Eq. 3.27). Conceptually, one easily realizes this, for if the clumps were indeed spherical shells, they would all be ‘hit’ by any ray of radiation, i.e., no ‘holes’ would be there for photons to escape through, and consequently all photons would be absorbed by the first optically thick shell. Thus, the assumptions inherent in writing Eq. 3.27 are those of *randomization* and *lateral fragmentation* of spherical shells, the latter occurring on a scale smaller than the typical area considered when setting up the expression for χ_{eff} . (Feldmeier et al. 2003 actually considered infinitely small lateral scales for the fragments.)

3.4.3 Fragmented shells, including non-radial photons.

The *effective* cross-section area of a given shell at radius r now depends on the angle θ the photon hits it with, i.e., $A_{\text{cl}} \rightarrow A_{\text{cl}}\mu$, with $\mu = \cos\theta$. The associated clump/inter-clump volumes, on the other hand, remain as in the preceding subsection. Therefore Eq. 3.28 now takes the form

$$\chi_{\text{eff}} = \mu \frac{1 - e^{-\tau_{\text{cl}}}}{h}. \quad (3.34)$$

However, the optical depths of the clumps are enhanced because of the longer path-lengths for photons not hitting the clump perpendicularly. That is,

$$\tau_{\text{cl}} = \frac{\langle \chi \rangle h}{\mu}, \quad (3.35)$$

where curvature effects have been neglected. Inserting into the expression for χ_{eff} , we obtain

$$\chi_{\text{eff}} = \langle \chi \rangle \frac{1 - e^{-\tau_{\text{cl}}}}{\tau_{\text{cl}}}. \quad (3.36)$$

That is, *the same opacity scaling as before*, however with a modified (increased for non-radial photons) clump optical depth. Because of this optical depth enhancement, one would also expect porosity effects to increase when allowing for non-radial photons.

Indeed, when applied to X-ray line formation, the models of Oskinova et al. (including non-radial photons) appear to predict larger porosity effects than corresponding models of Owocki et al. (using isotropic opacity), as was discussed in Sect. 1.4.3. However, it seems unlikely that this is the sole reason for current inconsistencies between results obtained by the two groups, because test calculations and comparisons made by Owocki (private communication), in which he modified his code to account for non-radial photons, indicate that his X-ray line profiles still differ from those computed by Oskinova et al., by much more than expected merely from the different modeling techniques used in the calculations. So, the inconsistencies in the X-ray results stated in Sect. 1.4.3 remain, and the reason(s) for them still seem(s) to be unresolved.

3.4.4 A porosity formalism for ρ^2 -diagnostics.

Continuum porosity formalisms have been developed only for processes depending linearly on the density (the attenuation of X-rays, Thomson scattering). However, for example the continuum based mass-loss diagnostics IR and radio emission depend on the square of the density, and for these diagnostics the effects of optically thick clumping are completely unexplored (at least to our knowledge). Here we show how an extension of the porosity formalisms developed in the preceding paragraphs to handle also ρ^2 processes is, in fact, trivial.

Eq. 3.28 for the effective opacity of a clump ensemble, including non-radial photons, is repeated for convenience,

$$\chi_{\text{eff}} = \mu \frac{1 - e^{-\tau_{\text{cl}}}}{h}. \quad (3.37)$$

The clump optical depth is now

$$\tau_{\text{cl}} = \frac{\rho_{\text{cl}}^2 \kappa_2 l_{\text{cl}}}{\mu} = \frac{\rho_{\text{sm}}^2 \kappa_2 l_{\text{cl}}}{f_V^2 \mu} = \frac{\chi h}{f_V \mu} = \frac{\chi_{\text{mc}} h}{\mu}, \quad (3.38)$$

where we have used results from Sect. 3.2 and assumed a void inter-clump medium, and χ_{mc} is the opacity in a *microclumped* model. Thus, the effective opacity may simply be written as

$$\chi_{\text{eff}} = \chi_{\text{mc}} \frac{1 - e^{-\tau_{\text{cl}}}}{\tau_{\text{cl}}}. \quad (3.39)$$

This expression now unifies the porosity formalisms for ρ - and ρ^2 -processes, since for the former $\chi_{mc} = \chi_{sm} = \langle \chi \rangle$. Actually, it illustrates how one should always measure opacity reductions from optically thick clumping relative to microclumped models, and not relative to smooth ones. We discuss this property further in Chapter 5, for the case of H_α line formation in O star winds (which is a ρ^2 process).

Let us point out that these porosity formalisms represent a class of techniques that attempt to find an *effective opacity* in order to capture the essence of the statistical medium (Sect. 3.1). The effective opacity can then be used in the ordinary equations of radiative transfer, rather than aiming to solve for the ensemble averaged intensity directly (which the ‘vorosity’ formalism presented earlier does). There are, however, dangers in applying these type of ‘effective opacity’ methods, as discussed in the book by Pomraning (1991). Essentially what one does is trying to approximate the sum of two exponentials (Eq. 3.11) with only one (Eq. 3.4). Thus the porosity formalisms are inherently approximative, except for, in this case, the very limiting case of Eq. 3.25, and the errors introduced can be very hard to estimate. On the other hand, the alternative approach, i.e. to try and find a corresponding expression to Eq. 3.11 but for a more complex medium, certainly is everything but straightforward (and in many cases impossible), as demonstrated in Pomraning (1991). Supposedly the best practical approach to test the simplified approaches rather is to perform suitable Monte-Carlo simulations, and simply compare the results stemming from the different methods (as has been done for resonance and recombination line formation in Chapters 4-5). Note, however, that for at least *line* diagnostics of hot star winds we cannot assume a pure absorption model, as done in this chapter, but must treat also the emission component (or, equivalently, the source function). An analytic approximation for the emission component in *recombination* lines formed in clumpy winds is provided in Chapter 5, whereas a corresponding treatment of the re-emission in *resonance* lines is still to be developed (although we comment on a possible first approximation in Sect. 5.7.2).

Finally, we notice also that whereas the Levermore et al. model was derived for the special case of a Markovian mixture, no assumptions regarding the underlying clump statistics were made in the corresponding techniques developed for hot star winds, suggesting that our basic results may perhaps not be so dependent on the particular statistics of the clumps.

Chapter 4

Mass loss from inhomogeneous hot star winds

I. Resonance line formation in 2D models

This chapter is a copy of Sundqvist, Puls, & Feldmeier (2010), *Astronomy & Astrophysics*, 510, A11. The only revision from the original version is that the two appendices here have been added at the end as normal sections (4.9 and 4.10).

4.1 Abstract

The mass-loss rate is a key parameter of hot, massive stars. Small-scale inhomogeneities (clumping) in the winds of these stars are conventionally included in spectral analyses by assuming optically thin clumps, a void inter-clump medium, and a smooth velocity field. To reconcile investigations of different diagnostics (in particular, unsaturated UV resonance lines vs. H_α /radio emission) within such models, a highly clumped wind with very low mass-loss rates needs to be invoked, where the resonance lines seem to indicate rates an order of magnitude (or even more) lower than previously accepted values. If found to be realistic, this would challenge the radiative line-driven wind theory and have dramatic consequences for the evolution of massive stars. We investigate basic properties of the formation of resonance lines in small-scale inhomogeneous hot star winds with non-monotonic velocity fields. We study inhomogeneous wind structures by means of 2D stochastic and pseudo-2D radiation-hydrodynamic wind models, constructed by assembling 1D snapshots in radially independent slices. A Monte-Carlo radiative transfer code, which treats the resonance line formation in an axially symmetric spherical wind (without resorting to the Sobolev approximation), is presented and used to produce synthetic line spectra. The optically thin clumping limit is only valid for very weak lines. The detailed density structure, the inter-clump medium, and the non-monotonic velocity field are all important for the line formation. We confirm previous findings that radiation-hydrodynamic wind models reproduce observed characteristics of strong lines (e.g., the black troughs) without applying the highly supersonic ‘microturbulence’ needed in smooth models. For intermediate strong lines, the velocity spans of the clumps are of central importance. Current radiation-hydrodynamic models predict spans that are too large to reproduce observed profiles unless a very low mass-loss rate is invoked. By simulating lower spans in 2D stochastic models, the profile strengths become drastically

reduced, and are consistent with higher mass-loss rates. To simultaneously meet the constraints from strong lines, the inter-clump medium must be non-void. A first comparison to the observed Phosphorus V doublet in the O6 supergiant λ Cep confirms that line profiles calculated from a stochastic 2D model reproduce observations with a mass-loss rate approximately ten times higher than that derived from the same lines but assuming optically thin clumping. Tentatively this may resolve discrepancies between theoretical predictions, evolutionary constraints, and recent derived mass-loss rates, and suggests a re-investigation of the clump structure predicted by current radiation-hydrodynamic models.

4.2 Introduction

Mass loss through supersonic stellar winds is pivotal for the physical understanding of hot, massive stars and their surroundings. A change of only a factor of two in the mass-loss rate has a dramatic effect on massive star evolution (Meynet et al., 1994). Winds from these stars are described by the line-driven wind theory (Castor et al., 1975; Pauldrach et al., 1986), which traditionally assumes the wind to be stationary, spherically symmetric, and homogeneous. Despite this theory's apparent success (e.g., Vink et al., 2000), evidence for an inhomogeneous and time-dependent wind has over the past years accumulated, recently summarized in the proceedings from the workshop 'Clumping in hot star winds' (Hamann et al., 2008) and in a general review of mass loss from hot, massive stars (Puls et al., 2008b).

That line-driven winds should be intrinsically unstable was already pointed out by Lucy & Solomon (1970), and was later confirmed first by linear stability analyses and then by direct, radiation-hydrodynamic modeling of the time-dependent wind (e.g., Owocki & Rybicki, 1984; Owocki et al., 1988; Feldmeier, 1995; Dessart & Owocki, 2005), where the line-driven (or line-deshadowing) instability causes a small-scale, inhomogeneous wind in both density and velocity.

Direct observational evidence of a small-scale, clumped stellar wind has, for O-stars, so far only been given for two objects, ζ Pup and HD 93129A (Eversberg et al., 1998; Lépine & Moffat, 2008). Much *indirect* evidence, however, has arisen from quantitative spectroscopy, where the standard way of deriving mass-loss rates from observations nowadays is via line-blanketed, non-LTE (LTE: local thermodynamic equilibrium) model atmospheres that include a treatment of both the photosphere and the wind. Wind clumping has been included in such codes (e.g., CMFGEN (Hillier & Miller, 1998), PoWR (Gräfener et al., 2002), FASTWIND (Puls et al., 2005)) by assuming statistically distributed *optically thin* density clumps and a void inter-clump medium, while keeping the smooth velocity law. The major result from this methodology is that any mass-loss rate derived from smooth models and density-squared diagnostics (H_α , infra-red and radio emission) needs to be scaled down by the square root of the clumping factor (which describes the over density of the clumps as compared to the mean density, see Sect. 4.3.2). For example, Crowther et al. (2002), Bouret et al. (2003), and Bouret et al. (2005) have concluded that a reduction of 'smooth' mass-loss rates by factors 3...7 might be necessary. Furthermore, from a combined optical/IR/radio analysis of a sample of Galactic O-giants/supergiants, Puls et al. (2006) derived upper limits on observed rates that were factors of 2...3 lower than previous H_α estimates based on a smooth wind.

On the other hand, the strength of UV resonance lines ('P Cygni lines') in hot star winds depends linearly on the density and is therefore not believed to be directly affected by optically thin clumping. By using the Sobolev with exact integration technique (SEI; cf. Lamers et al. 1987) on the unsaturated Phosphorus V (PV) lines, Fullerton et al. (2006) for a large number of Galactic O-stars derived rates

that were factors of 10...100 lower than corresponding smooth H_α /radio values (provided PV is the dominant ion in spectral classes O4 to O7). Such large revisions would conflict with the radiative line-driven wind theory and have dramatic consequences for the evolution of, and the feedback from, massive stars (cf. Smith & Owocki, 2006; Hirschi, 2008). Indeed, a puzzling picture has emerged, and it appears necessary to ask whether the present treatment of wind clumping is sufficient. Particularly the assumptions of optically thin clumps, a void inter-clump medium, and a smooth velocity field may not be adequate to infer proper rates under certain conditions.

Optically thin vs. optically thick clumps. Oskinova et al. (2007) used a porosity formalism (Feldmeier et al., 2003; Owocki et al., 2004) to scale the opacity from smooth models and investigate impacts from *optically thick* clumps on the line profiles of ζ Pup. Due to a reduction in the effective opacity, the authors were able to reproduce the PV lines without relying on a (very) low mass-loss rate, while simultaneously fitting the optically thin H_α line. This formalism, however, was criticized by Owocki (2008) who argued that the original porosity concept had been developed for continuum processes, and that line transitions rather should depend on the non-monotonic velocity field seen in hydrodynamic simulations. Proposing a simplified analytic description to account for this velocity-porosity, or ‘vorosity’, he showed how also this effect may reduce the effective opacity.

In this first paper we attempt to clarify the most important concepts by conducting a detailed investigation on the synthesis of UV resonance lines from inhomogeneous two-dimensional (2D) winds. We create both pseudo-2D, radiation-hydrodynamic wind models and 2D, stochastic wind models, and produce synthetic line profiles via Monte-Carlo radiative transfer calculations. We account for and analyze the effects from a wind clumped in *both* density and velocity as well as the effects from a non-void inter-clump medium. Especially we focus on lines with intermediate line strengths, comparing the behavior of these lines with the behavior of both optically thin lines and saturated lines. Follow-up studies will include a treatment of emission lines (e.g., H_α) and an extension to 3D, and the development of simplified approaches to incorporate effects into non-LTE models.

In Sect. 4.3 we describe the wind models and in Sect. 4.4 the Monte-Carlo radiative transfer code. First results from 2D inhomogeneous winds are presented in Sect. 4.5, and an extensive parameter study is carried out in Sect. 4.6. We discuss some aspects of the interpretations of these results and perform a first comparison to observations in Sect. 4.7, and summarize our findings and outline future work in Sect. 4.8.

4.3 Wind models

For wind models, we use customary spherical coordinates (r, Θ, Φ) with r the radial coordinate, Θ the polar angle, and Φ the azimuthal angle. We assume spherical symmetry in 1D models and symmetry in Φ in 2D models. In all 2D models Θ is sliced into N_Θ equally sized slices, giving a lateral scale of coherence (or an opening angle) $180/N_\Theta$ degrees. This 2D approximation is discussed in Sect. 4.7.4. Below we describe the model types primarily used in the present analysis; two are of stochastic nature and two are of radiation-hydrodynamic nature.

4.3.1 Radiation-hydrodynamic wind models

We use the time-dependent, radiation-hydrodynamic (hereafter RH) wind models from Puls et al. (1993, hereafter ‘POF’), calculated by S. Owocki, and from Feldmeier et al. (1997, hereafter ‘FPP’),

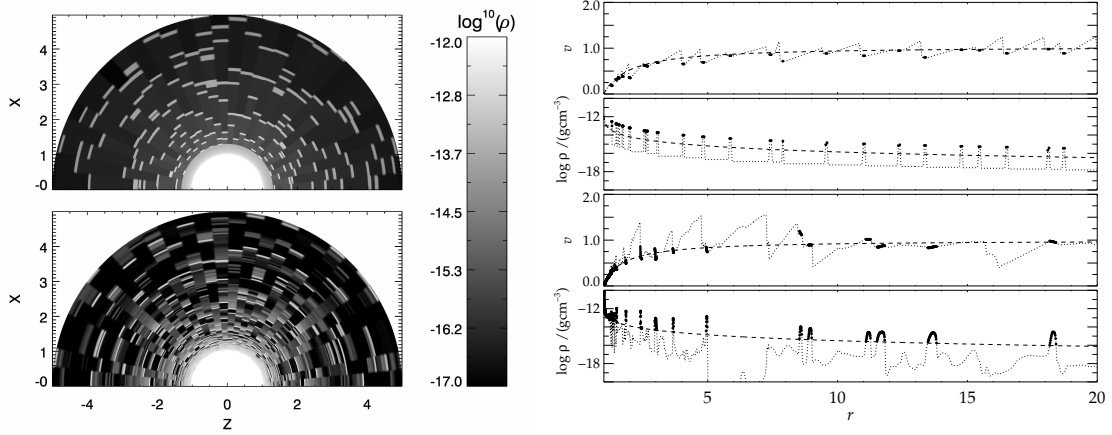


Figure 4.1: **Left panel:** Density contour plots of one stochastic (upper plot) and one RH (FPP, lower plot) model. The Cartesian coordinate Z is on the abscissa and X is on the ordinate. **Right panel:** Density and velocity structures of one slice in one stochastic (upper) and one RH (FPP, lower) model. Over densities are marked with filled dots. For model parameters and details, see Sect. 4.3.2.

and the reader is referred to these papers for details. Here we summarize a few important aspects. POF assume a 1D, spherically symmetric outflow, and circumvent a detailed treatment of the wind energy equation by assuming an isothermal flow. Perturbations are triggered by photospheric sound waves. The wind consists of 800 radial points, extending to roughly 5 stellar radii. FPP also assume a 1D, spherically symmetric outflow, but include a treatment of the energy equation. Perturbations are triggered either by photospheric sound waves or by Langevin perturbations that mimic photospheric turbulence. The wind consists of 4000 radial points, extending to roughly 30 stellar radii. Tests have shown that the FPP winds yield similar results for both flavors of perturbations, and, for simplicity, we therefore use only the results of the turbulence model.

Due to the computational cost of obtaining the line force, only initial attempts to 2D RH simulations have been carried out (Dessart & Owocki, 2003, 2005). These authors first used a strictly radial line force, yielding a complete lateral incoherent structure due to Rayleigh-Taylor or thin-shell instabilities, and in the follow-up study uses a restricted 3-ray approach to approximate the lateral line drag, yielding a larger lateral coherence but lacking quantitative results. Therefore, and because of the general dominance of the radial component in the radiative driving, we create fragmented 2D wind models from our 1D RH ones by assembling snapshots in the Θ direction, assuming independence between each slice consisting of a pure radial flow. After the polar angle has been sliced into N_Θ equally sized slices, one random snapshot is selected to represent each slice. This method for creating more-D models from 1D ones is essentially the same as the ‘patch method’ used by Dessart & Owocki (2002), when synthesizing emission lines for Wolf-Rayet stars, and the method used by, e.g., Oskinova et al. (2004), when synthesizing X-ray line emission from stochastic wind models. Fig. 4.1 displays typical velocity and density structures from this type of 2D model.

4.3.2 Stochastic wind models

We also study clumpy wind structures created by means of distorting a smooth, stationary, and spherically symmetric wind via stochastic procedures. This allows us to investigate the impacts from, and

to set constraints on, different key parameters without being limited by the values predicted by the RH simulations. For the underlying smooth winds we adopt a standard β velocity law $v_\beta(r) = (1 - b/r)^\beta$. Here and throughout the paper, we measure *all* velocities in units of the terminal velocity, v_∞ , and *all* distances and length scales in units of the stellar radius, R_\star . b is given by $v(r = 1) = v_{\min}$, the velocity at the base of the wind. $v_{\min} = 0.01$ is assumed, roughly corresponding to the sound speed. For a given \dot{M} , the homogeneous density structure then follows directly from the equation of continuity. We choose $\beta = 1$, which is appropriate for a standard O-star wind and allows us to derive simple analytic expressions for wind masses and flight times.

A model clumped in density. First we consider a two component density structure consisting of clumps and a rarefied inter-clump medium (hereafter ICM), but keep the $\beta = 1$ velocity law. Clumps are released randomly in radial direction at the inner boundary, independently from each slice. The release in radial direction means that a given clump stays within the same slice during its propagation through the wind. The average time interval between the release of two clumps is δt , which here and in the following is expressed in units of the wind's dynamic time scale $t_{\text{dyn}} = R_\star/v_\infty$.

The average distance between clumps thus is $v_\beta \delta t$, i.e. clumps are spatially closer in the inner wind than in the outer wind, and for example $\delta t = 0.5$ (in t_{dyn}) gives an average clump separation of 0.5 (in R_\star) at the point where $v = 1$ (in v_∞). We further assume that the clumps preserve mass and lateral angle when propagating outwards, and that the underlying model's total wind mass is conserved within every slice. This radial clump *distribution* is the same as the one used by Oskinova et al. (2006) when simulating X-ray emission from O-stars, but differs from the one used by Oskinova et al. (2007) when investigating porosity effects on resonance lines (see discussion in Sect. 4.7.5). The radial clump *widths* are here calculated from the actual wind geometry and clump distribution by assuming a *volume filling factor* f_v , defined as the fractional volume of the dense gas¹. A related quantity is the *clumping factor*

$$f_{\text{cl}} \equiv \frac{\langle \rho^2 \rangle}{\langle \rho \rangle^2}, \quad (4.1)$$

as defined by Owocki et al. (1988), where angle brackets denote temporal averages. Identifying temporal with spatial averages one may write for a two component medium (cf. Abbott et al., 1981)

$$f_{\text{cl}} = \frac{f_v + (1 - f_v)x_{\text{ic}}^2}{[f_v + (1 - f_v)x_{\text{ic}}]^2}, \quad (4.2)$$

with

$$x_{\text{ic}} \equiv \frac{\rho_{\text{ic}}}{\rho_{\text{cl}}}, \quad (4.3)$$

the ratio of low- to high-density gas (subscript ic denotes inter-clump and cl denotes clump). For a void ($x_{\text{ic}} = 0$) ICM, $\rho_{\text{cl}}/\langle \rho \rangle = f_v^{-1} = f_{\text{cl}}$, i.e. f_{cl} then describes the over density of the clumps as compared to the mean density.

¹ We here notice that f_v is normalized to the *total* volume, i.e., $f_v = 0 \dots 1$. In some literature f_v is identified with the straight volume ratio $V_{\text{cl}}/V_{\text{ic}}$, which then implicitly assumes that $V_{\text{cl}} \ll V_{\text{ic}}$.

Table 4.1: Basic parameters defining a stochastic wind model clumped in density and with a non-monotonic velocity field.

Name	Parameter	Considered range
Volume filling factor	f_v	$f_v = 0.01 \dots 1.0$
Average time interval between release of clumps	δt	$\delta t [t_{\text{dyn}}] = 0.05 \dots 1.5$
ICM density parameter, Eq. 4.3	x_{ic}	$x_{\text{ic}} = 0 \dots 0.1$
Velocity span of clump	δv	$\delta v / \delta v_\beta = -10.0 \dots 1.0$
Parameter determining the jump velocity	v_j	$v_j / v_\beta = 0.01 \dots 0.15$

A model clumped in density and velocity. Next we consider also a non-monotonic velocity law, using the spatial distribution and widths of the clumps described in the previous paragraph. The RH simulations indicate that, generally, strong shocks separate denser and slower material from rarefied regions with higher velocities. Building on this basic result, we now modify the velocity fields in our stochastic models by adding a random perturbation to the local v_β value prior to the starting point of each clump, so that the new velocity becomes v_{pre} . A ‘jump velocity’ is thereafter determined by a random subtraction from v_β , now using the added perturbation as the maximum subtraction. That is,

$$v_{\text{pre}} = v_\beta + v_j \times 2R_1 \quad v_{\text{post}} = v_\beta - v_j \times 2R_1R_2, \quad (4.4)$$

where R_1 and R_2 are two random numbers in the interval 0 to 1. $v_{\text{pre}} - v_{\text{post}}$ is the jump velocity as determined by the parameter v_j . By multiplying R_1 by two, we make sure that the mean perturbation at the ‘pre’ point is v_j , and R_2 allows for an asymmetry about v_β (see Fig. 4.2). The clump is assumed to start at v_{post} , and its velocity span is set by assuming a value for $\delta v / \delta v_\beta$, where δv is the velocity span of the clump and δv_β the corresponding quantity for the same clump with a smooth velocity law (see Fig. 4.2). Inspection of our RH models suggests that velocity gradients within density enhancements primarily are negative (see also Sect. 4.7.3), and negative gradients are also adopted in most of our stochastic models. Finally we assume a constant velocity gradient through the ICM.

Overall, the above treatment provides a phenomenological description of the non-monotonic velocity field seen in RH simulations. The description differs from the one suggested by Owocki (2008), who uses only one parameter to characterize the velocity field (whereas we have two). Our new formulation is motivated by both observational and modeling constraints from strong and intermediate lines, as discussed in Sect. 4.7.5.

The basic parameters defining a stochastic model are listed in Table 4.1. Fig. 4.1 (right panel) shows the density and velocity structures of one slice in a stochastic model, with density parameters $f_v = 0.1$, $\delta t = 1.0$, $x_{\text{ic}} = 0.005$, and velocity parameters $v_j = 0.15v_\beta$ and $\delta v = -\delta v_\beta$. Clump positions have been highlighted with filled dots and a comparison to a RH model (FPP) is given. In the RH model, we have identified clump positions by highlighting all density points with values higher than the corresponding smooth model. The left panel shows the density contours of the same models, where, for clarity, only the wind to $r = 5$ is displayed.

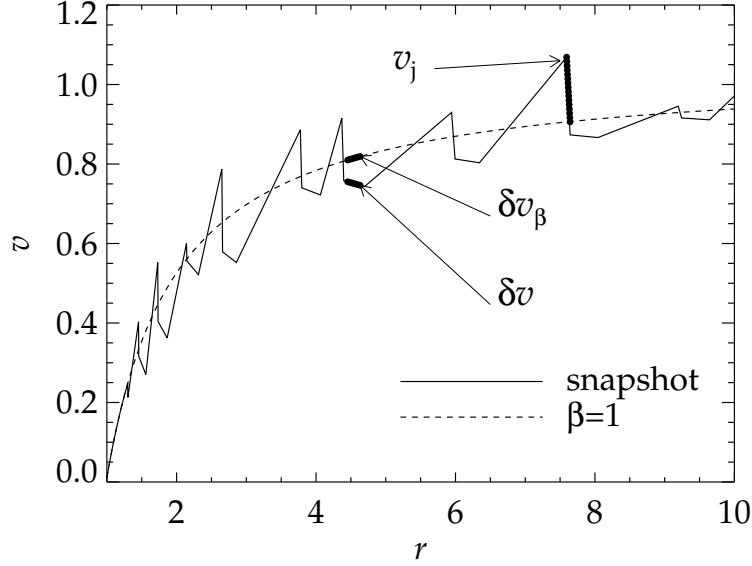


Figure 4.2: Non-monotonic velocity field and corresponding parameters in a stochastic model.

4.4 Radiative transfer

To compute synthetic line profiles from the wind models, we have developed a Monte-Carlo radiative transfer code (MC-2D) that treats resonance line formation in a spherical and axially symmetric wind using an ‘exact’ formulation (e.g., without resorting to the Sobolev approximation). The restriction to 2D is of course a shortage, but has certain geometrical and computational advantages and should be sufficient for the study of general properties, as discussed in Sect. 4.7.4. A thorough description and verification of the code can be found in Sect. 4.9.

Photons are released from the lower boundary (the photosphere) and each path is followed until the photon has either left the wind or been backscattered into the photosphere. Basic assumptions are a line-free continuum with no limb darkening emitted at the lower boundary, no continuum absorption in the wind, pure scattering lines, instantaneous re-emission, and no overlapping lines (i.e., singlets). These simplifying assumptions, except for doublet formation, are all believed to be of minor importance to the basic problem. By the restriction to singlet line formation we avoid confusion between effects on the line profiles caused by line overlaps and by other important parameters, but on the other hand it also prevents a direct comparison to observations for many cases (but see Sect. 4.7.6). A consistent treatment of doublet formation will be included in the follow-up study.

4.5 First results from 2D inhomogeneous winds

Throughout this section we assume a thermal velocity, $v_t = 0.005$ (in units of v_∞ and $\sim 10 \text{ km s}^{-1}$, appropriate for a standard O-star wind), and apply no microturbulence. After a brief discussion on the impact of the observer’s position and opening angles, we concentrate on investigating the formation of strong, intermediate, and weak lines. In our definition, an intermediate line is characterized by a

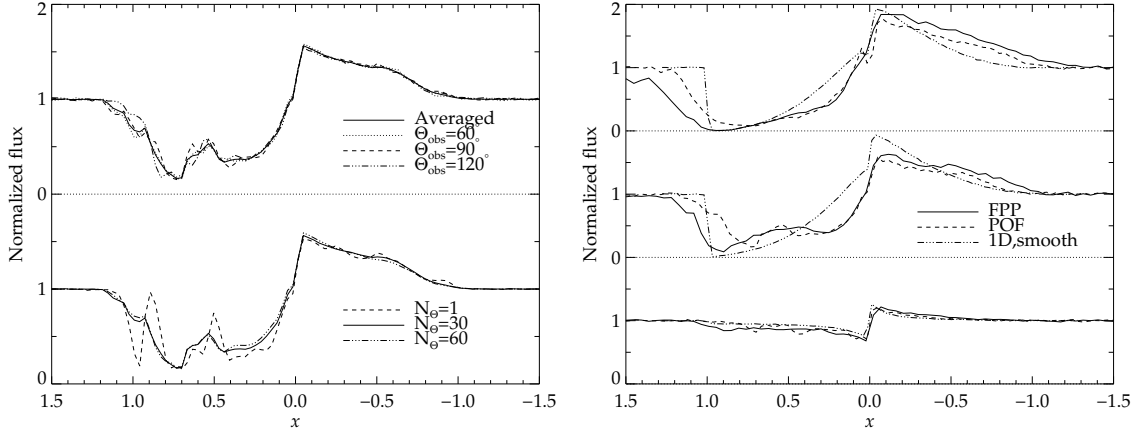


Figure 4.3: Synthetic line profiles calculated from 2D RH models. The abscissa is the dimensionless frequency x (Eq. 4.18), normalized to the terminal velocity, and the ordinate is the flux normalized to the continuum. **Upper panel:** Profiles from POF models with $\kappa_0 = 5.0$. The upper plot displays profiles for an observer placed at the Θ_{obs} angles as labeled in the figure and a profile averaged over all $N_\Theta = 30$ angles. The lower plot displays averaged profiles for three different N_Θ . **Lower panel:** Averaged profiles from FPP and POF models with $N_\Theta = 30$, and with $\kappa_0 = 100.0$ (upper) $\kappa_0 = 5.0$ (middle), and $\kappa_0 = 0.05$ (lower). For comparison, 1D, smooth profiles with the same values of κ_0 are shown as well.

line strength² $\kappa_0 = 5.0$ chosen such as to almost precisely reach the saturation limit in a *smooth* model (cf. Fig. 4.3).

By investigating these different line types, we account for the tight constraints that exist for each flavor: i) *weak lines* should be independent of density-clumping properties as long as the clumps remain optically thin, ii) for *intermediate lines* either smooth models overestimate the profile strengths or mass-loss rates are lower than previously thought (e.g. the PV problem, see Sect. 4.2), and iii) *strong saturated lines* are clearly present in hot star UV spectra, and observed features need to be reproduced, such as high velocity ($> v_\infty$) absorption, the black absorption trough, and the reduction of re-emitted flux blueward of the line center.

4.5.1 Observer’s position and opening angles

The observed spectrum as calculated from a 2D wind structure depends on the observer’s placement relative to the star (see Sect. 4.9). As it turns out, however, this dependence is relatively weak in both the stochastic and the RH models (the latter is demonstrated in the upper panel of Fig. 4.3). Tests have shown that the variability of the line profile’s emission part is insignificant. The variability of the absorption part may be detectable, at least near the blue edge, but is still insignificant for the integrated profile strength; the equivalent width of the absorption part is almost independent of the observer’s position. Also the opening angle, $180^\circ/N_\Theta$, primarily has a smoothing effect on the profiles. In Fig. 4.3, prominent discrete absorption features appear near the blue edge in the model with $N_\Theta = 1$ (spherical symmetry), but are smoothed out in the ‘broken-shell’ models with $N_\Theta = 30$ and 60. The equivalent widths of the absorption parts are approximately equal for all three models.

² with κ_0 proportional to the product of mass-loss rate and abundance of the considered ion, see Sect. 4.9.

Table 4.2: Primary stochastic wind models and parameters

Model name	f_v	δt [t _{dyn}]	x_{ic}	$\delta v / \delta v_\beta$	v_j / v_β	r_{st}^a	r_{ext}^b
Default	0.25	0.5	0.0025	-1.0	0.15	1.3	~ 25
RHcopy	0.1	0.5	0.005	-10.0	0.15	1.3	~ 5
Obs1	0.11	0.5, 4.0 ^c	0.005, 0.0025 ^c	-1.0	0.15	1.02	~ 25

^a Radial onset of clumping. ^b Radial extent of wind.

^c Left value inside the radius corresponding to $v_\beta = 0.6$, right value outside.

Because our main interest here is the general behavior of the line profiles, we choose to work only with $N_\theta = 30$ and profiles averaged over all observer angles from here on. Working with averaged line profiles has great computational advantages, because roughly a factor of N_θ fewer photons are needed.

4.5.2 Radiation-hydrodynamic models

Fig. 4.3 (lower panel) shows line profiles from FPP and POF hydrodynamical models. For the strong lines, the constraints stated in the beginning of this section are reproduced without adopting a highly supersonic and artificial microturbulence. These features arise because of the multiple resonance zones in a non-monotonic velocity field, and are present in spherically symmetric RH profiles as well (see POF for a comprehensive discussion); the main difference between 1D and 2D is a smoothing effect, partly stemming from averaging over all observer angles (see above). The absorption at velocities higher than the terminal is stronger in FPP than in POF, due to both a higher velocity dispersion and a larger extent of the wind ($r_{max} \sim 30$ as compared to $r_{max} \sim 5$, see Sect. 4.3.1); more overdense regions are encountered in the outermost wind, which (because of the flatness of the velocity field) leads to an increased probability to absorb at almost the same velocities.

For the intermediate lines, we again see the qualitative features of the strong lines, though less prominent. As compared to smooth models, a minor *absorption* reduction is present at velocities lower than the terminal, but compensated by the blue edge smoothing. Therefore the equivalent width of the line profile's absorption part in the FPP model is approximately equal to that of the smooth model, whereas in the POF model it is reduced by $\sim 10\%$. This minor reduction agrees with that found by Owocki (2008), and is not strong enough to explain the observations without having to invoke a very low mass-loss rate.

For the weak lines, the absorption part is marginally stronger than from a smooth, 1D model.

4.5.3 Stochastic models

In this subsection we use a 'default' 2D, stochastic model with parameters as specified in Table 4.2. By comparing this model to models in which one or more parameters are changed, we demonstrate key effects in the behavior of the line profiles.

Strong lines. For strong lines, the line profiles from the default model reproduce the observational constraints described in the first paragraph of this section. As in the RH models, we apply no microturbulence. Fig. 4.4 (left panels) demonstrates the importance of the ICM in the default model; the

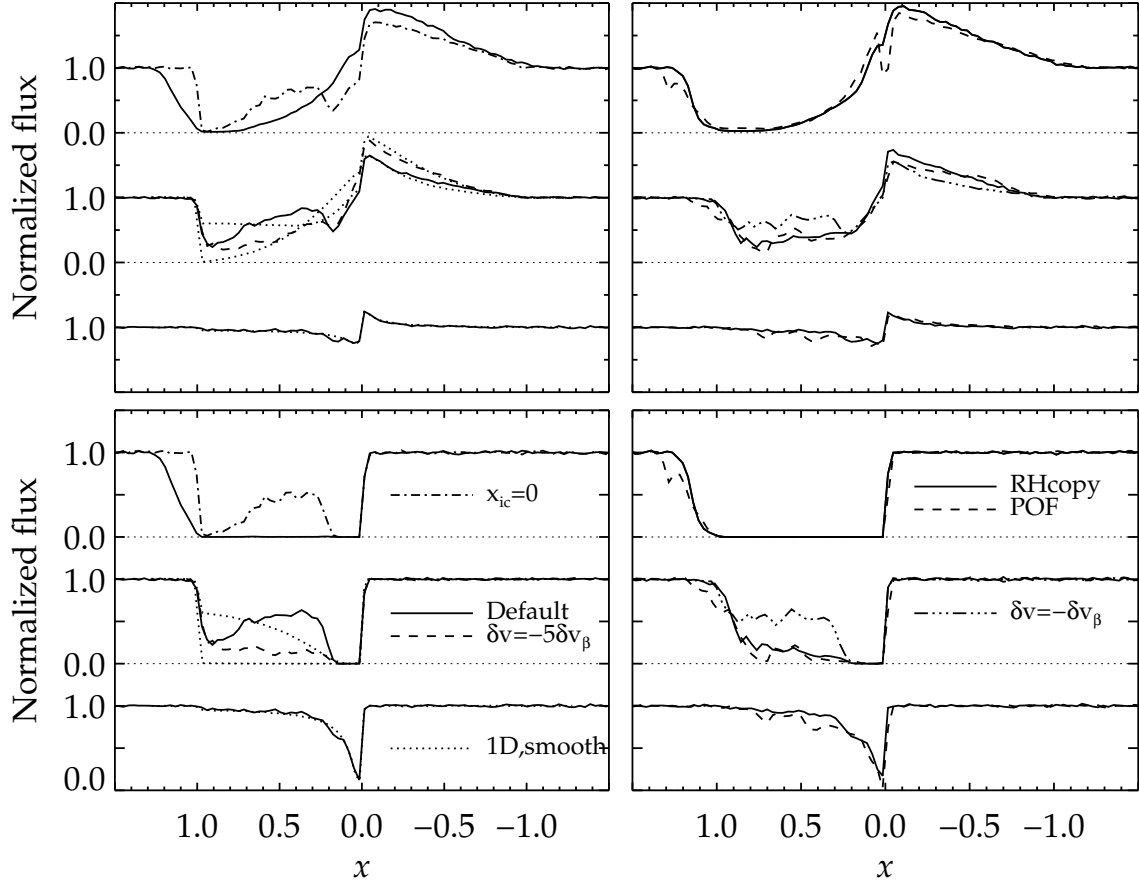


Figure 4.4: **Left panels:** Solid lines display total line profiles and the absorption part for the default stochastic model (see Table 4.2), with $\kappa_0 = 1000$ (upper), $\kappa_0 = 5.0$ (middle), and $\kappa_0 = 0.05$ (lower). Dotted lines display smooth models with $\kappa_0 = 5.0$ and $\kappa_0 = 0.5$ (middle), and $\kappa_0 = 0.05$ (lower). Dashed/dashed-dotted lines with modifications from the default model as labeled in the figure. **Right panels:** Same as the left panels, but for POF (dashed lines) and RHcopy (solid lines). Dashed-dotted lines with modifications from RHcopy as labeled in the figure.

absorption part of a very strong line is not saturated when $x_{ic}=0$. That is, with a void ICM we will, regardless of the opacity, always have line photons escaping their resonance zones without ever interacting with any matter, thereby de-saturating the line. This ICM finding agrees with that of Zsargó et al. (2008), who point out that a non-void ICM is crucial for the formation of highly ionized species such as O VI. We also notice that $\delta v = -\delta v_\beta$ (used in the default model) does not permit clumps to have velocities higher than the local v_β value, preventing absorption at velocities higher than the terminal one when the ICM is void.

Intermediate lines. For intermediate lines, the line profiles from the default model display the main observational requirement if to avoid a drastic reduction in ‘smooth’ mass-loss rates³, namely a strong absorption reduction as compared to a smooth model. The left panels of Fig. 4.4 show how the integrated profile strength of the default model with $\kappa_0 = 5.0$ roughly corresponds to that of a smooth model having $\kappa_0 = 0.5$, i.e., the smooth model would result in a mass-loss rate (as estimated from the integrated profile strength) ten times *lower* than the clumped model. The figure also illustrates how the main effect is on the absorption part of the line profile. In addition to the reduction in profile *strength*, the profile *shapes* of the absorption parts are noticeably different for the default and smooth models (the shapes of the re-emission parts, not shown here, are similar for the two models). We further discuss the shapes of the profiles in Sect. 4.7.1. The dramatic reduction in integrated profile strength occurs because of large velocity gaps between the clumps, in which the wind is unable to absorb (at this opacity the ICM may not ‘fill in’ these gaps with absorbing material).

We have identified $|\delta v|$ as a critical parameter for the formation of intermediate lines. The importance of the velocity spans of the clumps is well illustrated by the absorption part profiles in Fig. 4.4 (lower-left panel, middle plot). The absorption is much stronger in the comparison model with $\delta v = -5\delta v_\beta$ than in the default model with $\delta v = -\delta v_\beta$, because the former model covers more of the total velocity space *within* the clumps, thereby closing the gaps *between* the clumps. Consequently the wind may, on average, absorb at many more wavelengths.

In principle, however, this effect is counteracted by a decrease in the clump’s optical depths, because of the now higher velocity gradients ($|\delta v/\delta v_\beta| > 1$). Consider the *radial* Sobolev optical depth (proportional to $\rho/|\partial v/\partial r|$, see Sect. 4.9) in a stochastic wind model. As compared to a smooth model, the density inside a clump is enhanced by a factor of f_v^{-1} (assuming a negligible ICM), but also the velocity gradient is enhanced by a factor of $|\delta v/\delta v_\beta|$. Thus we may write for the radial Sobolev optical depth inside a clump,

$$\tau_{\text{Sob}} \approx \frac{\tau_{\text{Sob,sm}}}{f_v |\delta v/\delta v_\beta|} \approx \frac{\kappa_0}{v_\beta f_v |\delta v/\delta v_\beta|}, \quad (4.5)$$

where ‘sm’ indicates a quantity from a smooth wind, and the expression to the right is valid for an underlying $\beta = 1$ velocity law. From Eq. 4.5, we see how the effects on the optical depth from the increased density ($f_v = 0.25$) and the increased velocity gradients ($|\delta v/\delta v_\beta| = 5$) almost cancel each other in this example. Thus, the clumps are still optically thick for the intermediate line ($\kappa_0 = 5$), which means that the larger coverage of the total velocity space ‘wins’, and the net effect becomes an increase in absorption (as seen in Fig. 4.4, lower-left panel, middle plot). This will be true as long as not $f_v |\delta v/\delta v_\beta| \gg 1$, which is never the case in the parameter range considered here.

Finally, the prominent absorption dip toward the blue edge in the default model turns out to be a quite general feature of our stochastic models, and is discussed in Sects. 4.6.1 and 4.7.2.

Weak lines. The statistical treatment of density clumping included in atmospheric codes such as CMFGEN, PoWR, and FASTWIND is valid for optically thin clumps and a negligible ICM, and gives no direct effect on resonance lines scaling linearly with density. Here we test this prediction using detailed radiative transfer⁴. Our default model recovers the smooth results when $\kappa_0 = 0.05$ (Fig. 4.4,

³ Recall that $f_v = 0.25 \rightarrow f_{\text{cl}} \approx 4$, which implies $\dot{M} = \dot{M}_{\text{smooth}}/2$, if f_{cl} were derived from ρ^2 -diagnostics assuming optically thin clumps.

⁴ The *indirect* effect through the feedback on the occupation numbers is not included, because in this section we assume constant ionization.

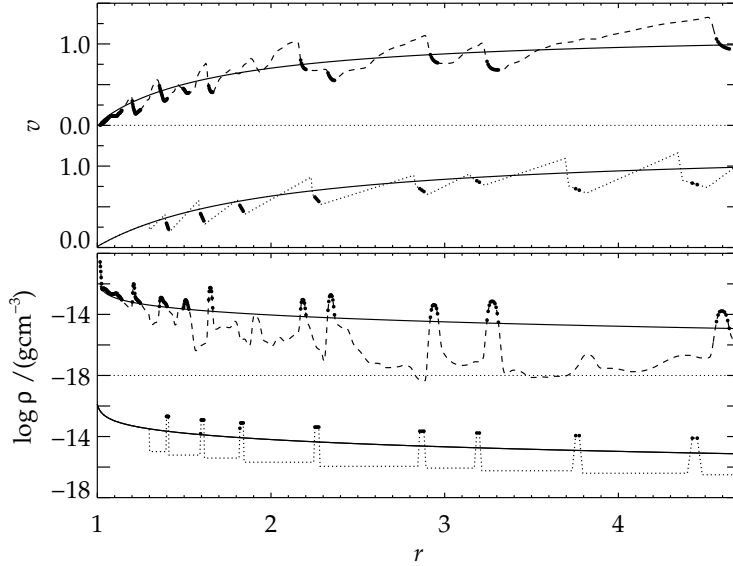


Figure 4.5: Velocity (upper panel) and density (lower panel) structures for one slice in POF (dashed) and RHcopy (dotted), see Table 4.2. Solid lines are the corresponding smooth structures, and clumps are highlighted as in Fig. 4.1.

left panels), confirming the expected behavior. However, from calculating spectra using different values of κ_0 , we have found that significant deviations from smooth models occur for the default model already before κ_0 reaches unity. This occurs because the clumps start to become optically thick, which may again be understood by considering the radial Sobolev optical depth (Eq. 4.5). With $f_v \leq 0.25$ and $\kappa_0 \geq 0.25$, one finds $\tau_{\text{Sob}} \geq 1.0$.

4.5.4 Comparison between stochastic and radiation-hydrodynamic models

Our stochastic wind models have been constructed to contain all essential ingredients of the RH models. Therefore they should also reproduce the RH results, at least qualitatively, if a suitable parameter set is chosen. To test this we used the POF model. In this model, the clumping factor increases drastically at $r \sim 1.3$, from $f_{\text{cl}} \sim 1.0$ to $f_{\text{cl}} \sim 10$, after which it stays basically constant. The average clump separation in the outer wind is roughly half a stellar radius. Important for the velocity field is that the velocity spans of the clumps are generally *larger* than corresponding ‘ β spans’, i.e., $|\delta v / \delta v_\beta| > 1$ (this is the case in FPP as well), a characteristic behavior that primarily affects the intermediate lines (details will be discussed in Sect. 4.7.3). Finally, a suitable v_j can be assigned from the position of the blue edge in a strong line calculated from POF. Table 4.2 (entry RHcopy) summarizes all parameters used to create this stochastic, ‘pseudo-RH’ model. Fig. 4.5 displays one slice of the velocity and density structures in the POF and RHcopy models, and Fig. 4.4 (right panels) displays the line profiles.

The line profiles of POF are matched reasonably well by RHcopy. The intermediate lines again demonstrate the importance of the velocity spans of the clumps; for an alternative model with $\delta v = -\delta v_\beta$, there is much less absorption in the stochastic model than in POF, i.e., we encounter the same effect as discussed in the previous subsection. We conclude that in RH models it is the large velocity

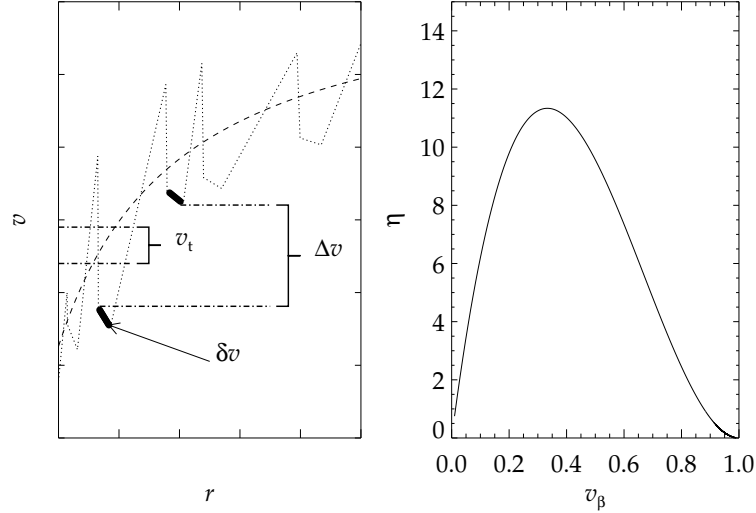


Figure 4.6: **Left:** Schematic of Δv , the velocity gap between two subsequent clumps, made up by velocities not covered by *any* of the clumps. δv is the velocity span of a clump and v_t the thermal velocity. **Right:** The effective escape ratio η (Eq. 4.7) as a function of $\beta = 1$ velocity, for the parameters of the default model (see Table 4.2).

spans inside the density enhancements that prevent a reduction in profile strength (as compared to smooth models) for intermediate lines.

4.6 Parameter study

Having established basic properties, we now use our stochastic models to analyze the influence from different key parameters in more detail. First, however, we introduce a quantity that turns out to be particularly useful for our later discussion.

4.6.1 The effective escape ratio

For the important intermediate lines, it is reasonable to assume that the clumps are optically thick and the ICM negligible (see Sect. 4.5.3 and the next paragraph). Under these assumptions, a decisive quantity for photon absorption will be the velocity gap *not* covered by the clumps, as compared to the thermal velocity (the latter determining the width of the resonance zone in which the photon may interact with the wind material). This is illustrated in the left panel of Fig. 4.6, and we shall call this quantity the ‘effective escape ratio’

$$\eta \equiv \frac{\Delta v}{v_t}, \quad (4.6)$$

where Δv is the velocity gap between two subsequent clumps, made up by all velocities not covered by *any* of the clumps (see Fig. 4.6). In principle, η determines to which extent the vorosity effect

(i.e., the velocity gaps between the clumps, cf. Owocki, 2008) is important for the line formation. As defined, η does not contain any assumptions on the *spatial* structure of the wind. $\eta \ll 1$ means that the velocity gaps between the clumps are much smaller than the thermal velocity, which in turn means that the probability for a photon to encounter a clump within its resonance zone is high. If we assume each clump to be optically thick, every encounter will lead to an absorption. Thus the probability for photon absorption is high when the value of η is low. Vice versa, $\eta \gg 1$ results in a high probability for the photon to escape its resonance zone without interacting with the wind material, i.e., a low absorption probability. If the entire velocity space were covered by clumps, $\eta = 0$.

For the wind geometry used in our stochastic models, we may write (see Sect. 4.10 for a derivation)

$$\eta \approx \frac{v_\beta \delta t (1 - f_v |\delta v / \delta v_\beta|)}{L_r} \approx \frac{\delta t (1 - f_v |\delta v / \delta v_\beta|)}{v_t} \frac{v_\beta}{r^2}, \quad (4.7)$$

where L_r is the radial Sobolev length of a smooth model, which for $\beta = 1$ is $L_r \approx v_t r^2$ (as usual, r and L_r in R_\star and δt in t_{dyn}). Note that in Eq. 4.7 also the density-clumping parameters have entered the expression for η , illustrating that there is an intimate coupling with the *spatial* clumping parameters, even though the vorosity effect initially depends on velocity parameters alone. For example, consider a wind with clumps that follow a smooth β velocity law. By bringing the clumps spatially closer together (for example by decreasing δt), the velocity gaps between them decrease as well. Thus one may choose to describe the changed situation either in terms of a less efficient porosity, because of fewer ‘density holes’ in the resonance zone through which the photons can escape (as done by Oskinova et al., 2007), *or* in terms of a less efficient vorosity, because of smaller velocity gaps between the clumps. Of course, one may also obtain a lower velocity gap between the clumps by increasing the actual velocity spans inside the clumps, as simulated in our stochastic models when $|\delta v / \delta v_\beta| > 1$. This effect, leading to a rather low vorosity, has already been demonstrated to be at work in the RH models (Sect. 4.5.4).

Using the parameters of our default model, Fig. 4.6 (right panel) displays η as a function of velocity and shows that η increases rapidly in the inner wind, reaches a maximum at $v \approx 0.33$, and then drops in the outer wind. To compare this behavior with that of the line profiles, we can associate absorption at some frequency x_{obs} with the corresponding value of the velocity, because absorption occurs at $x_{\text{obs}} \approx \mu v \approx v$ (radial photons dominate). In the default model’s absorption-part line profile (see Fig. 4.4, the middle plot in the lower-left panel), a strong de-saturation occurs directly after the clumping is set to start (at $r = 1.3$, $v \approx 0.23$), followed by a maximum at $x_{\text{obs}} \approx 0.35$, and finally an absorption dip toward the blue edge. The behavior of the line profile is thus well mapped by η , and we may explain the absorption dip as a consequence of the low value of η in the outer wind, which in turn stems from the slow variation of the velocity field (i.e., from radially extended resonance zones).

4.6.2 Density parameters

To isolate density-clumping effects, we use a smooth $\beta = 1$ velocity law in this subsection. Despite the smooth velocity field, there are still holes in velocity space (because of the density clumping, at the locations where the ICM is present), and the expression for η (Eq. 4.7) remains valid. Since a smooth velocity field corresponds to $\delta v = \delta v_\beta$, also the run of η is equal to the one displayed in Fig. 4.6. In this subsection we work only with integrated profile strengths (characterized by the equivalent width W_λ of the line’s absorption part). The shapes of the line profiles are discussed in Sect. 4.7.1.

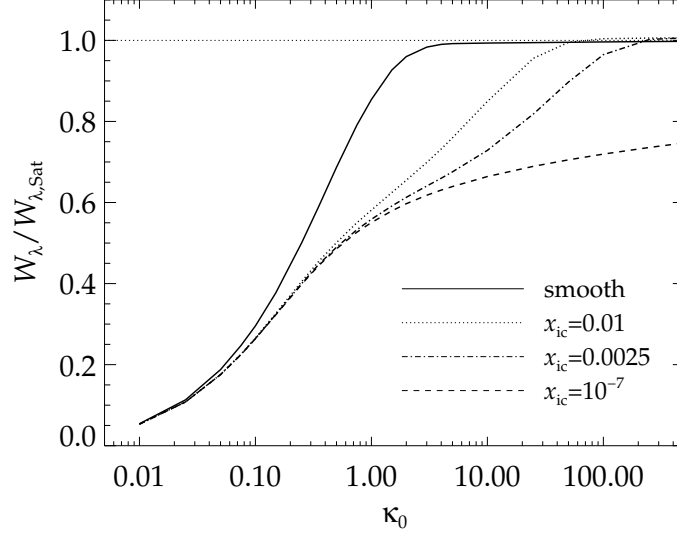


Figure 4.7: Equivalent widths W_λ of the absorption parts of line profiles, normalized to the value of a saturated line, as a function of line strength parameter κ_0 . The solid line is calculated from smooth models, and the dashed, dashed-dotted, and dotted lines from stochastic models with a smooth velocity field and $\delta t = 0.5$, $f_v = 0.25$, and x_{ic} as indicated.

Fig. 4.7 shows W_λ as a function of κ_0 , for smooth models as well as for stochastic models with and without a contributing ICM. The figure directly tells: i) The default model ($x_{ic} = 0.0025$) for the intermediate line ($\kappa_0 = 5.0$) displays a W_λ corresponding to a smooth model with a κ_0 roughly ten times lower. ii) Lines never saturate if the ICM is (almost) void. iii) The run of W_λ for the smooth and clumped models decouple well before κ_0 reaches unity. iv) For intermediate lines, the response of W_λ on variations of κ_0 is weak for clumped models. Points one to three confirm our findings from Sect. 4.5.3.

A variation of δt in the stochastic models affects primarily the high κ_0 part ($\kappa_0 \gtrsim 1.0$) of the curves in Fig. 4.7. For example, lowering δt in the model with a void ICM results in an upward shift of the dashed curve and vice versa. To obtain saturation with a void ICM, $\delta t \approx 0.05$ is required, which may be understood in terms of Eq. 4.7. For $\delta t = 0.05$, the η -values corresponding to the default model are decreased by a factor of ten, and η reaches a maximum of only about unity, with even lower values for the majority of the velocity space (cf. Fig. 4.6, right panel). The velocity gaps between the clumps then become closed, and the line saturates. In this situation, however, the intermediate line becomes saturated as well, again demonstrating the necessity of a *non-void* ICM to simultaneously saturate a strong line and not saturate an intermediate line. Only a properly chosen x_{ic} parameter ensures that the velocity gaps between the clumps become filled by low-density material able to absorb at strong line opacities, but *not* (or only marginally) at opacities corresponding to intermediate lines.

When varying x_{ic} , the primary change occurs at the high κ_0 end of Fig. 4.7. For higher (lower) values of x_{ic} , this part becomes shifted to the left (right), and the curve decouples earlier (later) from the corresponding curve for the void ICM. A higher ICM density obviously means that the ICM starts absorbing photons at lower line strengths and vice versa. Thus, observed saturated lines could

potentially be used to derive the ICM density (or at least to infer a lower limit), *if* the mass-loss rate (and abundance) is known from other diagnostics.

The behavior of the absorption with respect to the volume filling factor is as expected from the expression for η ; the higher f_v , the lower the value of η , and the stronger the absorption. This is because a higher f_v for a fixed δt implies that the clumps become more extended, whereas the distances between clump centers remain unaffected. Consequently, a larger fraction of the total wind velocity is covered by the clumps, leading to stronger absorption. For weak lines ($\kappa_0 \approx 0.05$), the ratio W_λ/W_{sm} deviates significantly from unity only when $f_v \lesssim 0.1$. Only for such low values can high enough clump densities be produced so that the clumps start to become optically thick.

From Fig. 4.7 it is obvious that, generally, clumped models have a different (slower) response in W_λ to an increase in κ_0 than do smooth models. This behavior may be observationally tested using UV resonance doublets (Massa et al., 2008), because the only parameter that differs between the two line components is the oscillator strength. Thus, if a smooth wind model is used and the fitted ratio of line strengths (i.e., $\kappa_{0,\text{blue}}/\kappa_{0,\text{red}}$) does not correspond to the expected ratio of oscillator strengths, one may interpret this as a signature of a clumped wind. Such behavior was found by Massa et al. (2008), where the observed ratios of the blue to red component of Si IV $\lambda\lambda$ 1394,1403 in B supergiants showed a wide spread between unity and the expected factor of two. This result indicates precisely the slow response to an increase in κ_0 that is consistent with inhomogeneous wind models such as those presented here, but not with smooth ones. In inhomogeneous models, the expected profile strength (or W_λ) ratio between two doublet components will depend on the adopted clumping parameters (as demonstrated by Fig. 4.7 and the discussion above) and may in principle take any value in the range found by Massa et al.. That is, while a profile-strength ratio deviating from the value expected by smooth models might be a clear indication of a clumped wind, the opposite is not necessarily an indication of a smooth wind. Furthermore, the degeneracy between a variation of clumping parameters and κ_0 suggests that un-saturated resonance lines should be used primarily as consistency tests for mass-loss rates derived from other diagnostics rather than as direct mass-loss estimators. We will return to this problem in Sect. 4.7.6, where a first comparison to observations is performed for the PV doublet.

4.6.3 Velocity parameters

The jump velocity parameter, v_j , affects only the strong lines (or, more specifically, the lines for which the ICM is significant), and determines the maximum velocity at which absorption can occur. For example, by setting $v_j = 0$, no absorption at frequencies higher than $x = 1$ is possible (unless δv is positive and very high). A higher v_j also implies more velocity overlaps, and thereby an increased amount of backscattering due to multiple resonance zones. Both effects are illustrated in Fig. 4.8. Judging from the line profiles of the lower panel, the blue edge and the reduction of the re-emitted flux blueward of the line center may both be used to constrain v_j . The upper panel shows one slice of the corresponding velocity fields, illustrating that the underlying β law is recovered almost perfectly when using $v_j = 0.01v_\beta$ and $\delta v = \delta v_\beta$. With this velocity law and a non-void ICM, the corresponding strong line profile is equivalent to a profile from a smooth model.

In Sects. 4.5.3 and 4.5.4, we showed that a higher value of the clumps' velocity spans led to stronger absorption for intermediate lines. In principle this is as expected from Eq. 4.7, where η always decreases with increasing $|\delta v/\delta v_\beta|$. However, with the very high value of $|\delta v/\delta v_\beta|$ used in, e.g., the RHcopy model, one realizes that η in Eq. 4.7 becomes identically zero, because $f_v|\delta v/\delta v_\beta| = 1$.

An $\eta = 0$ corresponds to the whole velocity space being covered by clumps, and the saturation limit should be reached. As is clear from Fig. 4.4, however, this is not the case. This points out two important details not included when deriving the expression for η and interpreting the absorption in terms of this quantity, namely that clumps are distributed randomly (with δt determining only the average distances between them) and that the parameter v_j allows for an asymmetry in the velocities of the clumps' starting points (see Sect. 4.3.2). These two issues lead to overlapping velocity spans for some of the clumps, whereas for others there is still a velocity gap left between them, through which the radiation can escape. Therefore the profiles do not reach complete saturation, despite that on average $\eta = 0$. This illustrates some inherent limitations when trying to interpret line formation in terms of a simplified quantity such as η .

The impact from the velocity spans of the clumps on the line profiles also depends on the density-clumping parameters. To achieve approximately the same level of absorption, a higher value of $\delta v/\delta v_\beta$ was required in the RHcopy model ($f_v = 0.1$) than in the default model ($f_v = 0.25$), see Fig. 4.4. Since $\delta v_\beta \propto f_v \delta t$ (see Sect. 4.10), the actual velocity spans of the clumps are different for different density-clumping parameters, even if $\delta v/\delta v_\beta$ remains unchanged.

By changing the sign of δv in the default model (that is, assuming a positive velocity gradient inside the clumps), we have found that our results qualitatively depend only on $|\delta v|$. Some details differ though. For example, a $\delta v > 0$ in our stochastic models permits absorption at velocities higher than the terminal one also within the clumps, whereas $\delta v < 0$ restricts the clump velocities to below the local v_β (see Fig. 4.2). In this matter v_j plays a role as well, since v_j controls where, with respect to the local v_β , the clumps begin. For reasonable values of v_j , however, its influence is minor on lines where the ICM is insignificant. Finally, tests have confirmed that optically thin lines are only marginally affected when varying $\delta v/\delta v_\beta$.

4.7 Discussion

4.7.1 The shapes of the intermediate lines

For intermediate lines, the shape of the absorption part of the default model differs significantly from the shape of a smooth model (see Fig. 4.4, the middle plot in the lower-left panel). We showed in Sect. 4.6.1 that the shapes could be qualitatively understood by the behavior of η . This is further demonstrated here by scaling the line strength parameter of a 1D, smooth model, using a parameterization $\kappa_0 \propto \eta^{-1}$ outside the radius $r = 1.3$ where clumping is assumed to start. Fig. 4.9 displays the line profiles of 1D, smooth models with $\kappa_0 = 5.0$ and $\kappa_0 = 5.0/(2\eta)$. These profiles are compared to those calculated from a 'real' 2D stochastic model with density-clumping parameters as the default model, but with a $\beta = 1$ velocity field. η was calculated from Eq. 4.7, using the parameters of the default model and a $\beta = 1$ velocity law, and the factor of 2 in the denominator of the scaled κ_0 was chosen so that the *integrated* profile strength of the 2D model was roughly reproduced. From Fig. 4.9 it is clear that the 1D model with scaled κ_0 well reproduces the 2D results, indicating that indeed η governs the shape of the line profile. We notice also that these profiles display a completely black absorption dip in the outermost wind, as opposed to the default model with a non-monotonic velocity field (see Fig. 4.4, the middle plot in the lower-left panel). This is because the β velocity field does not allow for any clumps to overlap in velocity space (see the discussion in Sect. 4.6.3), making the mapping of η almost perfect.

Let us also point out that the line shapes can be somewhat altered by using a different velocity law,

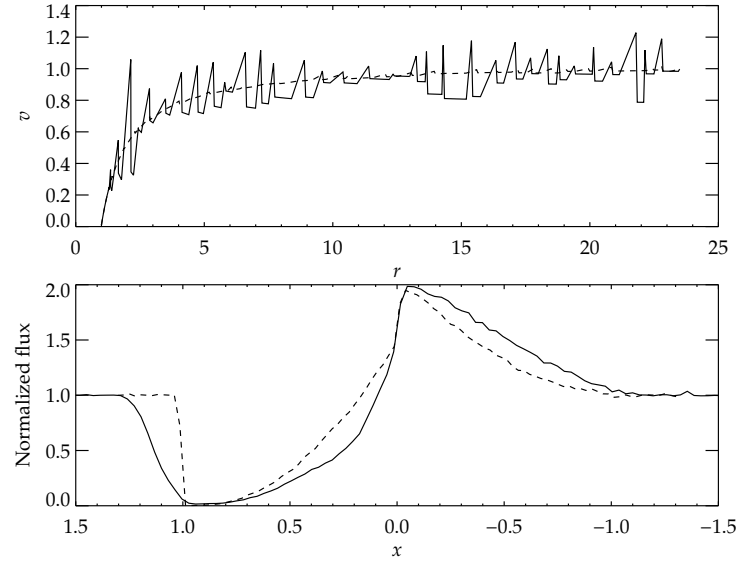


Figure 4.8: **Upper:** Velocity structures (one slice) in two stochastic models with density-clumping parameters as for the default model, and different velocity parameters. Dashed: $\delta v/\delta v_\beta = 1$ and $v_j/v_\beta = 0.01$. Solid: $\delta v/\delta v_\beta = -1$ and $v_j/v_\beta = 0.5$ below $v_\beta = 0.6$ and $v_j/v_\beta = 0.15$ above. **Lower:** Corresponding line profiles for a strong line.

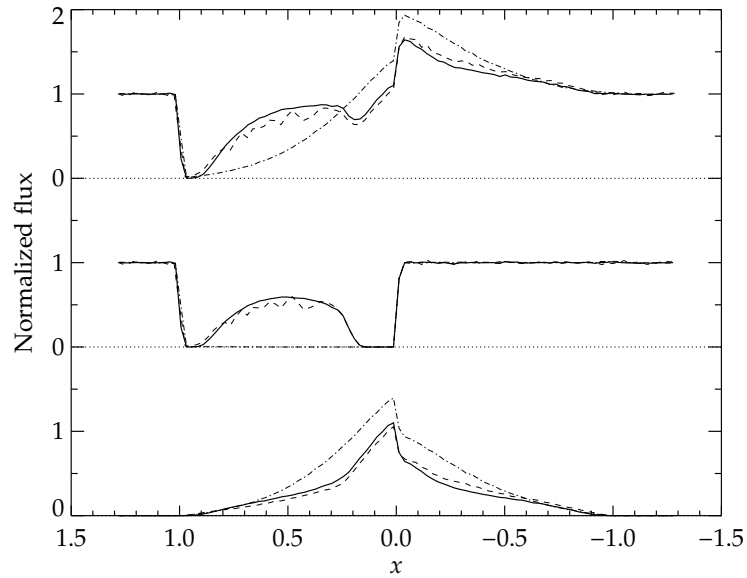


Figure 4.9: Total, absorption part, and re-emission part line profiles for 1D, smooth models with $\kappa_0 = 5.0$ (dashed-dotted lines) and $\kappa_0 = 5.0/(2\eta)$ (solid lines, see Sect. 4.7.1), and for a 2D, stochastic model with density parameters as the default model and a $\beta = 1$ velocity law (dashed lines).

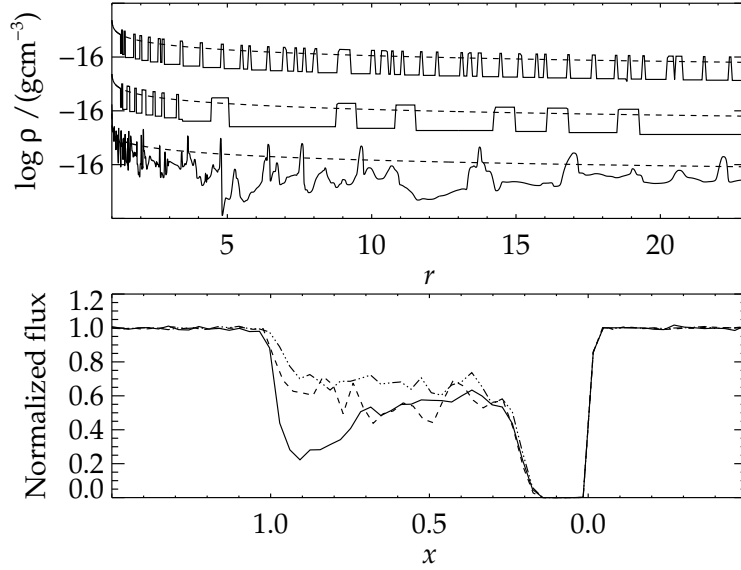


Figure 4.10: **Upper panel:** Density structures of one slice in the default stochastic model (upper), in the default stochastic model with a modified δt (middle, see Sect. 4.7.2), and in FPP (lower). **Lower panel:** Line profiles for the absorption part of an intermediate line for the default model (solid line), for the default model with a modified δt (dashed line), and for the default model with an ionization structure decreasing with increasing velocity (dashed-dotted line, see text).

e.g., $\beta \neq 1$. Such a change would affect the distances between clumps as well as the Sobolev length, and thereby the line shapes of both absorption and re-emission profiles. However, in all cases is the shape of the re-emission part similar in the clumped and smooth models.

4.7.2 The onset of clumping and the blue edge absorption dip

We have used $r = 1.3$ as the onset of wind clumping in our stochastic models, which roughly corresponds to the radius where significant structure has developed from the line-driven instability in our RH models. However, Bouret et al. (2003, 2005) analyzed O-stars in the Galaxy and the SMC, assuming optically thin clumps, and found that clumping starts deep in the wind, just above the sonic point. Also Puls et al. (2006) used the optically thin clumping approach, on ρ^2 -diagnostics, and found similar results, at least for O-stars with dense winds. With respect to our stochastic models, the qualitative results from Sects. 4.5 and 4.6 remain valid when choosing an earlier onset of clumping. Quantitatively, the integrated absorption in intermediate lines becomes somewhat weaker, because the clumping now starts at lower velocities, and of course the line shapes in this region are affected as well. The onset of wind clumping will be important when comparing to observations, as discussed in Sect. 4.7.6.

The stochastic models that de-saturate an intermediate line generally display an absorption dip toward the blue edge (see Figs. 4.4 and 4.9), which has been interpreted in terms of low values of η in the outer wind (see Sect. 4.6.1). However, this characteristic feature (not to be confused with the so-called DACs, discrete absorption components) is generally not observed, and one may ask whether it might be an artifact of our modeling technique. In the following we discuss two possibilities that may cause

our models to overestimate the absorption in the outer wind; the ionization fraction and too low clump separations.

Starting with the former, we have so far assumed a constant ionization factor, $q = 1$ (cf. Eq. 4.16). This is obviously an over-simplification. For example, an outwards decreasing q would result in less absorption toward the blue edge. Here we merely demonstrate this general effect, parameterizing $q = v_0/v_\beta$ in the stochastic default model (see Table 4.2), with $v_0 = 0.1$ the starting point below which $q = 1$. Fig. 4.10 (lower panel, dashed-dotted lines) shows how the absorption in the outer wind becomes significantly reduced.

The temperature structure of the wind is obviously important for the ionization balance. Whereas an isothermal wind is assumed in POF (see Sect. 4.3.1), the FPP model has shocked wind regions with temperatures of several million Kelvin. To roughly map corresponding effects on the line profiles, we re-calculated profiles based on FPP models assuming $q = 0$ in all regions with temperatures higher than $T = 10^5$ K, and $q = 1$ elsewhere. Since the hot gas resides primarily in the low-density regions, however, the emergent profiles were barely affected, and particularly intermediate lines remained unchanged.

On the other hand, the X-ray emission from hot stars (believed to originate in clump-clump collisions, see FPP) is known to be crucial for the ionization balance of highly ionized species such as CIV, NV, and OVI (see, e.g., the discussion in Puls et al., 2008b). X-rays have not been included here, but could in principle have an impact on our line profiles, by illuminating the over-dense regions and thereby changing the ionization balance. Krtićka & Kubát (2009), however, find that incorporating X-rays does not influence the PV ionization significantly. Finally, non-LTE analyses including feedback from optically thin clumping have shown that this as well has a significant effect on the derived ionization fractions of, e.g., PV (Bouret et al., 2005; Puls et al., 2008a). To summarize, it is clear that a full analysis of ionization fractions must await a future non-LTE application that includes relevant feedback effects from an inhomogeneous wind on the occupation numbers.

In RH models, the average distance between clumps increases in the outer wind, due to clump-clump collisions and velocity stretching (Feldmeier et al., 1997; Runacres & Owocki, 2002). Neglecting the former effect, our stochastic models have clumps much more closely spaced in the outer wind⁵. We have therefore modified the default model by setting $\delta t = 3$ outside a radius corresponding to $v_\beta = 0.7$. This is illustrated in the upper panel of Fig. 4.10. The mass loss in the new stochastic model is preserved (because the clumps are more extended, see the figure), and this model now better resembles FPP. Recall that differences in the widths of the clumps are expected, since in the default model $f_{cl} \approx f_v^{-1} = 4$, whereas in FPP $f_{cl} \approx 10$. The corresponding line profile shows how the absorption outside $x \approx 0.7$ has been reduced, as expected from the higher δt .

4.7.3 The velocity spans of the clumps

In Sect. 4.5.4 it was found that $|\delta v| > \delta v_\beta$ in the RH models. Fig. 4.11, upper panel, shows the velocity spans of density enhancements (identified as having a density higher than the corresponding smooth value) in the FPP model, and demonstrates that, after structure has developed, $|\delta v|$ is much higher than δv_β throughout the whole wind. These high values essentially stem from the location of the starting points of the density enhancements, which generally lie *before* the velocities have reached their post shock values (see Fig. 4.11, middle and lower panels). By using a β velocity law (which in principle corresponds to a stochastic velocity law with $v_j = 0$ and $\delta v = \delta v_\beta$, see Fig. 4.8) together

⁵ The effect is minor in POF, since these RH models only extend to $r \sim 5$ (see Sect. 4.3.1).

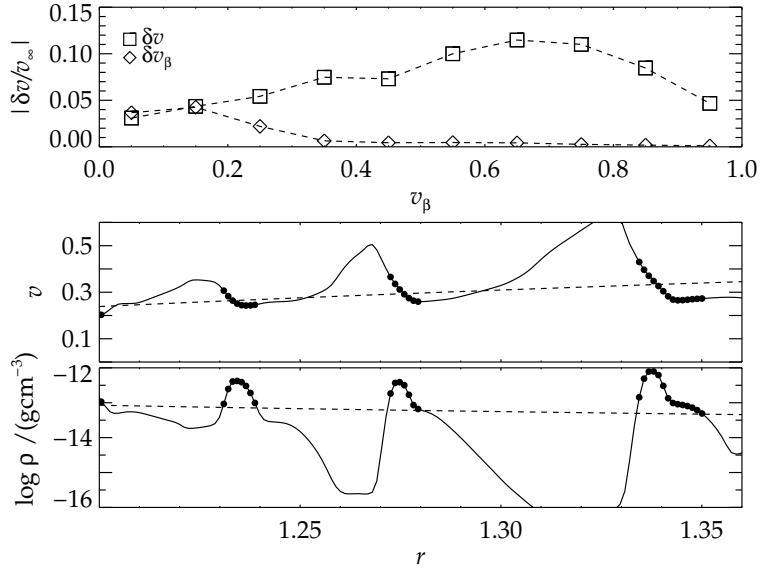


Figure 4.11: **Upper:** Velocity spans of density enhancements in the FPP model (squares) and corresponding β intervals (diamonds). **Lower:** Three density enhancements and corresponding velocity spans in the FPP model, highlighted as in Fig. 4.1.

with the density structure from FPP, we simulated a RH wind with low velocity spans. Indeed, for the corresponding intermediate line the equivalent width of the absorption part was $\sim 35\%$ lower than that of the original FPP model. The strong line, on the other hand, remained saturated, because the ICM in FPP is not void. So, again, the RH models would in parallel display de-saturated intermediate lines and saturated strong lines, were it not for the large velocity spans inside the clumps.

We suggest that the large velocity span inside a shell (clump) is primarily of kinematic origin, and reflects the formation history of the shell. The shell propagates outwards through the wind, essentially with a $\beta = 1$ velocity law (Owocki et al., 1988). Fast gas is decelerated in a strong reverse shock at the inner rim of the shell. The shell collects ever faster material on its way out through the wind. This new material collected at higher speeds resides on the star-facing side, i.e. at smaller radii, of the slower material collected before. Thus, a negative velocity gradient develops inside the shell. The fact that $|\delta v| \gg \delta v_\beta$ in FPP seems to reflect that the shell is formed at small radii, and then advects outwards maintaining its steep interior velocity gradient⁶. From this formation in the inner, steeply accelerating wind, velocity spans within the shells up to (a few) hundred km s^{-1} , as seen in Fig. 4.11, appear reasonable.

However, the dynamics of shell formation in hot star winds is very complex due to the creation and subsequent merging of subshells, as caused by nonlinear perturbation growth and the related excitation of harmonic overtones of the perturbation period at the wind base (see Feldmeier, 1995). Future work is certainly needed to clarify to which extent the large velocity spans inside the shells in RH models are a stable feature (see also Sect. 4.8.2).

⁶ Actually, the velocity gradient may further steepen during advection, due to faster gas trying to overtake slower gas ahead of it; however, this effect is balanced by pressure forces in the subsonic postshock domain.

4.7.4 3D effects

A shortcoming of our analysis is the assumed symmetry in Φ . The 2D rather than 3D treatment has in part been motivated by computational reasons (see Sect. 4.9). More importantly though, we do not expect our *qualitative* results to be strongly affected by an extension to 3D. Within the broken-shell wind model, all wind slices are treated independently, and distances between clumps increase only in the radial direction. Therefore the expected outcome from extending to 3D is a smoothing effect rather than a reduction or increase in integrated profile strength (similar to the smoothing introduced by N_{Θ} , see Sect. 4.5.1). Also, we have shown that the main effect from the inhomogeneous winds is on the absorption part of the line profiles (see, e.g., Sect. 4.7.1). The formation of this part is dominated by radial photons, especially in the outer wind, because of the dependence only on photons released directly from the photosphere. This implies that most photons stay within their wind slice, restricting the influence from any additional ‘holes’ introduced by a broken symmetry in Φ to the inner wind. Of course, these expectations hold only within the broken shell model, because in a real 3D wind the clumps will, for example, have velocity components also in the tangential directions.

4.7.5 Comparison to other studies

To scale the smooth opacity in the formal integral of the non-LTE atmospheric code PoWR, Oskinova et al. (2007) used a porosity formalism in which both f_v and the average distance between clumps enter. Other assumptions were a void ICM, a smooth β velocity field, and a microturbulent velocity $v_t \approx 50 \text{ km s}^{-1}$, the last identified as the velocity dispersion within a clump. However, a direct comparison between their study and ours is hampered by the different formalisms used for the spacing of the clumps. Here we have used the ‘broken-shell’ wind model as a base (see Sect. 4.3.2), in which each wind slice is treated independently and the distance between clumps increases only in the radial direction (clumps preserve their lateral angles). This gives a radial number density of clumps, $n_{\text{cl}} \propto v^{-1}$, the same as used by, e.g., Oskinova et al. (2006), when synthesizing X-ray emission from hot stars. In Oskinova et al. (2007), on the other hand, the distance between clumps increases in *all* spatial directions. In a spherical expansion, this gives a radial number density of clumps $n_{\text{cl}} \propto v^{-1} r^{-2}$, i.e., clumps are distributed much more sparsely within this model, especially in the outer wind. Therefore their choice of $L_0 = 0.2$ is not directly comparable with $\delta t = 0.2$ in our models. The shapes of the clumps differ between the two models as well; in Oskinova et al. clumps are assumed to be ‘cubes’, whereas here the exact shapes of the clumps are determined by the values of the clumping parameters. Despite these differences, our findings confirm the qualitative results of Oskinova et al. that the line profiles become weaker with an increasing distance between clumps as well as with a decreasing v_t . These results may be interpreted on the basis of the effective escape ratio, η (see Eq. 4.7). Both a decrease in v_t and an increase in the distance between clumps mean that the velocity span covered by a resonance zone becomes smaller when compared to the velocity gap between two clumps (see Fig. 4.6, left panel), leading to higher probabilities for line photons to escape their resonance zones without interacting with the wind material.

An important result of this paper is that models that de-saturate intermediate lines require a non-void ICM to saturate strong lines. This is confirmed by the Oskinova et al. model, in which the ICM is void and strong lines indeed do not saturate (Hamann et al., 2009).

Owocki (2008) proposed a simplified description of the non-monotonic velocity field to account for vorosity, i.e., the velocity gaps between the clumps. Here, the vorosity effect has been discussed using the quantity η (see Sect. 4.6.1), and we have introduced two new parameters to characterize a non-

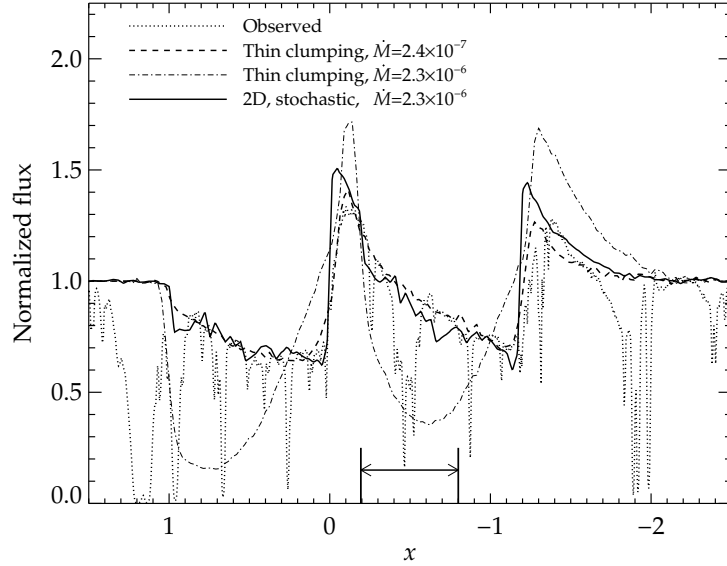


Figure 4.12: Observed FUSE spectra of the PV doublet $\lambda\lambda 1118$ -1128 for the O6 supergiant λ Cep (Fullerton et al., 2006). The synthetic spectra are calculated for two 1D models assuming optically thin clumping (see Sect. 4.7.6) and for one 2D stochastic model with parameters as in Table 4.2, model Obs1. The models have mass-loss rates \dot{M} [$M_{\odot} \text{ yr}^{-1}$] as given in the figure. The zero point frequency is shifted to the line center of the $\lambda 1118$ component, and the two arrows at the bottom of the figure indicate in which region the two components overlap.

monotonic velocity field, δv and v_j . The reason for introducing a new parameterization is that when using a single velocity parameter, we have not been able to simultaneously meet the constraints from strong, intermediate, and weak lines as listed in Sect. 4.5. Tests using a ‘velocity clumping factor’ $f_{\text{vel}} = \delta v / \Delta v$ as proposed by Owocki (2008), together with a smooth density structure, have shown that this treatment indeed can reduce the line strengths of intermediate lines, but that the observational constraints from strong lines may not be met. Still, the basic concept of vorosity holds within our analysis. For example, one may phrase the high values of δv in the RH models in terms of insufficient vorosity.

4.7.6 Comparison to observations

We finalize our discussion by performing a first comparison to observations. The two components of the Phosphorus V $\lambda\lambda 1118$ -1128 doublet are rather well separated, and the singlet treatment used here suffices to model the major part of the line complex. Nevertheless, the two components overlap within a certain region (indicated in Fig. 4.12), so when interpreting the results of this subsection, one should bear in mind that the overlap is not properly accounted for, but treated as a simple multiplication of the two profiles.

We used observed FUSE spectra (kindly provided by A. Fullerton) from HD 210839 (λ Cep), a supergiant of spectral type O6I(n)fp. When computing synthetic spectra, we first assumed optically thin clumping with a constant clumping factor $f_{\text{cl}} = 9$ and a smooth $\beta = 1$ velocity field. $f_{\text{cl}} = 9$ agrees fairly well with the analysis of Puls et al. (2006), who derived clumping factors $f_{\text{cl}} = 6.5$ for

$r \approx 1.2 \dots 4.0$ and $f_{\text{cl}} = 10$ for $r \approx 4.0 \dots 15$, assuming an un-clumped outermost wind.⁷ We took the ionization fraction $q = q(r)$ of PV from Puls et al. (2008a), calculated with the unified non-LTE atmosphere code FASTWIND for an O6 supergiant, using the Phosphorus model atom from Pauldrach et al. (2001). The feedback from optically *thin* clumping was accounted for and X-rays were neglected. This ionization fraction was then used as input in our MC-1D code when computing the synthetic spectra. We assigned a thermal plus a highly supersonic ‘microturbulent’ velocity $v_t = 0.05$ (corresponding to 110 km s^{-1}), as is conventional in this approach. The mass-loss rate was derived using the well known relation between κ_0 and \dot{M} (e.g., Puls et al., 2008b). For atomic and stellar parameters, we adopted the same values as in Fullerton et al. (2006).

The dashed line in Fig. 4.12 represents our fit to the observed spectrum, assuming optically thin clumping, resulting in a mass-loss rate $\dot{M} = 0.24$, in units of $10^{-6} M_{\odot} \text{ yr}^{-1}$. Fullerton et al. (2006) derived $\langle q \rangle \dot{M} = 0.23$ for this star. Because our clumped FASTWIND model predicts an averaged ionization fraction $\langle q \rangle \approx 0.9$ in the velocity regions utilized by Fullerton et al., the two rates are in excellent agreement. On the other hand, Repolust et al. (2004) for HD 210839 derived $\dot{M} = 6.9$ from H_{α} assuming an unclumped wind, yielding $\dot{M}_{H_{\alpha}} = 2.3$ when accounting for the reduction implied by our assumed $f_{\text{cl}} = 9$ ($\dot{M}_{H_{\alpha}} = \dot{M}_{H_{\alpha,sm}} f_{\text{cl}}^{-1/2}$). This rate is almost ten times higher than that inferred from PV, and thus results in PV line profiles that are much too strong (see Fig. 4.12, dashed-dotted line). That is, to reconcile the H_{α} and PV rates for HD 210839 with models that assume optically *thin* clumps also in PV, we would have to raise the clumping factor to $f_{\text{cl}} > 100$. In addition to this very high clumping factor, the low rate inferred from the PV lines conflicts with the theoretical value $\dot{M} = 3.2$ provided by the mass-loss recipe in Vink et al. (2000) (using the stellar parameters of Repolust et al., 2004), and is also strongly disfavored by current massive star evolutionary models (Hirschi, 2008).

Next we modeled the PV lines using our MC-2D code together with a stochastic 2D wind model. The same clumping factor ($f_{\text{cl}} = 9$) and ionization fraction (calculated from FASTWIND, see above) were used. This time, we assigned $v_t = 0.005$, i.e., applied no microturbulence. In previous sections, e.g. 4.5.3 and 4.7.1, we showed that stochastic models generally display a line shape different from smooth models, with a characteristic absorption dip at the blue edge as well as a dip close to the line center. Such shapes are not seen in the PV lines in λ Cep. Thus, to better resemble the observed line shapes, we used different values for δt and x_{ic} in the inner and outer wind (the former modification already discussed in Sect. 4.7.2) and let clumping start close to the wind base. Clumping parameters are given in Table 4.2, model Obs1.

As illustrated in Fig. 4.12, the synthetic line profiles using $\dot{M} = 2.3$, as inferred from H_{α} , are now at the observed levels. Because of our insufficient treatment of line overlap, we gave higher weight to the $\lambda 1118$ component when performing the fitting, but the profile-strength ratio between the blue and red component was nevertheless reasonably well reproduced (see also discussion in Sect. 4.6.2). However, though the fit appears quite good, we did not aim for a perfect one, and must remember the deficits of our modeling technique. For example, while the early onset of clumping definitely improved the fit (using our default value, there was a dip close to line center) and might be considered as additional evidence that clumping starts close to the wind base, the same effect could in principle be produced by non-LTE effects close to the photosphere or by varying the underlying β velocity law. Such effects will be thoroughly investigated in a follow-up paper, which will also include a

⁷ This stratification has been found to be prototypical for O-supergiants and was, together with its well developed PV P Cygni profiles, the major reason for choosing λ Cep as comparison object instead of, e.g., ζ Pup, which displays a somewhat unusual run of f_{cl} .

comparison to observations from many more objects.

Clearly, a consistent modeling of resonance lines (at least of intermediate strengths) requires the consideration of a much larger parameter set than if modeling via the standard diagnostics assuming optically thin clumping, and a reasonable fit to a single observed line complex can be obtained using a variety of different parameter combinations. The analysis of PV lines as done here can therefore, at present, only be considered as a consistency check for mass-loss rates derived from other, independent diagnostics, and not as a tool for directly estimating mass-loss rates. Additional insight might be gained by exploiting more resonance doublets, due to the different reactions of profile strengths and shapes on κ_0 . The different slopes of the equivalent width as a function of κ_0 in smooth and clumped models, especially at intermediate line strengths (Sect. 4.6.2), may turn out to be decisive. However, because of, e.g., the additional impact from the ICM density, also this diagnostics requires additional information from saturated lines. Taken together, only a consistent analysis using different diagnostics and wavelength bands, and embedded in a suitable non-LTE environment, will (hopefully) provide a unique view.

4.8 Summary and future work

4.8.1 Summary

Below we summarize our most important findings:

- When synthesizing resonance lines in inhomogeneous hot star winds, the detailed density structure, the non-monotonic velocity field, and the inter-clump medium are all important for the line formation. Adequate models must be able to simultaneously meet observational and theoretical constraints from strong, intermediate, and weak lines.
- Resonance lines are basically unaffected by the inhomogeneous wind structure in the limit of optically thin clumps, but the clumps remain optically thin only for very weak lines.
- We confirm the basic effects of porosity (stemming from optically thick clumps) and vorosity (stemming from velocity gaps between the clumps) in the formation of primarily lines of intermediate strengths.
- We point out the importance of a non-void ICM for the simultaneous formation of strong and intermediate lines that meet observational constraints.
- Porosity and vorosity are found to be intrinsically coupled and of similar importance. To characterize their mutual effect on intermediate lines, we have identified a crucial parameter, the ‘effective escape ratio’, that describes to which extent photons may escape their resonance zones without ever interacting with the wind material.
- We confirm previous results that time-dependent, radiation-hydrodynamic wind models reproduce observed characteristics for strong lines, without applying the highly supersonic microturbulence needed in smooth models.
- A significant profile strength reduction of intermediate lines (as compared to smooth models) is for the radiation-hydrodynamic models prevented by the large velocity spans of the density

enhancements, implying that the wind structures predicted by present day RH models are not able to reproduce the observed strengths of intermediate lines unless invoking a very low mass-loss rate.

- Provided a non-void ICM and not too large velocity spans inside the clumps, 2D *stochastic* wind models saturate strong lines, while simultaneously not saturating intermediate lines (that are saturated in smooth models). Using typical volume filling factors, $f_v \approx 0.25$, the resulting integrated profile strength reductions imply that these inhomogeneous models would be compatible with mass loss rates roughly a factor of ten higher than those derived from resonance lines using smooth models.
- A first comparison to observations was made for the O6 supergiant λ Cep. It was found that, indeed, the line profiles of PV based on a 2D stochastic wind model, accounting for a detailed density structure and a non-monotonic velocity field, reproduced the observations with a mass-loss rate almost ten times higher than the rate derived from the same lines, but with a model that used the optically thin clumping approach. This alleviated the discrepancies between theoretical predictions, evolutionary constraints, and previous mass-loss rates based on winds assumed either to be smooth or to have optically thin clumps.

4.8.2 Future work

We have investigated general properties of resonance line formation in inhomogeneous 2D wind models with non-monotonic velocity fields. To perform a detailed and quantitative comparison to observations, and derive mass-loss rates, simplified approaches need to be developed and incorporated into non-LTE models to obtain reliable occupation numbers. Extending our Monte-Carlo radiative transfer code to include line overlap effects in doublets is critical for more quantitative applications, and an extension to 3D is also necessary. Further applications involve synthesizing emission lines, for example to test the optically thin clumping limit both in the parameter range where this is thought to be appropriate (e.g., for O-/early B-stars), and in other more complicated situations. Indeed, the present generation of line-blanketed model atmospheres does not seem to be able to reproduce H_α line profiles from A-supergiants, which are observed as P-Cygni profiles with *non-saturated* troughs, whereas the simulations (assuming optically thin clumping) result in saturated troughs (R.-P. Kudritzki, private communication). Since H_α is a quasi-resonance line and not a recombination line in these cooler winds (e.g., Kudritzki & Puls, 2000), this behavior might be explained by the presence of optically thick clumps.

Finally, it needs to be clarified if the large velocity span inside clumps generated in RH models is independent of additional physics that is not, or only approximately, accounted for in present simulations (such as more-D effects and/or various exciting mechanisms). If the large velocity span is a stable feature, one might come to the (rather unfortunate) conclusion that either the observed clumping features are not, or only weakly, related to the line-driven instability, or the discrepancies between observed and synthetic flux distribution (from the X-ray to the radio regime) might involve processes different from the present paradigm of wind clumping.

4.9 The Monte-Carlo transfer code

4.9.1 The code

Here we describe our Monte-Carlo radiative transfer code (MC-2D) in some detail. For an overview of basic assumptions, see Sect. 4.4 in the main paper. For testing purposes, versions to treat spherically symmetric winds, either in the Sobolev approximation (MCS-1D) or exactly (MC-1D), have been developed as well.

Geometry. For wind models in which the spherical symmetry is broken, we can no longer restrict photon trajectories to rays with constant impact parameters (see below). Moreover, the observed spectrum will depend on the observer's placement relative to the star. Fig. 4.13 illustrates the geometry in use, a standard right-handed spherical system (r, Θ, Φ) defined relative to a Cartesian set (X, Y, Z) (transformations between the two may be found in any standard mathematical handbook). At each coordinate point we also construct a local coordinate system using the local unit vectors (r_u, Θ_u, Φ_u) , which for a photon propagating in direction n_u is related to the *radiation coordinates* (θ, ϕ) (see Fig. 4.13) via

$$\cos \theta \equiv \mu = r_u \cdot n_u, \quad (4.8)$$

$$\sin \phi \sin \theta = \Phi_u \cdot n_u = \frac{Z_u \times r_u}{|Z_u \times r_u|} \cdot n_u, \quad (4.9)$$

$$\cos \phi \sin \theta = \Theta_u \cdot n_u = [\Phi_u \times r_u] \cdot n_u. \quad (4.10)$$

The radiation coordinates are defined on the intervals $\theta = 0 \dots \pi$ and $\phi = 0 \dots 2\pi$, but due to the symmetry in Φ , only the range $\phi = 0 \dots \pi$ needs to be considered (see Busche & Hillier 2000). Also, for this symmetry, the direction cosines of n_u simplify to

$$n_x = \mu \sin \Theta + \sqrt{1 - \mu^2} \cos \phi \cos \Theta, \quad (4.11)$$

$$n_y = \sqrt{1 - \mu^2} \sin \phi, \quad (4.12)$$

$$n_z = \mu \cos \Theta - \sqrt{1 - \mu^2} \cos \phi \sin \Theta. \quad (4.13)$$

Eqs. 4.8-4.13 are used to update the physical position (r, Θ) of the photon and the local values of the radiation coordinates (θ, ϕ) . By tracking the photon on a radial mesh, both the physical and radiation coordinates can be updated exactly. Interpolations are necessary only when a photon is scattered or when it crosses a Θ -boundary to another wind slice. Essentially the same coordinate system is used by, e.g., Busche & Hillier (2000). We collect escaped photons according to their Θ -angles at 'infinity'⁸, and bin them using the same N_Θ bins as in the underlying wind model (see Sect. 4.3).

For spherically symmetric wind models, we adhere to the customary (p, z) spatial coordinate system with p being the impact parameter and z the direction toward the observer. Each time a photon is scattered and its direction determined, a new impact parameter is computed from the relation $p = r\sqrt{1 - \mu^2}$, appreciating that all points on a surface of constant radius can be treated equally in this geometry.

⁸ The full 3D problem would require binning in Φ as well, which in turn would require a large increase in the number of simulated photons.

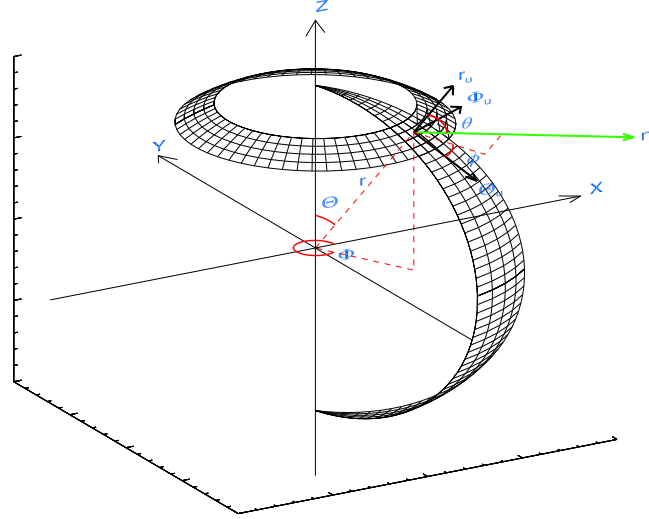


Figure 4.13: Illustration of the coordinate system, see text. *A color version of this figure is available in the web version.*

Releasing photons. We release photons from the lower boundary uniformly in ϕ and with a distribution function $\propto \mu d\mu$ in μ (e.g., Lucy, 1983). The angular coordinate Θ is selected so that photons are uniformly distributed over the surface area $dA = \sin \Theta d\Theta d\Phi$.

Absorption. The probability of photon absorption is $\propto e^{-\tau} d\tau$, hence the optical depth τ the photon travels before absorption can be selected according to $\tau = -\ln R_1$, where R_1 is a random number between 0 and 1. The position for absorption in the wind may then be determined by inverting the line optical depth integral along the photon path

$$\tau_v = \int \chi_v ds, \quad (4.14)$$

with the frequency-dependent opacity

$$\chi_v = \kappa_L \rho \phi_v, \quad (4.15)$$

with ϕ_v the absorption profile, κ_L the frequency integrated mass absorption coefficient, and ρ the mass density. All dependencies on spatial location are for simplicity suppressed here and in the following. For the opacity we use the parameterization from Hamann (1981) and POF,

$$\kappa_L \lambda \rho = \frac{4\pi R_* v_\infty^2}{\dot{M}} \kappa_0 \rho q, \quad (4.16)$$

where λ is the wavelength of the considered transition, κ_0 is a ‘line-strength’ parameter taken to be constant, \dot{M} the radially and laterally averaged mass-loss rate, and $q = q(r, \Theta)$ the fraction of the considered element that resides in the investigated ionic stage. Default here is $q = 1$, but effects from other ionization structures are discussed in Sect. 4.7.2. κ_0 is proportional to the product of mass-loss

rate and abundance of the considered ion, and, for a smooth wind, $\kappa_0 = 1$ and $\kappa_0 = 100$ give a typical medium and strong line, respectively. The parameterization as defined in Eq. 4.16 has the advantage that for smooth winds the radial optical depth in the Sobolev approximation collapses to

$$\tau_{\text{Sob}} = \frac{\kappa_0}{r^2 v dv/dr} q, \quad (4.17)$$

when v and r are expressed in normalized units. The corresponding expression for clumpy winds is provided in Eq. 4.5. The absorption profile is assumed to be a Gaussian with a Doppler width v_t that contains the contributions from thermal and (if present) ‘microturbulent’ velocities. To solve Eq. 4.14, we adopt the dimensionless frequency x with the terminal velocity of a smooth outflow as the reference speed,

$$x = \frac{v - v_0}{v_0} \frac{c}{v_\infty}, \quad (4.18)$$

and transform to the co-moving frame (hereafter CMF). v_0 is the rest-frame frequency of the line center and c the speed of light. We now assume that between two grid points the variation of the factor $\kappa_L \rho / |Q|$ (see below) is small and may be replaced by an average value. The optical depth $\Delta \tau_v$ between two subsequent spatial points (r, Θ) then becomes

$$\Delta \tau_v = \left| \frac{\lambda R_\star}{v_\infty} \frac{\kappa_L \rho}{Q} \times \frac{-\Delta \text{erf}[x_{\text{cmf}}/v_t]}{2} \right|, \quad (4.19)$$

where Δerf is the difference of the error-function between the points, x_{cmf} the dimensionless CMF frequency, and v_t is calculated in units of v_∞ . $Q \equiv n_u \cdot \nabla (n_u \cdot \vec{v})$ is the local directional derivative of the velocity in direction n_u , with velocities measured in units of v_∞ and radii in units of R_\star . By interpolating to the border whenever a photon crosses a Θ boundary, we *locally* recover the spherically symmetric expression

$$Q = \frac{\partial v}{\partial r} \mu^2 + \frac{v}{r} (1 - \mu^2). \quad (4.20)$$

For spherically symmetric winds, we have written a second implementation that allows for line transfer using the Sobolev approximation. With this method each resonance zone is approximated by a point and the line only collects optical depth at atmospheric locations where the observer’s frame frequency x_{obs} has been Doppler shifted to coincide with the CMF frequency for the line center. The condition for interaction thus is $x_{\text{obs}} = \mu v$ and the last factor in Eq. 4.19 collapses to unity when calculating the Sobolev optical depth. The Sobolev approach can be expected a reasonable approximation when the variation of the factor $\kappa_L \rho / |Q|$ is small within the whole resonance zone contributing to the optical depth in Eq. 4.19, i.e., small on length scales at least a few times the Sobolev length $L \equiv v_t / |Q|$. However, also in the Sobolev approximation more than one resonance point may be identified in a wind with a non-monotonic velocity field.

Re-emission. We assume complete redistribution and isotropic re-emission in the CMF, allowing for a multitude of scattering events within one resonance zone. When the Sobolev approximation is applied, re-emission is assumed to be coherent in the CMF and for the angular re-distribution we then use the corresponding escape probabilities (Castor, 1970), corrected for a treatment of negative

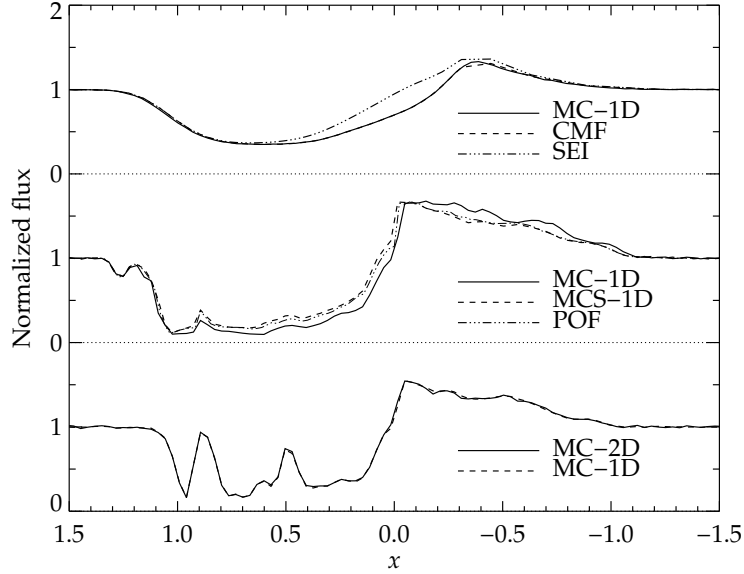


Figure 4.14: Synthetic line profiles for spherically symmetric models, calculated with the labeled methods. Profiles are shown for a smooth model with $\kappa_0 = 1.0$ and $v_t = 0.2$ (upper) and for two POF snapshots with $\kappa_0 = 100$ (middle) and $\kappa_0 = 5.0$ (lower) and $v_t = 0.005$. The 2D profile is for an observer at the equator. x is the normalized observer's frame frequency (see Eq. 4.18), and the ordinate displays the emergent flux normalized to the continuum flux.

velocity gradients (Rybicki & Hummer 1978; POF). In this case, there is only one effective scattering event inside the localized resonance zone.

After the photon has been re-emitted at some atmospheric location, the procedure runs again and searches for another absorption.

4.9.2 Radiative transfer code tests

In this subsection we describe some of the verification tests of our MC radiative transfer code that we have made. The MC-1D version was first applied on spherically symmetric winds, comparing profiles from smooth, stationary winds to profiles calculated using the well-established CMF (cf. Mihalas et al. 1975; Hamann 1981) and SEI methods, and profiles from time-dependent RH winds to profiles calculated using the Sobolev method developed in POF. Thereafter we applied the MC-2D version on models in which all lateral slices had the same radial structure, comparing the results to the MC-1D version.

First we calculated line profiles for smooth, 1D winds. We have verified that for low⁹ values of v_t , profiles from all the methods described above agree perfectly, whereas for higher values the MC-1D and CMF give identical results but the SEI deviates significantly, especially for a medium-strong line (see Fig. 4.14, upper panel). This is due to the hybrid nature of the SEI technique, which approximates the source function with its local Sobolev value but carries out the exact formal integral. Because of this, the method does not account for the increasing amount of photons close to line center that

⁹ For a typical terminal velocity value $v_\infty = 2000 \text{ km s}^{-1}$, $v_t = 0.005$ corresponds to 10 km s^{-1} and $v_t = 0.2$ to 400 km s^{-1} .

are backscattered into the photosphere when the resonance zone grows and overlaps with the lower boundary.¹⁰ Consequently the re-emitted flux in this region is higher when calculated via the SEI than when calculated via the CMF or MC methods. These discrepancies between the CMF and SEI are quite well documented and discussed (e.g., Hamann, 1981; Lamers et al., 1987), however we still emphasize that one should exercise caution when applying the SEI method with high microturbulence on wind resonance lines. Especially today, when increased computer-power enables us to compute fast solutions using both methods, the CMF is preferable.

Next we calculated line profiles for structured, 1D winds. Profiles computed with all three methods agreed for weak and intermediate lines. For strong lines, the agreement between MCS-1D and the method from POF, which uses a Sobolev source function accounting for multiple-resonance points, was satisfactory. However, minor discrepancies between Sobolev and non-Sobolev treatments occurred for the strong line also when no microturbulent velocity was applied (see Fig. 4.14), as opposed to the smooth case.

Finally we performed a simple test of our MC-2D code by applying it on models in which all lateral slices had the same radial structure, i.e., the wind was still spherically symmetric and all observers ought to see the same spectrum. We confirmed that indeed so was the case, both for smooth and structured models (in Fig. 4.14 the latter case is demonstrated).

4.10 The effective escape ratio

We define the ratio of the velocity gap Δv between two clumps (see Fig. 4.6 in the main paper) and the thermal velocity v_t as

$$\eta \equiv \frac{\Delta v}{v_t} \quad (4.21)$$

In the following, we derive an expression for η , for the wind geometry used throughout this paper. If $\Delta v_{\text{tot}} = \Delta v + |\delta v|$ is the velocity difference between two clump *centers*, we may write (omitting the absolute value signs here and in the following)

$$\Delta v = \Delta v_{\text{tot}} - \delta v = \frac{\Delta v_{\text{tot}}}{\Delta v_{\text{tot,fi}}} \Delta v_{\text{tot,fi}} - \frac{\delta v}{\delta v_{\beta}} \delta v_{\beta}, \quad (4.22)$$

where we have normalized the arbitrary velocity intervals to the corresponding β intervals. β suffixes are used to denote parameters of a smooth velocity law. For notational simplicity we write

$$\xi_1 = \frac{\Delta v_{\text{tot}}}{\Delta v_{\text{tot,fi}}}, \quad \xi_2 = \frac{\delta v}{\delta v_{\beta}}. \quad (4.23)$$

Assuming radial photons, Δv may be approximated by

$$\Delta v \approx \frac{\partial v_{\beta}}{\partial r} \Delta r_{\text{tot,fi}} \left(\xi_1 - \xi_2 \frac{\delta r_{\beta}}{\Delta r_{\text{tot},\beta}} \right), \quad (4.24)$$

¹⁰Remember that neither the SEI nor the CMF, as formulated here, include a transition to the photosphere, but treat the lower boundary as sharp with a minimum velocity v_{min} .

with the notations of r following those of v . The volume filling factor for the geometry in use is

$$f_v \equiv \frac{V_{\text{cl}}}{V_{\text{tot}}} \approx \frac{r_1^2 \delta r}{r_2^2 \Delta r_{\text{tot}}} \quad (4.25)$$

with V_{cl} the volume of the clump, V_{tot} the total volume, and $r_1 \approx r_2$ the radial points associated with the beginning of the clump and the ICM. Using Eq. 4.25 and $\Delta r_{\text{tot}} = v_\beta \delta t$ (see Sect. 4.3.2), we obtain

$$\Delta v \approx \frac{\partial v_\beta}{\partial r} v_\beta \delta t (\xi_1 - \xi_2 f_v), \quad (4.26)$$

and for η , using the radial Sobolev length of a smooth flow $L_r = v_t / (\partial v_\beta / \partial r)$,

$$\eta \approx \frac{v_\beta \delta t (\xi_1 - \xi_2 f_v)}{L_r}. \quad (4.27)$$

In our models ξ_1 is not given explicitly, but is on the order of unity, because we distribute clumps according to the underlying smooth $\beta = 1$ velocity law. Thus we approximate

$$\eta \approx \frac{v_\beta \delta t (1 - \xi_2 f_v)}{L_r}. \quad (4.28)$$

We notice that the porosity length h as defined by Owocki et al. (2004) is $h = l / f_v$, where l is the length associated with the clump. For the geometry used here this becomes $h \approx \delta r / f_v \approx v_\beta \delta t$. Hence, using $\xi_2 = 1$ for a smooth velocity field, η represents the porosity length corrected for the finite size of the clump, and divided by the radial Sobolev length.

Chapter 5

Mass loss from inhomogeneous hot star winds

II. Constraints from a combined optical/UV study

This chapter is a copy of Sundqvist, Puls, Feldmeier, & Owocki (2010), submitted to *Astronomy & Astrophysics (A&A)* in September 2010. Due to comments and suggestions by the referee is the version presented here slightly different from the version finally published in *A&A*. Also in this chapter is the original appendix added at the end as a normal section (Sect. 5.9).

5.1 Abstract

Mass loss is essential for massive star evolution, and thereby also for the variety of astrophysical applications relying on its predictions. However, mass-loss rates currently in use for hot, massive stars have recently been seriously questioned, mainly because of the effects of *wind clumping*. We investigate the impact of clumping on diagnostic ultra-violet resonance and optical recombination lines often used to derive empirical mass-loss rates of hot stars. Optically thick clumps, a non-void inter-clump medium, and a non-monotonic velocity field are all accounted for in one single model. The line formation is first theoretically studied, after which an exemplary multi-diagnostic study of an O-supergiant is performed. We use 2D and 3D stochastic and radiation-hydrodynamic wind models, constructed by assembling 1D snapshots in radially independent slices. To compute synthetic spectra, we develop and use detailed radiative transfer codes, for both recombination lines (solving the ‘formal integral’) and resonance lines (using a Monte-Carlo approach). In addition, we propose an analytic method to model these lines in clumpy winds, which does not rely on optically thin clumping.

The importance of the ‘vorosity’ effect for line formation in clumpy winds is emphasized. Resonance lines are generally more affected by optically thick clumping than recombination lines. Synthetic spectra calculated directly from present-day, radiation-hydrodynamic wind models of the line-driven instability are unable to reproduce strategic optical and ultra-violet lines in the Galactic O-supergiant λ Cep. Using our stochastic wind models, we obtain consistent fits essentially by increasing the clumping in the inner wind. A mass-loss rate is derived that is approximately two times lower than what is predicted by the line-driven wind theory, but much higher than the corresponding rate derived when assuming optically thin clumps. Our analytic formulation for line formation is used to demon-

strate the potential importance of optically thick clumping in diagnostic lines in so-called weak wind stars, and to confirm recent results that resonance doublets may be used as tracers of wind structure and optically thick clumping.

We confirm earlier results that a re-investigation of the structures in the inner wind predicted by line-driven instability simulations is needed. Our derived mass-loss rate for λ Cep suggests that only moderate reductions of current mass-loss predictions for OB-stars are necessary, but nevertheless prompts investigations on feedback effects from optically thick clumping on steady-state, NLTE wind models used for quantitative spectroscopy.

5.2 Introduction

Massive stars are fundamental in many fields of modern astrophysics. In the present Universe, they dynamically and chemically shape their surroundings and the inter-stellar medium by their output of ionizing radiation, energy and momentum, and nuclear processed material. In the distant Universe, they dominate the ultra-violet (UV) light from young Galaxies. Indeed, massive stars may be regarded as ‘cosmic engines’ (Bresolin et al., 2008). Hot, massive stars possess strong and powerful winds that affect evolutionary time scales, chemical surface abundances, and luminosities. In fact, changing the mass-loss rates of massive stars by only a factor of two has a dramatic effect on their overall evolution (Meynet et al., 1994). The winds from these stars are described by the radiative line-driven wind theory, in which the standard model (based on the pioneering works by Lucy & Solomon, 1970; Castor et al., 1975) assumes the wind to be stationary, spherically symmetric, and homogeneous. Despite this theory’s apparent success (e.g., Vink et al., 2000), theoretical as well as observational evidence for an inhomogeneous, time-dependent wind has over the past years become overwhelming (for a comprehensive summary, see Puls et al., 2008b).

Direct simulations of the time-dependent wind have confirmed that the so-called line-driven instability causes a highly structured wind in both density and velocity (Owocki et al., 1988; Feldmeier, 1995; Dessart & Owocki, 2005). Much indirect evidence of such *small-scale inhomogeneities* (clumping) has arisen from quantitative spectroscopy. Clumping has severe consequences for the interpretation of observed spectra, with the inferred mass-loss rates particularly affected. When deriving mass-loss rates from observations, wind clumping has traditionally been accounted for by assuming *optically thin* clumps and a void inter-clump medium, while keeping a smooth velocity field. Results based on this *microclumping* approach have, for example, led to a downward revision of empirical mass-loss rates from Wolf-Rayet (WR) stars by roughly a factor of three (reviewed in Crowther, 2007).

However, for O stars, highly clumped winds with very low mass-loss rates must be invoked in order to reconcile investigations of different diagnostics within the microclumping model. The most alarming example was the phosphorus v (Pv) UV analysis by Fullerton et al. (2006), which indicated reductions of previously accepted values by an order of magnitude (or even more), with dwarfs, giants, and supergiants all affected (but see also Waldron & Cassinelli 2010, who argued that XUV radiation could seriously alter the ionization fractions of Pv). Such low mass-loss rates would be in stark contrast with the predictions of line-driven wind theory, and have dramatic consequences for the evolution of, and feedback from, massive stars. Naturally, the widely discrepant values inferred from different observations and diagnostics drastically lower the reliability of mass-loss rates currently in use, and an explanation is urgently needed. A key question is: Does the microclumping model fail to deliver accurate empirical rates under certain conditions?

Simplified techniques to account for optically thick clumps in X-ray line formation have been developed (Feldmeier et al., 2003; Owocki et al., 2004), but it has yet to be settled whether or not this is important to consider when deriving empirical mass-loss rates from these diagnostics (Oskinova et al., 2006; Cohen et al., 2010). First attempts to relax the assumptions of the microclumping model for UV resonance lines were made by Oskinova et al. (2007) (optically thick clumps), Zsargó et al. (2008) (a non-void inter-clump medium), and Owocki (2008) (a non-monotonic velocity field). Sundqvist et al. (2010) (hereafter Paper I) carried out the first detailed investigation, relaxing *all* the above assumptions, and showed that, indeed, the microclumping approximation is not a suitable assumption for UV resonance line formation under conditions prevailing in typical OB-star winds. Recently, these results were empirically supported for the case of B supergiants by Prinja & Massa (2010), who analyzed profile-strength ratios of the individual components of resonance line doublets and found that the observed ratios were inconsistent with lines formed in a smooth or ‘microclumped’ wind. Furthermore, Paper I demonstrated that resonance line profiles calculated from 2D, stochastic wind models were compatible with mass-loss rates an order of magnitude higher than those derived from the same lines but using the microclumping technique. However, as pointed out in that paper, a consistent modeling of the resonance lines also introduces degeneracies among the parameters used to define the wind structure, degeneracies that can only be broken by considering different diagnostics (depending on different parameters) in parallel.

Here we make a first attempt toward such multi-diagnostic studies. We extend our 2D wind models from Paper I to 3D, and relax the microclumping approximation also for the optical mass loss diagnostics H_α and He II 4686 Å (Sect. 5.3). In Sect. 5.4 we theoretically investigate H_α and resonance line formation in clumpy winds, and propose an analytic treatment of the lines that does not rely on the microclumping approximation. A simultaneous optical and UV diagnostic analysis is carried out in Sect. 5.5 for the Galactic O6 supergiant λ Cep, using time-dependent radiation-hydrodynamic (RH) models as well as stochastic ones together with our new tools for the radiative transfer in clumped winds. These results are discussed in Sect. 5.6, while two initial applications of our analytic formulation are given in Sect. 5.7. We summarize the paper and outline future work in Sect. 5.8.

5.3 Wind models and radiative transfer

We create 2D and 3D RH and stochastic wind models by assembling snapshots in radially independent wind slices. A time-dependent RH model with parameters as given in Table 5.1 has been computed following Feldmeier et al. (1997). Stellar and wind parameters are taken from Repolust et al. (2004), except for the mass-loss rate (see Sect. 5.5). Basic assumptions of our structured stochastic winds were described in detail in Paper I. For resonance lines we use the Monte-Carlo code described in Paper I, but a new radiative transfer code has been developed for the synthesis of wind recombination lines presented here.

We investigate the O star recombination lines H_α and He II 4686. Recall that recombination lines and resonance lines are formed differently. First, the optical depths are calculated in different ways. For resonance lines, the optical depths may be computed via a line-strength parameter, κ_0 , and $\tau \propto \kappa_0$. κ_0 is assumed to be constant throughout the wind and is proportional to the product of the mass-loss rate and the abundance of the considered ion (Paper I). For H_α , the analog to κ_0 is the parameter A (Puls et al., 1996, Eqs. 1-3), and $\tau \propto A$. A is proportional to the mass-loss rate *squared* and to the NLTE departure coefficient, b_i , of the lower transition level (minus the correction factor for stimulated

Table 5.1: Parameters for the time-dependent RH model of λ Cep (see text).

Name	Parameter	Value
Spectral type		O6 I(n) fp
Effective temperature	T_{eff}	36 000 K
Stellar radius	R_*	$21.1 R_{\odot}$
Stellar luminosity	$\log L/L_{\odot}$	5.83
Terminal speed	v_{∞}	2200 km s^{-1}
Mass-loss rate	\dot{M}	$1.5 \times 10^{-6} M_{\odot}/\text{yr}$
Helium abundance	$n_{\text{He}}/n_{\text{H}}$	0.1
Projected rotation velocity	$v \sin i$	220 km s^{-1}
CAK exponent	α	0.7
Initial Langevin turbulence fluctuation	$v_{\text{turb}}/v_{\text{sound}}$	0.5

emission). $b_i = n_i/n_i^*$, where n_i^* is the occupation number of level i in LTE with respect to the ground state of the next ionization state. In addition to their different optical depths, recombination lines are (mainly) formed by recombining ions creating wind photons, whereas resonance lines are formed by re-distributing photospheric stellar continuum radiation by line scattering. That is, the line source function $S_l \propto (e^{h\nu/kT} b_l/b_u - 1)^{-1}$ for recombination lines is basically unaffected by the radiation field and its dilution. Therefore, the participating atomic levels for these lines are rather close to LTE with respect to the next ionization state (see Fig. 5.5), which allows us to prescribe the source functions (Puls et al., 1996, 2006) and simply carry out the ‘formal integrals’ within our stochastic and RH winds. In the following, we simply *assume* that changes in the NLTE departure coefficients due to optically thick clumps can be neglected for recombination-based line formation. Taking the example of H_{α} in O stars, this assumption should be reasonable, for the H_{α} departure coefficients in this domain are very close to unity and the ionization of hydrogen is complete. However, for the case of, e.g., A-supergiants, the assumption no longer holds, because in that stellar domain H_{α} ’s lower level becomes the effective ground state of hydrogen, which means that the line transforms to a quasi-resonance line (and thereby that S_l depends on the radiation field, Puls et al. 1998). The potential feedback effects of optically thick clumping on the departure coefficients will be investigated by incorporating the analytic methods developed in Sect. 5.4 into suitable NLTE atmosphere codes, which will be reported in a future paper.

The assumption of prescribed departure coefficients is an enormous simplification compared to the UV resonance lines, and has enabled us to extend our 2D wind models to 3D when modeling recombination lines. In the synthesis we follow the basic method introduced by Puls et al. (1996), with appropriate modifications for the line opacities of He II 4686. A core/halo approach is adopted, in which a photospheric profile is used as a lower boundary input (at $r = 1$, with r in units of the stellar radius) and the radiative transfer is solved only in the wind.

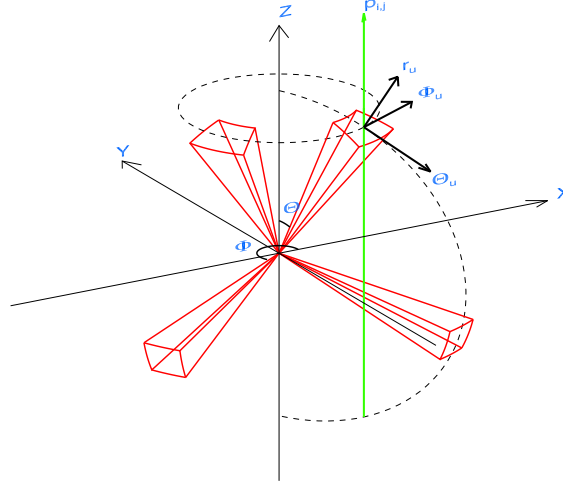


Figure 5.1: Illustration of the wind geometry, see text. A color version of this figure is available in the web-version.

5.3.1 Geometry

To construct (pseudo-)3D winds, we use the ‘patch-method’ from Dessart & Owocki (2002). A standard right-handed spherical system (r, Θ, Φ) is used, defined relative to a Cartesian set (X, Y, Z) . However, we no longer assume symmetry in the azimuthal (Φ) direction (as was done in Paper I). The lateral scale of coherence in the wind is set by the parameter N_Θ and by assuming that the physical coherence lengths in both lateral directions are approximately equal. This assumption is reasonable because, within our approach, which for example does not include an axis of rotation, all observer directions should be alike. Thus, if we desire a coherence scale of 3 degrees, the number of slices in the polar direction should be $N_\Theta = 180/3 = 60$ and in the azimuthal direction $N_\Phi = \text{int}[2N_\Theta \sin \Theta]$, i.e., $2N_\Theta$ at the equator but fewer toward the pole in order to preserve the *physical* length scales. Wind slices are then assigned randomly from a large number of spherically symmetric simulations (either RH or stochastic).

The observer is assumed to be located at infinity in the Z_u (subscript u denoting a unit vector) direction. The geometry is sketched in Fig. 5.1. We solve the radiative transfer using a traditional (P, Z) system for a set of P rays, each defined by the minimum radial distance to the Z axis and by the azimuthal angle Φ , which is constant along a given ray. If the angle between the ray and the radial coordinate is θ , then $\mu = \cos \theta$ and $P = r\sqrt{1 - \mu^2}$. Thus, for rays in direction Z_u the radiation angle θ coincides with the polar coordinate Θ , and it becomes trivial to calculate the physical locations at which wind-slice borders are crossed. The observed flux may then finally be computed by performing a double integral of the emergent intensity over P and Φ .

Table 5.2: Basic structure parameters defining a stochastic wind model.

Name	Parameter
Clumping factor ^a	f_{cl}
Average time interval between release of clumps	δt
Inter-clump medium density parameter	x_{ic}
Velocity span of clump	δv

^a f_{cl} may be replaced by the volume filling factor f_v .
 The two are related via x_{ic} (see Paper I).

5.3.2 Parameters describing a structured wind

When creating our *stochastic* wind models, we take an heuristic approach and use a set of parameters to define the structured medium. The clumping factor $f_{\text{cl}}(r) \equiv \langle \rho^2 \rangle / \langle \rho \rangle^2$, with the angle brackets denoting spatially averaged quantities, is the only necessary structure parameter when calculating spectra via the microclumping technique. Microclumping gives rise to the well known result that the opacities for processes that depend on the square of the density (for example $\text{H}\alpha$ emission in OB-stars) are augmented by f_{cl} as compared to a smooth model with the same mass-loss rate; in contrast, opacities for processes that depend linearly on the density (for example the UV resonance lines) are not directly affected. Thus, if the wind is clumped, mass-loss rates derived from smooth models applied to $\text{H}\alpha$ are overestimated by a factor of $\sqrt{f_{\text{cl}}}$. In addition, the occupation numbers are modified for all diagnostics because of the changed rates in the statistical equilibrium equations. For a comprehensive discussion on the effects of microclumping on various diagnostics, see Puls et al. (2008b).

If the assumptions behind the microclumping model are not satisfied (e.g. if clumps are optically thick for the investigated diagnostic), the line formation will depend on more structure parameters than just f_{cl} . Thus, relaxing the microclumping approximation means that we must consider additional parameters when describing the structured wind. These parameters (for a two component medium) were defined and discussed in Paper I, and are listed in Table 5.2. We stress that they are essential for the radiative transfer in an inhomogeneous medium, and not merely ‘ad-hoc parameters’ used in a fitting procedure.

In addition to the clumping factor f_{cl} (or alternatively f_v), $x_{\text{ic}} \equiv \rho_{\text{ic}} / \rho_{\text{cl}}$ denotes the density ratio of the interclump (ic) to clumped (cl) medium. The time interval δt (given in units of the wind’s dynamic time scale and not necessarily constant throughout the wind) effectively sets the physical distances between clumps, also known as the porosity length h (Owocki et al., 2004), which in our geometry is given by $h = v_\beta \delta t$. Moreover, assuming a smooth underlying field of customary β -type, $v_\beta(r) = v_\infty(1 - b/r)^\beta$ with b set by the assumed velocity at the wind base $v_{\text{min}} = v(r = 1)$, this time interval sets the *velocity separation* between the clumps $\Delta v \approx v_\beta \delta t dv_\beta / dr$ (see Sect. 5.9). Finally, the ratio of the clump velocity span δv to this velocity separation (representing a *velocity filling factor*; see Sect. 5.9) largely controls how strongly a perturbed velocity field affects line formation¹. In addition to these basic parameters, the radius r_{cl} at which clumping is assumed to start also plays an important role for the line formation. Note also that the parameters defining these stochastic winds

¹ In this paper, we do not consider the ‘jump velocity parameter’, defined in Paper I, since it was shown there that this parameter mainly influences the formation of very strong saturated lines, which are not considered here.

are independent of the origin to the inhomogeneities.

The stochastic models should be distinguished from the time-dependent RH simulations; in the latter the structure arises naturally from following the time evolution of the wind and stems directly from the line-driven instability. Thus, the time-averaged structure parameters, as functions of radius, are an *outcome* of these simulations (in contrast to the stochastic models, where they are used as fundamental parameters defining the structured wind). Nonetheless, the exact wind structure still depends on the chosen initial conditions, for example on whether the instability is self-excited or triggered by some excitation mechanism (the latter is done here, see Table 5.1). Finally, as shown in Paper I, by choosing a suitable set of structure parameters one can reconcile spectrum synthesis results stemming from the stochastic models with those from RH simulations.

In addition to the structure parameters, N_θ enters all our models. Paper I showed that this parameter does not change the strengths of the resonance lines. More tests have shown that also the effects on recombination lines are modest for investigated values. Therefore all 3D models in this paper assume $N_\theta = 60$, meaning a coherence length of 3 degrees at the equator, which is consistent with observational constraints derived from line-profile variability analysis (Dessart & Owocki, 2002). Theoretical constraints on N_θ are still lacking, and will require a careful treatment of the lateral radiation transport in RH models; the first 2D simulations by Dessart & Owocki (2003) neglected this transport and resulted in a laterally fragmented wind down to the grid scale but the follow-up study (Dessart & Owocki, 2005) included a simplified 3-ray approach and resulted in larger (but un-quantified) lateral coherence scales.

5.3.3 Code verifications

The recombination line code has been extensively tested and showed to yield equivalent results with Puls et al. (2006) for smooth winds. Also, results based on the microclumping technique are reproduced for stochastic as well as RH winds with low wind densities, as expected because the clumps then remain optically thin. In our applications, we use hydrogen and helium occupation numbers calculated by FASTWIND model atmospheres (Puls et al., 2005), under the microclumping approximation, as input for the radiative transfer to compute synthetic spectra. Photospheric profiles are taken from NLTE calculations of atmospheres with negligible winds. The consistency between unified (meaning a simultaneous treatment of the photosphere and wind) model atmosphere calculations and the simplified core/halo approach has been verified in the microclumping limit, for recombination lines as well as for resonance lines. Moreover, we have found that averaged recombination line profiles calculated from our earlier 2D, stochastic models are almost identical to those calculated from our new 3D ones, as was already anticipated for the UV resonance lines in Paper I.

The He II blend in H_α . The star's helium abundance has of course been considered in the calculation of the H_α wind opacity, but for simplicity we include the He II blend only in the photospheric profile, thus neglecting its direct contribution to the wind emission. This results in a slight underestimate of the total wind opacity of the line complex. However, by comparing to unified model atmosphere calculations that consistently treat the He II blend, we have found that the direct helium contribution is low for our typical stars of interest; in our applications for λ Cep it can even be neglected. Although sufficient for our purposes here, this approach should obviously not be generalized; it may yield unrealistic results for stars with parameters different from our template star.

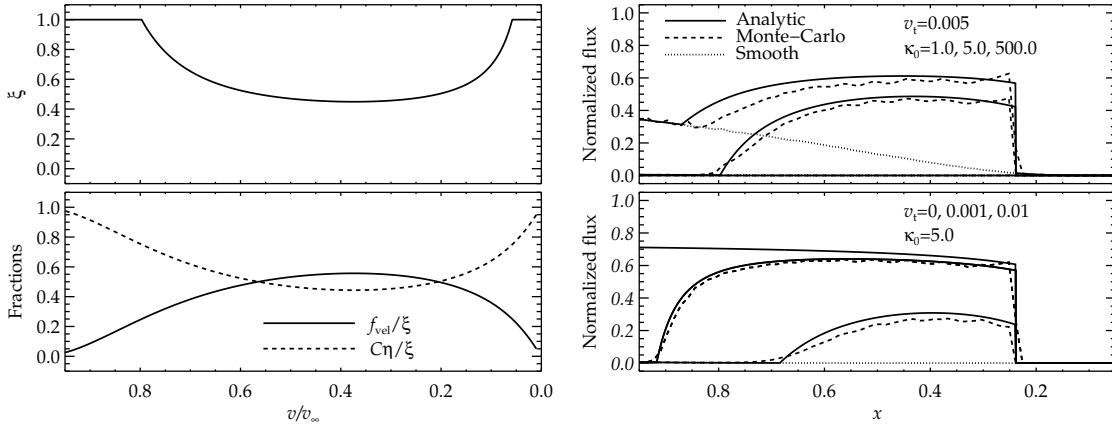


Figure 5.2: Panels a-d from top to bottom. *Panel a*: ξ (Eq. 5.2) as a function of wind velocity. *Panel b*: The relative contributions to ξ from f_{vel} and $C\eta$. Curves in panels a and b have been calculated with $\kappa_0 = 5$ and $v_t = 0.005$ (in units of v_∞). *Panels c and d*: Analytic (Eq. 5.1, solid lines) and Monte-Carlo (dashed lines) based absorption part resonance line profiles from clumped winds, as compared to smooth results (dotted lines). Clumping starts at $r = 1.3$. *Panel c*: Profiles for three different values of the line-strength κ_0 (indicated in the figure), with increased absorption for higher values of κ_0 . Only the $\kappa_0 = 1$ profile is not saturated for smooth models. *Panel d*: Profiles for $\kappa_0 = 5$ and two (Monte-Carlo) and three (analytic) different values of the thermal velocity v_t (values indicated in the figure), with increased absorption for higher values of v_t .

5.4 Theoretical considerations of resonance and recombination line formation in clumpy winds

Resonance line formation in clumpy hot star winds was discussed in detail in Paper I. There we identified an intrinsic coupling between the effects of porosity and vorosity (=‘velocity porosity’, Owocki, 2008), which we here further elaborate upon. In particular, we propose an analytic formulation of line formation in clumped hot star winds (that does not rely on the microclumping approximation). As already mentioned in Sect. 5.3, the development of such simplified approaches is important for properly including effects of optically thick clumping into atmospheric NLTE codes. For recombination lines, we focus on H_α and discuss impacts from optically thick clumping on its formation, using our stochastic wind models as well as an extension of the analytic treatment developed for the resonance lines.

5.4.1 Analytic treatment of resonance lines in clumpy winds

Throughout this subsection we assume a *smooth velocity field*. Despite this, the vorosity effect will be demonstrated to be important for the line formation (i.e., a non-monotonic velocity field is not required for vorosity to be at work). Following the basic arguments of Owocki (2008), we write the normalized absorption resonance line profile $R_{a,x}$ at frequency x from a radial ray as (see Sect. 5.9)

$$R_{a,x} = \xi_x e^{-\tau_{\text{cl},x}} + (1 - \xi_x) e^{-\tau_{\text{ic},x}}. \quad (5.1)$$

This expression describes the part of the profile that stems from absorption of continuum photons released from the photosphere. The *total* line profile is given by $R_x = R_{a,x} + R_{em,x}$, where $R_{em,x}$ is the re-emission profile, and is in this case the result of line photons escaping the wind after having been scattered. Recall, however, that $R_{a,x}$ controls the actual line-profile strengths of resonance lines, because these are pure scattering lines formed out of re-distributed continuum radiation emerging from the photosphere.

In Eq. 5.1 we define ξ as the *fraction of the velocity field over which photons may be absorbed by clumps*, with the τ 's representing the Sobolev optical depth for the clumped (subscript cl) and rarefied (subscript ic) regions. ξ describes the essential effects of Owocki's vorosity; the first term in Eq. 5.1 handles the part of the line profile emerging from absorption within the clumps, whereas the second term handles the part emerging from absorption within the inter-clump medium. What remains then is finding an appropriate expression for ξ . In Sect. 5.9 we argue that a reasonable approximation may be

$$\xi \approx \frac{\delta v}{\Delta v} + C \frac{v_t}{\Delta v} = f_{vel} + C\eta, \quad (5.2)$$

with Δv the velocity gap between two clump centers, f_{vel} the *velocity filling factor* (defined in full analogy with the traditional volume filling factor), η the *effective escape ratio* (here re-defined from Paper I, see Sect. 5.9), and C a correction factor that depends on the line strength. All radial dependencies in Eq. 5.2 are suppressed for simplicity. As shown in Sect. 5.9, we may write

$$f_{vel} = f_v \frac{\delta v}{\delta v_\beta}, \quad \eta = \frac{L}{h}, \quad (5.3)$$

where h is the porosity length of the medium and L the (in this case radial) Sobolev length. For the smooth velocity field considered in this subsection, $\delta v = \delta v_\beta$, which gives $f_{vel} = f_v$. Even though the principle effect of the optically thick clumps on resonance line formation is a velocity effect governed by f_{vel} , Eqs. 5.1-5.3 indicate there is also a dependence on spatial porosity through the ratio $\eta = L/h$. This coupling was argued for already in Paper I. However, it appears that ξ better characterizes the effects of clumping in resonance line formation than did our previous parametrization (see Sect. 5.9). We note also that all parameters used to define our stochastic wind models (Table 5.3.2) enter the expression for $R_{a,x}$, illustrating that indeed all these are important for the general line formation problem.

The upper two panels of Fig. 5.2 plot ξ as well as the relative contributions from f_{vel} and $C\eta$ for a resonance line with line-strength parameter $\kappa_0 = 5$. For a smooth model (with ionization fraction $q = 1$, assumed in this section), $\kappa_0 = 5$ results in a profile at the saturation threshold. In the lower two panels of Fig. 5.2 we show analytic absorption line profiles calculated using Eq. 5.1 and profiles calculated using our Monte-Carlo code. To make consistent comparisons between methods, we accounted only for radial photons in the Monte-Carlo simulations. Assigned density structure parameters were $f_{cl} = 4.0$, $\delta t = 0.5$, and $x_{ic} = 0.0025$. The agreement between the methods is very good, lending support to the proposed analytic treatment and providing a relatively simple explanation for the basic features of the synthetic profiles.

Evidently profile-strength reductions can be quite dramatic for 'moderately strong' cases such as $\kappa_0 = 5$. For the very strong $\kappa_0 = 500$ line also the inter-clump medium is optically thick and the

profiles are therefore saturated (which is a necessity because such saturated profiles are observed in hot stars). Note that, if δv were much higher than Cv_t , one could neglect the second term in Eq. 5.2 and ξ would become independent of the porosity length. If one also neglects the inter-clump medium (setting $x_{ic}=0$), and assumes that clumps are optically thick throughout the entire wind (appropriate for the $\kappa_0 = 5$ line), then the observer in our example would simply receive a constant residual flux $R_{a,x} = 1 - f_v = 0.75$. Fig. 5.2 shows that this generally does not hold (even for the idealized case of zero thermal speed, the inter-clump medium still plays a role), demonstrating that, along with the velocity filling factor f_{vel} , in general both x_{ic} and η also help shape the emergent profile for a wide range of line strengths and structure parameters. Fig. 5.2 illustrates the importance of accounting for the finite line profile width. $C\eta$ may not be neglected, even in models with very low, but finite thermal velocity, and becomes particularly important toward the blue edge of the line profiles. This occurs because the resonance zones in the outermost wind become very radially extended. L thus grows whereas the distances between the clumps (determining h) are unaffected due to the very slowly changing velocity field. Consequently η becomes very high and ξ eventually reaches unity. Since the $\kappa_0 = 5.0$ line is optically thick, a ‘blue absorption dip’ (extensively discussed in Paper I) is created. Randomization effects are here neglected because we have used a smooth velocity field. When clumps are allowed to have velocities higher and lower than those given by the mean velocity field, overlapping velocity spans of the clumps lead to increased escape of photospheric photons. The blue absorption dip then becomes less prominent than what is displayed in Fig. 5.2, as discussed in Paper I (see also Sect. 5.9, for some comments on randomization effects).

Nevertheless, this subsection demonstrates that the microclumping approximation can result in large errors if indeed the wind is clumped but the clumps are not optically thin. First applications of the analytic formulation are given in Sect. 5.7, for diagnostics of *weak wind stars* and for the predicted profile-strength ratios in resonance line *doublets*.

5.4.2 Recombination lines in clumpy winds

We now leave the resonance lines behind and turn to the formation of recombination lines. We focus on H_α , the primary spectroscopic mass-loss diagnostic for O stars. He II 4686 reacts similarly as H_α to clumping in our primary stars of interest (because He III is the dominant ion in the line forming regions) and will be considered only in our diagnostic study of λ Cep (Sect. 5.5).

First we present results from calculating H_α line profiles using our stochastic 3D wind models. Our main interest is to investigate differences with respect to the microclumping model, so main results are provided in terms of the deviation of the equivalent widths W_λ between the two methods, $(W_{\lambda,mic} - W_\lambda)/W_{\lambda,mic}$, as a function of mass-loss rate (here $W_{\lambda,mic}$ denotes W_λ as calculated from a model assuming microclumping). All models discussed in this subsection were calculated with unity departure coefficients, wind electron and radiation temperatures as for approximately λ Cep (calibrated using unified NLTE model atmospheres, see Puls et al., 2006), and no input photospheric absorption profiles. We used structure parameters $f_{cl}=9.0$, $\delta t=0.5$, $x_{ic} = 0.0025$, and a smooth velocity field characterized by $\beta = 1$.

For typical O-supergiants, the equivalent widths of profiles calculated from stochastic models are slightly lower than those based on the microclumping technique. Deviations stem from optically thick clumps. The dominating effect is on the wind *emission* of H_α photons rather than on the wind absorption of photospheric photons (in contrast to resonance lines, see previous subsection). This is because the source function for recombination lines is basically unaffected by the dilution of the radi-

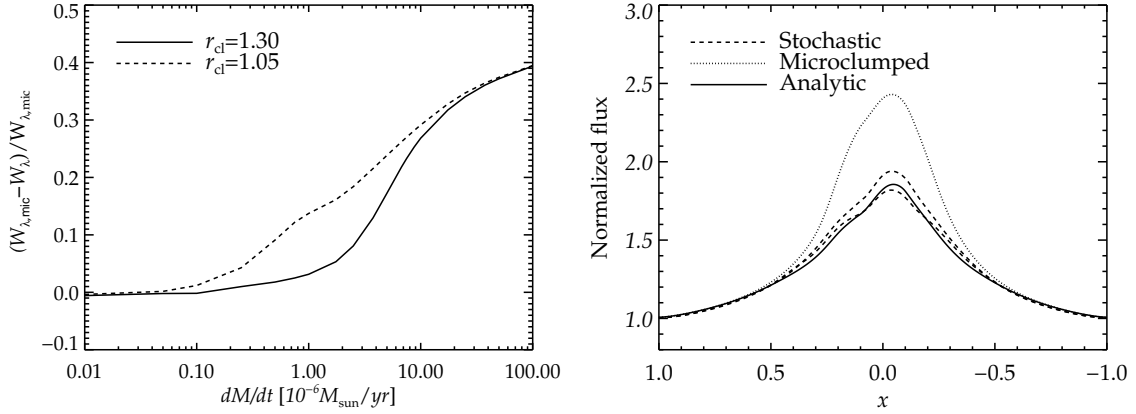


Figure 5.3: *Upper panel:* Deviations from the microclumping approximation of equivalent widths of synthetic H_α line profiles versus mass-loss rate (see text). Values of r_{cl} , the onset of clumping, as indicated in the figure. *Lower panel:* H_α line profiles as calculated by stochastic, analytic, and microclumped models with $f_{cl}=9$ and $\dot{M}=10 \times 10^{-6} M_\odot/\text{yr}$ and the rest of the stellar and wind parameters as for λ Cep. Clumping for all models starts at $r_{cl} = 1.3$. The dimensionless frequency x (see Sect. 5.9) is on the abscissa.

ation field, which for relatively strong and hot winds make these lines appear in emission and thereby suffer the main effect from a clumped wind on the emission part of the line profile. Moreover, the ρ^2 -dependence of recombination line-opacity increases the contrast between the optical depths for the clumps and those for the inter-clump medium, as compared to resonance line formation. This lowers the significance of the inter-clump medium and also causes the clump optical depths to decrease faster for increasing radii. The latter effect results in clumps that are optically thick only in the lower wind regions. Deviations from the microclumping limit are therefore more significant for cases with earlier onset of clumping. For example, the equivalent widths for the models with $\dot{M}=2.5 \times 10^{-6} M_\odot/\text{yr}$ are reduced by 7% and 17% when clumping starts at $r_{cl} = 1.3$ and $r_{cl} = 1.05$, respectively. The effect is thus modest, but noticeable. Note that reductions are measured against models assuming microclumping; the profiles are still much stronger than profiles computed from smooth models with the same mass-loss rate.

Our tests show that effects are confined to the line core and that the microclumping approximation provides accurate results in the line wings. However, Fig. 5.3 reveals prominent emission strength reductions for stronger winds, since then optical depth effects become important for ever larger portions of the total wind volume. Furthermore, the onset of clumping is irrelevant in these strong winds because the majority of the emission emerges from radii greater than r_{cl} . This insensitivity to the onset of clumping also recovers the scaling invariant for *microclumped* winds ($\propto \sqrt{f_{cl}}\dot{M}$, see Sect. 5.3.2). For typical OB-supergiants, this scaling does not hold because of the strong opacity contrast between wind radii lower than and greater than r_{cl} . Even though we for these strong winds have entered the WR regime, in which a reduced hydrogen content is expected (as well as a break-down of our assumption of an optically thin continuum), our analysis could, of course, be generalized to recombination lines of other chemical species (as has been done for He II 4686 in our application to λ Cep), and may point to significant optical depth effects in the strong emission peaks of stars with very high mass-loss rates. Indeed, lower emission peaks in the theoretical spectrum of a WR star were found by Oskinova et al.

Table 5.3: Structure parameters for an empirical stochastic wind model of λ Cep

Velocity range [v_β/v_∞]	f_{cl}	δt [t_{dyn}]	x_{ic}	$\delta v/\delta v_\beta$
$v_{min} - 0.15$	1.0		1.0	1.0
0.15 - 0.35	28.0	0.5	0.005	-5.0
0.35 - 0.60	14.0	0.5	0.0025	-5.0
0.60 - 0.95	14.0	3.0	0.0025	-5.0
0.95 - 1.0	4.0	3.0	0.0025	-5.0

(2007), on the basis of scaling smooth opacities using a porosity formalism. However, when deriving empirical mass-loss rates from microclumping models of WR stars one normally considers also the electron scattering wings (which are unaffected by microclumping, see Hillier, 1991), and because these probably are optically thin it may be that lower emission peaks would have a greater effect on the inferred clumping factors than on the mass-loss rates.

Analytic treatment of recombination lines. We can understand the reduction in H_α emission strengths using the same analytic treatment as outlined for resonance lines. Better yet, because the source function S is almost unaffected by the radiation field (see Sect. 5.3), we can for recombination lines simulate the total profile, $R_x = R_{a,x} + R_{em,x}$, writing

$$R_{em,x} = S\xi_x(1 - e^{-\tau_{cl,x}}) + S(1 - \xi_x)(1 - e^{-\tau_{ic,x}}). \quad (5.4)$$

$R_{em,x}$ is much more influenced by non-radial photons than is $R_{a,x}$, so accordingly the radial streaming assumption from the previous subsection must be relaxed here. Details are given in Sect. 5.9.

It was mentioned already in the previous paragraph that the ρ^2 -dependence of the line opacity lowers the significance of the inter-clump medium in recombination line formation. Actually, tests have shown that, in our typical stars of interest, the opacities in the inter-clump medium are so low that the second term in Eq. 5.4 can safely be neglected. The lower panel of Fig. 5.3 illustrates that profiles computed using the analytic approximation agree very well with those computed using our stochastic wind models.

5.5 A multi-diagnostic study of λ Cep

We have carried out a detailed study of the Galactic O6 supergiant λ Cep. This star was chosen in part to connect with Paper I and in part because it is a well observed and studied object, with significant mass loss, that appears to be less peculiar than, e.g., ζ Pup. A simultaneous investigation of optical diagnostics and the PV resonance lines is performed. The ionization fractions of PV and the hydrogen and helium departure coefficients (see Fig. 5.5) are calculated with the unified model atmosphere code FASTWIND, under the microclumping approximation and assuming the same clumping factors as in corresponding RH or stochastic models, with stellar and wind parameters as given in Table 5.1 and with a solar (Asplund et al., 2005) phosphorus abundance. Stellar rotation is treated by the standard convolution procedure of a constant $v \sin i$ (neglecting differential rotation). We use observed UV FUSE spectra from Fullerton et al. (2006), and optical spectra from Markova et al. (2005) and A. Herrero (described in Herrero et al., 2000). In addition to H_{ff} , He II 4686, and PV, we also consider the wind

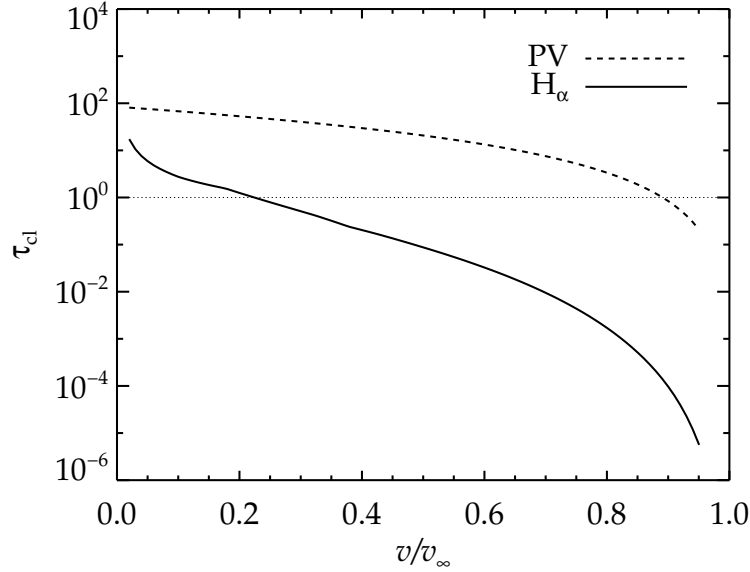


Figure 5.4: Radial clump optical depths for PV and H_α as functions of wind velocity.

sensitive cores of H_{β} and H_{γ} . However, for these diagnostics we rely entirely on the microclumping approximation, which because of their low wind optical depths should be sufficient.

5.5.1 Clump optical depths

The *clump optical depth* in the wind is the primary quantity governing the validity of the microclumping approximation. In Paper I we provided estimates of the clumps' radial *Sobolev* optical depths in resonance lines, estimates which may readily be modified to the case of H_α by following, e.g., Puls et al. (1996) (see also Sect. 5.4.2). However, clumps do not always cover a complete resonance zone, so the Sobolev optical depths must be replaced by optical depths calculated by including the actual line profile. Within our stochastic wind models, the radial extent of a clump is $l_r = v_\beta \delta t f_v$, and therefore, by transforming to the corresponding velocity width, we may calculate the 'actual' clump optical depth τ_{cl} .

Fig. 5.4 shows radial τ_{cl} for the mass-loss indicators H_α and PV in λ Cep, using constant structure parameters as for the inner clumped region given in Table 5.3. The figure shows that τ_{cl} is significantly higher for PV than for H_α and, moreover, that the only linear dependence on the density for resonance lines (as opposed to the quadratic dependence of recombination lines) causes clumps to remain optically thick in PV throughout almost the entire wind. Based only on these simple estimates, one might therefore expect that the basic results of Sect. 5.4 should hold in a diagnostic application of a typical O star. That is, H_α should be affected by optically thick clumping only in the line core, whereas resonance lines should be much more affected over the entire line profile.

5.5.2 Constraints from inhomogeneous radiation-hydrodynamic models

Fig. 5.6 displays line profiles calculated from our RH model of λ Cep. Consistent fits of the observed diagnostics are not achieved. The H_α line wings are reasonably well reproduced but the core emission

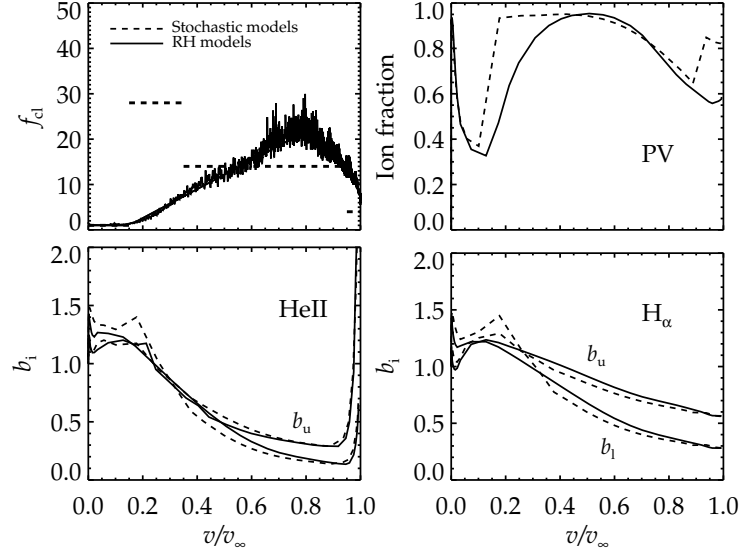


Figure 5.5: Clumping factors (*upper left*), PV ionization fractions (*upper right*), and He II 4686 and H α departure coefficients b_i (*lower left* and *lower right*, respectively) used in the RH and stochastic models of λ Cep. Mean wind velocities are on all abscissas.

is much too low. The PV profiles are, actually, better reproduced, although stronger than observed toward the blue edge of the line complex (the ‘blue edge absorption dip’ problem, see Sect. 5.4.1). The reasonable PV fits are due both to adopting a rather low mass-loss rate for λ Cep (see Table 5.1) and to lower velocity spans in these RH models than in those analyzed in Paper I². The mass-loss rate was essentially chosen from a best compromise when considering the complete diagnostic set.

The apparent mismatch between H α emission in the core and in the wings occurs because f_{cl} increases rather slowly with increasing velocity (Fig. 5.5), which for a given mass-loss rate implies that the optical depths in the H α core forming regions are too low as compared to the optical depths in the wing forming regions. He II 4686 is subject to the same mismatch as H α , and also the cores of H β and H γ are deeper than observed. The latter feature occurs because the photospheric absorption profiles are not sufficiently re-filled by emission from the only weakly clumped inner wind. Thus, the optical wind diagnostics all indicate that the clumping factor as a function of velocity in λ Cep differs from that predicted by the RH simulations (see also Puls et al., 2006; Bouret et al., 2008). On the other hand, any significant increase in the mass-loss rate to obtain a better fit of the higher Balmer lines and the core of H α would produce stronger than observed H α and He II 4686 line wings (as illustrated for H α in Fig. 5.6) and, vice versa, a reduction of the mass-loss rate to obtain a better fit of the (blue edge of the) PV lines would produce too weak wings.

Comparison with the microclumping technique. We now compare results from above with those from a microclumped FASTWIND model having the same (smoothed) clumping factors as the RH model. The PV profiles calculated using the FASTWIND model are stronger than those calculated using the RH model. We may characterize this difference by the difference in the equivalent widths W_λ of

² The exact reasons for the lower spans are still under investigation, and will be reported in a future paper.

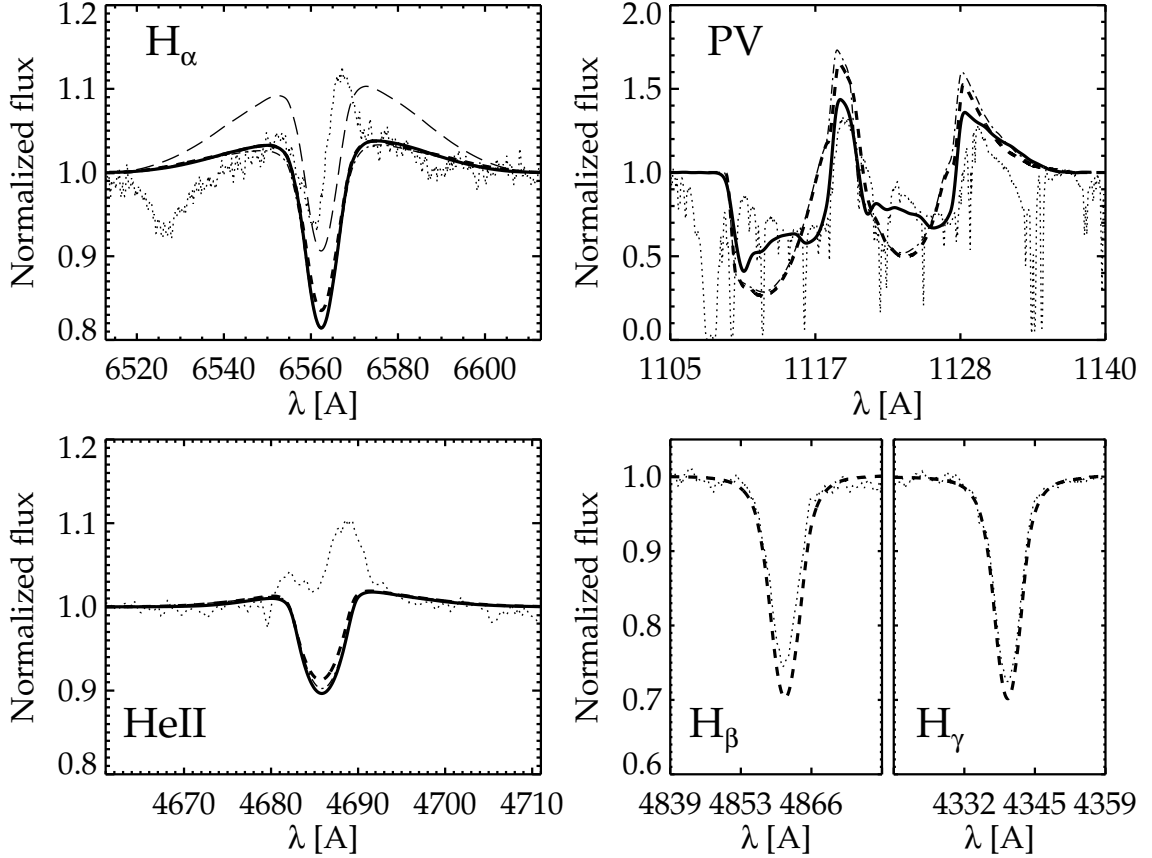


Figure 5.6: Observed and synthetic line profiles for λ Cep. *Dotted lines* are the observations. *Solid line* profiles are calculated from the inhomogeneous radiation-hydrodynamic model of λ Cep (Table 5.1), and *dashed lines* from a corresponding FASTWIND model including microclumping. The long-dashed line in the upper left panel is from a RH model in which the density has been scaled to mimic an increase in the mass-loss rate by 50%.

the absorption parts of the profiles. W_λ is roughly 15% lower for the RH model (see also Owocki, 2008). However, this moderate reduction in profile strength actually corresponds to a reduction in the mass-loss rate by a factor of approximately two, because of the resonance lines' slow response to mass loss.

Resonance line profiles stemming from the RH and microclumping models also display different line *shapes*. For RH models, significant velocity overlaps stemming from the non-monotonic velocity field ensure that the observed flux at the blue side of the line center is accurately reproduced without invoking any artificial and highly supersonic 'microturbulence', as must be done when using smooth as well as microclumping wind models. Although not analyzed here, also the absorption at velocities $>v_\infty$ of saturated resonance lines may be reproduced by RH models without invoking additional microturbulence (Puls et al., 1993, Paper I). For H_α and He II 4686, the RH and microclumping models yield almost identical results. This occurs because clumps are optically thin in these diagnostics

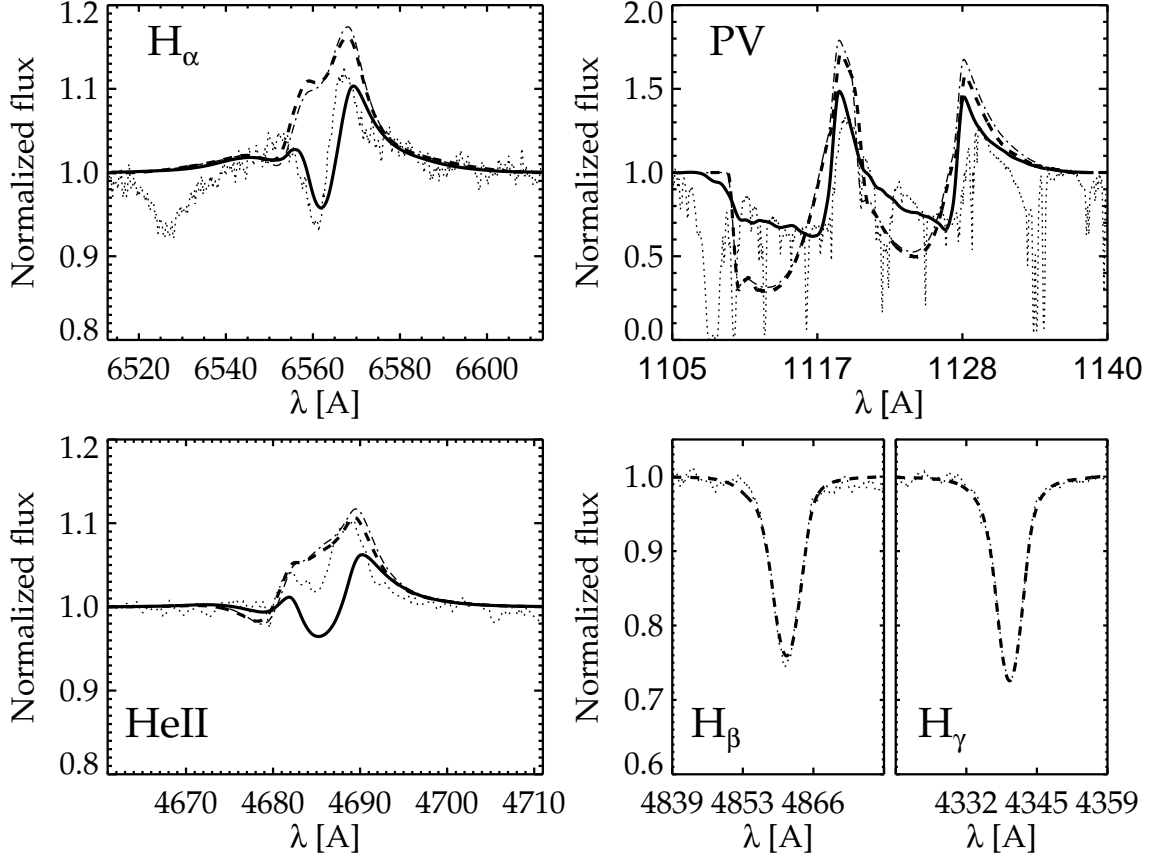


Figure 5.7: As Fig. 5.6, but using our stochastic models (solids) with corresponding inferred empirical structure parameters (see text). The assumed mass-loss rate is the same as for the RH model of λ Cep, see Table 5.1.

throughout almost the entire wind, due to the slow increase of f_{cl} with mean wind velocity, which in turn results in wind densities in the inner wind unable to produce optically thick clumps (compare to the empirical models in the following subsection).

5.5.3 Constraints from empirical stochastic models

Clearly, the RH models fail to deliver satisfactory line profiles when their structures are confronted with UV and optical wind diagnostics. Here we use our stochastic models to modify the wind-structure parameters and show how the results then may be reconciled. This is a first attempt toward our long-term aim of using consistent multi-diagnostic studies to obtain unique views of *empirical* mass-loss rates and structure properties of hot star winds.

The same mass-loss rate and terminal velocity as for the RH model of λ Cep is adopted (see Table 5.1). In the outermost wind, we for now adhere to the constraints on f_{cl} derived from radio emission by Puls et al. (2006), scaled with respect to the mass-loss rate derived here. In the inner wind, both the distinct

shape of H_α in λ Cep³ and the cores of the higher Balmer lines may be used as tracers of structure. The H_α absorption trough followed by the steep incline to rather strong emission can only be reproduced by our models if clumping is assumed to start quite late (see also Puls et al., 2006; Bouret et al., 2008), at a velocity marginally lower than predicted by the RH models, however with a much steeper increase with velocity (see Fig. 5.5). Also, in the particular case of λ Cep, the upper limit of the mass-loss rate derived by Puls et al. (2006) ($\dot{M}=3.0 \times 10^{-6} M_\odot/\text{yr}$, inferred by assuming a smooth outermost radio emitting wind) results in densities so high in the lowermost wind that the H_α trough never reaches below the continuum flux. Moreover, additional constraints come from the cores of the higher Balmer lines; the higher the densities in the lowermost wind, the stronger the re-filling of the photospheric absorption profile by wind emission. Here as well the upper limit from Puls et al. provides shallower than observed line cores. Thus, if we require $f_{\text{cl}}=1$ at the wind base, and if our interpretation of the abrupt shift from absorption to emission in H_α as due to clumping is correct, rather tight constraints on the mass-loss rate may be obtained using only optical diagnostics.

The H_α time-series of Markova et al. (2005) reveal that both the height of the emission peak and the depth of the absorption trough depend on the observational snapshot; variations can reach 0.04 in residual flux units. Therefore it is not critical that neither the peak nor the trough is perfectly reproduced by our models in Fig.5.7 (which displays a ‘representative’ observational snapshot). On the other hand, the observations do not indicate any significant variation in the *position* of the emission peak. This might be an issue; the late onset of clumping redshifts the emission peak too much (at least when neglecting differential rotation, see Sect. 5.6.1), whereas an earlier onset of clumping fails to produce an absorption trough. The offset in the position of the emission peak is larger than the estimated uncertainty in the radial velocity correction, which may indicate that clumping is only partly responsible for the shape of the H_α core. Indeed, other interpretations have been suggested, and we comment on this in Sect. 5.6.1.

The line shape of He II 4686 is well reproduced by our stochastic models, but not the emission strength. The line reacts similarly to clumping as H_α . In order to increase the central emission to the observed level we would have to raise the clumping factor in the inner wind even more, which in turn would produce stronger than observed H_α emission as well as shallower than observed H_{β} and H_{γ} cores. Since hydrogen generally has more reliable and robust departure coefficients than helium, we have given higher weights to fits of hydrogen lines. Interestingly, He II 4686 shows a similar offset as H_α in the position of the emission peak.

The PV resonance lines are much more sensitive to the wind structure parameters (see Sect. 5.4.1) than to the mass-loss rate. Hence these lines should be used only as a consistency check of mass-loss rates derived from other diagnostics. Using the structure parameters given in Table 5.2, our stochastic models yield reasonable fits of the PV lines. We use values of δt and x_{ic} as in Paper I but are able to adopt a higher value of $|\delta v/\delta v_\beta|$, which however is still lower than predicted by the RH models. This higher value stems from that we here consider also optical diagnostics and from these derive a lower mass-loss rate and higher clumping factors than what was assumed in Paper I.

f_{cl} in the inner wind is drastically different from that predicted by our RH model for λ Cep (Fig.5.5), and indicates that present-day RH simulations fail to predict observationally inferred clumping factors, at least for the inner wind. Regarding the outermost wind, let us point out that the RH simulations used here only extend to $r \approx 35$, at which f_{cl} is still decreasing. Simulations by Runacres & Owocki (2002), which extend to much larger radii, indicate that the clumping factor settles at ≈ 4 in the outermost

³ which only resembles the P Cygni shapes of the UV resonance lines, since it is formed differently

wind. $f_{\text{cl}} \approx 4$ is consistent with the assumed mass-loss rate $\dot{M}=1.5 \times 10^{-6} M_{\odot}/\text{yr}$ and the constraints from radio emission derived by Puls et al. (2006) (see above). This suggests that the outermost wind is better simulated by current RH models than the inner.

Comparison with the microclumping technique. Here we compare the stochastic models from above with microclumped models calculated with the same clumping factors. When using the microclumping technique, the PV resonance lines are not *directly* affected by the structured wind. The mass-loss rate adopted in the previous paragraph then produces much too strong absorption in these lines, see Fig. 5.7. Moreover, the high clumping factor in the inner wind adopted in our stochastic models results in so high densities that the clumps become optically thick in H_{α} and He II 4686 as well. This generally leads to weaker emission for the stochastic models than for the microclumped ones (Sect. 5.4.2), and f_{cl} 's drastic increase from 1 to 28 makes the deviation from the microclumping approximation prominent in this particular case. We have confirmed that the same emission strength reduction results when using our simplified analytic approach (Sect. 5.4.2), which supports the rather strong emission reduction that we find in the H_{α} core as well as indicates that our analytic approach indeed might be a promising tool for a consistent implementation into atmospheric NLTE codes.

In order to obtain reasonable fits of the PV lines within the microclumping approximation we had to lower the mass-loss rate significantly, to $\dot{M}=0.4 \times 10^{-6} M_{\odot}/\text{yr}$ (this is the so-called 'PV problem', see also Fullerton et al. 2006). In turn this meant that extreme clumping factors, $f_{\text{cl}} \sim 400$, in the inner wind were required to meet the observed amount of H_{α} wind emission. However, we have not been able to achieve a consistent fit of the optical diagnostics using these highly microclumped FASTWIND models; if for example H_{α} is fitted then the He II 4686 emission is much too weak. Overall, the results in this section support the view that the extremely low empirical mass-loss rates previously indicated from PV might be a consequence of neglecting optically thick clumping when synthesizing resonance lines.

5.6 Discussion

5.6.1 Are O star mass-loss rates reliable?

Theoretical rates. The time/spatial averaged mass-loss rate of our λ Cep RH model differs from the rate of the corresponding smooth star model (used for initialization) by less than 5%. From this one might expect that the clumped stellar wind should not significantly affect theoretical mass-loss rates based on the line-driven wind theory. However, Krtićka et al. (2008) (see also Muijres et al. 2010, submitted to A&A) made some first tests and included wind inhomogeneities in a (steady-state) theoretical wind model of an O star. They found that the predicted mass-loss rate increased when clumps were assumed to be optically thin, because of increased recombination rates that shifted the ionization balance to lower ionic states with more effective driving lines. On the other hand, their tentative attempts to account for optically thick clumps in the *continuum* opacity as well as for clumps with longer length scales than the Sobolev length reduced the line force and led to lower predicted rates.

The reduced profile strengths of resonance lines (which are the main drivers of the wind) found here should in principle also reduce the line driving in theoretical steady-state wind models, but let us point out that many lines that significantly contribute to the total driving force might still be saturated because of the non-void inter-clump medium. Nevertheless, it is clear that a thorough investigation

of the impact of clumping on predicted mass-loss rates is urgently needed. The mass-loss rate for λ Cep derived here is approximately a factor of two lower than the theoretical rate predicted by the mass-loss recipe in Vink et al. (2000).

Empirical rates. Our empirical mass-loss rate for λ Cep is 4.5 times lower than the rate inferred from synthesizing H_α using a smooth wind model (Repolust et al., 2004). The best constraints on the mass-loss rate in our analysis come from the distinct shape of the H_α line core and the higher Balmer lines (Sect. 5.5.3). Rotation in our models is treated by the standard convolution procedure. But λ Cep is a fast rotator (Table 5.1), so differential rotation might influence the formation of the line profiles, particularly the H_α core. Bouret et al. (published in Bresolin et al. 2008) found that the H_α line in ζ Pup can be fitted by assuming that clumping starts close to the wind base, *if* differential rotation is treated consistently. Since ζ Pup and λ Cep display similar H_α profiles, it is possible that the same effect could be at work also in the latter star, and thereby that the rather late onset of and the rapid increase of clumping in our stochastic model of λ Cep could be somewhat exaggerated. Naturally, this could then also affect the inferred mass-loss rate.

The influence of X-ray and XUV/EUV radiation as created by shocked wind regions (Feldmeier et al., 1997) on the occupation numbers is not included in our analysis. These contributors are not important for calculations of hydrogen occupation numbers (Pauldrach et al., 2001), but their significance for the ionization fractions of phosphorus is still debated (Krtićka & Kubát, 2009; Waldron & Cassinelli, 2010). We have used the alternative unified atmospheric code WM-Basic (Pauldrach et al., 2001), which treats X-ray and XUV/EUV radiation but *not* wind clumping, to estimate the impact of X-rays on the PV ionization fractions. We find that effects are negligible at wind velocities lower than $v/v_\infty \approx 0.5$ but profound at higher velocities, with the PV ionization fraction significantly reduced when X-rays (and of course the corresponding XUV/EUV radiation tail) are included. This suggests that a proper treatment of these hot radiation bands might resolve the earlier discussed ‘blue absorption dip’ problem, which is clearly visible in the PV line profiles calculated from RH models (Fig. 5.6, but note that we overcame this problem in our stochastic models by increasing the distances between clumps in the outermost wind, see Table 5.3).

5.6.2 Structure properties of the clumped wind

We identify two main problems when confronting synthetic spectra from the time-dependent RH simulations of the line-driven instability with observed lines in the UV and optical: i) the absorption toward the blue edge of unsaturated UV resonance lines is too deep in the simulations, and ii) the emission in the core of H_α is much too weak as compared to the emission in the wings. The first problem is related to the high predicted velocity spans in the RH models, and was extensively discussed already in Paper I. Moreover, in Sect. 5.6.1 we commented on that even if the large velocity spans turn out to be stable features, this problem might be overcome by a proper treatment of X-rays in the calculations of ionization fractions.

The second problem arises because the predicted clumping factors in the inner wind are too low as compared to those in the outer wind (Fig. 5.5). However, let us point out that velocity as well as density perturbations in the inner wind of our RH simulation may be overly damped, because we use the so-called smooth source function (SSF) approximation when calculating the contribution to the line force from the diffuse, scattered radiation field. In simulations that relax the SSF approximation and account for gradients in the perturbed source function (via an ‘escape-integral source function’

formulation, EISF, Owocki & Puls 1996, 1999), the structure in the inner wind is more pronounced and also develops closer to the photosphere.

In any case, however, it is questionable if *self-excited* instability simulations will be able to reproduce the observed clumping patterns (which have been found also in earlier investigations based on the microclumping approximation, e.g., Bouret et al. 2005; Puls et al. 2006), especially considering that our RH model of λ Cep actually already is triggered (Table 5.1), using Langevin perturbations mimicking photospheric turbulence (Feldmeier et al., 1997). Thus, while observations tracing the outer wind seem to confirm the structures predicted by the line-driven instability, observations tracing the inner wind might require the consideration of an additional triggering mechanism to be reproduced, which perhaps must be stronger than what is currently assumed. For example, Cantiello et al. (2009) proposed that gravity and/or acoustic waves emitted in sub-surface convection zones may travel through the radiative layer and induce clumping already at the wind base. However, regarding gravity waves, it is not certain that these would have high enough frequencies (i.e., higher than the atmosphere's acoustic cutoff frequency) that they can be radially transported through the wind. Another possibility for a strong clumping trigger might be non-radial pulsations in the photosphere. Certainly it would be valuable to investigate to what extent such triggers, within a line-driven instability simulation using the EISF formulation, could produce clumping patterns in the inner wind more compatible with the observations.

5.7 Additional considerations

In this section, we discuss two applications for the analytic formulation of line formation in clumpy winds presented in Sect. 5.4.1.

5.7.1 Weak wind stars

The so-called weak wind problem is associated with observations of (primarily) O-dwarfs of late types, which appear to have mass-loss rates much lower than what is predicted by the line-driven wind theory, and also much lower than other 'normal' O stars of earlier spectral types. However, a major problem with wind diagnostics in this domain is that the primary optical diagnostic, H_{α} , becomes insensitive to changes in the mass-loss rates, so that only upper limits can be inferred from this line. Therefore one must for these objects quite often rely solely on the intrinsically stronger UV resonance lines. For a comprehensive discussion on the weak wind problem, see Puls et al. (2008b).

In the following, we demonstrate the potential impact of optically thick clumping on diagnostic resonance lines in weak wind stars using the analytic formulation developed in Sect. 5.4.1. We use one component of the NV doublet at 1240 Å, assume a solar nitrogen abundance (Asplund et al., 2005), and take a generic O-dwarf with parameters $R_{*}=8.0 R_{\odot}$, and $v_{\infty}=1500 \text{ km s}^{-1}$. The NV doublet was among the lines utilized in the study of Marcolino et al. (2009), and also our chosen parameters correspond well to the parameters for the five stars analyzed and found to have very weak winds (more than an order of magnitude lower than predicted by theory) in that study. To avoid problems regarding the onset of clumping and the aforementioned 'blue absorption dip', we consider only the velocity interval $v/v_{\infty} = 0.25 - 0.75$. Line profiles for structured winds are calculated using Eq. 5.1 and adopting the same structure parameters as in Sect. 5.4.1 ($f_v=0.25$, $x_{ic}=0.0025$, $\delta t=0.5$, and a smooth ' $\beta=1$ ' velocity field).

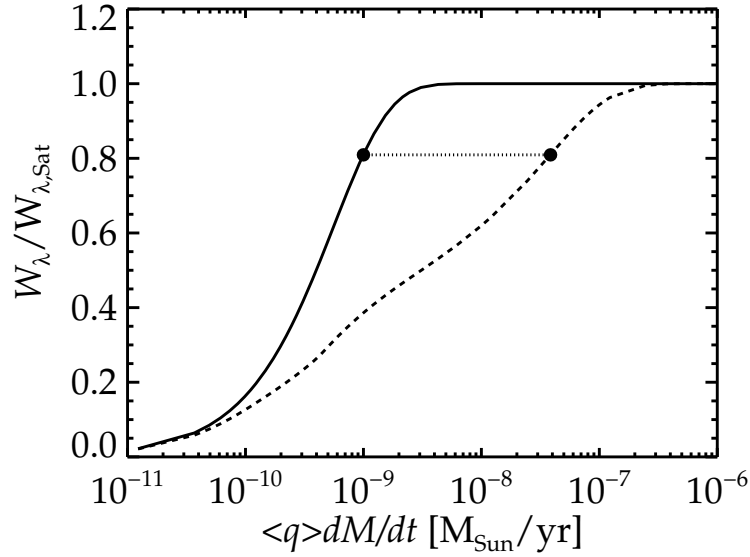


Figure 5.8: Equivalent widths, W_λ (normalized to the value for a saturated line), for the absorption part of the NV resonance line at 1240 \AA , as functions of the product of the ionization fraction of NV, $\langle q \rangle$, and the mass-loss rate. The solid line is calculated from smooth models and the dashed line from structured ones. The black dots denote W_λ 's for models corresponding to a smooth model with $\langle q \rangle \dot{M} = 10^{-9}$; see text.

Fig. 5.8 shows the curve-of-growths for structured and smooth models, respectively, as functions of the mean ionization fraction of NV times the mass-loss rate, $\langle q \rangle \dot{M}$. Clearly, mass-loss rates derived from smooth models may be severely underestimated also for stars with weak winds. For example, if we for this star were to infer $\langle q \rangle \dot{M} = 10^{-9} M_\odot/\text{yr}$ from a smooth model, the corresponding rate inferred from a structured one would be $(\langle q \rangle \dot{M})_{\text{struc}} = 3.8 \times 10^{-8} M_\odot/\text{yr} = 38(\langle q \rangle \dot{M})_{\text{smooth}}$ (see Fig. 5.8). Thus, if using smooth models (or microclumped, since microclumping has no effect on the resonance lines), one could easily derive mass-loss rates more than an order of magnitude lower than corresponding rates derived from structured models, and thereby one could also misinterpret observations as suggesting that mass-loss rates are much lower than predicted by theory.

We emphasize, however, that this simple example merely demonstrates how optically thick clumping *might* be important also for resonance line diagnostics in so-called weak wind stars, and that, *if* the winds are clumped, one must be careful not to simply assume that strongly de-saturated resonance lines also imply optically thin clumps. The actual mass-loss reductions will depend critically both on the assumed ionization fractions and on the adopted structure parameters. Thus, a multi-diagnostic study (to constrain the structure parameters), including a detailed consideration of X-rays (to obtain reliable ionization fractions), is required for more quantitative results. Nevertheless, we may safely say that, because of these inherent problems in UV line diagnostics, it is important to put further constraints on the weak wind problem by exploiting other diagnostics that are sensitive to mass loss but neither have optically thick clumps nor are affected by X-rays (as is probably true for, e.g., the infra-red Br_α line, Najarro et al., in prep., see also Puls et al. 2009).

5.7.2 Resonance line doublets

Massa et al. (2008) pointed out that additional empirical constraints on wind structure may be obtained by considering the observed profile-strength ratios of resonance line *doublets*. The line strength parameter, κ_0 , of such doublets must in a smooth (or microclumped) wind be in proportion to the oscillator strengths of the individual components, f , which for the cases of interest here are $f^b/f^r = 2$, with superscripts b and r denoting the blue and red line components, respectively. However, if the clumps are optically thick for the investigated lines but this is ignored in the analysis, the line-strength ratio may in principle take any value between unity and two (see discussion in Paper I). For example, in the case of very optically thick clumps and a void inter-clump medium, Eq. 5.1 simply gives $R_{a,x} = 1 - \xi_x$, i.e. the inferred line-strength ratio would be exactly one. The analogy for continuum diagnostics, or for line diagnostics in a *non-accelerating* medium, is the well-known result that for a medium consisting of infinitely dense absorbers embedded in a vacuum, the effective opacity is independent of the atomic opacity (see footnote 4 in Sect. 5.9). Also for such a situation would the inferred profile-strength ratio be exactly one.

A major advantage of this line diagnostic is that the dependence on X-rays should cancel out. Recently, Prinja & Massa (2010) extended the Massa et al. work to include a large number of B supergiants, for which they, from the Si IV $\lambda\lambda 1400$ resonance doublet, derived empirical profile-strength ratios using smooth wind models. The stars showed a wide spread between unity and the predicted factor of two, with the majority of them lying in the range 1.0 to 1.5, and with an overall mean of 1.46 (standard deviation ~ 0.31). In the following, we shall discuss this diagnostic under the assumption that the doublet components are well separated, so that each component can be treated as a single line, which is reasonable for, e.g., the just mentioned silicon lines in typical B-supergiants and for PV in OB-stars.

We now show that our analytic formulation for resonance line formation indeed predicts profile-strength ratios on the same order as those discussed above. Following the previous paragraph, we assume a solar abundance for silicon, make use of a generic B-supergiant with $R_* = 30.0 R_\odot$ and $v_\infty = 800 \text{ km s}^{-1}$, adopt the same structure parameters as before, and consider only the velocity interval $v/v_\infty = 0.25 - 0.75$. We then assume that for this generic star we derive $\langle q \rangle \dot{M} = 5 \times 10^{-9}$ from the Si IV resonance doublet formed in a *structured* wind model. By once more exploiting the curve-of-growth (as in Fig. 5.8, but now for the two components of Si IV), we can then easily translate the structured results to corresponding smooth ones. We find an effective ratio $(\kappa_0^b/\kappa_0^r)_{\text{smooth}} \approx 1.4$, which agrees well with the results derived by Prinja & Massa (2010).

The doublet ratios are, in fact, almost ideal diagnostics regarding structure properties, since all other dependencies cancel out. Therefore ratios deviating from two might be the cleanest indirect signatures of optically thick clumping that we presently have, and may in principle be used to extract empirical information on the behavior of ξ . We write the ratio of the blue and red absorption line profile at frequency x as

$$\frac{R_{a,x}^b}{R_{a,x}^r} = \frac{(1 - \xi_x)e^{-(2\tau_{ic}^r)} + \xi_x e^{-(2\tau_{cl}^r)}}{(1 - \xi_x)e^{-\tau_{ic}^r} + \xi_x e^{-\tau_{cl}^r}}. \quad (5.5)$$

Generally, this equation can be solved for ξ_x only if the line optical depths and the inter-clump densities are known (the latter for example from observations of saturated resonance lines, see Paper I). However, under certain circumstances we can eliminate the need for such external knowledge. For

example, assuming that *all clumps are optically thick*, we may write

$$\frac{R_{a,x}^b}{R_{a,x}^r} = e^{-\tau_{ic}^r} = \frac{R_{a,x}^r}{1 - \xi_x} \rightarrow \xi_x = 1 - \frac{(R_{a,x}^r)^2}{R_{a,x}^b}. \quad (5.6)$$

Applying the last formula to our line-profiles computed for Si IV using Eq. 5.1 reveals a mean value of $\xi = 0.48$ in a velocity bin $v/v_\infty = 0.4 - 0.5$, which agrees well with the actual mean (calculated from the assumed structure parameters), $\xi = 0.51$. Thus, this approximation can provide a quite good direct empirical mapping of ξ , without any knowledge about optical depths etc. Another case for which the profile-strength ratio can be directly related to ξ is that of a completely transparent background medium (i.e. in our case a void inter-clump medium). That limiting case of Eq. 5.5 has been long recognized and used by the quasar community (e.g., Ganguly et al., 1999), for the formation of intrinsic, narrow absorption-line doublets.

However, let us point out that this theoretical example only demonstrates that our basic formalism appears reasonable. In a real application, there will be a contribution also from the *re-emission* part of the line profile, i.e., what we actually measure from an observation is the total line profile $R_x = R_{a,x} + R_{em,x}$. Thus, to empirically infer ξ_x from Eq. 5.6 (which involves $R_{a,x} = R_x - R_{em,x}$), we must either simply neglect the re-emission contribution (which generally not will be possible) or actually calculate $R_{em,x}$, as predicted by a *structured* wind model. For resonance lines (as opposed to recombination lines, see Sect. 5.4.2), a simplified approach for $R_{em,x}$ in clumpy winds is still to be developed; it is a very demanding task because of the source function's scattering nature. In principle though, a treatment corresponding to the 'smooth source function' formalism used in our time-dependent RH simulations (see Sect. 5.6.2) might be a reasonable first approximation.

5.8 Summary and future work

We investigate diagnostic features for deriving mass-loss rates from the clumped winds of hot, massive stars, without relying on the microclumping approximation. It is found that present-day RH simulations of the line-driven instability are not able to consistently fit the UV and optical diagnostics in a prototypical O-supergiant. By creating empirical stochastic wind models, we achieve consistent fits mainly by increasing the clumping in the inner wind. A mass-loss rate is derived that is approximately a factor of two lower than what is predicted by theory. The best constraints come from the optical diagnostics. The UV resonance lines are much more sensitive to the wind's structure parameters (i.e. to the clumping factor, the inter-clump medium density, etc.) than to the mass-loss rate, and should, thus, not be the preferred choice when deriving empirical mass-loss rates.

We discuss both recombination line and resonance line formation in detail. Resonance lines always suffer the effects of optically thick clumping in typical diagnostic lines, and their profiles are thereby weaker for models with a sufficient treatment of clumping than for models that rely on the microclumping approximation. Recombination lines are less affected because of the lower optical depths in typical diagnostic lines. However, emission strength reductions as compared to microclumped models are significant for stars with high mass-loss rates (e.g., Wolf-Rayet stars) and can be so for O stars as well, *if*, for example, strong clumping is present in the lower wind, as illustrated by our diagnostic study of λ Cep.

An analytic method to model these lines in clumpy winds, without any restriction to microclumping, is suggested and shown to yield results consistent with those from detailed stochastic models. Some

first results are given, illustrating the potential significance of optically thick clumps for diagnostic lines in weak wind stars, and confirming recent results that profile-strength ratios of resonance line doublets may be used as tracers of wind structure and optically thick clumping. We intend to refine this method and incorporate it into suitable NLTE unified atmospheric codes, in order to investigate effects of optically thick clumping on the occupation numbers.

It is pivotal that 3D, time-dependent RH models of the line-driven instability be developed, with an adequate treatment of the 3D radiation transport. New models are required to investigate whether the structure predicted by present-day simulations is stable or a consequence of current physical assumptions and simplifications.

5.9 Analytic treatment of line formation in clumped hot star winds

Resonance lines. We propose to write the absorption part of a resonance line formed (from a radial ray) in a clumped wind as

$$R_{a,x} = \xi e^{-\tau_{cl,x}} + (1 - \xi) e^{-\tau_{ic,x}}, \quad (5.7)$$

where ξ is defined as the *fraction of the velocity field over which photons may be absorbed by clumps* and the optical depths are those for the clumped (subscript cl) and rarefied (subscript ic) medium.

Following Owocki (2008) we define the *velocity filling factor* f_{vel} as the fraction of the velocity field covered by clumps (in full analogy with the volume filling factor f_v). That is, f_{vel} is the ratio of the velocity span of the clump, δv , to the velocity separation between two clump-centers, Δv ,

$$f_{vel} \equiv \frac{\delta v}{\Delta v}. \quad (5.8)$$

In our stochastic models we have $\delta v \approx (\delta v / \delta v_\beta)(dv_\beta/dr)\delta r$ and from the definition of f_v (see Paper I) $\delta r \approx f_v \Delta r$, with $\Delta r = v_\beta \delta t$ the radial distance between two clump centers. Similarly one may approximate $\Delta v \approx (dv_\beta/dr)\Delta r$, which leads to

$$f_{vel} \approx \frac{\delta v}{\delta v_\beta} f_v. \quad (5.9)$$

Thus, a smooth velocity law ($\delta v = \delta v_\beta$) implies $f_{vel} = f_v$.

Actually, Eq. 5.7 is in form equivalent to the analytic transfer solution derived by Levermore et al. (1986), for the ensemble averaged intensity in a two-phase [$i = A, B$] Markovian model of a static purely continuum absorbing medium in the limit that the length scales l_i of fragments of both components are much longer than the domain of integration⁴, if we just substitute $l_i \rightarrow \delta v, \Delta v$. Thus, from this analogy it is clear that we may set $\xi = f_{vel}$ as long as the Sobolev-like requirement $\delta v \gg C_{v_t}$ is satisfied, where C_{v_t} is the velocity extent over which a photon of frequency x may be absorbed (that is, the velocity extent of a resonance zone). This limiting situation corresponds to the case that the

⁴ We mention in passing that the Levermore et al. model also yields the result $e^{-r/h}$ in the limit of infinitely dense absorbers in a background vacuum, which is equivalent to the result for a fully porous wind obtained by, e.g., Owocki et al. (2004).

line profile can be represented by a delta function, so that the sharp edges of the resonance zones prevent any absorption at frequencies not Doppler shifted to the very line center, resulting in a localized radiative transfer. The optical depths in Eq. 5.7 are then understood to be the Sobolev ones. That is, $\tau_{\text{cl}} = \tau/f_{\text{vel}}$ and $\tau_{\text{ic}} = \tau(x_{\text{ic}}/f_{\text{vel}})$, with τ the optical depth in the smooth case.

However, especially in the outer wind (but, depending on the onset of clumping, also in the innermost wind, see Fig. 5.2) we will generally have $\delta v < C v_t$ and the effective fraction of the velocity field over which photons can be absorbed by clumps will increase. The exact form of the radiation transport is then likely to be very complex. Nonetheless, let us in a first attempt try to simply modify ξ in order to account for the essential effects. We write

$$\xi \approx \frac{\delta v + C v_t}{\Delta v}, \quad (5.10)$$

where the factor $C v_t$ now represents a sort of correction to the limiting case of $\delta v \gg C v_t$. A linear addition is chosen because the basic equation determining whether or not a photon actually can be absorbed (i.e., whether or not it is located within its resonance zone) is $x_{\text{cmf}} = x_{\text{obs}} - v$, with x_{cmf} and x_{obs} the co-moving and observer's frame frequencies, respectively. The dimensionless frequency x is defined as

$$x = \frac{v - v_0}{v_0} \frac{c}{v_\infty}, \quad (5.11)$$

with speed of light c and line-center rest-frame frequency v_0 .

The factor C accounts for the fact that the 'effective resonance zone' over which photons can be absorbed by clumps is larger than that provided by v_t (at least for relatively strong lines). Photon absorption at x within clumps is given by the distribution function $e^{-\tau_{\text{cl},x}}$, with expectation value $\tau_{\text{cl},x} = 1$. Therefore we may estimate C using the 'effective profile width', determined by solving for the co-moving frame frequency at which unity optical depth is reached, *if* a clump is present,

$$\tau_{\text{cl}} \frac{1 - \text{erf}[x_{\text{cmf}}/v_t]}{2} = 1, \quad (5.12)$$

where erf is the error function. The effective profile width then is $C = 2x_{\text{cmf}}/v_t$, where x_{cmf} is given by the solution to Eq. 5.12. Note that C now is allowed to be velocity dependent, $C \rightarrow C(v)$. In addition, the expression for the clump optical depth should now be modified, $\tau/f_{\text{vel}} \rightarrow \tau/\xi$, to account for the fact that individual clumps no longer cover a complete resonance zone. We note that including these correction terms recovers the smooth optical depth τ in the limit $\Delta v \ll v_t$ (as expected because then the individual clumps obviously are optically thin).

With C determined we can cast ξ in the convenient form

$$\xi \approx f_{\text{vel}} + C \eta, \quad (5.13)$$

where $\eta \equiv v_t/\Delta v$ is the effective escape ratio. Note the difference between this definition of η and that given in Paper I. The two are related as

$$\eta = (1 - f_{\text{vel}})/\eta_{\text{old}}, \quad (5.14)$$

where η_{old} denotes our earlier definition. The advantage of re-defining η is that we may now separate out the porosity dependence in ξ , writing

$$\eta = \frac{v_t}{\Delta v} \approx \frac{v_t/(dv/dr)}{\Delta r} = \frac{L_r}{h}, \quad (5.15)$$

with $h = \delta r/f_v = \Delta r = v_\beta \delta t$ the porosity length of the medium and $L_r = v_t/(dv/dr)$ the radial Sobolev length. The coupling between vorosity and porosity becomes clear via η .

As defined, η may in principle take arbitrarily high values, so for the examples in this paper we simply set $\xi = 1$ whenever $\xi \geq 1$, because in a wind with a smooth velocity field the clumps obviously cannot absorb photons over a velocity space larger than that covered by the β velocity law. On the other hand, if we allow for clumps to be randomly positioned in velocity space, overlapping velocity spans will lead to a change in the effective coverage fractions. If velocity perturbations are sufficiently large, one may simply substitute $\xi \rightarrow (1 - e^{-\xi})$ and permit ξ to take arbitrarily high values. However, it is clear neither if velocity perturbations will be sufficiently large nor how to handle the case when more than one clump is crossed within a resonance zone. Thus we for now consider only the simple case of a smooth velocity field, deferring to future work a careful study of these randomization effects.

Finally, Eq. 5.7 has the proper behavior in the limiting cases of a smooth or microclumped wind. For the former ($x_{\text{ic}} = 1$ and $\tau_{\text{cl}} = \tau$),

$$R_x = e^{-\tau_x}, \quad (5.16)$$

and for the latter ($\tau_{\text{cl}} \ll 1$),

$$R_x \approx 1 - \tau_x, \quad (5.17)$$

where we recall that this last result is expected because resonance line formation depends linearly on the density (see Sect. 5.3.2).

Recombination lines. The absorption part of recombination lines such as H_α may also be approximated as described above. Furthermore, since the source function in these lines can be prescribed (see Sect. 5.3) we can make a similar approximation for the re-emission part

$$R_{\text{em},x} = S\xi(1 - e^{-\tau_{\text{cl},x}}) + S(1 - \xi)(1 - e^{-\tau_{\text{ic},x}}), \quad (5.18)$$

where S is the source function at the resonance point in units of the continuum intensity. The total line profile R_x is then given by $R_x = R_{\text{a},x} + R_{\text{em},x}$. It is important to realize that the re-emission profile is much more influenced by non-radial photons than is the absorption part profile. Thus we replace the radial approximation for ξ with a corresponding line-of-sight expression, $\xi \rightarrow \xi_z$, by substituting $L_r \rightarrow L_z$ and $h \rightarrow h/\mu$, where curvature effects for a clump have been neglected. The optical depths

from the previous paragraph must be replaced by corresponding ones for recombination lines, where of course care must be taken for the now angular dependent τ . Also Eq. 5.18 has the proper behavior for smooth as well as for microclumped winds. For the former

$$R_{\text{em},x} = S(1 - e^{-\tau_x}), \quad (5.19)$$

and for the latter

$$R_{\text{em},x} \approx S\tau_x f_{\text{cl}}, \quad (5.20)$$

which is expected because recombination line formation depends on the square of the density (see Sect. 5.3.2).

Comparisons between the analytic approximations outlined here and numerical simulations using our stochastic wind models and detailed radiative transfer codes are given in the main paper.

Chapter 6

Mg I emission lines at 12 & 18 μm in K giants

This chapter is a copy of Sundqvist, Ryde, Harper, Kruger, & Richter (2008), *Astronomy & Astrophysics*, 486, 985.

6.1 Abstract

The solar mid-infrared metallic emission lines have already been observed and analyzed well, and the formation scenario of the Mg I 12 μm lines has been known for more than a decade. Detections of *stellar* emission at 12 μm have, however, been limited to Mg I in very few objects. Previous modeling attempts have been made only for Procyon and two cool evolved stars, with unsatisfactory results for the latter. This prevents the lines' long predicted usage as probes of stellar magnetic fields. We want to explain our observed Mg I emission lines at 12 μm in the K giants Pollux, Arcturus, and Aldebaran and at 18 μm in Pollux and Arcturus. We discuss our modeling of these lines and particularly how various aspects of the model atom affect the emergent line profiles.

High-resolution observational spectra were obtained using TEXES at Gemini North and the IRTF. To produce synthetic line spectra, we employed standard one-dimensional, plane-parallel, non-LTE modeling for trace elements in cool stellar atmospheres. We computed model atmospheres with the MARCS code, applied a comprehensive magnesium model atom, and used the radiative transfer code MULTI to solve for the magnesium occupation numbers in statistical equilibrium. The Mg I emission lines at 12 μm in the K giants are stronger than in the dwarfs observed so far. We present the first observed stellar emission lines from Mg I at 18 μm and from Al I, Si I, and presumably Ca I at 12 μm . We successfully reproduce the observed Mg I emission lines simultaneously in the giants and in the Sun, but show how the computed line profiles depend critically on atomic data input and how the inclusion of energy levels with $n \geq 10$ and collisions with neutral hydrogen are necessary to obtain reasonable fits.

6.2 Introduction

Metallic solar emission lines around $12\ \mu\text{m}$ were first identified by Chang & Noyes (1983), with the most prominent lines originating from transitions¹ $7i \rightarrow 6h$ ($12.32\ \mu\text{m}$) and $7h \rightarrow 6g$ ($12.22\ \mu\text{m}$) between Rydberg states of neutral magnesium. Additional Rydberg emission lines from Al I, Si I, and tentatively Ca I were identified as well (Chang & Noyes, 1983; Chang, 1984). The Mg I line formation scenario remained unclear until Chang et al. (1991) and Carlsson et al. (1992), hereafter C92, in two independent studies reproduced the emission features by employing standard plane-parallel numerical radiative transfer with a detailed atomic model and a reliable solar atmosphere. They confirmed an origin below the atmospheric temperature minimum, refuted a chromospheric line contribution, and established a non-LTE (LTE: Local Thermodynamical Equilibrium) formation scenario. The solar lines have subsequently been used in, e.g., Mg I statistical equilibrium analysis by Zhao et al. (1998). C92 proposed a general Rydberg line formation mechanism for the highly excited metal lines, which implied that all visible metal emission lines in the solar spectrum around $12\ \mu\text{m}$ originated in the photosphere. A detailed non-LTE modeling of the Al I emission has been carried out by Baummueller & Gehren (1996), where they confirmed this mechanism.

The lack of suitable spectrometers and the low stellar flux in the mid-infrared have in the past made high-resolution spectroscopy in this wavelength region possible only for the Sun and a few luminous nearby stars. Ryde et al. (2004) observed the $12\ \mu\text{m}$ Mg I emission features in Procyon, and successfully reproduced the line profiles by employing the same modeling technique as C92. Uitenbroek & Noyes (1996) observed and modeled the evolved stars Arcturus (α Boo) and Betelgeuse (α Ori). Using the same model atom as C92, they were unable to fit the line profiles of the $7i \rightarrow 6h$ Mg I transition, which appeared both in emission (Arcturus) and absorption (Betelgeuse). Their observational sample also included five M giants and supergiants, in which the line appeared in absorption. However, Ryde et al. (2006) investigated water vapor lines for Betelgeuse in the same spectral region, and found a water line that coincided with the wavelength of the Mg I $12.32\ \mu\text{m}$ line. The group successfully modeled the water line, without considering the Mg I blend (which we predict to be very weak, see Sect. 6.7.3). This may explain the sample of observed M star absorption at $12.32\ \mu\text{m}$, since water vapor is expected in these stars, whereas the Mg I emission line contribution should be minor.

A well known potential use for the Mg I lines is as probes of magnetic fields, which play a fundamental role in the underlying physics of a cool stellar atmosphere. Zeeman line-splitting from an external magnetic field increases quadratically with wavelength, while the Doppler broadening only has a linear dependence. Thus a line's sensitivity to magnetic fields becomes higher at longer wavelengths. The splitting of the solar emission lines was pointed out early and has been extensively analyzed. We have performed observations of the magnetically active dwarf ϵ Eridani. These will be reported on in a forthcoming paper (Richter et al., in preparation), hence we defer further discussions about stellar disk-averaged magnetic fields until then.

Prior to (stellar) diagnostic applications, however, we should make sure that we are able to model and understand these lines in a range of stars. So far, as mentioned above, modeling attempts for evolved stars have been unsuccessful. We address this issue here by analyzing high-resolution observational spectra, which show strong Mg I emission lines in the three giants Pollux (K0 III), Arcturus (K1.5 III), and Aldebaran (K5 III). We model and analyze simultaneously the three K giants and the Sun, with particular emphasis on influences from atomic data, and discuss why previous modeling attempts have not succeeded. The organization of the paper is as follows; in Sect. 6.3, we describe the observations.

¹ Quantum state nl , where n denotes the principal quantum number and l the orbital

In Sect. 6.4 we review some concepts about the formation of the infrared Mg I emission lines and in Sect. 6.5 we describe our modeling procedure. Results are presented in Sect. 6.6 and we discuss them and give our conclusions in Sect. 6.7.

6.3 Observations

The observations were made with TEXES, the Texas Echelon-cross-echelle Spectrograph, Lacy et al. (2002). TEXES provides high spectral resolution in the mid-infrared and is available as a visiting instrument at both Gemini North and at IRTF, the Infra-Red Telescope Facility. The Pollux (β Gem) observations come from the November 2006 observing campaign at Gemini North. The Arcturus and Aldebaran (α Tau) observations were done over many years at the IRTF. In most cases, the observations were primarily intended for flux calibration or focus tests and not to study the stars themselves.

When observing stars with TEXES, we nod the source along the slit, typically every 10 seconds, to remove sky and telescope background. Before each set of 8 to 16 nod pairs, we observe a calibration sequence that includes an ambient temperature blackbody and an observation of blank sky emission. The difference of blackbody minus sky serves as a first order telluric correction and flatfield. Where possible, a featureless continuum object with emission stronger than the target is also observed to further correct for telluric features and flatfielding. The largest asteroids work very well for this purpose, as does Sirius (α CMa) with respect to Pollux.

At the frequencies of the mid-infrared Mg I emission lines, the spectral orders from the TEXES high-resolution echelon grating are larger than the 256^2 pixel detector array. This results in slight gaps in the spectral coverage. For the Pollux observations, which were the final observations before sunrise, we observed in two settings and adjusted the tilt of the collimator mirror feeding the echelon grating for the second setting. This shifts the spectral orders in the dispersion direction. By combining the data from these separate observational settings, we were able to fill in the gaps in the spectral orders. The Arcturus and Aldebaran data were constructed from many separate observing settings and no particular efforts were made to fill in the gaps.

Data reduction was done using a custom FORTRAN pipeline (Lacy et al., 2002). The pipeline corrects for spikes and optical distortions in the instrument, allows the user to set the wavelength scale based on telluric atmospheric features, flatfields the data, differences nod pairs to remove the background emission, and then combines the resulting differences. Finally it extracts a spectrum based on the spatial information within the two-dimensional echellogram. The pipeline also provides a fairly accurate estimate of the relative noise in each pixel.

To combine data from separate observations, we first established a common wavelength scale. We corrected each spectrum for the Earth's motion at the time of the observation and then interpolated the data onto the common scale. We used a fourth-order polynomial derived from line free regions to normalize each spectral order. We determined the signal-to-noise (S/N) for the normalized spectrum via a Gaussian fit to pixel values and used the relative noise estimate established during pipeline reduction to assign a weight for each spectral pixel. When combining data, we choose to weight by the signal-to-noise squared, which effectively means weighting by successful observing time.

Observations of low pressure gas cells near $13.7 \mu\text{m}$ at the November 2006 run indicate that the instrumental profile for the $12 \mu\text{m}$ observations of Pollux has a Gaussian core with a FWHM $\sim 3.0 \text{km s}^{-1}$, corresponding to a spectral resolution $R \sim 10^5$. As the Arcturus and Aldebaran spectra combined

data from four different runs and possible errors from the combinations may be significant, we were unable to make a reliable measurement of the instrumental profile in this region for these stars. At $18\ \mu\text{m}$, similar measurements indicate that these observations have a Gaussian instrumental profile with a FWHM $\sim 4.5\ \text{km s}^{-1}$. In Sect. 6.6 we display our observed data re-binned to approximately the spectral resolution, except for Fig. 6.5, where the pixel scale is used. Signal-to-noise ratios in the spectra vary but are generally high, reaching $S/N \sim 450$ per pixel for Pollux and ~ 300 for Arcturus and Aldebaran, in regions around the $12.22\ \mu\text{m}$ line. At $18.83\ \mu\text{m}$, the ratio is $S/N \sim 40$.

6.4 Departure coefficient ratios

Before proceeding to a modeling description, we briefly review some important concepts about the formation of the $12\ \mu\text{m}$ emission lines. In the following we use the departure coefficients $b_i = n_i/n_i^*$, where n_i is the actual number density (not to be confused with the principal quantum number n) of energy level i and n_i^* the corresponding LTE population, as calculated from the total magnesium abundance using the complete Saha-Boltzmann relations. In a spectral line, a departure coefficient ratio which differs from unity, $b_l/b_u \neq 1$, at line-forming depths causes a deviation of the line source function, S_ν^l , from the Planck function, B_ν , which affects the emergent intensity:

$$\frac{S_\nu^l}{B_\nu} = \frac{e^{h\nu/kT} - 1}{b_l/b_u \times e^{h\nu/kT} - 1} \quad (6.1)$$

For a characteristic wavelength $\lambda = 12.3\ \mu\text{m}$, and temperature $T = 5000\ \text{K}$, we get $e^{h\nu/kT} \sim 1.26$, and may directly from Eq. 6.1 realize that already a small deviation from unity in the departure coefficient ratio causes a significant change in the line source function. The physical reason for this is the increasing importance of stimulated emission in the infrared. If $b_u/b_l > 1$ and increases outwards in the atmosphere, we may get a rising total source function and a line profile appearing in emission despite an outwards decreasing temperature structure. Such departure coefficient divergence occurs between highly excited Rydberg levels in the outer layers of the modeled stellar photospheres considered in this study, and is the reason for the modeled emission lines.

Departure coefficient ratios that deviate from unity are set up by three-body recombination from the Mg II ground state and a ‘deexcitation ladder’ that preferably takes $\Delta n, \Delta l = -1$ downward steps (see Fig. 6.1 for an illustration). In the solar case, all Mg I Rydberg levels are strongly collisionally coupled to each other and to the Mg II ground state. The main effects that drive the line source function out of LTE come from lines elsewhere in the term diagram, primarily lines between levels with intermediate excitation energies, which are optically thin in the outer atmosphere and experience photon losses (Rutten & Carlsson, 1994). These levels impose a lower limit to the Rydberg state deexcitation ladder. The number densities of the Rydberg energy levels adjust to the upper and lower limits, and a radiative-collisional population flow occurs. It was shown, for the solar case by C92, how a high probability for $\Delta n, \Delta l = -1$ downward transitions is necessary for the Rydberg state ladder to be efficient and that these transitions dominate only if the collisional coupling is strong in the uppermost Mg I levels. It was also shown how this high probability arises from the regular character of the collisional cross-sections of transitions between highly excited levels. We thus remind of the remark in C92 that for a correct description of the ladder flow between highly excited levels, it is more important to have a *consistent* set of collisional data, than to have the most accurate cross-sections for a few transitions. These considerations are important to keep in mind when we later discuss our extension of the model

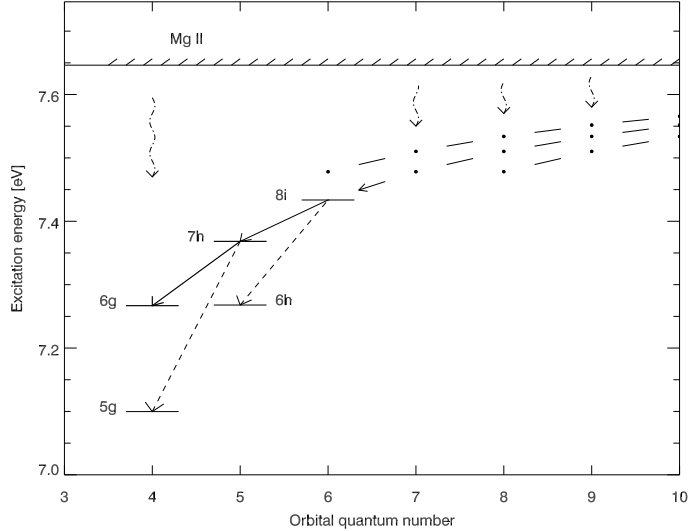


Figure 6.1: Illustration of the ‘Rydberg ladder’ (see text), using a *selected* part of the Mg I term diagram. Five levels about the $7h \rightarrow 6g$ transition are labeled with corresponding quantum numbers nl . Dots mark energy levels with $n \geq 9$ and $l \geq n - 3$. Solid lines between levels show transitions with $\Delta n, \Delta l = -1$, dashed show two alternative transitions ($\Delta n = 2, \Delta l = -1$). Dashed-dotted illustrate recombination from the Mg II continuum.

atom and the influence from collisions with neutral hydrogen. A more comprehensive description of non-LTE effects throughout the Mg I term diagram that affect the solar 12 μm lines can be found in Rutten & Carlsson (1994).

6.5 Modeling

To produce synthetic line spectra, we employ standard one-dimensional, plane-parallel, non-LTE modeling for trace elements in cool stellar atmospheres. We generate model atmospheres from the MARCS code (Gustafsson et al., 1975, 2008), adopt a comprehensive magnesium model atom, and use the radiative transfer code MULTI (Carlsson, 1986, 1992) to solve for the magnesium occupation numbers in statistical equilibrium, while holding the structure of the atmosphere fixed.

6.5.1 Model atmospheres and stellar parameters

The MARCS hydrostatic, plane-parallel models are computed on the assumptions of LTE, chemical equilibrium, homogeneity, and the conservation of the total flux (radiative plus convective; the latter treated using the mixing-length theory). No chromospheric temperature rise is invoked but, as shown by C92, omitting a chromosphere has a negligible impact on the solar Mg I 12 μm transitions. The findings in this work and that by Ryde et al. (2004) suggest that this holds true also for other investigated stars. Apart from the temperature and density stratifications, a detailed MARCS radiation field was generated using opacity samplings including millions of lines. A sampled version of this radiation

field was used when MULTI calculated the photoionization rates, in order to properly account for the line-blocking effect. We discuss some variations to our procedure in Sect. 6.7.

The stellar parameters we used for Pollux were $T_{\text{eff}} = 4865 \text{ K}$, $\log g = 2.75$ (cgs), a solar metallicity (as given by Grevesse et al. 2007), and a depth independent ‘microturbulence’ $\xi = 1.5 \text{ km s}^{-1}$, all based on a spectral analysis of optical iron and calcium lines made by Drake & Smith (1991). For the parameters of Aldebaran we adopted $T_{\text{eff}} = 3900 \text{ K}$, $\log g = 1.5$ (cgs), a metallicity² $[M/H] = -0.25$, and $\xi = 1.7 \text{ km s}^{-1}$. These are from primarily Decin et al. (2003) but considering also sources accessible at the SIMBAD astronomical database. Finally for Arcturus we used $T_{\text{eff}} = 4280 \text{ K}$, $\log g = 1.5$ (cgs), $[M/H] = -0.50$, and $\xi = 1.7 \text{ km s}^{-1}$. A discussion of these Arcturus parameters can be found in Ryde et al. (2002). The stars are all nearby and well-studied objects, and their parameters should be fairly accurate. Model grids show that the effects on the lines from (reasonable) variations in $\log g$ or T_{eff} are smaller than effects from, e.g., atomic input data, which will be investigated in the following sections.

We convolved our computed intrinsic line profiles with the instrumental profile, the projected rotational velocity ($v \sin i$), and the ‘macroturbulence’ (none of which affect the line strength but only the profile shape). We adopted $v \sin i$ values from Smith & Dominy (1979), which for Pollux, Arcturus and Aldebaran are, respectively, $v \sin i = 0.8, 2.7, 2.7 \text{ km s}^{-1}$. As we were unable to obtain a fair estimate of the instrumental profile for the Arcturus and Aldebaran spectra around $12 \mu\text{m}$, we choose first to assign an isotropic Gaussian shape with characteristic Doppler velocity v_m for the combined effect of the instrumental profile and the macroturbulence. For Pollux, where the instrumental profile could be separated out, we obtained $v_{\text{macro}} \sim 3.3 \text{ km s}^{-1}$. However, it became clear that the modeled line wings of the K giants better fitted the observations when assuming a radial-tangential Gaussian shape (Gray, 1976) for the macroturbulence. Therefore we decided to assign the Pollux instrumental profile for all three stars (the exact values are not so significant since the macroturbulence is the dominating external line broadening), and adopted a radial-tangential macroturbulence $v_{m,R-T} = 5.5, 6.0, 5.5 \text{ km s}^{-1}$ to fit the observed line-widths. Our values are $\sim 2 \text{ km s}^{-1}$ higher than those measured from Fourier analysis in optical spectra by Smith & Dominy (1979).

6.5.2 The model atom

Our Mg I model atom is essentially an enlarged and slightly modified version of the one compiled by C92, and a full description can be found there. The original model atom has also been used in the analysis of solar magnetic fields (e.g., Bruls et al. 1995), for the Mg I $12 \mu\text{m}$ flux profiles of Procyon (Ryde et al., 2004), and in a previous attempt to model giants (Uitenbroek & Noyes, 1996). In short, the atom is complete with all allowed transitions up to principal quantum number $n = 9$ and includes the ground state of Mg II. We now describe changes and tests we have made.

Enlargement of the model atom

Lemke & Holweger (1987), who also pointed out a possible photospheric line-origin through a rising line source function, made a statistical equilibrium investigation for the Sun but were unable to reproduce the Mg I $12 \mu\text{m}$ emission due to a combination of their adopted collisional data treatment and an inadequate model atom. Their exclusion of levels higher than $n = 7$ resulted in an incorrect

² Here we do not specify individual metal abundances, but $[M/H]$ is taken as the characteristic metallicity where as usual $[A/B] = \log(n_A/n_B)_* - \log(n_A/n_B)_\odot$.

description of the replenishment of the Rydberg levels from the ion state. C92 experimented with the $n = 8, 9$ levels and confirmed that these were necessary to have top-levels that were fully dominated by collisions and to obtain sufficient departure coefficient differences in line-forming layers to match the observed solar emission features. In this work we have extended the model atom to include levels with $n \geq 10$ to investigate if the departure coefficient differences are further enhanced.

The model atom was first enlarged to include all energy levels and allowed transitions with $n = 10$. To ensure homogeneity throughout the model atom, all new atomic data were calculated using the same formalisms as those employed by C92. The only exception was absorption oscillator strengths for transitions with $l \leq 3$ for which data was drawn from the opacity project (OP) TOP-BASE (Cunto & Mendoza, 1992), since the tabulation used by C92 (Moccia & Spizzo, 1988) only extend to $n = 9$. The enlargement caused an upward shift in the Mg I departure coefficients, and the effect became more pronounced as n increased; thus producing larger departure coefficient differences between adjacent levels. The same effect was seen in the Mg I statistical equilibrium for all our template atmospheres. To investigate the influence of the low l levels, a test-run was also made where only $n = 10$ levels and transitions with $l \geq 4$ were included. This model atom and the complete $n = 10$ atom produced almost indistinguishable results.

After this initial enlargement, atomic models were constructed step-wise, including higher principal quantum numbers. The enhancement continued until the atom's uppermost n level and the second uppermost were Boltzmann populated with respect to each other at all atmospheric layers (i.e., $b_{top-1}/b_{top} = 1$). This criterion was met for all atmospheric models when reaching $n = 15$, illustrated for the solar case in Fig. 6.2 (where our model actually meets the criterion already at $n = 12$). Sensitivity tests verified that no differences in results occurred when adding the final $n = 15$ top-levels. The main difference between the solar departure coefficients (Fig. 6.2) and those of the K giants is that the latter have Mg II ground states that are more overpopulated relative to LTE in their outer atmospheres. This is mainly because Mg I and Mg II are competing ionization states in these cooler atmospheres, so that the ion ground state becomes more sensitive to deviations from LTE in Mg I population densities. In Arcturus and Aldebaran, the overionization is further enhanced by the lower metallicity, which reduces the important line-blocking effect.

As the influence from levels with low l was negligible already for $n = 10$, we have confined the enlargement to levels and transitions with $l \geq 4$.

Collisional data

Ryde et al. (2004) compared *radiative* bound-bound and bound-free data from our model atom with OP data and found an overall good agreement. We have therefore restricted our analysis here to some aspects of the *collisional* data, which usually introduce the largest uncertainty in the model atom, due to a large number of poorly known cross-sections.

Collisions with neutral hydrogen

The role of collisions with neutral hydrogen in cool stellar atmospheres has long been a subject for debate. Despite small cross-sections (as compared to electron impacts), one may expect them to contribute significantly to collisional rates due to large n_{HI}/n_e ratios. In the outer parts of the model atmospheres in this study, this ratio ranges from about 10^4 in the Sun to 10^5 in the cooler and more metal-poor Arcturus. No collisions with neutral hydrogen were considered in the original model atom.

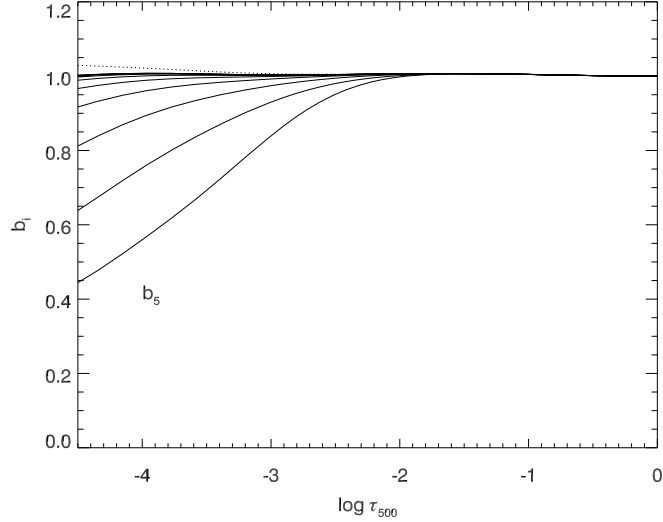


Figure 6.2: Solar departure coefficients for Rydberg state energy levels with $n \geq 5$, as functions of the continuum optical depth at 500 nm. b_5 is indicated in the figure, and an increment of one follows upwards in the figure. The displayed coefficients combine all $b_{n,l}$ coefficients with the same n and $l \geq 4$. The Mg II ground state is labeled with dots.

When inelastic collisions with neutral hydrogen are explicitly included in non-LTE calculations, a standard procedure is to adopt the recipe of Drawin (1969), as given by Steenbock & Holweger (1984). The Drawin formula has often been criticized. Steenbock & Holweger state an accuracy of an order of magnitude, but a rather common remark is that the recipe may overestimate the cross-sections with as much as one to six orders of magnitudes (see, e.g., Asplund 2005, and references therein). Unfortunately, more reliable cross-sections are scarce, especially for non-LTE calculations that require data for a large set of transitions. A customary way around this shortage is to adopt a scaling factor S_H to the Drawin formula, calibrated on solar or stellar observations.

In studies concerning the solar Mg I $12 \mu\text{m}$ lines, the Drawin formula was adopted by Lemke & Holweger (1987) and Zhao et al. (1998). The latter group scale their values with a factor that decreases exponentially with increasing excitation energy. Consequently, they apply $S_H = 3 \times 10^{-10}$ for the $12 \mu\text{m}$ transitions, which give them essentially the same result as if neglecting hydrogen collisions. Recall also that the former group was unsuccessful in producing an emission line core in their statistical equilibrium analysis.

Here we have estimated the collisional rates due to neutral hydrogen impacts using the Drawin formula. When introduced without scaling factor, our models reveal solar $12 \mu\text{m}$ lines in pure absorption and this case will therefore not be considered. By calibrating on the solar observations, we have adopted $S_H = 10^{-3}$ in all computations involving collisions with neutral hydrogen. However, in view of the existing uncertainties, we present results both from including these collisions for all radiatively allowed bound-bound (for which we have oscillator strengths) and all bound-free transitions, and excluding them.

Collisional excitation from electrons

The bulk of the collisional cross-sections from electron impacts for radiatively allowed transitions are calculated, as was done in C92, using the impact parameter approximation (Seaton, 1962). Mashonkina (1996) showed that, overall, this approach predicts significantly smaller cross-sections than the alternative semi-empirical formula of van Regemorter (1962) (applied for the solar Mg I lines in, e.g., Zhao et al. 1998). Avrett et al. (1994) used both formalisms when modeling the solar Mg I lines and concluded that using van Regemorter gave somewhat weaker emission. In C92, the impact parameter approximation is claimed to give a consistent set of rates accurate to within a factor of two for transitions between closely spaced levels.

Note that the above mentioned formalisms relate the collisional cross-section to the oscillator strength and may therefore not be applied to radiatively forbidden transitions. The ‘forbidden’ cross-sections are here set to a multiplying factor times that of the closest allowed (see C92). The original choice (C92) for this factor was 0.05, but Bruls et al. (1995) discovered some errors regarding a few oscillator strengths, accounted for here as well, and the factor was revised to 0.3 in order to reproduce the previous results. We also adopt 0.3, which was used by Ryde et al. (2004) as well. A similar treatment for solar Mg I analysis has been used by Mauas et al. (1988) who assumed 0.1, the same value as estimated in Allen (1973). Sigut & Lester (1996) also adopted 0.1 for Mg II (in work where they, for B type stellar photospheres, predicted the corresponding Rydberg emission lines for Mg II), which they found to be in rough agreement with a few more rigorously calculated rates from low excitation transitions. We have tested using the enlarged model atom without collisions with neutral hydrogen and concluded that by a raise to 0.7 times the cross-section of the nearest allowed transition we are able to reproduce the observed solar lines, but that the modeled emission in the K giants remain far lower than the observed.

An alternative approach for the radiatively forbidden transitions, applied in, e.g., Mg I (and II) non-LTE abundance analyses (Zhao et al., 1998; Przybilla et al., 2001; Gehren et al., 2004; Mashonkina et al., 2008), is to set a constant collisional strength $\Omega = 1$. Overall, this gives considerably lower collisional rates. The collisional strength Ω for collisions with electrons is related to the Maxwellian averaged downward collisional rate C_{ji} [s^{-1}] via:

$$C_{ji} = 8.63 \times 10^{-6} \Omega T_e^{-1/2} g_j^{-1} n_e \quad (6.2)$$

where T_e is the electron temperature, g_j the statistical weight of the upper level, and n_e the number density of free electrons. The upward rate, C_{ij} , then follows from the principle of detailed balance. We have also tested assuming a constant $\Omega = 1$ on the solar and Arcturus model, and verified that the modeled emission for Arcturus still is inadequate, remaining on the same low level as that displayed in Fig. 6.3, when collisions with neutral hydrogen are not included. The solar emission increases by this approach, but not enough to drastically change the suitable S_H factor. Overall, our experiments with the radiatively forbidden transitions tell us that the solar emission lines are somewhat sensitive to these rates, whereas the models of the K giants are much less responsive.

l-changing collisions

No explicit calculations of collisional transitions of type $n, l \rightarrow n, l'$ with high orbital quantum numbers ($l' \geq 4$) were made in the original model atom, but rather it was assumed that these collisional rates

were high enough to ensure strong coupling between closely spaced levels. This was established by setting $\Omega = 10^5$ if the difference in effective principal quantum number ($n - \delta$ where δ is the quantum defect) in the transition was less than 0.1. The high value of Ω causes very high collisional rates, which essentially force all levels with the same n and $l \geq 4$ to share a common departure coefficient (i.e., to be Boltzmann populated with respect to each other), in agreement with the proposed assumption. This, however, only holds for all relevant atmospheric layers in the Sun, whereas in the more diluted model atmospheres of the K giants, we find deviations between departure coefficients in outer layers (for Arcturus outside $\log \tau_{500} \sim -2$) for levels with relatively low orbital quantum numbers, when setting $\Omega = 10^5$. Apparently, such a value does not suffice for the K giants and we need to either raise the factor or explicitly estimate the rates. Note that C92 based the assumption of common departure coefficients mostly on the large cross-sections for l -changing collisions with neutral hydrogen calculated by Omont (1977), cross-sections later shown to be over-estimated by an order of magnitude (Hoang-Binh & van Regemorter, 1995).

In this work, we have calculated explicit electron/ion collisional rates for transitions with $\Delta l = \pm 1, \Delta n = 0$ and $l, l' \geq 3$ by using a cut-off at large impact parameters, as outlined by Pengelly & Seaton (1964). We find that the radial cut-off for transitions with low l is set by the non-degeneracy of the energy levels. For ion rates, this happens inside the radius where the strong interaction dominates and hence the impact parameter approximation is not expected to be reliable. However, for electron impacts the cut-off is at larger distances and since electron rates dominate over ion rates for these transitions, our approach should provide rates accurate to at least an order of magnitude also in the low l range. Ion rates surpass electron rates from $l \sim 9$ and higher, where the cut-off is well within the weak-interaction limit. We assume only singly ionized elements ($n_{ion} = n_e$) with the largest electron/ion donor being magnesium, providing $\sim 40\%$ of the total electron/ion pool in the relevant atmospheric layers in our MARCS models.

The calculated rates are in good agreement with the electron rates tabulated in Hoang-Binh & van Regemorter (1994), who exclusively considered l -changing collisions for the $n = 6, 7$ levels. Our rates are higher than those inferred from $\Omega = 10^5$ (by typically a factor of ~ 4 for, e.g., $n = 7$), hence no changes in results occur for the solar atmosphere. For the K giants, small differences between departure coefficients with the same n and $l \geq 4$ still exist but effects from using explicit rates are small. When forcing common departure coefficients for all equal n levels with $l \geq 4$ (by drastically increasing our computed rates), we still obtain normalized emission peaks for the K giants that differ only by a few percentage points.

6.6 Results

6.6.1 Emission lines at $12 \mu\text{m}$

We plot observed and computed line profiles for the Mg I $12 \mu\text{m}$ lines in the Sun, Pollux, Arcturus, and Aldebaran in Figs. 6.3, 6.4 and 6.5. In Arcturus and Aldebaran, the $12.32 \mu\text{m}$ line is blended with a water vapor absorption line (see Ryde et al. (2006) for an identification), which in the latter star is so influential that we choose to exclude the Aldebaran $12.32 \mu\text{m}$ line from the analysis. The observed emission lines from the K giants are stronger than the solar lines. In addition to the Mg I lines, we also identify emission lines from Si I, Al I, and Ca I in the observed spectra of Pollux and Arcturus (three of the lines are displayed in Fig. 6.5), all identified as $n = 7 \rightarrow 6$ transitions with high orbital quantum numbers. The flux maximum in the observed and normalized spectra (and the FWHM for

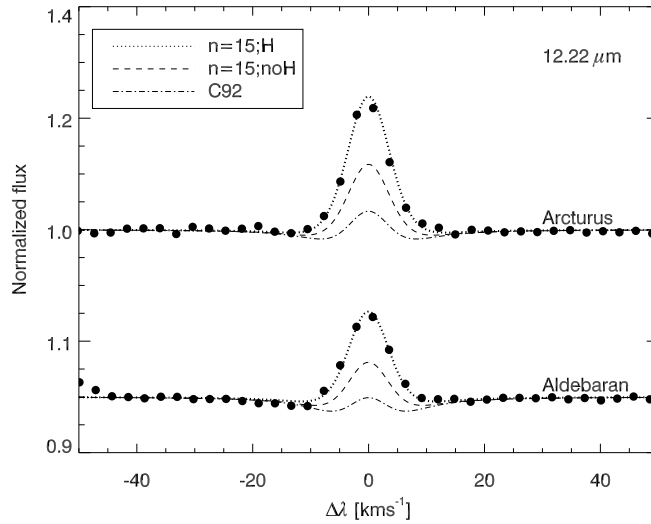


Figure 6.3: Observed and modeled line profiles in Arcturus and Aldebaran for the 12.22 μm line, plotted on a velocity scale. Labels as indicated in the figure; where C92 denotes the original model atom, $n=15;\text{noH}$ the extended excluding collisions with neutral hydrogen and $n=15;\text{H}$ the one including such. The filled dots denote the observed data.

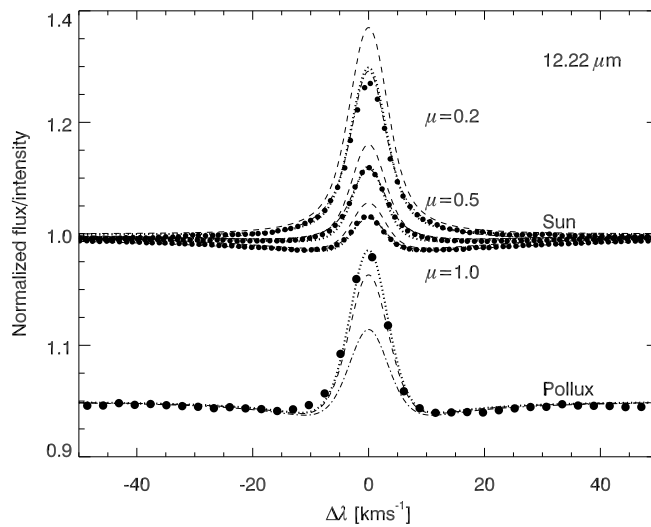


Figure 6.4: Observed and modeled line profiles in Pollux and for three positions on the solar disk (indicated in the figure) for the 12.22 μm line, plotted on a velocity scale. Labels as in Fig. 6.3.

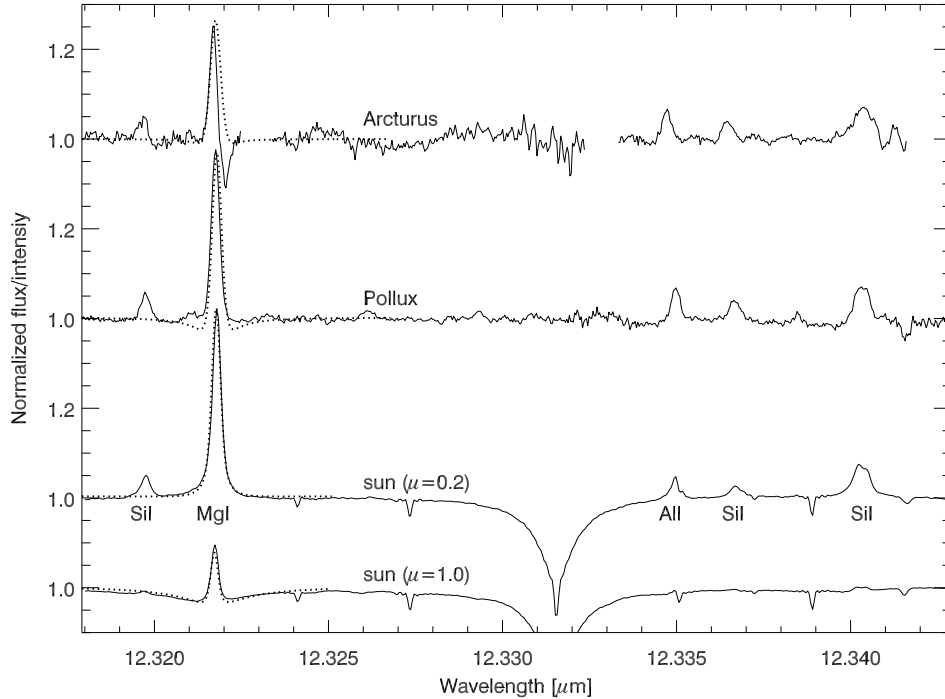


Figure 6.5: Observed spectra around the $12.3 \mu\text{m}$ region, shifted to the solar frame, for Pollux, Arcturus, and for two positions on the solar disk (indicated in the figure). Solar observations are from Brault & Noyes (1983). Models for the Mg I $12.32 \mu\text{m}$ line are labeled with dots, and use the $n=15;H$ model atom (see Fig. 6.3). The solar absorption features are telluric lines, and the missing parts in the Arcturus spectrum are due to gaps between spectral orders. Visible emission lines as indicated in the figure. The Arcturus absorption line at $12.32 \mu\text{m}$ is a water vapor line.

the Mg I lines) are given in Tables 6.1 and 6.2. More line data can be found in Chang & Noyes (1983) and Chang (1984). We have also added results from modeled Mg I flux profiles for the Sun (from a disk integration over solar intensity profiles in a model that reproduces the observations) in Table 6.1, to enable a fair comparison between solar and stellar observations. This illustrates that the K giants have stronger emission than the Sun.

The line-center average depth of formation in the modeled Mg I $12 \mu\text{m}$ lines is, for the Sun and Pollux, in atmospheric layers slightly below $\log \tau_{500} \sim -3$, with the weaker $12.22 \mu\text{m}$ line shifted approximately 0.2 dex toward the inner photosphere. In Arcturus and Aldebaran, the line formation takes place deeper inside the atmosphere. The average depth of formation for the line-center in the $12.22 \mu\text{m}$ line in Arcturus and Aldebaran is $\log \tau_{500} = -1.8$ and -1.6 respectively. This is partly because of the lower amount of H_{ff}^- opacity in these atmospheres (due mainly to lower electron abundances), which shifts the continuum formation to about $\log \tau_{500} \sim -0.8$, as compared with $\log \tau_{500} \sim -1.2$ in Pollux.

The extension of the model atom has a significant impact on the synthetic line spectra, with computed intensity/flux profiles being much stronger when using the enlarged model atom. We note the failure of the smaller atom to reproduce the observed emission for the K giants, whereas it provides a good

Table 6.1: Summary of observed magnesium emission line properties.

Star,	line [μm]	Normalized flux maximum			FWHM [km s^{-1}]		
		12.22	12.32	18.83	12.22	12.32	18.83
Pollux		1.28	1.37	1.20	6.8	7.1	8.2
Arcturus		1.24	^a	1.23	8.0	^a	9.7
Aldebaran		1.16	^a	-	8.0	^a	-
Sun ^b		1.09	1.15	-	5.8	6.1	-

^a Emission line blended with H₂O absorption line.

^b Modeled solar flux profiles (see text).

match for the solar lines, in agreement with previous studies. The larger model atom without collisions with neutral hydrogen predicts emission lines well below the observed level for Arcturus and Aldebaran, in contrast to the Sun where the modeled lines now are too strong. However, when including collisions with neutral hydrogen (as described in Sect. 6.5.2) the models reproduce the observed emission in all cases. These different responses to the ‘added’ collisions demonstrate the complexity of the Rydberg state deexcitation ladder, and are further discussed in Sect. 6.7.2.

Our models predict narrow absorption troughs in the Pollux lines, only matched by observations in the red wing of the 12.22 μm line. However, due to uncertainties in the observed normalized spectra imposed by, e.g., the continuum setting, we are not able to draw any firm conclusions from the absence of absorption troughs. A discussion about shifts in the solar absorption troughs, visible in Fig. 6.5, can be found in, e.g., Chang (1994). We also note how the line-wings in Arcturus and Aldebaran are too broad to be fitted by an isotropic Gaussian, and require a radial-tangential macroturbulence (see Sect. 6.5.1).

6.6.2 Mg I emission lines at 18 μm

We also observed the $8h \rightarrow 7g$ Mg I transition at 18.83 μm in Pollux and Arcturus, and present here the first stellar observations of this line. The emission is high here as well, see Fig. 6.6 and Table 6.1. Our synthetic line spectra reproduce the observed emission also for this line, which suggest that our model atom accounts for the Rydberg state deexcitation ladder in an accurate way. For comparison reasons, we display also a solar disk-center intensity profile³. The observed solar line feature is barely visible, which further illustrates the stronger emission from K giants.

The difference between departure coefficients in $n = 8 \rightarrow 7$ transitions is of similar magnitude as that between 7 and 6, causing comparable emission line strengths. The continuum formation is shifted about 0.3 dex outwards when compared to the spectral region around 12 μm (the H_{ff}^- opacity increases) but the average height of formation for the line-center in the 18.83 μm line in Pollux is located at $\log \tau_{500} \sim -2.5$, slightly further in than the 12 μm lines. This is because the line is merely the third strongest $8l \rightarrow 7l'$ transition with $\Delta l = -1$. We thus predict that the next two Rydberg transitions in the chain ($8i \rightarrow 7h$ located at 18.99 μm and $8k \rightarrow 7i$ at 19.03 μm) should appear even stronger, however these were not covered in our observational setup.

³ Observations from the Kitt Peak solar atlas

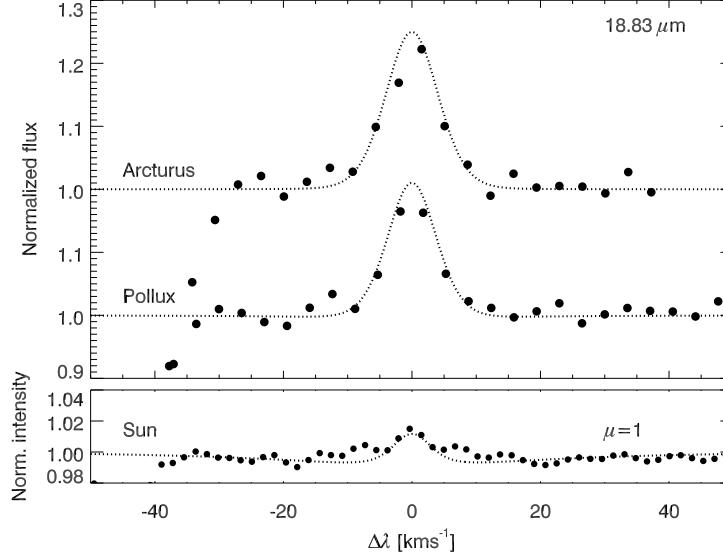


Figure 6.6: Observed and modeled line profiles for the $18.83 \mu\text{m}$ line in Pollux, Arcturus, and at the solar disk-center. Labels as in Fig. 6.3. The feature to the left in the figure is an OH absorption line. Note the scale difference between the upper and lower ordinate.

Table 6.2: Summary of observed emission line properties around $12 \mu\text{m}$ (other elements than magnesium) for Pollux and Arcturus.

Element ^a	Wavenumber ^b		Normalized flux maximum	
	Wavelength [cm ⁻¹]	[μm]	Pollux	Arcturus
Si I	810.360	12.340	1.07	1.08
Si I	810.591	12.337	1.04	1.04
Al I	810.704	12.335	1.07	1.06
Si I	811.709	12.320	1.06	1.05
Si I	813.380	12.294	1.06	1.07
Si I ^c	814.273	12.281	1.04	-
Ca I ^d	814.969	12.270	1.05	1.02
Al I ^c	815.375	12.264	1.03	-
Si I ^c	815.979	12.255	1.03	-

^a Line identifications based on

Chang & Noyes (1983) and Chang (1984).

^b From the solar observations by Brault & Noyes (1983).

^c Emission line blended with OH absorption line.

^d Line identification in Chang & Noyes (1983) stated as ‘suspicious’.

6.7 Discussion and conclusions

The model atom extension and the introduction of collisions with neutral hydrogen remove the discrepancy between observed and modeled emission in our study. *Before* the model atom was extended, we undertook a number of tests to investigate the large discrepancies between observations and models. We therefore start our discussion by a short summary of these, with the purpose to simplify future work.

The lines are sensitive to the photoionization rates as these affect the recombination to the Rydberg levels. We thus made an *ad-hoc* increase in the photospheric MARCS radiation field until the modeled Mg I emission lines matched the observed, but found that the required additional mean intensities gave rise to surface fluxes that by far exceeded observed ones. We included a chromospheric temperature-rise in Arcturus and found it to have a negligible impact, with the lines forming in atmospheric layers below the temperature minimum. We computed MARCS models in spherical geometry and employed the spherical version of MULTI, S-MULTI (Harper, 1994), but differences from plane-parallel models were small. No attempt to analyze influences from atmospheric inhomogeneities has been made in this work. A discussion about how granulation affects the solar lines can be found in Rutten & Carlsson (1994).

6.7.1 The model atom extension

All Mg I departure coefficients are shifted upwards (increased) by the extension of the model atom, but the upward shift is more pronounced in the higher energy levels. It is this change in the departure coefficient *ratio* in the line-forming regions that is sufficient to cause a significant change in results, i.e., higher emission peaks for the larger atom. The enhanced collisional coupling in the uppermost Mg I levels and to the Mg II ground state strengthens the cascading process in rather the same manner as the model atom with top-levels $n = 9$ did when compared to one reaching only $n = 7$ (see Sect. 6.5.2). Qualitatively, more recombinations enter at the top-levels, channel down through transitions that take part of the Rydberg ladder (see Fig. 6.1) and set up larger departure coefficient differences between adjacent levels. The extension thus has a significant impact on the mid-infrared emission lines, whereas the overall character of the Mg I statistical equilibrium remains.

To include the energy levels with $n \geq 10$ seems especially pertinent when applying the model atom on diluted stellar atmospheres with low surface gravities (as shown by the large differences in the modeled line profiles of the K giants). These are more influenced by radiative transitions, and thus the extension ensures that the Rydberg level replenishment from the ion state is properly accounted for by including top-levels that are fully dominated by collisions.

6.7.2 Effects from extra collisions

Higher rates of collisional excitation and ionization affect the 12 μm lines in the implemented stellar model atmospheres differently. Figs. 6.3 and 6.4 show how (by the introduction of collisions with neutral hydrogen) the Mg I 12 μm emission is reduced in the Sun, increased in Arcturus and Aldebaran and almost unchanged in Pollux. Apparently, a homogeneous increase of collisional rates actually results in stronger emission in the low surface gravity atmospheres of Arcturus and Aldebaran (which one would perhaps not expect since, generally, collisions act to thermalize lines toward LTE).

We have analyzed this result by computing additional models for the Sun and Arcturus, where we included radiatively allowed bound-bound collisions with neutral hydrogen for 1) only the three tran-

sitions $7i \rightarrow 6h$, $7h \rightarrow 6g$, and $7g \rightarrow 6f$ and 2) only transitions with $\Delta n, \Delta l = -1$ and $n \geq 8$ and $l \geq 4$. The first test imposes stronger collisional coupling only in the $n = 7 \rightarrow 6$ transitions themselves, whereas the second serves to strengthen the collisional bound-bound coupling in transitions in the uppermost levels that take part of the Rydberg ladder (see Fig. 6.1), while maintaining all other rates.

We quantify the results of this experiment by the normalized flux maximum in the $12.22 \mu\text{m}$ line. In the first case, both models give lower emission, as expected from the direct thermalizing effect on the $n = 7 \rightarrow 6$ transitions. The modeled flux maximum above the continuum decreased by $\sim 30\%$ and $\sim 25\%$ for the Sun and Arcturus respectively, as compared with the model excluding collisions with neutral hydrogen. For the second case, however, the emission increased with a similar percentage in the solar model, whereas in Arcturus, the modeled flux maximum doubled its value. Thus, in a star like Arcturus the enhancement effect from highly excited lines (see Sect. 6.4) dominates the reduction effect from the higher collisional rates in the line transitions themselves, so that when introducing collisions with neutral hydrogen homogeneously throughout the model atom, the outcome is an emission increase (as seen in Fig. 6.3). We can understand this by noting that, e.g., the ratio between collisional and radiative deexcitation rates for the $8i \rightarrow 7h$ transition (supplying the $12.22 \mu\text{m}$ line) is $C_{ji}/R_{ji} \sim 15.0$ (Sun) and ~ 0.2 (Arcturus) in typical line-forming layers when collisions with neutral hydrogen are excluded. In principle, this means that the contribution from hydrogen is needed in the giants to ensure an efficient Rydberg ladder.

6.7.3 Observations of Rydberg emission lines around $12 \mu\text{m}$

The observed emission-line flux spectra for Pollux and Arcturus in the $12 \mu\text{m}$ region closely resembles the solar limb intensity spectrum, whereas the solar disk-center spectrum lacks emission features from other elements than magnesium (see Fig. 6.5). It is evident that strong emission features from the K giants, as compared with solar-type dwarfs, appear for more metallic Rydberg lines than magnesium, and the observability of different elements so far follows the same pattern as in the Sun. Future observations will tell if this observed trend remains for a larger sample. Model tests with K dwarfs indeed predict lower Mg I emission for dwarfs than for giants also within the same spectral class (supported as well by observations of the magnetically active K dwarf ϵ Eridani, Richter et al., in preparation).

For cooler K giants, absorption from water vapor starts to influence the $12 \mu\text{m}$ spectrum and we have detected a blend at $12.32 \mu\text{m}$ in Arcturus and Aldebaran. Observations from this spectral region in the yet cooler M supergiant Betelgeuse (Ryde et al., 2006) reveal no emission lines above the noise level, which is consistent with our modeling of the Mg I lines in this star (using the same stellar parameters as in Ryde et al.).

6.7.4 Comparison with other studies

Uitenbroek & Noyes (1996) modeled the Mg I $12.32 \mu\text{m}$ line in Arcturus and concluded that the computed line was, roughly, half as strong as the observed. When using the 'C92' model, we find an even larger discrepancy for the $12.22 \mu\text{m}$ line (see Fig. 6.3). As already discussed, these longstanding discrepancies between observations and models for K giants are removed when using our new model atom. We note also that Uitenbroek & Noyes did not detect the water vapor absorption line, which is blended with the Mg I $12.32 \mu\text{m}$ line in our Fig. 6.5. The extension of the model atom changes the

results in the solar case as well (as compared with C92 and Ryde et al. 2004), placing the Mg I lines in higher emission, but the former results are recovered by the introduction of collisions with neutral hydrogen.

We have settled here with the rather questioned, albeit standard, Drawin recipe for collisions with neutral hydrogen while we await results from more rigorous quantum mechanical calculations. We have shown the influence from these collisions on the formation of the mid-infrared Mg I emission lines, however we stress that it has not been an aim of this investigation to put detailed empirical constraints on their efficiency. Such a task would require a larger set of lines, including also other wavelength regions. Nevertheless, we may still compare our adopted scaling factor to the Drawin formula for Mg I collisions with neutral hydrogen, $S_{\text{H}} = 10^{-3}$, with other values from the literature. Mentioned in Sect. 6.5.2 was the exponential decrease resulting in $S_{\text{H}} = 3 \times 10^{-10}$ for the 12 μ m transitions (Zhao et al., 1998), a model which was later abandoned by the same group in favor of a constant $S_{\text{H}} = 0.05$ (Gehren et al., 2004), inferred only from optical lines. In a recent non-LTE abundance study of magnesium in metal-poor stars (Mashonkina et al., 2008), $S_{\text{H}} = 0.1$ is used. The value we find based on the mid-infrared lines is more than one order of magnitude lower than the values obtained from these two optical studies. Our model atom has not been applied to optical lines, however such a combined study should be given high priority in future work. We thus conclude that the mid-infrared emission lines from near-by giant stars may be suitable diagnostics for testing atomic input data in future non-LTE analyses.

Finally, as we are now able to model and explain the observed emission lines for both dwarfs and giants, diagnostic applications regarding stellar disk-averaged magnetic fields are possible.

Chapter 7

Summary and outlook

7.1 Summary

The mass-loss rate is a key parameter of hot, massive stars. It directly affects their evolution and ultimate fates, and is furthermore crucial for various feedback effects from these stars on their surroundings, such as ionizing fluxes, stellar yields, and energy and momentum releases (Sect. 1.1). Large reductions of O-star mass-loss rates currently in use have been suggested, by an order of magnitude or even more, as due to the effects of wind inhomogeneities (clumping). If confirmed, such low rates would have enormous implications for massive star evolution and feedback, and thereby also for the large number of astrophysical applications relying on their predictions.

However, both atmospheric modeling and spectral synthesis accounting for the effects of clumping are still in their infancies, and results stemming from present-day models have recently been challenged by several studies (Sect. 1.4). In particular, the normally made assumption of *optically thin clumps* ('microclumping') certainly is questionable for many of the spectral diagnostics used to estimate the mass-loss rates of these stars.

Spurred by this, we have developed new, improved methods to model the structured wind and the line formation in hot, massive star atmospheres, and investigated in detail the impacts from optically thick clumps, a non-void inter-clump medium, and a non-monotonic velocity field on UV resonance and optical recombination line formation (Chapters 4-5). These lines are standard to use when deriving 'observed' mass-loss rates by comparing synthetic and observed spectra. It is found that, indeed, the microclumping assumption is generally not valid for line formation under typical conditions prevailing in clumped, hot star winds. Especially the resonance lines are affected by optically thick clumps, and we show that if using the microclumping approximation when modeling these lines, one may seriously underestimate the observed mass-loss rates.

First quantitative results from an exemplary *multi-diagnostic* study are presented, using the prototypical Galactic O-supergiant λ Cep (Chapter 5). It is shown that synthetic spectra computed from present-day inhomogeneous, time-dependent, radiation-hydrodynamic wind models are unable to reproduce observed diagnostic lines in the optical and UV. Consequently, we develop stochastic, *empirical* wind models aiming to capture the essence of the structured medium. By means of these models, we obtain consistent fits of the diagnostics, essentially by assuming a higher clumping in the inner wind, and lower intrinsic velocity widths of the clumps, than what is predicted by self-consistent models. We derive an observed mass-loss rate for λ Cep that is approximately two times lower than predicted by the line-driven wind theory. Note, however, that this rate is still a factor of five higher

than the one derived when assuming microclumping. Thus, by properly accounting for the effects of optically thick clumps in wind diagnostics, we alleviate (although not completely resolve) the very large discrepancies between observations and theory indicated by previous studies.

Moreover, an analytic method to model resonance and recombination lines in clumpy winds, without any restrictions to microclumping, has been developed and shown to yield results consistent with those from detailed stochastic models. Some first, tentative but promising, results of the method are given, and we here suggest that this method, accompanied with those presented for continuum diagnostics in Chapter 3, may be explored to perform consistent, quantitative multi-wavelength studies of clumped hot star winds, ranging from the X-ray to the radio region (see also Sect. 7.2.1).

A side project of this thesis has been an investigation of the NLTE line formation of the photospheric emission lines of (primarily) Mg I at $12\ \mu\text{m}$ in cool stars (Chapter 6). These lines can, e.g., potentially be used to measure upper photospheric stellar magnetic fields, due to their sensitivity to Zeeman splitting. However, the lines have so far been observed in a very limited number of stars, and modeling attempts had previously been carried out only for two dwarf stars (including the Sun) and two cool giants, with very unsatisfactory results for the latter. We present new observations of IR emission lines at 12 , and $18\ \mu\text{m}$ in giants of K type, and show by a detailed magnesium NLTE modeling that the same line formation mechanism as for the solar case is at work there. We also point out why previous modeling attempts have been unsuccessful. It is emphasized how the formation of these lines are very sensitive to the input atomic data, and thus that they, in addition to magnetic field studies, may be used as crucial consistency checks for model atoms used in *multi-wavelength* abundance studies.

7.2 Outlook

7.2.1 Quantitative spectroscopy

The main long-term goal of the project started with this thesis, is to develop (and subsequently, of course, to apply) reliable methods for quantitative spectroscopy of hot, massive stars with winds. Only if our diagnostic tools are sufficiently well developed may we with some confidence draw conclusions on various observed properties of these objects, such as effective temperatures, chemical abundances, and mass-loss rates.

From the results of Chapters 4 and 5 we have learned that the description of clumping included in present-day, state-of-the-art, unified model atmospheres may not be adequate under certain circumstances. Using the basic methods developed in those chapters, we intend to update FASTWIND (Sect. 1.5.5) shortly, with a more appropriate description of wind clumping, accounting both for the presence of optically thick clumps and for a non-monotonic velocity field. A treatment of X-rays will be implemented as well. Thereafter we shall be ready to derive empirical mass-loss rates, as well as structure properties, of unprecedented reliability for large samples of hot, massive stars, by means of *multi-diagnostic, multi-wavelength* studies.

With this, we hope to set a new standard for empirical mass-loss rates from hot, massive stars, and shed light on current conflicts between observations and theory (e.g., the clumping in the inner wind and the velocity spans of the clumps, see previous sections). Most importantly, we aim to answer the key question: *Can we trust mass-loss rates currently in use in models of massive star evolution?*

Also, chemical surface abundances of stars provide constraints on both stellar and galactic evolution models as well as probe the conditions both in the present-day and in the early Universe. The mass-loss rate is important when deriving chemical surface abundances of hot stars with significant wind

strengths, for the modeled ionization equilibria and synthesized profiles are both affected by mass loss. As an example, nitrogen is a key element for constraining massive star evolution as well as galactic chemical evolution. However, first results from the VLT-FLAMES project (see Chapter 2) revealed apparent conflicts between observed nitrogen surface abundances in B-stars and the predictions from stellar interior models including rotational mixing (Hunter et al., 2007, 2009). On the other hand, primary nitrogen, presumably produced by strong rotational mixing in massive stars, is needed in galactic chemical evolution models, to reproduce the observed abundance patterns of the very old low-mass, metal-poor, halo stars that have survived until today (Chiappini et al., 2006). Nitrogen model atoms appropriate for O stars are currently being developed within our group (PhD thesis of J. Rivero González), and reliable atmospheric structures including the stellar wind (and accounting for the effects of wind clumping, see above) will be essential in order to use these model atoms for deriving abundances of desired accuracy, and in the extension to put further constraints on the evolution models.

The importance of adequate model atoms in quantitative spectroscopy was also demonstrated in a side project of this thesis, in which we used the NLTE approach for trace elements to model and analyze infra-red Mg I emission lines in late-type stars (Chapter 6). Although observations of these lines so far have been scarce indeed, the advent of NASA's airborne Stratospheric Observatory for Infrared Astronomy (SOFIA)¹ opens up for more regular observations in the future. Then it might finally be possible to explore these lines' long recognized potential to detect upper photospheric magnetic fields, due to Zeeman splitting, as well as to use them to, e.g., empirically test the efficiency of collisions with neutral hydrogen, which generally are a great factor of uncertainty in NLTE spectral analyses of cool stellar atmospheres, and to which the lines are very sensitive.

A future major (and somewhat exciting) application for quantitative spectroscopy of stars might be analyses of AB-supergiants in distant galaxies beyond the local group. These stars are the intrinsically brightest ('normal') stars in the optical, and are thus ideal objects to study when pushing the distance limits for observations of individual stars. From studying single stars in environments very different from our own we may obtain invaluable information not only about stellar and wind properties, but also about chemical compositions of and even distances to² their host galaxies (for a summary of first results, see Kudritzki et al., 2008). However, at such distances only the very brightest stars are accessible to us, stars which indeed have strong and powerful winds. Therefore it is critical that winds be considered in these analyses. Currently FASTWIND is used only for the B supergiants, whereas the hybrid NLTE approach (see Sect. 1.5.3) still is utilized for the A supergiants. Actually, also present-day unified model atmospheres cannot reproduce the observed H_{α} line profiles from local A-supergiants, which are observed as un-saturated lines but modeled as saturated ones. Since H_{α} behaves like a quasi-resonance line in this domain (e.g., Kudritzki & Puls, 2000), this behavior might be explained by the presence of optically thick clumps, in analogy with our findings for UV resonance lines in O stars (Chapters 4 and 5). We will explore this possibility anon, by making appropriate updates of FASTWIND.

¹ which recently, finally, has made its 'first light flight', see <http://www.sofia.usra.edu/>

² Via a purely spectroscopic distance indicator, the so-called flux-weighted gravity - luminosity relation, FGLR, see Kudritzki et al. (2008).

7.2.2 Theoretical wind models of hot stars

Considering the large number of astrophysical applications requiring estimates of mass loss from hot, massive stars (Sect. 1), it is pivotal not only that adequate theoretical wind models are developed for these stars, but also that they are made available for simple use by the community. For example, the models developed by Vink and collaborators (e.g., Vink et al., 2000) are today the most popular ones to use in evolution calculations, which at least partly is because the authors present a ‘mass-loss recipe’ that is very simple to implement.

The evidence for wind clumping in hot, massive stars has over the past years become overwhelming, but generally it has been assumed that clumping mainly affects mass-loss rates derived from observations (Sect. 1). Thus, all available theoretical rates still are based on the standard model, and are thereby calculated assuming a stationary, smooth, and spherically symmetric wind. But as discussed in Chapter 5, feedback effects from clumping (optically thin as well as optically thick) upon, e.g., the wind ionization balance may affect also these predicted mass-loss rates.

Clumping might be accounted for in various ways when calculating theoretical mass-loss rates. For example, all radiation-hydrodynamic wind models of the line-driven instability result in *time/spatial*-averaged mass-loss rates that are very similar to those of the smooth models used to initiate the simulations (Sect. 1.4.1). Therefore it seems reasonable that the major effects of wind clumping on predicted mass-loss rates should be indirect, via for example the modified ionization equilibrium. Under this assumption, one could use averaged structure parameters as predicted from time-dependent simulations, when calculating the line force in corresponding *stationary* wind models, and by this obtain self-consistent theoretical mass-loss rates, as predicted by the line-driven wind theory and including the effects of the line-driven instability.

However, recall that we in Chapters 4 and 5 showed that the structures predicted by present-day instability simulations were unable to reproduce diagnostic wind lines in prototypical O-star supergiants. Obviously this prompts development of new, improved time-dependent models of the line-driven instability, as already discussed in the mentioned chapters. In addition, it suggests that a second, alternative, approach to obtain theoretical mass-loss rates from stationary wind models, including the effects of clumping, might be to derive *empirical* wind structures, as functions of stellar parameters, and then to use these, rather than the theoretical structures, when calculating corresponding wind models. In principle, this approach would correspond to ‘trusting’ the basic line-driven wind theory, but not the structures predicted by present-day instability simulations. Indeed, initial work based on this approach is already underway (Muijres et al., submitted to A&A, see also Krtićka et al. 2008), where the authors investigate the effects from *typical* clumping values on predicted mass-loss rates.

Finally, a third way to obtain rates accounting for clumping is, of course, to directly rely on so-called *empirical* values, i.e. values inferred from observations of stars by means of quantitative spectroscopy (see Sect. 7.2.1). Such empirical rates are standard to use for the evolved stages of massive stars (e.g., for WR stars and LBVs), since general theoretical predictions for these stages are not available. Thus, further theoretical investigations certainly are needed not only for the line-driven winds of OB-stars, but also for pinning down the mass-loss rates of the more evolved stages of massive stars. For example, the mass loss in eruptive LBV phases, presumably driven by *continuum* radiation moderated by porosity effects, might be critical for the evolution of massive stars, especially in the early Universe (Sect. 1.4.4), but the rates for these phases are at present almost completely unknown, with quantitative estimates scarce indeed.

7.2.3 Further applications

Radiative transfer through clumpy media obviously finds astrophysical applications also outside the arena of single hot star winds. We finalize this section by mentioning a few such, but of course our selected subset of applications is both personally biased and very limited.

In Sect. 1.4.4, we discussed how the effects of porosity may under certain circumstances allow a LBV star to exceed its classical Eddington luminosity and initiate a very powerful stellar wind (see also previous subsection). Actually, it is believed that when radiation pressure dominated atmospheres come sufficiently close to the Eddington luminosity limit, they naturally develop strong instabilities, leading to lateral inhomogeneities and thereby, if the medium is optically thick, to a reduction of the effective opacity (e.g., Shaviv, 2001a). Thus, these ‘super-Eddington’ states may exist in other astrophysical systems as well. For example, Shaviv (2001b) has proposed that this mechanism can explain the observed super-Eddington luminosities and corresponding mass-loss rates of classical novae, and very recently Dotan & Shaviv (2010) applied the idea also to slim accretion disk models around stellar as well as super-massive black holes.

Switching context, also the propagation of ionizing radiation in H II regions may be subject to porosity effects, due to the inhomogeneous inter-stellar medium (e.g., Giammanco et al., 2004; Wood et al., 2005), and obviously also the predictions themselves for ionizing fluxes from hot, massive stars might be significantly influenced by wind clumping (since they are strongly dependent on both the mass-loss rates and the ionization equilibria, the former mentioned already in Sect. 1.1). To our knowledge, it has never been investigated how, e.g., the by clumping modified wind ionization balance affects the ionizing fluxes. For example, the current standard option in the widely used STARBURST99 population synthesis code (Leitherer et al., 1999) is a UV spectral library calculated by the un-clumped unified model atmosphere WM-Basic (Sect. 1.5.5). We intend to investigate this unexplored and important question shortly, once we have made the appropriate updates of FASTWIND (see Sect. 7.2.1).

Appendix A

More on the radiative transfer codes

In Chapters 4 and 5 we developed and used radiative transfer methods for synthesizing *resonance* and *recombination* lines in clumped hot star winds. Basic assumptions and brief descriptions of corresponding codes were given in those Chapters. Here we add considerable detail regarding the assumed *geometry* in the codes and the calculations of the *line opacities*.

A.0.4 Geometry - the Monte-Carlo resonance line code

We use a standard right-handed spherical system (r, Θ, Φ) defined relative to a Cartesian set (x, y, z) (transformations between the two may be found in any standard mathematical handbook). Photons

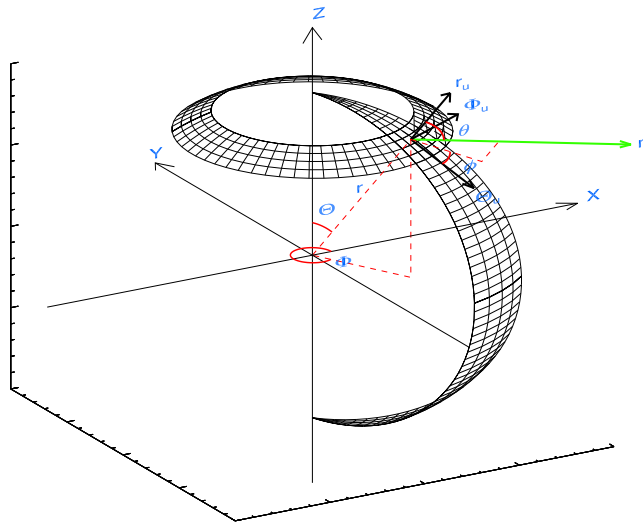


Figure A.1: Illustration of the coordinate system. Note that unit vectors in this figure, as well as in Chapters 4 and 5, are denoted by, e.g., r_u (using a subscript u), instead of \hat{r} , as in this appendix. Also, the photon propagation vector is denoted with n instead of with l . This figure is a copy of Fig. 4.13 in Chapter 4.

are emitted from some position on the stellar surface (given by $r = r_1, \Theta = \Theta_1, \Phi = \Phi_1$), with their directions specified by the *radiation coordinates* (θ, ϕ) , defined as in Fig. A.1 (see also Chapter 4). The photon path may then be traced by customary vector addition

$$\vec{r}_2 = \vec{r}_1 + \vec{l}, \quad (\text{A.1})$$

where \vec{l} is the photon path-length vector. The vector addition can be performed by at each point constructing a *local* coordinate system using the local unit vectors $(\hat{r}, \hat{\Theta}, \hat{\Phi})$. The key point here is that, locally, the transformations of the radiation coordinates to spherical ones behave as the transformation between a Cartesian and a spherical system (as may be seen from Fig. A.1). That is, the photon path lengths are

$$l_r = l \cos \theta, \quad (\text{A.2})$$

$$l_\Theta = l \sin \theta \cos \phi, \quad (\text{A.3})$$

$$l_\Phi = l \sin \theta \sin \phi, \quad (\text{A.4})$$

so that for the propagation vector

$$\vec{l} = l \cos \theta \hat{r} + l \sin \theta \cos \phi \hat{\Theta} + l \sin \theta \sin \phi \hat{\Phi}. \quad (\text{A.5})$$

Transforming the spherical unit vectors to *global* Cartesian ones,

$$\hat{r} = \hat{x} \sin \Theta \cos \Phi + \hat{y} \sin \Theta \sin \Phi + \hat{z} \cos \Theta, \quad (\text{A.6})$$

$$\hat{\Theta} = \hat{x} \cos \Theta \cos \Phi + \hat{y} \cos \Theta \sin \Phi - \hat{z} \sin \Theta, \quad (\text{A.7})$$

$$\hat{\Phi} = -\hat{x} \sin \Phi + \hat{y} \cos \Phi. \quad (\text{A.8})$$

Collecting terms we then get for $\vec{r}_2 = x_2 \hat{x} + y_2 \hat{y} + z_2 \hat{z}$

$$x_2 = r_1 \sin \Theta_1 \cos \Phi_1 + l [\cos \theta \sin \Theta_1 \cos \Phi_1 + \sin \theta \cos \phi \cos \Theta_1 \cos \Phi_1 - \sin \theta \sin \phi \sin \Phi_1], \quad (\text{A.9})$$

$$y_2 = r_1 \sin \Theta_1 \sin \Phi_1 + l [\cos \theta \sin \Theta_1 \sin \Phi_1 + \sin \theta \cos \phi \cos \Theta_1 \sin \Phi_1 + \sin \theta \sin \phi \cos \Phi_1], \quad (\text{A.10})$$

$$z_2 = r_1 \cos \Theta_1 + l [\cos \theta \cos \Theta_1 - \sin \theta \cos \phi \sin \Theta_1]. \quad (\text{A.11})$$

In general, these equations should be used to track the photons on their way through the spherical atmosphere. However, for our case of assumed symmetry in Φ , the expressions simplify considerably. We may, without loss of generality, choose $\Phi = 0$, for which Eqs. A.9-A.11 reduce to

$$x_2 = x_1 + \tilde{l}_x = r_1 \sin \Theta_1 + l [\cos \theta \sin \Theta_1 + \sin \theta \cos \phi \cos \Theta_1], \quad (\text{A.12})$$

$$y_2 = y_1 + \tilde{l}_y = 0 + l [\sin \theta \sin \phi], \quad (\text{A.13})$$

$$z_2 = z_1 + \tilde{l}_z = r_1 \cos \Theta_1 + l [\cos \theta \cos \Theta_1 - \sin \theta \cos \phi \sin \Theta_1], \quad (\text{A.14})$$

where we have defined the unit path lengths \tilde{l}_i , $i = x, y, z$. Obviously, the calculated \vec{r}_2 vector in the next step becomes the ‘new’ \vec{r}_1 vector, and the same procedure may be applied again. Moreover, by rotating the star in the Φ direction, we may then once again set $\Phi = 0$, so that, actually, Eq. A.13 does not need to be considered in the calculations.

Updating the radiation coordinates. To repeatedly apply Eqs. A.12-A.14, we must know also how to update the radiation coordinates (which are not constant in this spherical configuration, as opposed to in a Cartesian system). By geometrical arguments, we can write

$$\cos \theta = \hat{r} \cdot \hat{l}, \quad (\text{A.15})$$

$$\sin \phi \sin \theta = \hat{\Phi} \cdot \hat{l} = \frac{\hat{z} \times \hat{r}}{|\hat{z} \times \hat{r}|} \cdot \hat{l}, \quad (\text{A.16})$$

$$\cos \phi \sin \theta = \hat{\Theta} \cdot \hat{l} = (\hat{\Phi} \times \hat{r}) \cdot \hat{l}. \quad (\text{A.17})$$

We may now update the radiation coordinates by noticing that the photon propagation direction \hat{l} is *fix* in the local Cartesian coordinates. Thus,

$$\cos \theta = \frac{\vec{r}_2 \cdot \vec{l}}{r_2 l}, \quad (\text{A.18})$$

$$\cos \phi = \frac{\cos \Theta_2 \cos \theta - l_z / |l|}{\sin \theta \sin \Theta_2}, \quad (\text{A.19})$$

where $\cos \Theta_2 = z_2 / r_2$ provides the updated Θ angle.

The path length l . In principle, we could now track photons on a micro-grid by simply assuming some path length l . However, since the *physical* parameters of the stellar wind are assumed to be functions of the radius, it is much more convenient to do so on a micro-grid in r . From a given step size Δr in r , we obviously have $r_2 = r_1 + \Delta r$, and the corresponding path length is then found by simple trigonometry in the photon plane

$$l = r_2 \cos \theta_2 - r_1 \cos \theta_1, \quad (\text{A.20})$$

where θ_2 is found from Eq. A.18, or equivalently given directly by the sine-law in the photon plane

$$\sin \theta_2 = \frac{r_1}{r_2} \sin \theta_1. \quad (\text{A.21})$$

The major advantage with tracking photons on a radial grid is that we *avoid all interpolations between the grid points at which physical wind properties are specified*, except for when wind-slice borders in Θ are crossed or when a photon is scattered. (When the latter occurs, the new radiation coordinates are randomly computed from the corresponding distribution functions, see Chapter 4.)

Crossing wind-slice borders in Θ . When a wind slice border in Θ is crossed, the photon will at the crossing point no longer be on the radial micro-grid. Since the physical conditions change between the slices, it is, thus, necessary to find the exact location for the crossing. We denote by (r_c, Θ_c) the point at which the crossing occurs (recall that we assume symmetry in Φ). Obviously we already know Θ_c (pre-specified by assuming some coherence-length for the wind slices, see Chapter 4), so the question is; how to find r_c ?

Now, r_c may be written as

$$r_c = \frac{z_c}{\cos \Theta_c}. \quad (\text{A.22})$$

Using Eq. A.14 to update the z coordinate we directly obtain

$$r_c = \frac{r_1 \cos \Theta_1 + (\cos \theta_1 \cos \Theta_1 - \sin \Theta_1 \cos \phi_1 \sin \Theta_1) l}{\cos \Theta_2}. \quad (\text{A.23})$$

Eqs. A.20 and A.21 give for l

$$l = \sqrt{r_c^2 - r_1^2 \sin^2 \theta_1} - \cos \theta_1 r_1. \quad (\text{A.24})$$

Combining Eqs. A.23 and A.24, we end up with a non-linear equation for r_c (the square-root in Eq. A.24), but one that may readily be solved numerically. However, each Monte-Carlo simulation contains a large number of photons (say, $\sim 10^6$ or so) and border crossings will occur frequently for, in principle, all photons. That is, it becomes very computationally demanding to always solve numerically for r_c . Therefore, we instead apply an analytic approximation whenever possible.

Noticing that the non-linear behavior in the equations above essentially stems from the radiation coordinate term $\cos \theta$, we linearize in $\mu = \cos \theta$

$$\mu_c = \sqrt{1 - \frac{r_1^2(1 - \mu_1^2)}{r_c^2}} \quad (\text{A.25})$$

→

$$\mu_c \approx \mu_1 + \frac{(1 - \mu_1^2)\Delta r}{r_1 \mu_1}, \quad (\text{A.26})$$

where we have used

$$\mu_c = \mu(r_1 + \Delta r) \approx \mu(r_1) + \Delta r \frac{d\mu}{dr} \Big|_{r=r_1, \mu=\mu_1} \quad (\text{A.27})$$

$$\frac{d\mu}{dr} \Big|_{r=r_1, \mu=\mu_1} = \frac{1 - \mu_1^2}{r_1 \mu_1}. \quad (\text{A.28})$$

We now (again) use z_c , as given by Eq. A.14, and Eq. A.20 for the photon path length, and use these expressions to write for the update in r , Δr ,

$$(r_1 + \Delta r)\mu_c = r_1 \mu_1 + l, \quad (\text{A.29})$$

$$z_c = (r_1 + \Delta r) \cos \Theta_c, \quad (\text{A.30})$$

where, obviously, $r_c = r_1 + \Delta r$. Using Eq. A.26 for μ_c and eliminating l , we now end up with a 2nd order equation in Δr ,

$$\Delta r^2 C - \Delta r D - E = 0, \quad (\text{A.31})$$

with the well-known roots

$$\Delta r = \frac{-D \pm \sqrt{D^2 - 4CE}}{2C}, \quad (\text{A.32})$$

and with the constants C, D , and E given by

$$C = \frac{1 - \mu_1^2}{r_1 \mu_1} \tilde{l}_{z_1}, \quad (\text{A.33})$$

$$D = \cos \Theta_c - \tilde{l}_{z_1} / \mu_1, \quad (\text{A.34})$$

$$E = r_1 (\cos \Theta_c - \cos \Theta_1), \quad (\text{A.35})$$

$$\tilde{l}_{z_1} = \mu_1 \cos \Theta_1 - \sqrt{1 - \mu_1^2} \cos \phi_1 \sin \Theta_1. \quad (\text{A.36})$$

Tests have shown that, for most cases, (the correct root of) this approximation provides a good estimate for r_c . However, the approximation brakes down for tangential photons ($\mu_1 = 0$, see Eq. A.26). In practise, we use a numerical bisection method if $\mu_1 \leq 10^{-3}$, and the analytic approximation otherwise. Notice, however, that we in the code always check so that the calculated r_c is within the allowed range. For example, should the analytic approximation (with $\mu_1 > 10^{-3}$) fail, the numerical method is used instead. Tests indicate that this does occur for some photons in a typical simulation, but actually quite seldom.

Collecting escaping photons. Photons that escape the wind are collected according to their position on a spherical surface located at infinity ($r = r_\infty, \Theta = \Theta_\infty, \Phi = \Phi_\infty$). Again we may use the symmetry in Φ and only bin in Θ . Denoting with subscript e the position at which the photon escape the wind, we can write

$$x_\infty = x_e + l_\infty \tilde{l}_x, \quad (\text{A.37})$$

$$y_\infty = 0 + l_\infty \tilde{l}_y, \quad (\text{A.38})$$

$$z_\infty = z_e + l_\infty \tilde{l}_z. \quad (\text{A.39})$$

Transforming to the spherical coordinate system

$$r_\infty = \sqrt{x_\infty^2 + y_\infty^2 + z_\infty^2} = \sqrt{l_\infty^2 A}, \quad (\text{A.40})$$

with A in the limit that $l = l_\infty \rightarrow \infty$ given by

$$A = \frac{x_e^2}{l_\infty^2} + \frac{2x_e \tilde{l}_x}{l_\infty} + \frac{z_e^2}{l_\infty^2} + \frac{2z_e \tilde{l}_z}{l_\infty} + \tilde{l}_x^2 + \tilde{l}_y^2 + \tilde{l}_z^2 \approx \tilde{l}_x^2 + \tilde{l}_y^2 + \tilde{l}_z^2 = 1. \quad (\text{A.41})$$

Thus we have for Θ_∞

$$\cos \Theta_\infty = z_\infty / r_\infty = z_e / l_\infty + \tilde{l}_z \approx \tilde{l}_z, \quad (\text{A.42})$$

with \tilde{l}_z simply given by

$$\tilde{l}_z = \cos \theta_e \cos \Theta_e - \sin \theta_e \cos \phi_e \sin \Theta_e. \quad (\text{A.43})$$

However, the structured wind within our assumptions has no preferred direction (for example no axis of rotation) (see Chapters 4 and 5). Therefore an averaged spectra computed from these winds should be independent of observer's position, implying that we for most practical purposes can average over all emerging Θ angles, which of course greatly reduces the computational cost.

A.0.5 Geometry - the recombination line code

For recombination line formation, we may *pre-describe* the source function and only carry out the so-called *formal integral* within our inhomogeneous wind structures (see Chapter 5). Because of this, we have been able to drop the assumed symmetry in Φ when modeling the recombination lines H_α and $\text{He II } 4686\text{\AA}$. (Note that in our Monte-Carlo simulations for resonance line formation, the source function is implicitly given by our assumption of *pure scattering* lines.) Moreover, by using the same arguments as above regarding no preferred direction, we may simply *choose* to place the observer at z_∞ . Then three crucial simplifications occur: i) the radiation coordinate θ *coincides* with the coordinate Θ (i.e. $\Theta = \theta$, as is easily seen from Fig. 5.1 in Chapter 5), ii) the other radiation coordinate ϕ is always equal to π , and iii) the coordinate Φ is *constant* along a ray. Using these simplifications, we can solve the radiative transfer for a set of P rays, each defined by the minimum radial distance to the z axis, p , and the constant Φ coordinate, i.e. $P = P(p, \Phi)$. Then the observed flux F at frequency x is proportional to

$$F_x \propto \int_0^{2\pi} \int_{p=0}^{p=r_{\max}} I_x^{\text{em}}(p, \Phi) dp d\Phi, \quad (\text{A.44})$$

where $I_x^{\text{em}}(p, \Phi)$ is the emergent intensity at frequency x , obtained by a standard solution to the equation of radiative transfer (Eq. 1.2) with known opacities and source functions. Moreover, because $\Theta = \theta$ and $\Phi = \text{const.}$ along a ray, it becomes trivial to analytically calculate the positions at which photons cross a border to another wind slice.

A.0.6 Geometry - the patch wind model

Here we discuss potential effects of other geometries than the ‘patch geometry’ assumed in all our wind models in Chapters 4 and 5. (See these chapters for a description of the patch model.) Let us first point out, however, that most of the effects discussed here still are subjects to (sometimes quite lively) debates among practitioners in the field, and that a real consensus regarding their importance has not yet been reached.

As a first example, let us consider a wind consisting of spherical, isotropic clumps with characteristic length scales l , volumes $\approx l^3$ (neglecting π factors of order unity), and distances Λ between them that are equal in all spatial directions. Assuming $\Lambda \gg l$, we have $f_v \approx l^3/\Lambda^3$ and $h = l/f_v \approx f_{\text{cl}}^{2/3}\Lambda$. The equation of continuity in a spherical expansion may be used as a constraint for Λ ’s radial dependence, implying $n_{\text{cl}} \propto (r^2v)^{-1}$ with clump number density n_{cl} . Since $n_{\text{cl}} = 1/\Lambda^3$, it follows that $\Lambda \propto (r^2v)^{1/3}$. (This is the model used by Oskinova et al. 2007, in their application of an isotropic porosity formalism, Sect. 3.4, to *line* opacity.) But consider now clumps that are spread out over the surface of the star and start propagating radially outwards, obeying some velocity law $v(r)$. If clumps do not collide or merge, the physical distances between clumps in the Θ direction will be $\Lambda_\Theta \propto r$, but the radial distances between clumps will be controlled by the velocity law. So if $\Lambda_r = \Lambda_\Theta$ is to hold, we must have $v \propto r$. Thus, if we interpret the assumption of Λ equal in all spatial directions strictly, we may not let the clumps flow according to a β -type velocity law and simultaneously assume equal distances between clumps in all directions.

A similar problem is encountered in the combined assumptions of clumps of equal length scales l in all spatial directions and a constant f_v ; the radial distances between clumps no longer increase in the outer wind where the asymptotic velocity is almost reached, but the distances in the *tangential*

directions still increase as $\Lambda_\Theta \propto r$. Then if we demand that f_v must be kept constant, l must increase in all directions to preserve the equal length scales, and will eventually become *larger* than Λ_r . To avoid this somewhat strange picture of radially overlapping clumps (which in principle is the same as having clumps that are ‘infinite’ in the radial direction, at least as long as clumps are radially aligned, i.e. have no or very small lateral velocity components), one must make also the radial distances between clumps proportional to r (either by a homologous expansion, $v(r) \propto r$, or by not letting clumps flow with the velocity field). Naturally, this would further imply that $h \propto r$.

However, it may be that these apparent problems are only illusionary. The way around them is to *not* interpret Λ and l in the strict meanings of physical distances, but instead as quantities determining an *average mean free path* between the clumps,

$$mfp = \frac{1}{n_{cl}A_{cl}} \approx \frac{\Lambda^3}{l^2} = \frac{l}{f_v} = h. \quad (\text{A.45})$$

In this picture, the average mean free paths, and thereby the porosity lengths h , remain isotropic, independent of the assumed expansion of the medium, and despite the fact that the physical distances between the clumps are not equal in all directions. Then it is not necessary to invoke $v \propto r$ to obtain a consistent wind model with isotropic clumps. In terms of the above mentioned picture of radially elongated clumps that overlap, the essential point is that the spherical expansion opens up for holes in between these through which photons can escape, so that the *mean* free path still is preserved, also in the radial direction. However, at least within a modification of our present patch geometry, this kind of model might be problematic, as now discussed.

Modifying the patch geometry. Clumps in our stochastic models expand in the tangential directions preserving their solid angles. Thus for clump length scales $l, l_\Theta, l_\Phi \propto r$. On the other hand, the clumps’ radial widths $l_r = v_\beta \delta t f_v$ are calculated by *pre-describing* f_v and δt . This leads to very anisotropic ‘pancake shaped’ clumps, as is easily seen from density contour plots of corresponding models (Figs. 2.1 and 4.1). Moreover, clumps are released from the stellar surface with a complete covering fraction.

It might be, however, that clumps do not preserve their solid angles, but experience ‘lateral break-up’ when traversing outward in the wind. As a first guess, let us assume that such lateral break-up scales as r^{-2} (which essentially means that clumps keep their initial lateral extensions). Then $l_r = f_v \Lambda_r r^2$, and we encounter the same problem as above with clumps that eventually all overlap each other in the radial direction (since the radial distances between them are determined by $v_\beta \delta t$, i.e. is constant when the terminal speed is reached). Physically, it may be questionable that such a clump geometry, i.e. one in which clumps are extremely long in the radial direction but have large lateral holes between them, could exist in a hot star wind. To circumvent the radially overlapping clumps, one might assume that also f_v decreases with r^{-2} (which recovers the original expression for l_r), but this would produce much higher clumping factors in the outer wind than in the inner, which is not consistent with observational constraints from radio emission (Puls et al., 2006).

Another way to modify the geometry of the patch model might be to assume that, in the tangential directions, only a *fixed* fraction of the total wind volume of one slice is covered by clumps. Denoting with C_c the fraction of the total wind slice that is covered by clumps, we obtain $l_r = f_v \Lambda_r C_c^{-1}$, i.e. a radial extension of the clumps for a given volume filling factor, which compensates for the lateral holes created. However, for a radial photon within a given wind slice that encounters precisely one clump within its resonance zone, the probability of actually hitting this is now C_c instead of 1, as in the

original patch model. This *coverage fraction* therefore becomes important when clumps are optically thick; for the resonance lines a lower than unity C_c would open up for additional escapes, which in turn would reduce the profile strengths. We may connect this to the ‘broken shell’ porosity models that were presented in Sect. 3.4; if clumps were optically thick for a specific *continuum* process, no radial photons could escape through our original patch models. However, if C_c were to be used and clumps were to be randomly positioned within the wind slice, holes would open up, and radial photons would have a chance to escape without ever encountering a clump¹. In principle, this corresponds to the assumptions of *fragmentation* and *lateral randomization* that are inherent in the broken shell wind models for porosity.

As illustrated, details on clump geometry as well as on coverage fractions might be important for the radiation transport in clumped hot star winds. Unfortunately, however, little is known of either. Therefore we have adhered to the ‘patch geometry’ in Chapters 4 and 5 in this thesis, deferring to future studies, e.g., the inclusion of coverage fractions into our wind models.

A.0.7 Line opacities

Resonance lines. To predict where in the wind scatterings occur in our Monte-Carlo simulations of resonance lines, we must know the *line optical depths*. The continuum is assumed to be optically thin in the wind. As described in Chapter 4, the line optical depth may be parametrized in form of a line-strength parameter, κ_0 , which in turn may be described via atomic constants, the wind ionization fraction, and some of the stellar and wind parameters, as outlined below.

For UV resonance lines, we may to a good approximation neglect stimulated emission. Thus the frequency integrated extinction coefficient is

$$\chi = \frac{\pi e^2}{m_e c} f_{lu} n_{ijk}, \quad (\text{A.46})$$

with e the electron charge, m_e the electron mass, c the speed of light, f_{lu} the oscillator strength of the transition, and n_{ijk} the occupation number of the lower level. We now parametrize the opacity using the dimensionless quantity κ_0 , writing (Chapter 4, Eq. 4.16)

$$\chi = \frac{4\pi R_* v_\infty^2}{M\lambda} \kappa_0 \rho, \quad (\text{A.47})$$

where λ is the wavelength of the transition. If we measure velocities in units of v_∞ and radii in units of R_* , we then have

$$\kappa_0 = \frac{r^2 v R_* \lambda \chi}{v_\infty} = \frac{r^2 v R_* \lambda}{v_\infty} \frac{\pi e^2}{m_e c} f_{lu} n_{ijk}. \quad (\text{A.48})$$

The advantage of this parametrization is that the radial *Sobolev* optical depth in a smooth wind collapses to (Chapter 4, Eq. 4.17)

$$\tau_{\text{Sob}} = \frac{\kappa_0}{r^2 v dv/dr}. \quad (\text{A.49})$$

¹ Note that, for *line* formation, the situation is different; here radial photons may escape simply because their complete resonance zones are void of clumps, cf. Fig. 3.1.

To obtain an explicit expression for κ_0 , we must know the occupation number n_{ijk} of level l in ionization state j of element k . We write

$$n_{ijk} = \frac{n_{ijk}}{n_{jk}} \frac{n_{jk}}{n_k} \frac{n_k}{n_H} n_H = E q \alpha_k n_H, \quad (\text{A.50})$$

where E , q , and α_k now denote, respectively, the excitation fraction of level l , the ionization fraction of state j , and the abundance of element k , relative to hydrogen. Noticing that the bulk of the wind mass consists of hydrogen and helium, we can approximate

$$\rho \approx m_H n_H + m_{\text{He}} n_{\text{He}} = m_H n_H (4Y_{\text{He}} + 1), \quad (\text{A.51})$$

where $Y_{\text{He}} \equiv \frac{n_{\text{He}}}{n_H}$ is the *number* abundance of helium. Normally, Eq. A.51 provides a sufficient estimate for calculations of line profiles in OB stars, but for strongly evolved hot stars a significant amount of metals produced by nuclear burning in the stellar core may have been mixed up the surface. In this case one might need to consider also the contribution from the metals in the calculation of the density, which then, in principle, requires that one knows the abundances of *all* elements in the gas, rather than only the abundances of helium and the element under consideration. We shall not consider such cases here.

From the equation of continuity we have

$$\rho = \frac{\dot{M}}{4\pi R_*^2 v_\infty r^2 v}, \quad (\text{A.52})$$

and by combining Eqs. A.48-A.52 we obtain

$$\kappa_0 = qE \frac{\dot{M}}{R_* v_\infty^2} \frac{\pi e^2 / m_e c}{4\pi m_H} \frac{\alpha_k}{1 + 4Y_{\text{He}}} f_{lu} \lambda. \quad (\text{A.53})$$

In Chapters 4 and 5 we have slightly re-defined κ_0 by explicitly accounting for the ionization fraction q . Moreover, we there assumed $E = 1$ (most often sufficient for resonance lines, at least if the considered ionization state is a majority state). In that definition then, κ_0 essentially is a constant. (In Eq. A.53, κ_0 is constant only if qE is constant as well.) For un-saturated lines formed in smooth winds, κ_0 may be empirically inferred from observations, and then translated to an ‘observed’ mass-loss rate, if R_* , v_∞ , Y_{He} , and the abundance α_k all are known from other diagnostics. In this approach, one sometimes chooses not to separate out the ionization fraction q , so that the derived quantity is $\langle q \rangle \dot{M}$ instead of \dot{M} directly (e.g., Fullerton et al., 2006, see also Chapter 5, Sect. 6). Furthermore, we notice that i) the profile-strength is *independent* of κ_0 if the lines are saturated, so that then only lower limits of κ_0 can be inferred, and ii) it considerably complicates the analysis if the wind is *structured* rather than smooth, as extensively discussed in Chapters 4 and 5.

Recombination lines - H_α . In contrast to the UV resonance lines, H_α is a so-called recombination line under typical conditions prevailing in OB star winds, mainly because hydrogen is almost completely ionized in these winds and H_α is formed by transitions between two excited levels (see Chapter 5, also for some comments on H_α ’s transition to a *quasi-resonance* line in the A star regime). Moreover, for recombination line formation (especially in the IR) we can no longer neglect stimulated emission. Thus the frequency integrated extinction coefficient is

$$\chi = \frac{\pi e^2}{m_e c} f_{lu} \left(n_{ljk} - \frac{g_l}{g_u} n_{ujk} \right), \quad (\text{A.54})$$

where l and u now denote the lower and upper levels of the transition, respectively, and we need estimates for both levels (compare to Eq. A.46). We shall use the *departure coefficients* $b_i \equiv n_i/n_i^*$, where n_i^* is defined by the Saha-Boltzmann relation

$$n_{i,j,k}^* = C_1 n_{0,j+1,k} n_e \frac{g_{i,j,k}}{g_{0,j+1,k}} T_e^{-3/2} e^{\varepsilon/k_b T_e}, \quad (\text{A.55})$$

where $C_1 = 2.07 \times 10^{-16}$ in cgs units, and ε is the energy difference between the i, j, k state and the (ground level of the) next ionization state ($0, j+1, k$). Note that, in this definition, the ‘LTE population’ n_i^* is defined *relative to the NLTE population of the ground state of the next ionization stage*, $n_{0,j+1,k}$, and using the *actual* (NLTE) electron densities and temperatures. In some literature (for example in Chapter 6) are the departure coefficients defined relative to the true LTE populations instead, $b_i = n_i/n_i^{\text{LTE}}$, where n_i^{LTE} is calculated using Eq. A.55 but with LTE values of n_e , T_e , and $n_{0,j+1,k}$.²

We shall assume *complete ionization* of hydrogen, which is appropriate for OB-star winds. Thus $n_{0,\text{II,H}} \approx n_{\text{H}}$ and we get for the H_α opacity

$$\chi = \frac{\pi e^2}{m_e c} (f_{lu} g_l) C_1 T_e^{-3/2} (n_e n_{\text{H}}) (b_l e^{\varepsilon_l/k_b T_e} - b_u e^{\varepsilon_u/k_b T_e}). \quad (\text{A.56})$$

As for the resonance lines, we assume a pure hydrogen and helium gas, which may for completely ionized hydrogen be used to calculate the electron density

$$n_e = n_p + n_{\text{He}} I_{\text{He}} = \frac{\rho(1 + Y_{\text{He}} I_{\text{He}})}{m_{\text{H}}(1 + 4Y_{\text{He}})}, \quad (\text{A.57})$$

where I_{He} is the number of free electrons per helium atom, and $I_{\text{He}} \approx 2$ in a typical O-star wind (He III is the dominant ionization state). We then have

$$n_{\text{H}} n_e = \frac{\rho^2(1 + Y_{\text{He}} I_{\text{He}})}{m_{\text{H}}^2(1 + 4Y_{\text{He}})^2}. \quad (\text{A.58})$$

This relation is the reason why diagnostic lines of this type often are called ‘ ρ^2 -diagnostics’. As in the previous paragraph, we may now use the equation of continuity to translate the density to a mass-loss rate, i.e. the greater sensitivity in density also means a greater sensitivity to mass loss, which essentially makes these lines superior to resonance lines for inferring mass-loss rates from observations.

In analogy with the κ_0 parameter, we parametrize the opacity via a line-strength parameter A , defined so that the radial Sobolev optical depth in a smooth wind becomes

$$\tau_{\text{Sob}} = \frac{\chi \lambda R_\star}{v_\infty dv/dr} \left(\propto \frac{\rho^2 \lambda R_\star}{v_\infty dv/dr} \propto \frac{\dot{M}^2 \lambda}{v_\infty^3 R_\star^3 dv/dr v^2 r^4} \right) = \frac{A}{r^4 v^2 dv/dr}. \quad (\text{A.59})$$

A then is

$$A = \frac{\pi e^2}{m_e c} (f_{lu} g_l) \frac{\lambda C_1}{(4\pi)^2 m_{\text{H}}^2} T_e^{-3/2} \frac{\dot{M}^2}{R_\star^3 v_\infty^3} \frac{(1 + Y_{\text{He}} I_{\text{He}})}{m_{\text{H}}(1 + 4Y_{\text{He}})} (b_l e^{\varepsilon_l/k_b T_e} - b_u e^{\varepsilon_u/k_b T_e}). \quad (\text{A.60})$$

² Unfortunately, not everywhere is this notation for the departure coefficients used; although its definition is clear from the text, in for example Chapter 6 we call n_i^* what is here called n_i^{LTE} .

Inserting atomic values for the H_α transition, this becomes

$$A = 49.3 T_e^{-3/2} \frac{\dot{M}^2}{R_\star^3 v_\infty^3} \frac{(1 + Y_{\text{He}} I_{\text{He}})}{m_{\text{H}}(1 + 4Y_{\text{He}})} (b_{\text{l}} e^{3.945/T_e} - b_{\text{u}} e^{1.753/T_e}), \quad (\text{A.61})$$

where T_e is given in units of 10^4 K. In addition to the line opacity we must also specify the source function when modeling the recombination lines (recall again that the source function is only implicit in our Monte-Carlo simulations for resonance lines). Actually, the behavior of the source function is the main reason to the distinct differences between recombination line profiles and resonance line profiles in OB stars, as discussed in Chapter 5. Anyway, since we are neglecting the continuum contribution in the wind (see the previous paragraph), the total source function simply equals the *line* source function, given by Eq. 1.6. Thus, for given departure coefficients, radiation temperature (to set the continuum level), and electron temperatures, we may now calculate synthetic H_α line profiles and, given knowledge of v_∞ , R_\star , and Y_{He} , infer mass-loss rates from comparing to observed ones. Again, if the wind is structured rather than smooth, this considerably complicates a derivation of a unique mass-loss rate, see Chapter 5.

In Chapter 5, we use departure coefficients, electron temperatures, and radiation temperatures as given by corresponding FASTWIND models (see Sect. 1.5.5) calculated under the microclumping approximation. Another, much faster but slightly less precise, approach is to *calibrate* these quantities using a grid of models, as described and done by, e.g., Puls et al. (1996, 2006).

Recombination lines - He II 4686 Å. For formation of the He II 4686 Å line in OB star winds, only small modifications with respect to the H_α approach above are necessary. First of course, the atomic constants must be changed. Moreover, the $(n_e n_{\text{HeIII}})$ term in the Saha-Boltzmann equation should be replaced by $(n_e n_{\text{HeIII}})$. Now, even though He III is the dominant ionization stage throughout the major part of a typical O-star wind, in general it may recombine in the outer wind, and, thus, it is *not* sufficient to assume $n_{\text{He}} \approx n_{\text{HeIII}}$ when calculating the line opacity. This problem is circumvented by introducing the ionization fraction, writing $n_{\text{He}} = n_{\text{HeIII}} q$, with $q = n_{\text{HeIII}}/n_{\text{He}}$. Then we may write

$$n_e n_{\text{HeIII}} = (n_e n_{\text{H}}) Y_{\text{He}} q. \quad (\text{A.62})$$

Thus, Eq. A.60 must only be modified by multiplying with $Y_{\text{He}} q$, and the only additional input-parameter required, as compared to the H_α case, is the ionization fraction q of He III (which we in Chapter 5 also take from corresponding FASTWIND calculations).

Bibliography

Abbott, D. C. 1982, *ApJ*, 259, 282

Abbott, D. C., Bieging, J. H., & Churchwell, E. 1981, *ApJ*, 250, 645

Abbott, D. C. & Lucy, L. B. 1985, *ApJ*, 288, 679

Allen, C. W. 1973, *Astrophysical quantities* (London: University of London, Athlone Press, —c1973, 3rd ed.)

Asplund, M. 2005, *ARA&A*, 43, 481

Asplund, M., Grevesse, N., & Sauval, A. J. 2005, in *Astronomical Society of the Pacific Conference Series*, Vol. 336, *Cosmic Abundances as Records of Stellar Evolution and Nucleosynthesis*, ed. T. G. Barnes III & F. N. Bash, 25–

Asplund, M., Grevesse, N., Sauval, A. J., & Scott, P. 2009, *ARA&A*, 47, 481

Auer, L. H. & Mihalas, D. 1969, *ApJ*, 156, L151

Auer, L. H. & Mihalas, D. 1972, *ApJS*, 24, 193

Aufdenberg, J. P., Hauschildt, P. H., Baron, E., et al. 2002, *ApJ*, 570, 344

Avrett, E. H., Chang, E. S., & Loeser, R. 1994, in *IAU Symposium*, Vol. 154, *Infrared Solar Physics*, ed. D. M. Rabin, J. T. Jefferies, & C. Lindsey, 323–

Baumüller, D. & Gehren, T. 1996, *A&A*, 307, 961

Bouret, J., Lanz, T., Hillier, D. J., & Foellmi, C. 2008, in *Clumping in Hot-Star Winds*, ed. W.-R. Hamann, A. Feldmeier, & L. M. Oskinova, 31–

Bouret, J.-C., Lanz, T., & Hillier, D. J. 2005, *A&A*, 438, 301

Bouret, J.-C., Lanz, T., Hillier, D. J., et al. 2003, *ApJ*, 595, 1182

Brault, J. & Noyes, R. 1983, *ApJ*, 269, L61

Bresolin, F., Crowther, P. A., & Puls, J., eds. 2008, *IAU Symposium*, Vol. 250, *Massive Stars as Cosmic Engines*

Bromm, V. & Larson, R. B. 2004, *ARA&A*, 42, 79

- Bromm, V., Yoshida, N., Hernquist, L., & McKee, C. F. 2009, *Nature*, 459, 49
- Bruls, J. H. M. J., Solanki, S. K., Rutten, R. J., & Carlsson, M. 1995, *A&A*, 293, 225
- Busche, J. R. & Hillier, D. J. 2000, *ApJ*, 531, 1071
- Butler, K. & Giddings, J. R. 1985, *Newsl. Anal. Astron. Spectra*, 9
- Cannon, C. J. 1973, *ApJ*, 185, 621
- Cantiello, M., Langer, N., Brott, I., et al. 2009, *A&A*, 499, 279
- Carlsson, M. 1986, *Uppsala Astronomical Observatory Reports*, 33
- Carlsson, M. 1992, in *Astronomical Society of the Pacific Conference Series*, Vol. 26, *Cool Stars, Stellar Systems, and the Sun*, ed. M. S. Giampapa & J. A. Bookbinder, 499–
- Carlsson, M., Rutten, R. J., & Shchukina, N. G. 1992, *A&A*, 253, 567
- Castelli, F. & Kurucz, R. L. 2004, *ArXiv Astrophysics e-prints*
- Castor, J. I. 1970, *MNRAS*, 149, 111
- Castor, J. I., Abbott, D. C., & Klein, R. I. 1975, *ApJ*, 195, 157
- Chang, E. S. 1984, *Journal of Physics B Atomic Molecular Physics*, 17, L11
- Chang, E. S. 1994, in *IAU Symposium*, Vol. 154, *Infrared Solar Physics*, ed. D. M. Rabin, J. T. Jefferies, & C. Lindsey, 297–
- Chang, E. S., Avrett, E. H., Noyes, R. W., Loeser, R., & Mauas, P. J. 1991, *ApJ*, 379, L79
- Chang, E. S. & Noyes, R. W. 1983, *ApJ*, 275, L11
- Chiappini, C., Hirschi, R., Meynet, G., et al. 2006, *A&A*, 449, L27
- Chlebowski, T. & Garmany, C. D. 1991, *ApJ*, 368, 241
- Cohen, D. H., Leutenegger, M. A., Wollman, E. E., et al. 2010, *MNRAS*, 405, 2391
- Collet, R., Asplund, M., & Trampedach, R. 2007, *A&A*, 469, 687
- Conti, P. S. 1976, *Memoires of the Societe Royale des Sciences de Liege*, 9, 193
- Crowther, P. A. 2007, *ARA&A*, 45, 177
- Crowther, P. A., Hillier, D. J., Evans, C. J., et al. 2002, *ApJ*, 579, 774
- Crowther, P. A., Lennon, D. J., & Walborn, N. R. 2006, *A&A*, 446, 279
- Cunto, W. & Mendoza, C. 1992, *Revista Mexicana de Astronomia y Astrofisica*, vol. 23, 23, 107
- Debye, P., Anderson, Jr., H. R., & Brumberger, H. 1957, *Journal of Applied Physics*, 28, 679

- Decin, L., Vandebussche, B., Waelkens, C., et al. 2003, *A&A*, 400, 709
- Dessart, L. & Owocki, S. P. 2002, *A&A*, 383, 1113
- Dessart, L. & Owocki, S. P. 2003, *A&A*, 406, L1
- Dessart, L. & Owocki, S. P. 2005, *A&A*, 437, 657
- Dotan, C. & Shaviv, N. J. 2010, ArXiv e-prints
- Drake, J. J. & Smith, G. 1991, *MNRAS*, 250, 89
- Drawin, H. W. 1969, *Zeitschrift fur Physik*, 225, 483
- Drew, J. E., Hoare, M. G., & Denby, M. 1994, *MNRAS*, 266, 917
- Ekström, S., Meynet, G., & Maeder, A. 2008, in *IAU Symposium*, Vol. 250, *IAU Symposium*, ed. F. Bresolin, P. A. Crowther, & J. Puls, 209–216
- Evans, C., Hunter, I., Smartt, S., et al. 2008, *The Messenger*, 131, 25
- Evans, C. J., Lennon, D. J., Smartt, S. J., & Trundle, C. 2006, *A&A*, 456, 623
- Evans, C. J., Lennon, D. J., Trundle, C., Heap, S. R., & Lindler, D. J. 2004, *ApJ*, 607, 451
- Evans, C. J., Smartt, S. J., Lee, J.-K., & 23 coauthors. 2005, *A&A*, 437, 467
- Eversberg, T., Lepine, S., & Moffat, A. F. J. 1998, *ApJ*, 494, 799
- Feldmeier, A. 1995, *A&A*, 299, 523
- Feldmeier, A., Hamann, W., Rätzel, D., & Oskinova, L. M. 2008, in *Clumping in Hot-Star Winds*, ed. W.-R. Hamann, A. Feldmeier, & L. M. Oskinova, 115–
- Feldmeier, A., Oskinova, L., & Hamann, W.-R. 2003, *A&A*, 403, 217
- Feldmeier, A., Puls, J., & Pauldrach, A. W. A. 1997, *A&A*, 322, 878
- Foellmi, C., Moffat, A. F. J., & Guerrero, M. A. 2003a, *MNRAS*, 338, 360
- Foellmi, C., Moffat, A. F. J., & Guerrero, M. A. 2003b, *MNRAS*, 338, 1025
- Friend, D. B. & Abbott, D. C. 1986, *ApJ*, 311, 701
- Friend, D. B. & Castor, J. I. 1983, *ApJ*, 272, 259
- Fullerton, A. W., Massa, D. L., & Prinja, R. K. 2006, *ApJ*, 637, 1025
- Gabler, R., Gabler, A., Kudritzki, R. P., Puls, J., & Pauldrach, A. 1989, *A&A*, 226, 162
- Gal-Yam, A. & Leonard, D. C. 2009, *Nature*, 458, 865
- Ganguly, R., Eracleous, M., Charlton, J. C., & Churchill, C. W. 1999, *AJ*, 117, 2594

- Gehren, T., Liang, Y. C., Shi, J. R., Zhang, H. W., & Zhao, G. 2004, *A&A*, 413, 1045
- Giammanco, C., Beckman, J. E., Zurita, A., & Relaño, M. 2004, *A&A*, 424, 877
- Gräfener, G. & Hamann, W.-R. 2005, */aap*, 432, 633
- Gräfener, G. & Hamann, W.-R. 2008, *A&A*, 482, 945
- Gräfener, G., Koesterke, L., & Hamann, W.-R. 2002, *A&A*, 387, 244
- Gray, D. F. 1976, *The observation and analysis of stellar photospheres* (Research supported by the National Research Council of Canada. New York, Wiley-Interscience, 1976. 484 p.)
- Grevesse, N., Asplund, M., & Sauval, A. J. 2007, *Space Science Reviews*, 130, 105
- Güdel, M. & Nazé, Y. 2009, *A&A Rev.*, 17, 309
- Gustafsson, B., Bell, R. A., Eriksson, K., & Nordlund, A. 1975, *A&A*, 42, 407
- Gustafsson, B., Edvardsson, B., Eriksson, K., et al. 2008, *A&A*, 486, 951
- Hamann, W. ., Graefener, G., Oskinova, L. M., & Feldmeier, A. 2009, *ArXiv e-prints*
- Hamann, W.-R. 1981, *A&A*, 93, 353
- Hamann, W.-R., Feldmeier, A., & Oskinova, L. M., eds. 2008, *Clumping in hot-star winds*
- Harnden, Jr., F. R., Branduardi, G., Gorenstein, P., et al. 1979, *ApJ*, 234, L51
- Harper, G. M. 1994, *MNRAS*, 268, 894
- Hauschildt, P. & Baron, E. 2005, *Memorie della Societa Astronomica Italiana Supplement*, 7, 140
- Herrero, A., Puls, J., & Villamariz, M. R. 2000, *A&A*, 354, 193
- Hillier, D. J. 1991, *A&A*, 247, 455
- Hillier, D. J., Lanz, T., Heap, S. R., et al. 2003, *ApJ*, 588, 1039
- Hillier, D. J. & Miller, D. L. 1998, *ApJ*, 496, 407
- Hirschi, R. 2008, in *Clumping in Hot-Star Winds*, ed. W.-R. Hamann, A. Feldmeier, & L. M. Oskinova, 9–
- Hoang-Binh, D. & van Regemorter, H. 1994, in *IAU Symposium, Vol. 154, Infrared Solar Physics*, ed. D. M. Rabin, J. T. Jefferies, & C. Lindsey, 353–
- Hoang-Binh, D. & van Regemorter, H. 1995, *Journal of Physics B Atomic Molecular Physics*, 28, 3147
- Hubeny, I. & Lanz, T. 1995, *ApJ*, 439, 875
- Hunter, I., Brott, I., Langer, N., et al. 2009, *A&A*, 496, 841

- Hunter, I., Dufton, P. L., Smartt, S. J., et al. 2007, *A&A*, 466, 277
- Iglesias, C. A., Rogers, F. J., & Wilson, B. G. 1992, *ApJ*, 397, 717
- Karlsson, T., Johnson, J. L., & Bromm, V. 2008, *ApJ*, 679, 6
- Kobulnicky, H. A. & Fryer, C. L. 2007, *ApJ*, 670, 747
- Krtićka, J. 2006, *MNRAS*, 367, 1282
- Krtićka, J. & Kubát, J. 2000, *A&A*, 359, 983
- Krtićka, J. & Kubát, J. 2001, *A&A*, 369, 222
- Krtićka, J. & Kubát, J. 2004, *A&A*, 417, 1003
- Krtićka, J. & Kubát, J. 2009, *MNRAS*, 323
- Krtićka, J., Puls, J., & Kubát, J. 2008, in *Clumping in Hot-Star Winds*, ed. W.-R. Hamann, A. Feldmeier, & L. M. Oskinova, 111–
- Kubat, J. 2010, *ArXiv e-prints*
- Kudritzki, R., Urbaneja, M. A., Bresolin, F., et al. 2008, *ApJ*, 681, 269
- Kudritzki, R.-P. 2002, *ApJ*, 577, 389
- Kudritzki, R.-P., Lennon, D. J., & Puls, J. 1995, in *Science with the VLT*, ed. J. R. Walsh & I. J. Danziger, 246
- Kudritzki, R.-P., Pauldrach, A., Puls, J., & Abbott, D. C. 1989, *A&A*, 219, 205
- Kudritzki, R.-P. & Puls, J. 2000, *ARA&A*, 38, 613
- Kudritzki, R.-P., Puls, J., Gabler, R., & Schmitt, J. H. M. M. 1991, in *Extreme Ultraviolet Astronomy*, ed. R. F. Malina & S. Bowyer, 130
- Kurucz, R. L. 1979, *ApJS*, 40, 1
- Lacy, J. H., Richter, M. J., Greathouse, T. K., Jaffe, D. T., & Zhu, Q. 2002, *PASP*, 114, 153
- Lamers, H. J. G. L. M. & Cassinelli, J. P. 1999, *Introduction to Stellar Winds*, ed. Lamers, H. J. G. L. M. & Cassinelli, J. P.
- Lamers, H. J. G. L. M., Cerruti-Sola, M., & Perinotto, M. 1987, *ApJ*, 314, 726
- Langer, N. 1998, *A&A*, 329, 551
- Leitherer, C. 2010, in *Astronomical Society of the Pacific Conference Series*, Vol. 425, *Astronomical Society of the Pacific Conference Series*, ed. C. Leitherer, P. Bennet, P. Morris, & J. van Loon, 171–
- Leitherer, C., Ortiz Otálvaro, P. A., Bresolin, F., et al. 2010, *ArXiv e-prints*
- Leitherer, C., Schaerer, D., Goldader, J. D., et al. 1999, *ApJS*, 123, 3

- Lemke, M. & Holweger, H. 1987, *A&A*, 173, 375
- Lépine, S. & Moffat, A. F. J. 2008, *AJ*, 136, 548
- Levermore, C. D., Pomraning, G. C., Sanzo, D. L., & Wong, J. 1986, *Journal of Mathematical Physics*, 27, 2526
- Levesque, E. 2009, ArXiv e-prints
- Lucy, L. B. 1983, *ApJ*, 274, 372
- Lucy, L. B. 2007a, *A&A*, 468, 649
- Lucy, L. B. 2007b, *A&A*, 474, 701
- Lucy, L. B. & Solomon, P. M. 1970, *ApJ*, 159, 879
- Macfarlane, J. J., Waldron, W. L., Corcoran, M. F., et al. 1993, *ApJ*, 419, 813
- Maeder, A. & Meynet, G. 2000, *ARA&A*, 38, 143
- Marcolino, W. L. F., Bouret, J., Martins, F., et al. 2009, *A&A*, 498, 837
- Markova, N. & Puls, J. 2008, *A&A*, 478, 823
- Markova, N., Puls, J., Scuderi, S., & Markov, H. 2005, *A&A*, 440, 1133
- Martins, F., Schaerer, D., Hillier, D. J., & Heydari-Malayeri, M. 2004, *A&A*, 420, 1087
- Martins, F., Schaerer, D., Hillier, D. J., et al. 2005, *A&A*, 441, 735
- Mashonkina, L., Zhao, G., Gehren, T., et al. 2008, *A&A*, 478, 529
- Mashonkina, L. J. 1996, in *Astronomical Society of the Pacific Conference Series*, Vol. 108, M.A.S.S., Model Atmospheres and Spectrum Synthesis, ed. S. J. Adelman, F. Kupka, & W. W. Weiss, 140–
- Massa, D., Fullerton, A. W., Sonneborn, G., & Hutchings, J. B. 2003, *ApJ*, 586, 996
- Massa, D. L., Prinja, R. K., & Fullerton, A. W. 2008, in *Clumping in Hot-Star Winds*, ed. W.-R. Hamann, A. Feldmeier, & L. M. Oskinova, 147–
- Massey, P. 2003, *ARA&A*, 41, 15
- Massey, P., Zangari, A. M., Morrell, N. I., et al. 2009, *ApJ*, 692, 618
- Mauas, P. J., Avrett, E. H., & Loeser, R. 1988, *ApJ*, 330, 1008
- Meynet, G., Maeder, A., Schaller, G., Schaerer, D., & Charbonnel, C. 1994, *A&AS*, 103, 97
- Mihalas, D. 1978, *Stellar atmospheres /2nd edition/*, ed. J. Hevelius
- Mihalas, D., Kunasz, P. B., & Hummer, D. G. 1975, *ApJ*, 202, 465
- Moccia, R. & Spizzo, P. 1988, *Journal of Physics B Atomic Molecular Physics*, 21, 1133

- Moffat, A. F. J., Drissen, L., Lamontagne, R., & Robert, C. 1988, *ApJ*, 334, 1038
- Mokiem, M. R., de Koter, A., Evans, C. J., et al. 2007a, *A&A*, 465, 1003
- Mokiem, M. R., de Koter, A., Evans, C. J., et al. 2006, *A&A*, 456, 1131
- Mokiem, M. R., de Koter, A., Puls, J., et al. 2005, *A&A*, 441, 711
- Mokiem, M. R., de Koter, A., Vink, J. S., et al. 2007b, *A&A*, 473, 603
- Müller, P. E. & Vink, J. S. 2008, *A&A*, 492, 493
- Nieva, M. F. & Przybilla, N. 2007, *A&A*, 467, 295
- Omont, A. 1977, in *Physics of Electronic and Atomic Collisions: ICPEAC X*, 166–
- Oskinova, L. M., Feldmeier, A., & Hamann, W.-R. 2004, *A&A*, 422, 675
- Oskinova, L. M., Feldmeier, A., & Hamann, W.-R. 2006, *MNRAS*, 372, 313
- Oskinova, L. M., Hamann, W.-R., & Feldmeier, A. 2007, *A&A*, 476, 1331
- Owocki, S. P. 2008, in *Clumping in Hot-Star Winds*, ed. W.-R. Hamann, A. Feldmeier, & L. M. Oskinova, 121–
- Owocki, S. P., Castor, J. I., & Rybicki, G. B. 1988, *ApJ*, 335, 914
- Owocki, S. P. & Cohen, D. H. 2006, *ApJ*, 648, 565
- Owocki, S. P., Gayley, K. G., & Shaviv, N. J. 2004, *ApJ*, 616, 525
- Owocki, S. P. & Puls, J. 1996, *ApJ*, 462, 894
- Owocki, S. P. & Puls, J. 1999, *ApJ*, 510, 355
- Owocki, S. P. & Puls, J. 2002, *ApJ*, 568, 965
- Owocki, S. P. & Rybicki, G. B. 1984, *ApJ*, 284, 337
- Pauldrach, A. 1987, *A&A*, 183, 295
- Pauldrach, A., Puls, J., & Kudritzki, R. P. 1986, *A&A*, 164, 86
- Pauldrach, A. W. A., Hoffmann, T. L., & Lennon, M. 2001, *A&A*, 375, 161
- Pauldrach, A. W. A., Hoffmann, T. L., & Méndez, R. H. 2004, *A&A*, 419, 1111
- Pauldrach, A. W. A., Kudritzki, R. P., Puls, J., Butler, K., & Hunsinger, J. 1994, *A&A*, 283, 525
- Pauldrach, A. W. A. & Puls, J. 1990, *A&A*, 237, 409
- Pengelly, R. M. & Seaton, M. J. 1964, *MNRAS*, 127, 165
- Pomraning, G. C. 1991, *Linear kinetic theory and particle transport in stochastic mixtures*, ed. Pomraning, G. C.

- Prinja, R. & Massa, D. 2010, ArXiv e-prints
- Prinja, R. K., Massa, D., & Searle, S. C. 2005, *A&A*, 430, L41
- Przybilla, N. & Butler, K. 2004, *ApJ*, 609, 1181
- Przybilla, N., Butler, K., Becker, S. R., & Kudritzki, R. P. 2001, *A&A*, 369, 1009
- Puls, J. 1987, *A&A*, 184, 227
- Puls, J. 2009, *Communications in Asteroseismology*, 158, 113
- Puls, J., Kudritzki, R., Santolaya-Rey, A. E., et al. 1998, in *Astronomical Society of the Pacific Conference Series*, Vol. 131, *Properties of Hot Luminous Stars*, ed. I. Howarth, 245–
- Puls, J., Kudritzki, R.-P., Herrero, A., et al. 1996, *A&A*, 305, 171
- Puls, J., Markova, N., & Scuderi, S. 2008a, in *Astronomical Society of the Pacific Conference Series*, Vol. 388, *Mass Loss from Stars and the Evolution of Stellar Clusters*, ed. A. de Koter, L. J. Smith, & L. B. F. M. Waters, 101–
- Puls, J., Markova, N., Scuderi, S., et al. 2006, *A&A*, 454, 625
- Puls, J., Owocki, S. P., & Fullerton, A. W. 1993, *A&A*, 279, 457
- Puls, J., Springmann, U., & Lennon, M. 2000, *A&AS*, 141, 23
- Puls, J., Sundqvist, J. O., Najarro, F., & Hanson, M. M. 2009, in *American Institute of Physics Conference Series*, Vol. 1171, *American Institute of Physics Conference Series*, ed. I. Hubeny, J. M. Stone, K. MacGregor, & K. Werner, 123–135
- Puls, J., Urbaneja, M. A., Venero, R., et al. 2005, *A&A*, 435, 669
- Puls, J., Vink, J. S., & Najarro, F. 2008b, *A&A Rev.*, 16, 209
- Repolust, T., Puls, J., Hanson, M. M., Kudritzki, R., & Mokiem, M. R. 2005, *A&A*, 440, 261
- Repolust, T., Puls, J., & Herrero, A. 2004, *A&A*, 415, 349
- Robert, C. 1994, *Ap&SS*, 221, 137
- Romano, D., Karakas, A. I., Tosi, M., & Matteucci, F. 2010, ArXiv e-prints
- Runacres, M. C. & Owocki, S. P. 2002, *A&A*, 381, 1015
- Runacres, M. C. & Owocki, S. P. 2005, *A&A*, 429, 323
- Rutten, R. J. & Carlsson, M. 1994, in *IAU Symposium*, Vol. 154, *Infrared Solar Physics*, ed. D. M. Rabin, J. T. Jefferies, & C. Lindsey, 309–
- Rybicki, G. B. & Hummer, D. G. 1978, *ApJ*, 219, 654
- Rybicki, G. B. & Hummer, D. G. 1991, *A&A*, 245, 171

- Ryde, N., Harper, G. M., Richter, M. J., Greathouse, T. K., & Lacy, J. H. 2006, *ApJ*, 637, 1040
- Ryde, N., Korn, A. J., Richter, M. J., & Ryde, F. 2004, *ApJ*, 617, 551
- Ryde, N., Lambert, D. L., Richter, M. J., & Lacy, J. H. 2002, *ApJ*, 580, 447
- Sana, H., Rauw, G., Nazé, Y., Gosset, E., & Vreux, J. 2006, *MNRAS*, 372, 661
- Scharmer, G. B. 1981, *ApJ*, 249, 720
- Schmutz, W. 1995, in *IAU Symposium*, Vol. 163, *Wolf-Rayet Stars: Binaries; Colliding Winds; Evolution*, ed. K. A. van der Hucht & P. M. Williams, 127–
- Seaton, M. J. 1962, in *Atomic and Molecular Processes*, ed. D. R. Bates, 375–
- Shaviv, N. J. 2001a, *ApJ*, 549, 1093
- Shaviv, N. J. 2001b, *MNRAS*, 326, 126
- Sigut, T. A. A. & Lester, J. B. 1996, *ApJ*, 461, 972
- Simón-Díaz, S. 2010, *A&A*, 510, A22
- Smith, M. A. & Dominy, J. F. 1979, *ApJ*, 231, 477
- Smith, N. 2008, in *Astronomical Society of the Pacific Conference Series*, Vol. 388, *Mass Loss from Stars and the Evolution of Stellar Clusters*, ed. A. de Koter, L. J. Smith, & L. B. F. M. Waters, 129–
- Smith, N., Davidson, K., Gull, T. R., Ishibashi, K., & Hillier, D. J. 2003, *ApJ*, 586, 432
- Smith, N. & Owocki, S. P. 2006, *ApJ*, 645, L45
- Sobolev, V. V. 1960, *Moving envelopes of stars* (Cambridge: Harvard University Press, 1960)
- Springmann, U. W. E. & Pauldrach, A. W. A. 1992, *A&A*, 262, 515
- Steenbock, W. & Holweger, H. 1984, *A&A*, 130, 319
- Stein, R. F. & Nordlund, A. 1998, *ApJ*, 499, 914
- Sundqvist, J. O., Puls, J., & Feldmeier, A. 2010, *A&A*, 510, A11
- Sundqvist, J. O., Ryde, N., Harper, G. M., Kruger, A., & Richter, M. J. 2008, *A&A*, 486, 985
- ud-Doula, A. & Owocki, S. P. 2002, *ApJ*, 576, 413
- Uitenbroek, H. & Noyes, R. W. 1996, in *Astronomical Society of the Pacific Conference Series*, Vol. 109, *Cool Stars, Stellar Systems, and the Sun*, ed. R. Pallavicini & A. K. Dupree, 723–
- van Marle, A. J., Owocki, S. P., & Shaviv, N. J. 2008, *MNRAS*, 389, 1353
- van Regemorter, H. 1962, *ApJ*, 136, 906
- Vink, J. S., de Koter, A., & Lamers, H. J. G. L. M. 2000, *A&A*, 362, 295

- Vink, J. S., de Koter, A., & Lamers, H. J. G. L. M. 2001, *A&A*, 369, 574
- Voss, R., Diehl, R., Vink, J. S., & Hartmann, D. H. 2010, ArXiv e-prints
- Waldron, W. L. & Cassinelli, J. P. 2010, *ApJ*, 711, L30
- Wood, K., Haffner, L. M., Reynolds, R. J., Mathis, J. S., & Madsen, G. 2005, *ApJ*, 633, 295
- Woosley, S. E. 1993, *ApJ*, 405, 273
- Woosley, S. E., Heger, A., & Weaver, T. A. 2002, *Reviews of Modern Physics*, 74, 1015
- Yoon, S., Langer, N., & Norman, C. 2006, *A&A*, 460, 199
- Zhao, G., Butler, K., & Gehren, T. 1998, *A&A*, 333, 219
- Zsargó, J., Hillier, D. J., Bouret, J.-C., et al. 2008, *ApJ*, 685, L149

Acknowledgments

I am deeply grateful to my thesis supervisor Joachim Puls for his, in all possible respects, great support during my PhD. Through countless and endless discussions with him did this thesis ‘slowly, but surely’ develop, ‘one step after the other’. It is absolutely impossible for me to in a few lines here express a proper thanks to him for all that I have learned (for I have also been taught that sometimes when writing, one really needs space in order to explain). I will only say that it is my hope, as well as my belief, that our collaboration will not come to an end after this thesis, but rather continue for long, so that together we can make sure that ‘excellent progress continuous to be made’ (which may not be an original, but for me is what truly characterizes what it’s like working with Jo).

I am equally grateful to Karin Lind, without whom I could have never achieved what I have actually achieved. Over the past six years, first as undergraduates in Uppsala then as graduates in Munich, she has been my touchstone in school and science and my support in life.

It has been a privilege to meet and work with a number of excellent astronomers. I am indebted to Achim Feldmeier and Stan Owocki for many fruitful discussions and collaborations. I thank Paco Najarro in particular for my stay in Madrid, and Alex Fullerton for providing invaluable observational data. A special thanks to Nils Ryde, my old supervisor in Uppsala, who initiated the magnesium project that came to be a part also of this thesis. From my Uppsala time, I also thank Kjell Eriksson and Bengt Gustafsson for many stimulating discussions.

I would like to extend my thanks to all the people that strive to create the nicest possible working atmosphere at the Sternwarte. Also, I thank the lunch-group in particular for the salad that rests beside my Indisch dish every Thursday, Johannes Koppenhöfer and the running-group in particular for once more making me try to reach below 40 minutes in 10 kilometers, and the football-team in particular for Adi Pauldrach, who never ceases to amaze the rest of us with his unwavering spirit.

Finally, I gratefully acknowledge a grant from the International Max-Planck Research School of Astrophysics (IMPRS), Garching.

Curriculum Vitae

Personal information

Name: Jon Olof Sundqvist
Date of birth: 12. September 1980
Place of birth: Östersund, Sweden
Civil status: Single

Education

Aug. 1997 - Jun. 1999 High-school degree, majoring in economics and social science, Wargentinskolan Östersund, Sweden
Sep. 2000 - Jun. 2001 Base year of natural science degree, University of Gävle, Sweden
Aug. 2002 - Dec. 2002 Exchange student at Eastern Connecticut State University, USA
Sep. 2003 - Aug. 2007 Master of Science degree, majoring in physics and astrophysics, University of Uppsala, Sweden
Thesis title: 'Modeling stellar Mg I emission lines at 12 μm '
Sep. 2007 - Sep. 2010 PhD in astrophysics, Ludwig Maximilian University, Munich, Germany. Thesis title: 'Quantitative spectroscopy of stellar atmospheres and clumped hot star winds - new methods and first results for deriving mass-loss rates'

Publications

J.O. Sundqvist, J. Puls, A. Feldmeier, S.P. Owocki
Mass loss from inhomogeneous hot star winds II. Constraints from a combined optical/UV study
accepted for publication in *Astronomy & Astrophysics*

J.O. Sundqvist, J. Puls, A. Feldmeier
Mass loss from inhomogeneous hot star winds I. Resonance line formation in 2D models
Astronomy & Astrophysics, 2010, 510, A11

J.O. Sundqvist, N. Ryde, G.M Harper, A. Kruger, M.J. Richter
Mg I emission lines at 12 and 18 μm in K giants
Astronomy & Astrophysics, 2008, 486, 985S

J.O. Sundqvist, J. Puls, A. Feldmeier, S.P. Owocki
A proper description of clumping in hot star winds: the key to obtaining reliable mass-loss rates?
Conference proceedings article presented at ‘The multi-wavelength view of hot, massive stars’; 39th
Liège Int. Astroph. Coll., 12-16 July 2010

J. Puls, **J.O. Sundqvist**, J.G. Rivero González
OB-stars as extreme condition test beds
Review article to be published in the proceedings book of the IAUS 272, Cambridge University Press.
Editors C. Neiner, G. Wade, G. Meynet and G. Peters, pre-print available at arXiv:1009.0364

J. Puls, **J.O. Sundqvist**, F. Najarro, M.M. Hanson
Mass loss from OB-stars
Review article in AIPC 1171, American Institute of Physics Conference Series, ed. I. Hubeny, J. M. Stone, K. MacGregor, & K. Werner, 123-135

Work experience

1995 - 1997	Q8 Gas station Krokomb, Sweden, Shop assistant/Cashier (part time substitute)
1997 - 1999	ICA Supermarket Krokomb, Sweden, Shop assistant/Cashier (part time substitute)
Jun.1999 - Feb.2000	ICA Supermarket Krokomb, Sweden, Shop assistant/Cashier (full time employee)
Feb.2000 - Aug.2000	Swedbank, Krokomb, Sweden, Bank cashier (full time employee)
Aug.2001 - Jun.2002	Dvårsätt elementary school, Sweden, Personal assistant/Subs. teacher (70 % of full time employee)
Jun.-Aug. 2003, 2004,2006	Swedbank, Krokomb, Sweden, Bank cashier (full time substitute employee)

Languages

Swedish	Native language
English	Fluent
German	Good